Constraints on the primordial spectrum and inflationary potential from cosmological observations.

International Relativistic Astrophysics Ph.D

Dottorato di Ricerca in Astrofisica Relativistica – 26 Ciclo Sapienza, IX IRAP

Candidate

Micol Benetti

ID number 694626

Thesis Advisor

Prof. Alessandro Melchiorri

Co-Advisor

Dr. Massimiliano Lattanzi

A thesis submitted in partial fulfillment of the requirements for the degree of Doctor of Philosophy in PhD

20 February 2014

Thesis defended on March 2014
in front of a Board of Examiners composed by:

Prof. Paolo **De Bernardis** - *Professore Ordinario presso Sapienza, Università di Roma.* (chairman)

Prof. Carlo **Baccigalupi** - *Professore Associato presso SISSA, Scuola Internazionale Superioriore di Studi Avanzati di Trieste.*

Dr. Fabio **Finelli** - *Ricercatore presso INAF - IASF, Istituto di Astrofisica Spaziale e Fisica cosmica, Bologna.*

Constraints on the primordial spectrum and inflationary potential from cosmological observations.
Ph.D. thesis. Sapienza – University of Rome

This thesis has been typeset by LaTeX and the Sapthesis class.

Version: 20 February 2014

Author's email: Micol.Benetti@gmail.com

Contents

Introduction

Cosmology today is a vibrant scientific enterprise. New precision measurements are revealing a universe with surprising and unexpected properties and the theory of *general relativity* has allowed the development of theoretical models capable of describing quantitatively for the structure and the evolution of the present universe. The greatest progress in cosmology was achieved in the last two decades and the primary role has been played by the observation of the *cosmic microwave background* anisotropies, formed at the time of recombination, about thirteen billion years ago and just four hundred thousand years after the *big bang*. These anisotropies provide crucial information on quantities such as the density of dark matter or the density of baryons present in the universe, the curvature of the universe itself and the spectrum of primordial perturbations. Moreover, these involve important implications in the fields of fundamental and particle physics, making it possible to investigate phenomena at high energies that are difficult to reach in standard laboratories. An important example is the neutrino: the amount of primordial relativistic neutrinos changes the epoch of the matter- radiation equality, leaving an imprint on both cosmic microwave background data anisotropies and on structure formation, while non relativistic neutrinos in the recent universe suppress the growth of matter density fluctuations and galaxy clustering.
The currently available data are several and highly accurate: galaxy surveys such as the Sloan Digital Sky Survey are making the first large-scale maps of the universe, and satellites such as WMAP and Planck have make exquisitely precise measurements of the cosmic microwave background. A special mention goes to the Planck satellite and its first data release (made available in March 2013) which provide measurements of the cosmic background radiation anisotropies with an unprecedented accuracy, due to a higher angular resolution and a broader frequency range. Furthermore, we have high expectations for the next decade mission Euclid, which will provide complementary measurements of the large scale structures of the universe.
This brings us to the current state of modern cosmology: we have a theory that makes predictions, and these predictions can be tested by observations.
Although the ΛCDM *model* is in an impressive agreement with all the available observations, on the one hand it depends on some parameters whose value has to be constrained through observations, and on the other hand it has some known critical issues that led cosmologists to formulate some complementary or alternative theories beyond the *standard model* in order to address these features. Indeed, even in the simplest picture of the universe provided by the standard model there are still some open questions in cosmology, among which we can mention the existence and the nature of the two dark components of the universe and the initial conditions (and

the shape) of the primordial perturbations.
In this thesis, the attention is focused on the *inflation*. The inflationary paradigm is an integral part of the currently accepted concordance cosmological model, explaining the flatness and homogeneity of the observed universe, as well as providing a mechanism to produce the primordial curvature perturbations that eventually led to the formation of structures. The cosmic microwave background data are in excellent agreement with the prediction of the simplest inflationary scenario of a single, minimally-coupled scalar field slowly rolling down a smooth potential which produce a nearly scale-invariant power spectrum of scalar perturbations. Nevertheless, a scale-invariant power spectrum could be easily put in agreement with data in some non-minimal models.
One of the aims of our work is to derive constraints on the parameters of slow-roll inflation also in the context of non-minimal models, like those that include massive neutrinos and/or a non-standard number of relativistic degrees of freedom.
On the other hand, models with localized features in the power spectrum (like those generated by violation of slow roll) may provide a better fit to the data with respect to a smooth power-law spectrum. This is mainly due to the presence, in the temperature anisotropy spectrum, of two outliers at large scale. Features in the primordial power spectrum can be generated following departures from slow roll, that can happen in more general inflationary models. In particular, in multi-field super-gravity- or M-theory-inspired models, a field coupled to the inflaton can undergo a symmetry-breaking phase transition and acquire a vacuum expectation value. Such a phase transition corresponds to a sudden change in the inflaton effective mass and can be modeled as a step in the inflationary potential. The presence of the step produces, in turn, a burst of oscillations in the power spectrum of curvature perturbations, localized around the scale that is crossing the horizon at the time the phase transition occurred.

Summarizing, in this thesis we will focus on some specific topics, namely:

- the inflationary theory in the context of the standard cosmological model and its prediction;
- implications of considering an inflationary scenario on the constraints on a minimal cosmological model;
- constraints on inflationary parameters from current data and reconstruction of the inflationary initial potential;
- constraints on effective number and masses of neutrinos using current data, and their impact on the reconstruction of the inflationary potential;
- the presence of such a step-like feature in the inflaton potential, implications and constraints from the data;

The first chapter introduces the standard cosmological model, the definition of the Cosmological Principle and the Friedmann-Lemaître-Robertson- Walker metric. We introduce background evolution of the homogeneous universe and give a picture of the universe history at the best of our knowledge.

The second chapter complicates the assumptions, studying the case of non-homogeneous universe. We present the current theory of structure formation based on a linear perturbations of Einstein equations, obtaining a system of linear differential equations which must be integrated numerically. In the second part of the chapter, we give an overview of the properties of the cosmic microwave background radiation describing the basic mechanisms of the formation of the anisotropies dividing them into two categories: primary and secondary anisotropies.

In order to solve the perturbed equations it is necessary to define the initial conditions determined during the inflationary process. The third chapter describes the fundamental principles of the inflationary model and we show how it solves the well known problems of the big bang theory and how it provides the production mechanism of the primordial perturbations which, in turn, form the seeds of the cosmological structures.

In the last two chapters we present the results obtained in the work performed during my Ph.D. In the fourth chapter, we show the constraints that can be obtained on minimal *Harrison-Zel'dovich models* extended with both parameters of inflation and of neutrino. So, we extract information from recent observations on the inflationary theory and we show how to reconstruct the initial inflationary potential from the data.

Finally, in chapter five, we address particular inflationary models able to produce features in the anisotropy spectrum of the cosmic background. We discuss the theory and constraint its parameters, seeing how much they are in agreement with the recent cosmological experiments.

In appendix, we review some of the statistical methods used in cosmology for extracting information from current data.

Chapter 1

The Standard Cosmological Model

The aim of cosmology is the development of a universe evolution model that is in agreement with the observed data.
A good description of the universe is provided by the theory of general relativity. As gravity is the overriding force at cosmological distances, Einstein's theory allows the description of space-time geometry and explains the distorting effect of gravity on space. However, the relevant equations get very complicated when applied to the universe, since the universe is not homogeneous. Nevertheless, the problem can be simplified in the first instance by considering a model which approximates a homogeneous universe. This is called the *standard cosmological model* and allows the study of the universe as a first-order perturbation of a homogeneous universe.

In this chapter we introduce the Cosmological Principle and the Friedmann-Lemaître-Robertson-Walker metric. We also define the concept of distances in an expanding universe and we describe how we measure them. Then, we give an overview of the components of the universe and the history of the early universe. However, in the next chapter, we will complicate the assumptions studying the case of non-homogeneous universe.

1.1 The cosmological principle: Metric and dynamic of universe.

The standard cosmological model is based on the assumption of the so-called *Cosmological Principle* which state isotropy (rotational invariance) and homogeneity (translational invariance) of the universe on large scales (larger than $100 - 200$Mpc). This leads to the absence of a privileged position or direction in the universe.
The application of the cosmological principle significantly limits the great variety of possible cosmological models. Isotropy has been confirmed on large scales by many factors, such as:

- the distribution of clusters and super-clusters of galaxies,
- the distribution of radio-sources,

- the uniformity of the background radiation, particularly the *Cosmic Microwave Background radiation* (CMB) temperature, with $\delta T/T \simeq 10^{-5}$, which describes a strongly isotropic universe at the time of the emission of the radiation (about 300000 years after the big-bang), or the background X-radiation between 2 and 20 keV produced by unresolved sources up to distances of thousands of Mpc.

It can be shown that, by increasing the number of samples of cosmological object, isotropy rises. According to the Copernican principle, there is no reason to consider our position privileged, hence there must be isotropy in each point of the universe. At last, there is a theorem of geometry that states that isotropy at every point implies homogeneity [1].

1.2 The Friedmann-Lemaître-Robertson-Walker metric.

Once the cosmological principle is proved, the metric to use for four dimensional space-time is the Roberson-Walker metric. We assume a system of coordinates in the space-time: three space coordinates (x^α where $\alpha = 1, 2, 3$) and a temporal coordinate (t), measured by a freely-falling observer. As known from the theory of general relativity, the geometrical properties of the coordinate system are determined by the metric tensor $g_{\mu\nu}$. The interval ds between two events in space-time is given by the following expression:

$$ds^2 = g_{\mu\nu} dx^\mu dx^\nu. \tag{1.1}$$

In a space-time that is not curved by gravitational effects, as in the theory of special relativity, we have:

$$g_{\mu\nu} = \begin{pmatrix} -1 & 0 & 0 & 0 \\ 0 & 1 & 0 & 0 \\ 0 & 0 & 1 & 0 \\ 0 & 0 & 0 & 1 \end{pmatrix}.$$

The interval ds can be written in the simplest form $ds^2 = -c^2dt^2 + dx^2 + dy^2 + dz^2$ from which, converting to spherical coordinates, we can obtain Minkowsky's metric (which is therefore only applicable within special relativity):

$$ds^2 = -c^2dt^2 + dr^2 + r^2 d\Omega^2, \tag{1.2}$$

where $d\Omega^2 = d\theta^2 + \sin^2\theta d\varphi^2$.

When gravity is also included, Minkowsky's metric is no longer applicable. In 1939, A. Friedmann [2], G. Lemaître [3] , H. P. Robertson [4] and A. G. Walker [5] independently developed a metric of a homogeneous and isotropic space, where the distances can expand or contract as functions of time. The Friedmann-Lemaître-Robertson-Walker (FLRW) metric can be written in the following way:

$$ds^2 = -c^2dt^2 + a^2(t)[d\chi^2 + S_k(\chi)^2 d\Omega^2], \tag{1.3}$$

where:

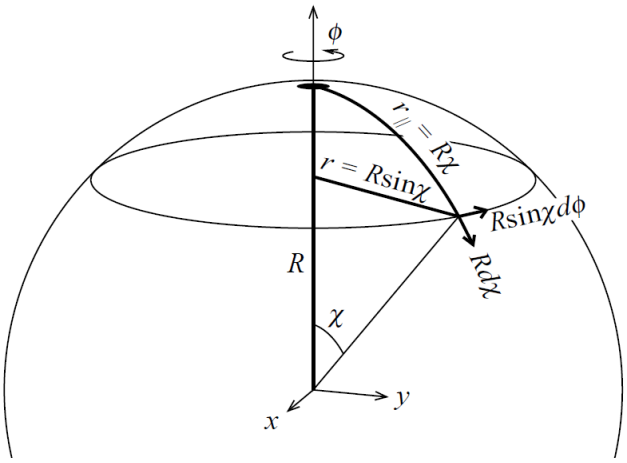

Figure 1.1. It shows an embedding diagram of a 3D hypersphere in 4D Euclidean space. The horizontal directions in the diagram represent the normal spatial x, y, z dimensions, with one dimension z suppressed, while the vertical dimension represents the 4th spatial dimension.

- the coordinate t, called *cosmic time* or proper cosmological time, is the time measured by an observer who sees the universe evolving in a uniform expansion around him;
- the spatial variables (see Fig.(1.1)) are called *comoving coordinates* because they describe the position of an object in the expanding universe reference frame. Therefore they are constant because they label material objects that are in their rest frame;
- the *scale factor* $a(t)$, which describes the way in which the distances contract or expand in function of time, is normalized to $a(t_0) = 1$ at the present time. The expansion can be described only for scales greater than 100Mpc, where the cosmological principle is valid and there is a homogeneous and isotropic expansion;
- the value of the function $S_k(\chi)^2$ depends on the curvature of the universe.

A more general form of the FLRW metric can be written in the following way [6]:

$$ds^2 = -c^2dt^2 + a^2(t)\left[\frac{dr^2}{1-kr^2} + r^2d\Omega^2\right], \tag{1.4}$$

where we use the comoving radial coordinate r and the *curvature constant* k. It is dimensionless and can always be renormalized so that can take the values:

- $k = +1$, for universe positively curved with spherical geometry,
- $k = 0$, for universe spatially flat,
- $k = -1$, for universe negatively curved with hyperbolic geometry.

The comoving coordinate distance r is related to χ by $\chi = r$ if $k = 0$, by $\chi = \sin^{-1} r$ if $k = 1$, and by $\chi = \sinh^{-1} r$ if $k = -1$.

1.3 Hubble law and expansion of the universe.

The observed shift of a galaxy's spectrum through the identification of spectral absorption lines allows the calculation of the relative motion between source and observer on the basis of the Doppler effect:

$$z = \frac{\lambda_0 - \lambda_e}{\lambda_e}, \tag{1.5}$$

where λ_e is the emission wavelength and λ_0 the observed wavelength. There are three possible cases:

- if $z < 0$, the source is approaching the observe, this will result in a *blueshift* (all spectral lines are displaced towards shorter wavelengths).
- If $z = 0$, the source would not be moving either towards or away from the observer.
- If $z > 0$, the source is moving away from the observer. This will result in a *redshift* (all spectral lines are displaced towards longer wavelengths).

Since the first studies made by V. Slipher [7], C. W. Wirtz [8] and E. Hubble [9] on the redshift of distant galaxies, in most cases the spectral lines of galaxies are red-shifted. In 1929, Edwin Hubble established the existence of a linear relationship between the recession speed of a galaxy v and its distance from the observer (Fig.(1.2)). The Hubble law states that

$$v \simeq H_0 d = cz, \tag{1.6}$$

where c is the speed of light and H_0 is the Hubble constant, which corresponds, as we will see, to the present value of the Hubble parameter that appears in the Friedmann equation.
A recent estimate of the value of H_0 has been obtained using data from a mid-infrared calibration of the Cepheid distance scale based on recent observations at 3.6 μm with the *Spitzer Space Telescope*: $H_0 = 74.3 \pm 0.4$(statistical) ± 2.1(systematic) km s^{-1}/Mpc [10].

The correct interpretation of the redshift and the recession of galaxies establishes that, as time elapses, space expands, leading to an increase in the distance between galaxies. By the same token, the wavelengths of photons are stretched, since they expand with space. In other words, wavelengths extend in the same manner as intergalactic distances lengthen. From this law we infer that the observable universe must have a finite range, approximately equal to what has been called the *Hubble time*:

$$t_0 \simeq \frac{r}{v} = \frac{r}{rH_0} = {H_0}^{-1} \simeq (14.0 \pm 1.4) Gyrs. \tag{1.7}$$

In fact, assuming that the relative velocity is constant, since galaxies are rapidly moving away from one another, they should have been much closer in the past. About 14 Gyrs ago (a Hubble time ago) they must have been compressed in an extremely small volume. This leads naturally to the big-bang model for the evolution of the universe. This model implies that the universe has expanded to its present low-density state from an initial hot and dense state, in a homogeneous and isotropic way. However

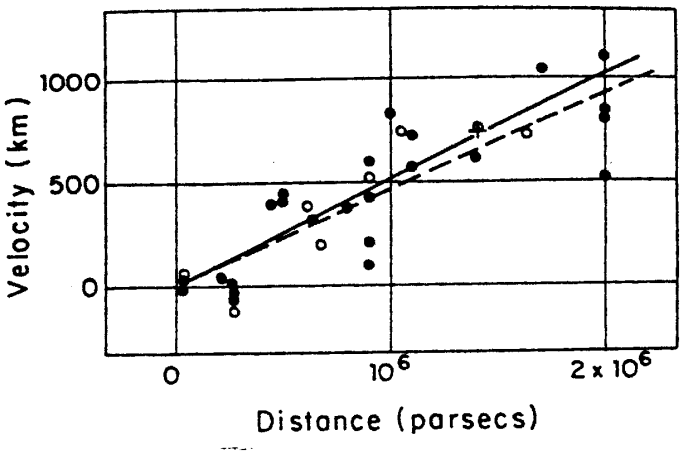

Figure 1.2. Diagram of the recession velocity in km/sec of extragalactic nebulae (the units are accidentally written as km rather km/s) plotted against their distances in parsecs as originally observed by Edwin Hubble in 1929.

the Hubble time only gives a natural scale of time. The age of the universe might not necessarily be equal to H_0^{-1}. Indeed, if the expansion velocity in the past had been different than it is now, then the age of the universe would be different from H_0^{-1}.

The *proper distance* $d_p(t)$ is the length of the spatial geodesic between the two points for a defined value of $a(t)$, referring to a given instant of time. This distance can change over time due to the expansion of the universe and we can obtain it by integrating over the comoving radial coordinate r the Eq.(1.4), since the universe is flat and angles are constant over the spatial geodesic:

$$d_p(t) = a(t) \int_0^r dr = a(t)r. \tag{1.8}$$

Indeed the *proper velocity* of a receding galaxy is:

$$v_p(t) = \dot{d}_p(t) = \dot{a}(t)r \equiv \frac{\dot{a}(t)}{a(t)} d_p(t) = H(t) d_p(t), \tag{1.9}$$

where $H(t) \equiv \frac{1}{a}\frac{da}{dt} = \frac{\dot{a}}{a}$ measures how fast the scale factor changes with time.

It is convenient to define the *conformal time*, the distance that light can travel (in the absence of interactions) since $t = 0$. In a time dt, light travels a comoving distance $dx = dt/a$ (if we set $c = 1$), so the total comoving distance is:

$$\eta \equiv \int_0^t \frac{dt'}{a(t')}. \tag{1.10}$$

The *Hubble causal horizon* is the spacetime region in which one point could affect or have been affected by other points. Objects separated by comoving distances larger than η today were not ever in causal contact: there is simply no way information could have propagated over distances larger than η. It exists a maximum distance

to which the observer can see, known as the *particle horizon distance* and it exists a limit to space-time events which can be influenced by the emitter, known as the *event horizon distance*.
Just as the Hubble time H_0^{-1} provides a rough guide for the age of the universe, the Hubble distance:

$$d_H(t_0) = \frac{c}{H_0}, \tag{1.11}$$

provides a rough estimate of the event horizon distance in a matter- or radiation-dominated universe. It is a critical distance such that two points at a distance greater than $d_H(t_0)$ will have $v_p > c$. This result refers to the relative motion of objects inside an expanding universe and therefore does not violate the law limiting the speed of massive objects at the speed of light. With H_0 obtained from prior observations, we have $d_H(t_0) \sim 4062$ Mpc. Galaxies farther than this distance are moving away from us at superluminar speeds.

There is also a very important relation between the redshift of a galaxy z and the value of the scale factor at the time t_e of the emission of observed photon, $a(t_e)$: it shows that the redshift of a distant object depends only on the ratio of the scale factor at the times of emission and observation and not on the way in which the light travelled between $a(t_e)$ and $a(t_0)$. Since photons follow a null geodesic [1], we have that $c^2dt^2 = a(t)^2dr^2 \rightarrow c\frac{dt}{a(t)} = dr$. Integrating between t_e and t_0 and considering a monochromatic wave with wavelength λ_e we have [6]:

$$c\int_{t_e}^{t_0} \frac{dt}{a(t)} = \int_0^r dr = r. \tag{1.12}$$

For the next crest emitted at the time $t_0 + \frac{\lambda_0}{c}$ it will be possible to write a similar integral. By equating the integrals of two successive wave crests it is possible to obtain:

$$c\int_{t_e}^{t_e+\frac{\lambda_e}{c}} \frac{dt}{a(t)} = c\int_{t_0}^{t_0+\frac{\lambda_0}{c}} \frac{dt}{a(t)}. \tag{1.13}$$

Since $H_0 \gg \frac{\lambda}{c}$, we can assume that between the emission and the observation of two wave crests the universe has not expanded by a significant amount. Hence we can say that $a(t)$ has remained constant during that time. Thus we get, by integrating the Eq.(1.13):

$$\frac{\lambda_e}{a(t_e)} = \frac{\lambda_0}{a(t_0)}. \tag{1.14}$$

By substituting the Eq.(1.5), we obtain:

$$1 + z = \frac{a(t_0)}{a(t_e)} = \frac{1}{a(t_e)}, \tag{1.15}$$

where the equation has been normalized with $a(t_0) = a_0 = 1$. Therefore, measuring the redshift z of a galaxy allows to determine $a(t_e)$.

[1] with $ds^2 = 0$ and constant angles θ and φ.

1.4 Einstein equations and Friedmann equations.

The Einstein equations.

In order to explain the dynamic of the universe, it is necessary to determine the evolution of the scale factor. This can be done by establishing the relationship between the description of the metric of a homogeneous and isotropic space and the mass-energy contained in the universe. This relationship is given by Einstein's field equations which describe the dynamics of the universe by determining the evolution of the scale factor $a(t)$. If $G_{\mu\nu}$ is the Einstein tensor, T^{μ}_{ν} the *stress-energy tensor* (also called *energy-momentum tensor*), $R_{\mu\nu}$ the *Ricci curvature tensor*, and R the *scalar curvature*, defined by $R = g^{\mu\nu}R_{\mu\nu}$, then *Einstein's equations* can be written:

$$G_{\mu\nu} \equiv R_{\mu\nu} - \frac{1}{2}Rg_{\mu\nu} = 8\pi G T_{\mu\nu}, \tag{1.16}$$

where G is the Newton constant.
This set of ten equations describes the fundamental interaction of gravity as a result of space-time being curved by matter and energy. It gives the relationship between space-time geometry (represented by the metric and the Ricci tensor and scalar) and the energy and pressure at a point in space-time (related to the stress-energy-tensor). Einstein's equations will eventually require the calculation of the tensor components of the equation. First we consider the left side of Eq.(1.16). The Ricci tensor $R_{\mu\nu}$ can be expressed through the *Christoffel symbols* $\Gamma^{i}_{jk} = \frac{1}{2}g^{\alpha\beta}[g_{\mu\beta,\nu} + g_{\nu\beta,\mu} + g_{\mu\nu,\beta}]$ [11] in the following way:

$$R_{\mu\nu} = \Gamma^{\alpha}_{\mu\nu,\alpha} - \Gamma^{\alpha}_{\mu\alpha,\nu} + \Gamma^{\alpha}_{\beta\alpha}\Gamma^{\beta}_{\mu\nu} - \Gamma^{\alpha}_{\beta\nu}\Gamma^{\beta}_{\mu\alpha}, \tag{1.17}$$

where the commas indicate the derivatives with respect to the coordinate. Using the expression of the metric given by Eq.(1.4) in the above expression of $\Gamma^{\mu}_{\alpha\beta}$, we obtain the Christoffel symbols and, consequently, the Ricci tensor and Ricci scalar. This allows the calculation of the Einstein tensor, which can then be written:

$$G_{00} = 3\left(\frac{\dot{a}}{a}\right)^2 + \frac{3k}{a^2}, \tag{1.18}$$

$$G_{11} = G_{22} = G_{33} = -2\frac{\ddot{a}}{a} - \left(\frac{\dot{a}}{a}\right)^2 - \frac{k}{a^2}, \tag{1.19}$$

$$G_{others} = 0. \tag{1.20}$$

The Friedmann's Equations.

On cosmological scales it is possible to model the energy content of the universe as a perfect fluid[2]. Considering this particular case, the energy-momentum tensor $T_{\mu\nu}$ takes the form:

$$T_{\mu\nu} = (\rho + P)U_{\mu}U_{\nu} + Pg_{\mu\nu}, \tag{1.21}$$

[2]A perfect fluid is defined as a medium for which at every point there is a locally inertial Cartesian frame of reference, comoving with the fluid, in which the fluid appears the same in all directions. It is an isotropic fluid with negligible viscosity and heat conduction.

where ρ is the *energy density* of the fluid, P its *pressure* and U_μ its *four-velocity*, with the normalization $U^\mu U_\mu = 1$. According to the FLRW metric, the pressure P must be isotropic. Hence it can be written, with P and ρ only depending on time, as:

$$T^\mu_\nu = \begin{pmatrix} -\rho & 0 & 0 & 0 \\ 0 & P & 0 & 0 \\ 0 & 0 & P & 0 \\ 0 & 0 & 0 & P \end{pmatrix}.$$

Combining the expression of the stress-energy tensor with the FLRW metric equation, we can obtain the *first Friedmann's equation* [2] [6]:

$$H^2 = \left(\frac{\dot{a}}{a}\right)^2 = \frac{8\pi G}{3c^2}\sum_i \rho_i - \frac{kc^2}{a^2}. \tag{1.22}$$

For any given value of the Hubble parameter, we can define the *critical energy density* as:

$$\rho_c = \frac{3H^2c^2}{8\pi G}. \tag{1.23}$$

If the energy density is greater than ρ_c, the universe is positively curved ($k = 1$) and vice versa. Therefore, we can introduce the *density parameter* as the ratio of the total energy density and the critical energy density:

$$\Omega_{tot}(t) = \frac{\sum_i \rho_i}{\rho_c}. \tag{1.24}$$

Friedmann's equation can then be written:

$$1 - \Omega_{tot}(t) = -\frac{kc^2}{a(t)^2H(t)^2}. \tag{1.25}$$

The density parameter relates the total energy density to the geometry of the universe:

$$\Omega_{tot} > 1 \rightarrow k = 1,$$

$$\Omega_{tot} = 1 \rightarrow k = 0,$$

$$\Omega_{tot} < 1 \rightarrow k = -1.$$

We define the *curvature component*:

$$\Omega_k(t) = 1 - \Omega_{tot}(t) = -\frac{kc^2}{a(t)^2H(t)^2}. \tag{1.26}$$

The curvature of the universe depends on the total energy density at any time t, knowing $\Omega_{tot}|_{today}$ the sign of the curvature k can be found.

Looking again the energy-momentum tensor $T_{\mu\nu}$ (Eq.(1.21)), the energy-momentum conservation is expressed in general relativity as $\bigtriangledown_\mu T^{\mu\nu} = 0$. For the assumption of FLRW metric with $\nu = 0$ component and flat geometry $k = 0$, *energy conservation* reads:

$$\frac{d\rho}{dt} + 3H(\rho + P) = 0. \tag{1.27}$$

This equation is actually not independent on the Friedmann and acceleration equations, but is required for consistency. It implies that the expansion of the universe can lead to local changes in the energy density. Note that there is no notion of conservation of total energy, as energy can be interchanged between matter and the space-time geometry.

It is convenient to define an equation of *state parameter*, that relates pressure and density. Assuming that the universe is well described by a perfect fluid, it is possible to use the simple formulation:

$$w \equiv \frac{P}{\rho}. \tag{1.28}$$

If w is constant (with value dependent on the considered component and varying in the range $-1 < w < 1$), then the solution of Eq.(1.27) is straightforward:

$$\rho \propto a^{-3(1+w)}. \tag{1.29}$$

Note that the behaviours of dust (non-relativistic particles, $w = 0$) and radiation (gas of radiation, whether it be actual photons or other highly relativistic species, $w = 1/3$) is consistent with what we would have obtained by more heuristic reasoning.
If we consider a fixed comoving volume of the universe with a given fixed number of dust particles (of mass m) inside, the energy density will scale just as the physical volume, $a(t)^{-3}$, in agreement with Eq.(1.29) with $w = 0$.
To make a similar argument for radiation, we see Eq.(1.5). First, we note that the expansion of the universe with the time results in a shift to longer wavelength λ of photons propagating in this background. Therefore the energy density, in a fixed number of photons in a fixed comoving volume, drops with the physical volume (as for dust) and by an extra factor as the expansion of the universe stretches the wavelengths of light. Thus, the energy density of radiation will scale as $a(t)^{-4}$, once again in agreement with Eq.(1.29) with $w = 1/3$.

Combining Eq.(1.27) with Eq.(1.22) we can derive the acceleration equation which gives the variation of acceleration with time:

$$\frac{\ddot{a}}{a} = -\frac{4\pi G}{3c^2}\sum_i(\rho_i + 3P_i). \tag{1.30}$$

It is the *second Friedmann's equation* [6], the *acceleration equation*. It describes the time variation of the expansion rate of the universe and so the possibility of accelerated or decelerated expansion. If the energy density is greater than or equal to zero [3], it gives a negative acceleration which means that the relative speed of two points decreases. Hence, both components of matter and radiation cause negative acceleration.
A case of particular interest is $w \leq -1/3$, a component with negative pressure that

[3] noting that a gas of ordinary baryonic matter has a positive pressure, resulting from the random thermal motions of the molecules, atoms or ions of which the gas is made. A gas of photons also has a positive pressure.

determines the acceleration of the universe, generally called *dark energy* (it will be discussed afterwards).
A particularly interesting kind of dark energy is the *cosmological constant* Λ, because its existence is strongly supported by observational evidence.

1.5 The deceleration parameter.

The time evolution of the scale factor can be studied by expanding in a Taylor series around t_0:

$$a(t) = a(t_0) + \dot{a}(t_0)(t - t_0) + \frac{1}{2}\ddot{a}(t_0)(t - t_0)^2. \tag{1.31}$$

We define the dimensionless *deceleration parameter*:

$$q_0 = -\left(\frac{\ddot{a}a}{\dot{a}^2}\right)_{t=t_0} = -\left(\frac{\ddot{a}}{aH^2}\right)_{t=t_0}. \tag{1.32}$$

Its value is negative if the expansion of the universe is accelerating, vice versa if is decelerating. The above equation became, at t_0 ($a(t_0) = 1$):

$$a(t) = 1 + H_0(t - t_0) - \frac{1}{2}q_0 H_0^2(t - t_0)^2. \tag{1.33}$$

In order to measure the value of the scale factor and to understand the evolution of the universe, we need to know q_0 and H_0. The value of q_0 in a universe with many components can be provided by the acceleration equation (Eq.(1.30)). Considering this equation for the present time, we obtain the relationship between q_0 and the density parameter at the present moment:

$$q_0 = \frac{1}{2}\sum_i \Omega_{i,0}(1 + 3\omega), \tag{1.34}$$

where for each component is defined the density parameter $\Omega_i = \frac{\rho_i}{\rho_c}$. Hence, for a universe formed on radiation, matter and cosmological constant we have:

$$q_0 = \Omega_{r,0} + \frac{1}{2}\Omega_{m,0} - \Omega_{\Lambda,0}. \tag{1.35}$$

1.6 The luminosity distance and the angular diameter distance.

Measurement of H_0 in principle is simple. For small value of the redshift we use the Eq.(1.6). Knowing d and the redshift value by the measure of a great number of galaxies, from the plot of cz versus d we can obtain the slope of the interpolation, which give an estimate of H_0.
To measure the distance of distant galaxies, we have already introduced the proper distance and derive the Eq.(1.12).
Since $a(t_e) \sim \frac{1}{z_e}$ from Eq.(1.5), and the expansion in a Taylor series of the scale factor (Eq.(1.33)), by inverting the relation we obtain:

$$t_0 - t = \frac{1}{H_0}\left[z - \left(1 + \frac{q_0}{2}\right)z^2 + ...\right]. \tag{1.36}$$

The distance can be approximated inserting the expansion of the scale factor (Eq.(1.33)) in the Eq.(1.12), that is:

$$dp(t_0) \simeq c(t_0 - t_e) + \frac{cH_0}{2}(t_0 - t_e)^{-2}. \tag{1.37}$$

A critical issue is to measure distances using the observation of the physical properties of other galaxies. One of the most important methods is based on the use of the so-called *standard candles*, which are objects whose *luminosity* L is known. Measuring the *energy flux* f received on earth and knowing the luminosity we can define a function called *luminosity distance*:

$$d_L = \left(\frac{L}{4\pi f}\right)^{1/2}. \tag{1.38}$$

In an expanding universe governed by the FLRW metric, the relationship between flux and luminosity is:

$$f = \frac{L}{4\pi S_k^2(1+z)^2}. \tag{1.39}$$

Hence the luminosity distance is $d_L = S_k(1+z)$.
The luminosity distance of an object with redshift z depends both on the geometry of the universe and on its dynamics. In our case the latest observational data seem to indicate a flat geometry for our universe. Since $k = 0$, the luminosity distance can then be written [6]:

$$d_L = r(1+z) = d_p(t_0)(1+z). \tag{1.40}$$

Moreover, when $z \ll 1$, using Eq.(1.36) we can write d_L as:

$$d_L \simeq \frac{c}{H_0} z \left[1 + \frac{1-q_0}{2} z\right]. \tag{1.41}$$

For a flat universe and assuming $z \to 0$, the luminosity distance is a good approximation of the proper distance at the present time. Indeed, $d_p(t_0) \simeq d_L \simeq (c/H_0)z$.

We now introduce another kind of distance, the *angular diameter distance*.
Knowing the length of an object l (*proper length*), assuming for simplicity that this object is disposed perpendicularly to the view line and measuring the angular dimension $\delta\theta$ of the object, we can define:

$$d_A \equiv \frac{l}{\delta\theta}. \tag{1.42}$$

The angular distance corresponds to the proper distance only if the universe is static and euclidean. For the FLRW metric, the length l measured at time t_e of the emission of the light is $l = ds = a(t_e)S_k(r)\delta\theta = \frac{S_k(r)\delta\theta}{1+z}$, from which:

$$d_A = \frac{S_k(r)}{1+z}. \tag{1.43}$$

Comparing this relationship with the definition of d_L when $k = 0$ (Eq.(1.40)) we obtain the relationship between the angular diameter and the luminosity distance:

$$d_A = \frac{d_L}{(1+z)^2} = \frac{d_p(t_0)}{1+z} = d_p(t_e). \tag{1.44}$$

Furthermore, if $z \ll 1$, $d_A \simeq \frac{c}{H_0} z \left[1 - \frac{3+q_0}{2} z\right]$. As $z \to 0$, becomes:

$$d_A \simeq d_L \simeq d_p(t_0) \simeq \frac{c}{H_0} z. \tag{1.45}$$

The angular diameter distance has a maximum for a precise value of z, denoted by z_{max}. In a model with $\Omega_{m,0} = 0.3$ and $\Omega_{\Lambda,0} = 0.7$, $z_{max} = 1.6$ which corresponds to the angular distance $d_{A,max} = 1800$Mpc.

1.7 The cosmological constant.

In 1917, Einstein applied his equations to the universe as a whole and, without experimental evidence, he was persuaded that the universe was static. He imagined that much of the radiation in the universe was provided by stars and that the main contribution to the energy density came from non-relativistic matter. He therefore considered the approximation of a universe without pressure.
Einstein realised that a universe that contains nothing but matter could not be static, so he inserted in his equations a term Λ called cosmological constant. It can be treated as an energy-density component with the energy-momentum tensor $T_{\mu\nu} = -\frac{\Lambda}{8\pi G} g_{\mu\nu}$. It is defined as a component of the universe with:

$$w = -1, \qquad P = -\rho, \qquad \rho = \frac{\Lambda}{8\pi G} = constant, \tag{1.46}$$

where ρ_Λ does not depend on the scale factor which means that it remains unchanged over time. We say that the cosmological constant is equivalent to vacuum energy.
The Friedmann equations that describe a static universe filled with matter are:

$$\left(\frac{\dot{a}}{a}\right)^2 = \frac{8\pi G}{3c^2}\rho - \frac{kc^2}{a^2} + \frac{\Lambda}{3}, \tag{1.47a}$$

$$\frac{\ddot{a}}{a} = \frac{4\pi G}{3c^2}(\rho + 3P) + \frac{\Lambda}{3}. \tag{1.47b}$$

In order to have a static universe, both $\dot{a}$ and $\ddot{a}$ must be zero, then $\Lambda = 4\pi G\rho/c^2$.

From these equations, adding the density parameter of dark energy Ω_{DE} and developing the Hubble parameter expression in terms of the redshift z, in the case of a flat universe ($\Omega_m + \Omega_{DE} = 1$) we obtain:

$$H(z) = H_0[\Omega_{m,0}(1+z)^3 + \Omega_{DE}(1+z)^{3(1+w)^{1/2}}]. \tag{1.48}$$

If $w = -1$, then $\Omega_{DE} = \Omega_\Lambda$. In the standard model of cosmology, dark energy accounts for 74% of the total mass-energy of the universe. The cosmological constant is one of the proposed forms for dark energy and it is physically equivalent to vacuum energy (other form include, for instance, quintessence which is a dynamical quantity whose energy density can vary in time and space).

1.8 Component of cosmological fluid.

The main components of the universe are photons, baryons, dark matter, neutrinos and dark energy. As they appear in the Friedmann's equations and influence the cosmological evolution of our universe, it is necessary to introduce these components and know their energy density and the evolution with the scale factor. Here, we also provide a density estimation for each component of the universe, referring to the first data release of the recent and highly precise Planck experiment.

1.8.1 Matter.

In order to obtain the density of matter present in the universe, we must consider that there are two kinds of matter: ordinary matter which can be observed directly (called baryonic matter), and dark matter whose existence can only be measured by its gravitational effect on baryonic matter but whose nature is still unknown.
We will now analyse these two kinds of matter.

Baryonic matter. Baryonic matter is no longer homogeneous. Indeed, there are such great density perturbations that we cannot define a simple distribution function depending, for example, only on temperature. Consequently, the baryonic density must be determined from observation. It can be determined from measurement of the CMB anisotropy power spectrum or through hydrogen absorption lines of distant quasar (their strength indicates the quantity of gas the light has passed through before it is observed). Another method consists of determining the baryonic density from visible sources in nearby galaxies, although this method does not take into account the vast amount of baryonic matter in the interstellar gas, which is not contained in stars and galaxies.
Moreover, the study of primordial *nucleosynthesis* allows a good estimation of baryonic density. Nucleosynthesis is the process of creating new atomic nuclei from nucleons (protons and neutrons). Primordial nucleosynthesis took place a few minutes after the big-bang (we see this briefly later) and during it are created the first heavier isotopes of hydrogen, known as deuterium. These deuterium nuclei reacted between themselves, forming the helium isotopes (He-3 and He-4) and the lithium isotopes (Li-6 and Li-7). The amount of deuterium is very sensitive to the conditions at this early stage, from the amount of deuterium left we can estimate the baryonic density. Nowadays there are about 30 atoms of deuterium per a million hydrogen atoms and it can be shown that about 25% of the total density of particles in the universe is made up of helium and almost all the remaining is hydrogen.
Several different methods give similar values for the baryonic density. The Planck collaboration has estimated for the matter density the value of:

$$\Omega_b = 0.02205 \pm 0.00028,$$

with $h = 0.673 \pm 0.12$ km s-1 Mpc-1 (this value is in tension with recent direct measurements of H_0 we have said, but are in excellent agreement with geometrical constraints from baryon acoustic oscillation (BAO) surveys).

Dark matter. The existence of dark matter was first hypothesized by F. Zwicky [14] to account for evidence of missing mass in the orbital velocities of galaxies in galactic clusters. He estimated, studying the characteristic of the Coma cluster, the mass of the orbiting galaxies from their luminosity and compared it with the mass estimated from the measure of the dispersion velocity of the galaxies. He found that the virial theorem gave a mass 400 times greater than the mass obtained from the luminosity of the Coma cluster. The gravity of the visible galaxies in the cluster would be far smaller for such fast orbits, so extra mass was required. Based on these conclusions, Zwicky inferred that there must be some non-visible form of matter which would provide enough mass and gravity to hold the cluster together: the dark matter.
The comparison of the speed curve in spiral galaxies against the distance from the centre is another approach that has given irrefutable evidence of the existence of dark matter. In the 1950s V. Rubin [15] shows that the observed speed profile, at great distances from the galactic centre, does not decrease as $1/\sqrt{r}$, as would be expected, but remains constant. This show that there must be a large amount of mass that is not visible, an enormous dark matter halo around the visible mass of the galaxy.
Dark matter can also be revealed through gravitational effect on other observed radiation sources. The phenomenon is called *gravitational lensing*, and consists of unseen matter that bends light from sources behind it. This fact makes dark matter extremely difficult to detect, as it can only be observed through its gravitational effect.
Candidates for nonbaryonic dark matter are hypothetical particles such as *axions*, or *supersymmetric particles*; neutrinos can only form a small fraction of the dark matter, due to limits from large-scale structure and high-redshift galaxies. Nonbaryonic dark matter is classified in terms of the mass of the particle(s) that is assumed to make it up, and/or the typical velocity dispersion of those particles (since more massive particles move more slowly).
There are three prominent hypotheses for non-baryonic dark matter, called *cold dark matter* (CDM), *warm dark matter* (WDM), and *hot dark matter* (HDM), depending on its speed at the moment of decoupling from baryonic matter (*i.e.* hot if the speed is relativistic, that is $kT_{dec} > mc^2$).
The most widely discussed models for nonbaryonic dark matter are based on the CDM hypothesis, and the corresponding particle is most commonly assumed to be a weakly interacting massive particle (WIMP).
Many methods allow the measurement of the density parameter of dark matter (among them, the study of the CMB anisotropies). The Planck data provides for the CDM density today a value of:

$$\Omega_{dm} h^2 = 0.1199 \pm 0.0027.$$

1.8.2 Neutrinos.

The neutrino was postulated first by W. Pauli [17] to explain how beta decay could conserve energy, momentum, and spin. E. Fermi, who developed the theory of beta decay, coined the term *neutrino* and gave a solid theoretical basis for future

experimental work [17].
Overlooking the interesting history that leads to the current knowledge of neutrino physics, we briefly introduce that neutrinos are created from radioactive decay or nuclear reactions, such as those taking place in the sun, in nuclear reactors or when cosmic rays hit atoms. Neutrinos do not carry electric charge, which means that they are not affected by the electromagnetic forces that act on charged particles such as electrons and protons; they are affected only by the weak sub-atomic force, of much shorter range than electromagnetism, and gravity, which is relatively weak on the subatomic scale. Therefore a typical neutrino passes through normal matter unimpeded. Neutrinos have half-integer spins ($\frac{\hbar}{2}$) and is therefore a fermion. There are three types (or *flavors*) of neutrinos: electron neutrinos ν_e, muon neutrinos ν_μ and tau neutrinos ν_τ. Each type of neutrino is associated with an antiparticle, called *antineutrino*, which also has neutral electric charge and half-integer spin.
The discovery of neutrino flavor oscillations implies that neutrinos have mass. The strongest upper limit on the masses of neutrinos comes from cosmology: the big-bang model predicts that there is a fixed ratio between the number of neutrinos and the number of photons in the CMB, from this we can obtain the number of neutrinos. It can be demonstrated that if the total energy of all three types of neutrinos exceeded an average of 50 eV per neutrino, there would be so much mass in the universe that it would collapse. Clearly, this not happened. This limit can be circumvented by assuming that the neutrino is unstable (first hypothesized by B. Pontecorvo [18]); however, there are limits within the standard model that make this difficult.
A stringent constraint comes from a careful analysis of cosmological data, such as the CMB radiation, galaxy surveys, and the Lyman-alpha forest. By the Planck experiment, we estimate the effective number of relativistic degrees of freedom for neutrino: $N_{eff} = 3.30 \pm 0.27$, and the upper limit value for the sum of neutrino masses: $\sum m_\nu = 0.23$ eV (in comparison, the electron mass is 0.5 MeV).
As the mass of neutrinos is very small, we can conclude that neutrinos are relativistic particles. At low energies the density values is

$$\Omega_\nu h^2 \sim 10^{-4},$$

insignificant in the space-time evolution of the universe. Despite this, neutrino research is very important in astrophysics because of its implication in many fields, such as probing astrophysical sources beyond our solar system or measuring the neutrinos produced in the galactic core of the Milky Way. These are only two of many examples of the reasons to observe neutrinos in astrophysics. We will talk more about neutrino and we will put constraints on its parameters in Chapter 4.

In the 1980s it was proposed that these may be the explanation for the dark matter thought to exist in the universe. Neutrinos have one important advantage over most other dark matter candidates: we know they exist. However, they also have serious problems. First, neutrino speeds close to the speed of light. Thus, dark matter made from neutrinos is termed *hot dark matter*. The problem is that being fast moving, the neutrinos would tend to spread out evenly in the universe before cosmological expansion made them cold enough to congregate in clumps. This would cause the part of dark matter made of neutrinos to be smeared out and unable to cause the large galactic structures that we see. Further, these same galaxies and

groups of galaxies appear to be surrounded by dark matter that is not fast enough to escape from those galaxies. Presumably this matter provided the gravitational nucleus for the formation. This implies that neutrinos make up only a small part of the total amount of dark matter.
From cosmological arguments, relic background neutrinos are estimated to have a density of 56 of each type per cubic centimeter and temperature 1.9 K if they are massless, much colder if their mass exceeds 0.001 eV. Although their density is quite high, due to extremely low neutrino cross-sections at sub-eV energies, the relic neutrino background has not yet been observed in the laboratory. In contrast solar neutrinos, which are emitted with a higher energy, have been detected definitively despite having a space density that is lower than that of relic neutrinos by some 6 orders of magnitude.

1.8.3 Photons. The Cosmic Microwave Background radiation.

The photon is an elementary particle, the quantum of the electromagnetic interaction. It is massless, has no electric charge, is stable and has two possible polarization states. Photons are emitted in many natural processes. For example, when a charge is accelerated it emits synchrotron radiation. During a molecular, atomic or nuclear transition to a lower energy level, photons of various energy will be emitted, from radio waves to gamma rays. A photon can also be emitted when a particle and its corresponding antiparticle are annihilated (for example, electron-positron annihilation). Certainly there is much to say on the subject, what we'll do in this section is to briefly recall the photons in the CMB.

In the *recombination epoch* (see later), the universe became transparent and neutral. At that time were formed first atoms and the photons started to travel freely through space rather than constantly being scattered by electrons and protons in plasma. The photons that existed at the time of *photon decoupling* have been propagating ever since, though growing fainter and less energetic, the expansion of space causes their wavelength to increase over time. This is the source of the alternative term relic radiation. The temperature of the decoupled photons at the recombination time was about 3000 K, now extremely less and their temperature will continue to drop as the universe expands. These photons form the CMB radiation, discovered by A. Penzias and R.W.Wilson which were awarded the 1978 Nobel Prize in Physics.
At first approximation, from the last scattering to the present time there are not processes able to change the shape of this spectrum. The only variation concerns the temperature. This has been well verified by several observation of the last 15 years, starting from the COsmic Background Explorer (COBE) [21]. COBE confirmed the black body nature of the background, measuring a temperature $T_0 = 2.725 \pm 0.002K$ through the spectrometer FIRAS (Far Infrared Absolute Spectro-photometer). Moreover the Differential Microwave Radiometer (DMR) carried on COBE allowed the first observation of an intrinsic anisotropy in the CMB temperature on scales of several degrees. The most relevant characteristic of the CMB is its noticeably isotropy. Temperature fluctuations are of the order of $\sim 10^{-5}$, that is at the order of μK. These small fluctuation are indeed of greatest interest and they will be discussed in detail in the next chapter. As the angular dimensions of

these anisotropies depend on the curvature of the universe (the angular dimension of an object of fixed linear dimension are smaller in a negatively curved universe rather then in positively curved universe), the current measures of the angular dimension of these anisotropies lead to the conclusion that we leave in flat universe with zero curvature ($k = 0$).
For our aim, let us look the relationships:

$$T_{CMB} = 2.728(1 + z),$$
$$\rho_{\gamma,CMB} = \frac{\pi^2}{15} T^4.$$

We can see that the energy density of photons in the universe only depends on T. The number of photons per unitary volume is $n_\gamma = 4.11 \times 10^8 m^{-3}$, i.e. there are 411 photons per cubic centimeter in the present universe.
The energy of the photons is very low, and the fact that it is called Cosmic Microwave Background depends on the mean energy density of the photons that corresponds to a wavelength of two millimeters, that is placed in the millimetric range of the electromagnetic spectrum.
Considering the energy density of photons equation with the current value of the temperature, we obtain ρ_γ and hence the density parameter:

$$\Omega_\gamma(t_0) = \Omega_\gamma = \frac{2.47 \times 10^{-5}}{h^2 a^4}.$$

We have seen that neutrinos are relativistic and therefore they are coupled with photons, which allow us to treat them together: we define the *radiation density parameter* $\Omega_r = \Omega_\gamma + \Omega_\nu$.

1.8.4 Dark energy.

Dark energy is the most accepted hypothesis to explain observations from Supernovae[4], CMB[5] and other[6,7] indicate that the universe is expanding at an accelerating rate. It is, therefore, a hypothetical form of energy that permeates all of space and tends to accelerate the expansion of the universe [23].

Two proposed forms for dark energy are the *cosmological constant* [24], briefly

[4]The Nobel Prize in Physics 2011 won by S. Perlmutter, B. P. Schmidt and A. G. Riess "for the discovery of the accelerating expansion of the universe through observations of distant supernovae" [22].

[5]Measurements of CMB anisotropies indicate that the universe is close to flat. To get this shape, the mass/energy density of the universe must be equal to the critical density. If the total amount of matter in the universe accounts for only about 30% of the critical density, then there must be an additional form of energy to account for the remaining 70%.

[6]Confirmation to cosmic acceleration independent of supernovas come from the WiggleZ galaxy survey (2011), scanned more than 200,000 galaxies to determine their redshift. The data confirmed cosmic acceleration up to half of the age of the universe (7 billion years) and constrain its inhomogeneity to 1 part in 10.

[7]The Integrated Sachs-Wolfe effect (ISW) shows that accelerated cosmic expansion causes gravitational potential wells and hills to flatten as photons pass through them, producing cold spots and hot spots on the CMB aligned with vast supervoids and superclusters. It is a direct signal of dark energy in a flat universe.

introduced in the previous paragraph it is a constant energy density filling space homogeneously, and *scalar fields* such as quintessence or moduli, dynamic quantities whose energy density can vary in time and space. It is crucial to understand how the dark energy evolves: measure the equation of state for dark energy is one of the biggest efforts in observational cosmology today. Assuming the cosmological constant the simplest solution for the dark matter problem, according to the Planck mission team [13] and based on the standard model of cosmology, the total mass-energy of the universe contains 4.9% ordinary matter, 26.8% dark matter and 68.3% dark energy. It is clear, therefore, that the dark energy plays a key role, although it is still matters of speculation. By the Planck experiment, the dark energy density divided by the critical density today has the values:

$$\Omega_\Lambda = 0.685^{+0.018}_{-0.016}$$

1.9 The evolution of the scale factor.

The study of the evolution of the universe is complicated by the presence of many components, each with a different equation of state. We have seen the different components of the universe, we understand now what role plays these components in our universe and in the last paragraph of the chapter we will talk briefly about their history in the history of the universe.

The energy density and the pressure can be summed for each component: the total energy density can then be written:

$$\rho = \sum_w \rho_w, \tag{1.50}$$

where ρ_w is the energy density of the component with the equation of state characterized by the parameter w; the total pressure, using the Eq.(1.28) is:

$$P = \sum_w P_w = \sum_w w\rho_w. \tag{1.51}$$

Assuming that there are no interactions between the different components, the fluid equation can be written as in Eq.(1.27). Integrating and normalizing to the present time when $a_0 = 1$ and the energy density is $\rho_{w,0}$, the Eq.(1.29) is written as:

$$\rho_w(a) = \rho_{w,0} a^{-3(1+w)}. \tag{1.52}$$

A flat universe constituted of radiation, matter, curvature and cosmological constant is the model that best fits with our universe: $\Omega_0 = \Omega_{r,0} + \Omega_{m,0} + \Omega_{c,0} + \Omega_{\Lambda,0}$. In this case, recalling Eq.(1.24) and Eq.(1.26), we have:

$$\left(\frac{H}{H_0}\right)^2 = \left(\frac{\Omega_{r,0}}{a^4} + \frac{\Omega_{m,0}}{a^3} + \frac{\Omega_{c,0}}{a^2} + \Omega_{\Lambda,0}\right). \tag{1.53}$$

Looking at the Fig.(1.3), we see the evolution of the single components and we see that each period of the universe story has a dominant component in which the Friedmann equation can be considerably simplified. Considering a flat universe ($\Omega = 1$,$k = 0$), and neglecting the period dominated by the curvature, we have:

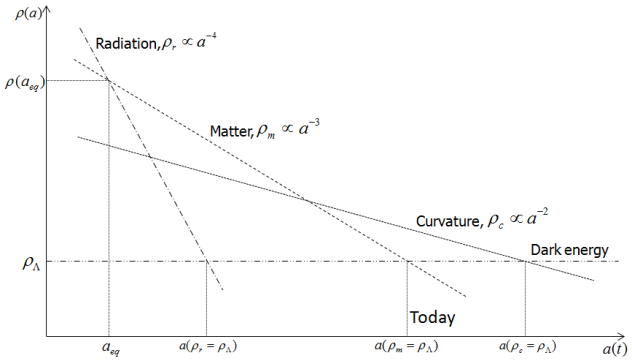

Figure 1.3. Evolution of ρ(a) as function of the scale factor a in the universe story.

- Radiation-dominated era: $\Omega_r a^{-4} \gg \Omega_m a^{-3} + \Omega_\Lambda$.
  $\frac{\dot{a}}{a}^2 = \Omega_r \frac{H_0^2}{a^4} \longrightarrow a(t) = \sqrt{\Omega_r}.H_0^{\frac{1}{2}} t^{\frac{1}{2}}$
- Matter-dominated era: $\Omega_m a^{-3} \gg \Omega_r a^{-4} + \Omega_\Lambda$.
  $\frac{\dot{a}}{a}^2 = \Omega_m \frac{H_0^2}{a^3} \longrightarrow a(t) = \left(\frac{3}{2} H_0 \sqrt{\Omega_m}\right)^{\frac{2}{3}} t^{\frac{2}{3}}$.
- Dark energy-dominated era: $\Omega_\Lambda \gg \Omega_m a^{-3} + \Omega_r a^{-4}$.
  $\frac{\dot{a}}{a}^2 = \Omega_\Lambda H_0^2 \longrightarrow a(t) = e^{\sqrt{\Omega_\Lambda} H_0 (t - t_0)}$.

During the equivalent time we must consider both components that participate in the change of domination. In that case $a(t)$ does not have a simple analytical form and the Friedmann equation (Eq.(1.22)) became:

$$\dot{a}^2 = \frac{8\pi G}{3c^2} \sum_w \rho_{w,0} a^{-1-3w} - kc^2. \tag{1.54}$$

Considering now the phase when matter and cosmological constant dominated in the Eq.(1.53), rewrite using $\Omega_{\Lambda,0} = 1 - \Omega_{m,0}$:

$$\left(\frac{H}{H_0}\right)^2 = \frac{\Omega_{m,0}}{a^3} + (1 - \Omega_{m,0}). \tag{1.55}$$

Depending on the value of $\Omega_{m,0}$, as we can see in Fig.(1.4), different scenarios are possible:

- $\Omega_{m,0} < 1$. In this case the second term is positive and the expansion will last forever.
- $\Omega_{m,0} > 1$. In this case the cosmological constant will be attractive. There will a phase of expansion until the maximum value $a_{max} = \frac{\Omega_{m,0}}{\Omega_{m,0} - 1}$, followed by a phase of contraction with $t_c = \frac{2\pi}{3H_0} \frac{1}{\sqrt{\Omega_{m,0} - 1}}$ which will be earlier if $\Omega_{m,0}$ is greater.

The most general expression for the age of universe is:

$$H_0 t = \int_0^a \frac{da}{\left(\frac{\Omega_{r,0}}{a^2} + \frac{\Omega_{m,0}}{a} + \Omega_{\Lambda,0} a^2 + (1 - \Omega_0)\right)^{1/2}}. \tag{1.56}$$

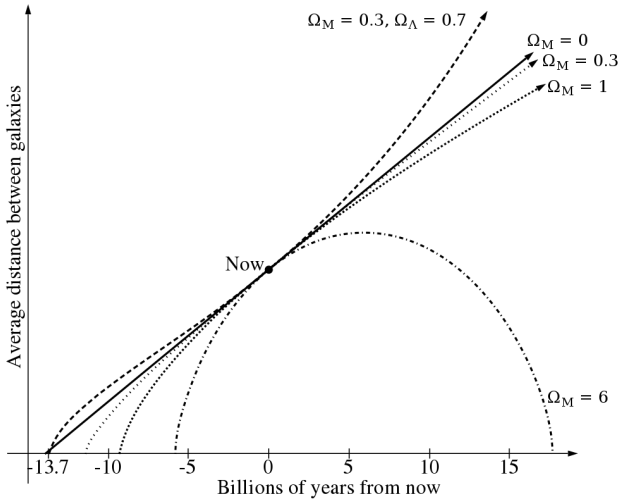

Figure 1.4. The ultimate fate of an expanding universe depends on the matter density Ω_m and the dark energy density Ω_Λ

In the case with $\Omega_{m,0} = 0.3$, $\Omega_{\Lambda,0} = 0.7$ and $H_0 = 72 \pm 8 km/s/\text{Mpc}$, results $t_0 = 13.5 \pm 1.3 Gyrs$.

For completeness (and in anticipation of the next section) we report the estimates of the redshift of the equivalent time *matter-radiation* and *matter*-Λ (see Fig.(1.3)).

The *equivalent time for matter and* Λ correspond to:

$$a_{m,\Lambda} = \left(\frac{\Omega_{m,0}}{\Omega_{\Lambda,0}}\right)^{1/3} \sim \left(\frac{0.3}{0.7}\right)^{1/3} \sim 0.75, \tag{1.57}$$

which corresponds to the redshift $z_{m,\Lambda} \sim 0.33$.
For the *equivalent time for radiation and matter* we have:

$$a_{r,m} = \frac{\Omega_r}{\Omega_m} \sim \frac{8.4 \times 10^{-5}}{0.3}, \tag{1.58}$$

which correspond to the redshift $z_{r,m} \sim 3600$.

1.10 Early universe, epochs and thermal history.

With the knowledge seen before, we could turn the clock back and extrapolate the epochs of the universe.
Since the universe is expanding now, it is probable that in the early time $a \to 0$. If it is so, it must have been in a very different physical state than the current one: the universe must have been much hotter going back in time, with the baryonic matter component in an ionized state and the photons not free to propagate itself in the primordial plasma, trapped in this very dense environment.
Starting from the very early era, we assumed the existence of different epochs during

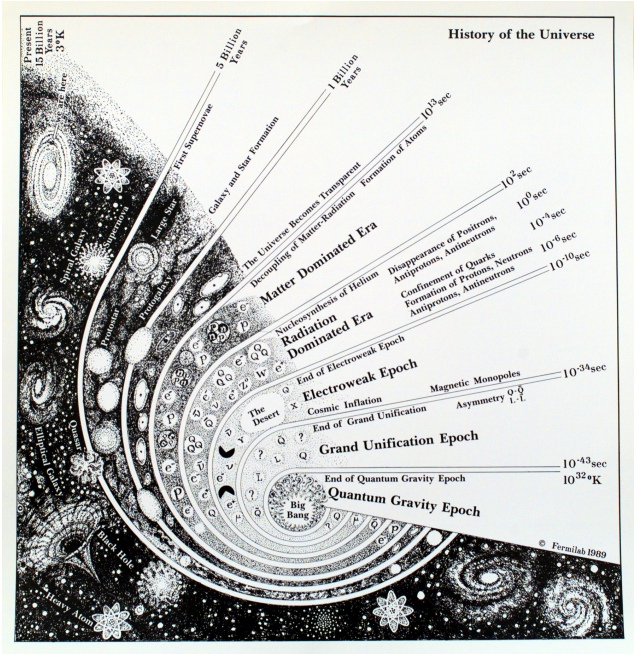

Figure 1.5. History of the universe in a concise picture. Credit: Fermilab

the cooling process of the expanding universe. Here we speak briefly about the very early universe as the modern cosmology now suggests (see Fig.(1.5)), omitting to talk about the structure formation and the recent periods of our universe.

The Planck Epoch.

This period was at *Planck time* $t_{Pl} < 10^{-43}s$ and at *Planck energy* $E_{Pl} \sim 10^{19}$ GeV. In these energy conditions the theory of general relativity has to take into account the quantum effect and the field theories must abandon the assumption of static Minkowsky space time background. During this epoch the fundamental forces (electromagnetism, gravitation, weak nuclear interaction, and strong nuclear interaction) may have been unified.
Traditional big-bang cosmology predicts a gravitational singularity before this time, but this theory is based on general relativity and is expected to break down due to quantum effects. Proposed theories of quantum gravitation, such as string theory, loop quantum gravity, and causal sets, could lead to a better understanding of this epoch.
In inflationary cosmology, before the end of inflation ($t < 10^{-34}s$) the universe is a near-vacuum with a very low temperature, and persists for much longer than $10^{-34}s$. Times from the end of inflation are based on the big-bang time of the non-inflationary big-bang model, not on the actual age of the universe at that time, which cannot be determined in inflationary cosmology. Thus, in inflationary cosmology there is no the Planck epoch in the traditional sense, though similar conditions may have prevailed in a pre-inflationary era of the universe.

The Grand Unification Epoch.

The Planck epoch may have inaugurated a period of unification, known as the grand unification epoch, and that symmetry breaking then quickly led to the era of cosmic inflation, during which the universe greatly expanded in scale over a very short period of time.
At the time $10^{-43}s < t < 10^{-34}s$, the temperature of the universe was comparable to the characteristic temperatures of *grand unified theories* ($E_{GUT} \sim 10^{15}$ GeV). During this period, three of the four fundamental interactions (electromagnetism, the strong interaction, and the weak interaction) were unified as the electronuclear force and, further cooling, the strong force separated from the other fundamental forces[8]. During the grand unification epoch, physical characteristics such as mass, charge, flavour and colour charge were meaningless.
This phase transition is also thought to have triggered the process of cosmic inflation that dominated the development of the universe during the following inflationary epoch. In addition, this transition should produce magnetic monopoles in large quantities, which are not observed today. The lack of magnetic monopoles was one problem solved by the introduction of inflation theory.

The Electroweak Epoch.

In traditional big-bang cosmology, the electroweak epoch was at $t > 10^{-34}$, when the temperature of the universe is low enough $\sim 10^{15}$ GeV to separate the strong force from the electroweak force. Particle interactions in this phase were energetic enough to create large numbers of exotic particles, including W and Z bosons and *Higgs bosons* [26].
Around this time also the process called *Baryogenesis* could take place (when $10^{17}\text{GeV} < T < 10^{12}\text{GeV}$). It is required to explain why, by observational evidence, today the universe contains far more baryons than antibaryons.
The quantum field theory guarantees that a particle and its antiparticle have exactly the same mass and lifetime, and exactly opposite charge. Given this symmetry, it is puzzling that the universe does not have equal amounts of matter and antimatter. Indeed, there is no experimental evidence that there are any significant concentrations of antimatter in the observable universe, we can then think about a set of phenomena contributed to a small imbalance in favour of matter over time.
We may think that during this phase, the universe becomes asymmetric in the baryon number: the number of baryons is slightly higher than the number of antibaryons. Following the decrease of the temperature, the antibaryons annihilate leaving an excess of baryons, which they survived until today. A candidate explanation for this phenomenon must allow the *Sakharov conditions*[9] [27] to be satisfied at some time after the end of cosmological inflation. While particle physics suggests asymmetries under which these conditions are met, these asymmetries are too small empirically to account for the observed baryon-antibaryon asymmetry of the universe.
This can be explained by inflationary theory. The inflationary epoch comprises the

[8] Gravity had separated from the electronuclear force at the end of the Planck era.

[9] These are: baryon number violation, C-symmetry and CP-symmetry violation, interactions out of thermal equilibrium. We do not deepen this argument, and not even introduce the basics of CPT symmetry.

first part of the electroweak epoch following the grand unification epoch. It lasted from $10^{-36}s$ to $\sim 10^{-34}s$. Following the inflationary period, the universe continued to expand, but at a slower rate.
We will see in depth the inflationary theory after in chapter *inflation model*, let us just say here that this is in a rapid exponential expansion. This rapid expansion increased the linear dimensions of the early universe by a factor of at least $\sim 10^{26}$ (and possibly a much larger factor), and so increased its volume by a factor of at least $\sim 10^{78}$. The rapid expansion of space meant that elementary particles remaining from the grand unification epoch were now distributed very thinly across the universe. However, the huge potential energy of the inflation field was released at the end of the inflationary epoch, repopulating the universe with a dense, hot mixture of quarks, anti-quarks and gluons as it entered the electroweak epoch.

The Radiation Dominated Epoch.

This epoch extends to the temporal range $10^{-10}s < t < 10^2 s$ and it includes some important sub-steps with the decrease of temperature that lead to a value of energy $\sim 10^2$ GeV, to ensure the unification of forces, to energies ~ 0.1 MeV that allow the formation of ^{4}He.
First, we have the *electroweak symmetry breaking* at time $< 10^{-6}s$ and energy lower than the electroweak symmetry scale. In this epoch the weak force and electromagnetic force, and their respective bosons (the W and Z bosons and photon), manifest differently in the present universe, with different ranges. At the end of this epoch, the fundamental interactions of gravitation, electromagnetism, the strong interaction and the weak interaction have now taken their present forms, and fundamental particles have mass, but the temperature of the universe is still too high to allow quarks to bind together to form hadrons. Indeed the universe was filled with a dense, hot quark-gluon plasma, containing quarks, leptons and their antiparticles. Collisions between particles were too energetic to allow quarks to combine into mesons or baryons. It was called *quark epoch* of the universe and ended at time of $10^{-6}s$, when the average energy of particle interactions had fallen below the binding energy of hadrons and quarks became confined within hadrons. This period is known as the *hadron epoch.* Initially the temperature was high enough to allow the formation of hadron/anti-hadron pairs, which kept matter and anti-matter in thermal equilibrium. However, as the temperature of the universe continued to fall, hadron/anti-hadron pairs were no longer produced. Most of the hadrons and anti-hadrons were then eliminated in annihilation reactions, leaving a small residue of hadrons.
The elimination of anti-hadrons was completed by one second after the big-bang, when the following *lepton epoch* began. It started roughly 1 second after the big-bang, the temperature of the universe was still high enough to create lepton/anti-lepton pairs, so leptons and anti-leptons were in thermal equilibrium. Approximately 10 seconds after the big-bang the temperature of the universe had fallen to the point where lepton/anti-lepton pairs were no longer created. Most leptons and anti-leptons were then eliminated in annihilation reactions, leaving a small residue of leptons.
When the temperature of the universe falls to the point where atomic nuclei can begin to form, at energy of ~ 0.1 MeV, starts the process of *nucleosynthesis.* It

occurred during the first few minutes of the photon epoch; protons (hydrogen ions) and neutrons begin to combine into atomic nuclei in the process of nuclear fusion, free neutrons combine with protons to form deuterium. Deuterium rapidly fuses into ^{4}He. Nucleosynthesis only lasts for about seventeen minutes, since the temperature and density of the universe have fallen to the point where nuclear fusion cannot continue. By this time, all neutrons have been incorporated into helium nuclei. This leaves about three times more hydrogen than ^{4}He (by mass) and only trace quantities of other nuclei.
For the remainder of the radiation epoch the universe contained a hot dense plasma of nuclei, electrons and photons.

The Matter Dominated Epoch.

Around 7×10^4 year, the densities of non-relativistic matter (atomic nuclei) and relativistic radiation (photons) are equal.
The *Jeans length* $\lambda_J = \sqrt{\frac{\pi c_s^2}{G\rho_0}}$ [10] [28], which determines the smallest structures that can form, begins to fall and perturbations begin to grow in amplitude. At this stage, cold dark matter dominates paving the way for gravitational collapse to amplify the tiny inhomogeneities left by cosmic inflation, making dense regions denser and rarefied regions more rarefied.
At the time of $\sim 10^4$ years, the temperature of the universe falls to around 1 eV, that is the order of the binding energy of the hydrogen atom. For the first time after the big-bang, the universe becomes something other than dense plasma of photons, electrons, and protons. This plasma was effectively opaque to electromagnetic radiation, as the distance each photon could travel before encountering a charged particle was very short.
As the universe expanded, it also cooled to the point that the formation of neutral hydrogen was energetically favored: ionized hydrogen and helium atoms capture electrons thus neutralizing their electric charge. This time was named *recombination epoch*, by the name of this transition.
Shortly after, at $\sim$ 380,000 years and energy of $\sim$ 0.1 eV, photons *decoupled* from matter in the universe. This allows them to travel freely through the universe without interacting with matter, making this the earliest epoch observable today. The photons present at the time of decoupling are the same photons that we see in the CMB radiation, after being greatly cooled by the expansion of the universe.
By the end of this period, the universe consists of a fog of about 75% of hydrogen and 25% of helium, with just traces of lithium.

[10] where c_s is the sound velocity in the fluid, and ρ_0 is the density of the static fluid.

Chapter 2

Cosmological perturbation theory and structure formation

In the previous chapter we have treated the universe as isotropic and homogeneous, with a gravitational field described by the FLRW metric. Now, we can move to a more realistic scenario. The observed universe, indeed, is far from perfectly homogeneous and isotropic, as matter is arranged in clusters and large voids containing very little matter and in CMB radiation tiny anisotropies are clearly seen. The universe, at small scale, it is too inhomogeneous to be described in a simple way. We should therefore consider the primordial universe, when matter had not yet gravitationally collapsed and the inhomogeneities of matter were so small ($\delta\rho/\rho \ll 1$) that they could be treated as first-order perturbations. Starting from here, the study of the evolution of the perturbations in the distribution function of photons by perturbing at linear order around the solution of a FLRW universe will help to have a deeper understanding of the CMB anisotropies.

The aim of this chapter is the analysis of these perturbations that represent the seeds of the structures we see nowadays in our universe. We will show how to treat the perturbations of the different components of the universe by deriving the general relativistic equations that govern such small fluctuations. This will allow us to obtain a much better description of the universe, which also takes into account the presence of inhomogeneities. The comprehension of the role of perturbations is crucial to understand the anisotropies in the cosmic distribution of photons and inhomogeneities in the matter. We will see here in detail the anisotropies of the CMB radiation, that corresponds to density, velocity and gravitational potential fluctuations present at the decoupling epoch. In what follows, we will derive a set of linear differential equations that we need to integrate in order to compute the value of the CMB fluctuations today. We will leave to the next chapter the discussion of the initial conditions necessary to solve the equations derived here.

2.1 Perturbation Theory and the Boltzmann equation.

As a first step, we need to perturb the FLRW metric. We consider a most general form for the metric:

$$ds^2 = g_{00}(cdt)^2 + 2g_{0i}dx^i dt - g_{ij}dx^i dx^j. \tag{2.1}$$

In order to observe the effects of a space-time coordinate transformation on the perturbation, we need to have transformations that do not affect the coordinates and the unperturbed fields but have only effect on the perturbations to the fields. This problem can be solved by fixing a coordinate system and considering gauge transformations, which only affect the perturbations.
Two popular choices are the *synchronous gauge* and the *conformal Newtonian gauge*. Historically, most calculations of linear fluctuation growth have been carried out in the synchronous gauge, so called because the t coordinate defines proper time for all comoving observers. Although this gauge is affected by ambiguities, the synchronous coordinates are generally considered the most efficient reference system for doing numerical calculations, and are used in many modern cosmology codes, such as CAMB. The results presented in this thesis in chapters 4 and 5 are obtained using "exact" equations and synchronous gauge, as shown in Ref. [29].
The conformal Newtonian gauge, instead, is free of the gauge ambiguities associated with the synchronous gauge and we choose to use it in our review. Using this gauge transformation with the potentials Φ and Ψ, we obtain:

$$g_{00}(\vec{x}, t) = -1 - 2\Psi(\vec{x}, t), \tag{2.2a}$$

$$g_{0i}(\vec{x}, t) = 0, \tag{2.2b}$$

$$g_{ij}(\vec{x}, t) = a^2\delta_{ij}(1 + 2\Phi(\vec{x}, t)), \tag{2.2c}$$

where function Ψ corresponds to the gravitational Newtonian potential and the function Φ to the perturbation to the spatial curvature. If Φ and Ψ are both zero we obtain the unperturbed FLRW metric.
It can be shown that the degrees of freedom of the perturbed metric can be of three kinds: scalar, vectorial or tonsorial. Eqs.(2.2) contains only scalar perturbations and the two scalar potentials transform themselves as scalar quantities (they are invariant under transformation of coordinates).
As said, in principle it is possible that the metric of our universe also has vector or tensor perturbations. If so, $g_{\mu\nu}$ would require other functions besides Φ and Ψ to fully describe all perturbations. For example, the off-diagonal elements become non-zero if there are vector perturbations. Indeed, there are many cosmological theories wherein there are both tensor and vector perturbations. For example, the inflation model tends to predict that there will be tensor perturbations, while models based on topological defects tend to produce large vector perturbations.
For now we focus on the scalar perturbations; these are the only ones that couple to matter perturbations and are the most important that couple to photon perturbations as well. Moreover, the *Decomposition Theorem* allows one to treat the scalar, vector and tensor perturbation separately since each of these evolves independently at linear level and it is not incorrect to build a perturbative model based only on scalar perturbations.

We notice also that these functions are small perturbations at the scale of interest, therefore, as we will see, it is possible to neglect the quadratic and higher-order terms when we will consider the Einstein equations.

2.1.1 The Boltzmann equation.

The metric which determines the gravitational forces is influenced by all the components of the universe, thus to solve for the photon and dark matter distributions we need to simultaneously solve for all the other components.
There is a systematic way to account for all of these couplings: we will write a Boltzmann equation for each species in the universe. The most general form of the equation for a distribution function $f(\vec{x}, \vec{p}, t)$ is:

$$\frac{df}{dt} = \frac{\partial f}{\partial t} + \frac{\partial f}{\partial x^i}\frac{dx^i}{dt} + \frac{\partial f}{\partial p}\frac{dp}{dt} + \frac{\partial f}{\partial \widehat{p}^i}\frac{d\widehat{p}^i}{dt} = C[f]. \tag{2.3}$$

The term on the left-hand side is the total derivative of the distribution function with respect to time and it represents the explicit time variation of the distribution function. The right-hand side contains all the collision-related terms of the component under consideration by all the other component (for instance the scattering process) and hence represents the effects of collisions; it is therefore a complicated function of all the distribution functions of the various components.
For $df/dt = 0$ (in the absence of collisions), the equation means that the number of particles in a given element of phase space does not change with time and that we can still progress systematically by re-expressing the full derivative in terms of partial derivatives.
Each of the total derivatives at the right of equation must be expressed explicitly, starting from the definitions of the four-momentum and Christoffel symbols [11].

With the risk of being too detailed for the purpose of this thesis, we will discuss in detail only the treatment for photons. As we will see, for the remaining components of the universe we can have a similar discussion and we can directly write the conclusions.

Boltzmann equation for photons.

Let us now remember the definition of the four-momentum of a particle: $P^\mu = \frac{dx^\mu}{d\lambda}$, where the *affine connection* λ parametrizes the path of the particle in space-time. It is used in general relativity as the parameter in function of which it is possible to express the coordinate variation.
Photons or massless particles satisfy the condition for the four-momentum:

$$P^2 = g_{\mu\nu}P^\mu P^\nu = 0. \tag{2.4}$$

So there are only three independent components of the momentum vector. We can therefore write the time component, defining $p^2 = g_{ij}P^iP^j$, and using Eqs.(2.2) as:

$$P^2 = 0 = -(1+2\Psi)(P^0)^2 + p^2 \;\longrightarrow\; P^0 = \frac{p}{\sqrt{1+2\Psi}} = p(1-\Psi). \tag{2.5}$$

The last equality is because we are truncating at first-order perturbation theory in the small quantity Ψ. We use the convention for which an over-dense region has $\Psi < 0$. Therefore, in an over-dense region, the term in parentheses on the right-hand side here is greater than one. Thus, Eq.(2.5) tells us photons lose energy as they move out of a potential well.
The spatial component of the four-momentum at the first-order in perturbation theory takes the form:

$$P^i = p\hat{p}^i \frac{1-\Phi}{a}, \tag{2.6}$$

which involves $\frac{dx^i}{dt} = \frac{\hat{p}^i}{a}(1+\Psi+\Phi)$. An over-dense region has $\Psi < 0$ and $\Phi > 0$, making the term in parentheses less than one. This expression shows that a photon "slows down", or rather loses energy (dx/dt becomes smaller), when traveling through an over-dense region. This makes perfect sense: we expect the gravitational force of an over-dense region to "slow down" even photons.
At once, it is possible to write dp/dt as (the complete calculations can be found in [11]):

$$\frac{1}{p}\frac{dp}{dt} = -H - \frac{\partial\Phi}{\partial t} - \frac{\hat{p}^i}{a}\frac{\partial\Psi}{\partial x^i}. \tag{2.7}$$

It describes the change in the photon momentum as it moves through a perturbed FRW universe. The first term accounts for the loss of momentum due to the Hubble expansion. To understand the significance of the next two terms we remember the definition of over-dense region in conventions. Therefore, the second term says that a photon in a deepening gravitational well ($\partial\Phi/\partial t > 0$) loses energy. This is understandable: the deepening well makes it more difficult for the photon to emerge, thereby increasing the magnitude of the redshift. Finally, a photon travelling into a well ($\hat{p}^i\partial\Psi/\partial x^i < 0$) gains energy because it is being pulled toward the centre. Conversely, as it leaves the well, it gets red-shifted.
The last term of Eq.(2.3) does not contribute of first-order in the perturbation theory, because it turns out to be the product of first-order terms (which makes of this a term of the second-order). In this way we obtain the Boltzmann equation for photons:

$$\frac{df}{dt} = \frac{\partial f}{\partial t} + \frac{\hat{p}^i}{a}\frac{\partial f}{\partial x^i} - p\frac{\partial f}{\partial p}\left[H + \frac{\partial\Phi}{\partial t} + \frac{\hat{p}^i}{a}\frac{\partial\Psi}{\partial x^i}\right] = C[f]. \tag{2.8}$$

The equation includes all the information on the behaviour of photons in an expanding universe: the first two terms on the right are due to the classical equation of hydrodynamics; the third term dictates that photons lose energy in an expanding universe; the last two encode the effects of under/over-dense regions on the photon distribution function.

The **perturbation** of the distribution function can be characterized by introducing the function Θ, that does not depend on the magnitude of the momentum, as it is assumed that during Compton scattering the total momentum is conserved.
The distribution function for photons at zero-order is identified with the Bose-Einstein distribution [11] with zero chemical potential:

$$f^{(0)} \equiv (e^{p/T} - 1)^{-1}.$$

The perturbed expression becomes:

$$f(\vec{x}, p, \hat{p}, t) = \left[\exp\left(\frac{p}{T(t)[1+\Theta(\vec{x}, \hat{p}, t)}\right) - 1\right]^{-1}. \tag{2.9}$$

where $\Theta = \delta T/T$ depends on both the position $\vec{x}$ and the direction of propagation $\hat{p}$. Since Θ is small, we can expand to first-order as follows:

$$f(\vec{x}, p, \hat{p}, t) \sim \frac{1}{e^{(p/T)} - 1} + \left(\frac{\partial}{\partial T}[e^{p/T} - 1]^{-}1\right) T\Theta = f^{(0)} - p\frac{\partial f^{(0)}}{\partial p}\Theta. \tag{2.10}$$

The left term of the Boltzmann equation for the photon at first-order assumes then the form:

$$\left(\frac{df}{dt}\right)_{Iorder} = -p\frac{\partial f^{(0)}}{\partial p}\left[\frac{\partial \Theta}{\partial t} + \frac{\hat{p}^i}{a}\frac{\partial \Theta}{\partial x^i} + \frac{\partial \Phi}{\partial t} + \frac{\hat{p}^i}{a}\frac{\partial \Psi}{\partial x^i}\right]. \tag{2.11}$$

In the next step we show the **collision term** due to the *Compton scattering*. The process of scattering is given by $e^-(\vec{q}) + \gamma(\vec{p}) \longleftrightarrow e^-(\vec{q}') + \gamma(\vec{p}')$.
In the case in which we neglect the angular dependence and polarization, it is possible to write the collision term $C[f(\vec{p})]$ expanding and truncating at the first-order:

$$C[f(\vec{p})] = -p\frac{\partial f^{(0)}}{\partial p} n_e \sigma_T [\Theta_0 - \Theta(\hat{p}) + \hat{p} \cdot \vec{v}_b], \tag{2.12}$$

where we have defined the *monopole* moment perturbation as:

$$\Theta_0(\vec{x}, t) \equiv \frac{1}{4\pi}\int d\Omega' \Theta(\hat{p}', \vec{x}, t). \tag{2.13}$$

We must highlight the inability to absorb the term of the monopole in the definition of temperature of the zero-order since the latter is constant over all space. The perturbation Θ_0 represents the deviation of the monopole at a given point in space from its average in all space.
In the case where the bulk speed of the electrons is zero, the Compton scattering should be very efficient and only the monopole perturbation survives; all other moments are washed out. Intuitively, strong scattering means that the mean free path of a photon is very small. Therefore, photons arriving at a given point in space last scattered off very nearby electrons if Compton scattering is efficient. These nearby electrons most likely had a temperature very similar to the point of observation. Therefore, photons from all directions have the same temperature. This is the characteristic signature of a monopole distribution: the temperature on the sky is uniform.
The situation changes slightly if the electrons carry a bulk velocity. In that case, the photons will also have a dipole moment, fixed by the amplitude and direction of the electron velocity. Even in this case, though, all higher moments will vanish. The shape of the photon distribution takes a simple form (being characterized only by its monopole and dipole) and photons behave like a fluid. Indeed, strong scattering, or tight coupling, produces a situation where in the photons and electrons behave as a single fluid.

Equating Eq.(2.11) and Eq.(2.12) we have:

$$\frac{\partial\Theta}{\partial t}+\frac{\widehat{p}^i}{a}\frac{\partial\Theta}{\partial x^i}+\frac{\partial\Phi}{\partial t}+\frac{\widehat{p}^i}{a}\frac{\partial\Psi}{\partial x^i}=n_e\sigma_T[\Theta_0-\Theta+\widehat{p}\cdot\vec{v}_b]. \tag{2.14}$$

In terms of the conformal time (Eq.(3.16)), the Boltzmann equation (Eq.(2.14)) becomes:

$$\dot{\Theta}+\widehat{p}^i\frac{\partial\Theta}{\partial x^i}+\dot{\Phi}+\widehat{p}^i\frac{\partial\Psi}{\partial x^i}=n_e\sigma_T a[\Theta_0-\Theta+\widehat{p}\cdot\vec{v}_b], \tag{2.15}$$

where overdots represent derivatives with respect to conformal time. Eq.(2.15) is a partial differential linear equation coupling Θ to Φ and Ψ variables and $\vec{v}_b$. Since it is linear (true if Θ is small), each mode k evolves independently.
The Fourier transform of the perturbation variable is:

$$\Theta(\vec{x})=\int\frac{d^3k}{(2\pi)^3}e^{i\vec{k}\cdot\vec{x}}\tilde{\Theta}(\vec{k}). \tag{2.16}$$

Before rewriting Eq.(2.15) in terms of Fourier modes, let us make two final definitions. First, define the angle between the wave number $\vec{k}$ and the photon direction $\widehat{p}$ to be

$$\mu\equiv\frac{\vec{k}\cdot\widehat{p}}{k}. \tag{2.17}$$

The wavevector $\vec{k}$ points in the direction in which the temperature changes, so it is perpendicular to the gradient. If $\mu=1$, the photon travels in the direction along which the temperature changes, while if $\mu=0$ the photon travels in a direction in which the temperature remains the same.
Next, we define the *optical depth*:

$$\tau(\eta)\equiv\int_\eta^{\eta_0}d\eta' n_e\sigma_T a, \tag{2.18}$$

where σ_T is the Thompson scattering cross-section, n_e is the electron number density and a the scale factor. At late times, the free electron density is small, so $\tau\ll 1$, while at early times it is very large.
With these definitions, we are finally left with:

$$\dot{\tilde{\Theta}}+ik\mu\tilde{\Theta}+\dot{\tilde{\Phi}}+ik\mu\tilde{\Psi}=-\dot{\tau}[\tilde{\Theta}_0-\tilde{\Theta}+\mu\tilde{v}_b]. \tag{2.19}$$

We found useful to define the monopole (Eq.(2.13)) of the photon distribution. More generally, it is useful to define the lth multipole moment of the temperature field as

$$\Theta_\ell\equiv\frac{1}{(-i)^l}\int_{-1}^{1}\frac{d\mu}{2}P_\ell(\mu)\Theta(\mu), \tag{2.20}$$

where P_ℓ is the Legendre polynomial of order ℓ. The quadrupole corresponds to $\ell=2$, octopole to $\ell=3$, etc. The higher Legendre polynomials have a structure on smaller scales, so the higher moments capture information about the small scale structure of the temperature field. So the photon perturbations can be described either by $\Theta(k,\mu,\eta)$ or by a whole hierarchy of moments, $\Theta_\ell(k,\eta)$.

The temperature anisotropies are coupled to the polarization field, so an accurate determination of the former requires a treatment of the latter. Θ_P describes the change in the polarization field in space and, upon Fourier transforming, it depends on k, μ and η.
Adopting the convention $\tilde{\Theta} \equiv \Theta$ to describe perturbation in Fourier space and defining $\Pi = \Theta_2 + \Theta_{P2} + \Theta_{P0}$ (that accounts for the angular dependence of Compton scattering) and $P_2(\mu) = (3\mu^2 - 1)/2$ the Legendre polynomial of order 2, the *equation for the radiation* is:

$$\dot{\Theta} + ik\mu\Theta = -\dot{\Phi} - ik\mu\Psi - \dot{\tau}[\Theta_0 - \Theta + \mu v_b - \frac{1}{2}P_2(\mu)\Pi]. \tag{2.21}$$

Note that Θ_P is sourced by the quadrupole, Θ_2 , and none of the other temperature moments.

Boltzmann equation for the Neutrino component.

In the most part of the universe history, the Neutrinos are ultra-relativistic and we can assume them massless. We introduce Fourier transform of the perturbation variable analogous to Θ of radiation component, $\tilde{N}(k, \mu, \eta)$, in order to find the evolution equation of the perturbations for the neutrino. We can observe that there is no scattering term since neutrinos interact only very weakly, so the *Boltzmann equation for the neutrino distribution* is:

$$\dot{N} + ik\mu N = -\dot{\Phi} - ik\mu\Psi. \tag{2.22}$$

Boltzmann equation for Cold Dark Matter.

There are several ways in which the dark matter distribution differs from the photon. First, by definition that does not interact with other constituents in the universe, thus we need not deal with any collision terms. Second, the cold dark matter is non-relativistic.
Therefore we need to redo some of the kinematics which led to the left side of the Boltzmann equation. Starting from Eq.(2.4), this becomes:

$$P^2 = g_{\mu\nu}P^\mu P^\nu = -m^2. \tag{2.23}$$

The equivalent of Eq.(2.5) and Eq.(2.6) for the four-momentum of a massive particle is:

$$P^\mu = \left[E(1-\Psi)\ ,\ p\widehat{p}^i\frac{1-\Phi}{a}\right], \tag{2.24}$$

with $E = \sqrt{p^2 + m^2}$. We can see that only the time component is different from that of a massless particle, with E replacing p.
Using E as one of the dependent variables, the total time derivative of the dark matter distribution function f_{dm} (Eq.(2.3)) becomes:

$$\frac{df_{dm}}{dt} = \frac{\partial f_{dm}}{\partial t} + \frac{\partial f_{dm}}{\partial x^i}\frac{dx^i}{dt} + \frac{\partial f_{dm}}{\partial E}\frac{dE}{dt} + \frac{\partial f_{dm}}{\partial \widehat{p}^i}\frac{d\widehat{p}^i}{dt}. \tag{2.25}$$

The last term (again) can be neglected since it is a second-order term. Since the dark matter is non-relativistic (cold), the thermal motion can be neglected too.

Instead we cannot neglect the velocity completely, because the density perturbations themselves induce velocity flows in the dark matter via the continuity equation. We must consider the term $p/m \sim v$, but we explicitly drop all terms on second and higher-order, closing the hierarchy for the dark matter distribution. If we are interested in dark matter particles with much smaller masses, such as massive neutrinos, we would need to keep these higher moments.
Instead of finding an explicit form for f_{dm}, we multiply both sides by the phase space volume $d^3p/(2\pi)^3$ and integrate:

$$\begin{aligned} &\frac{\partial}{\partial t}\int \frac{d^3p}{(2\pi)^3} f_{dm} + \frac{1}{a}\frac{\partial}{\partial x^i}\int \frac{d^3p}{(2\pi)^3} f_{dm}\frac{p\widehat{p}^i}{E} \\ &- \left[\frac{da/dt}{a} + \frac{\partial \Phi}{\partial t}\right]\int \frac{d^3p}{(2\pi)^3}\frac{\partial f_{dm}}{\partial E}\frac{p^2}{E} - \frac{1}{a}\frac{\partial \Psi}{\partial x^i}\int \frac{d^3p}{(2\pi)^3}\frac{\partial f_{dm}}{\partial E}\widehat{p}^i p = 0 \end{aligned} \tag{2.26}$$

The last term can be neglected since the integral over the direction vector is non-zero only for the perturbed part of f_{dm}. To simplify the equation, we use the expressions for the dark matter number density and velocity:

$$n_{dm} = \int \frac{d^3p}{(2\pi)^3} f_{dm} \tag{2.27}$$

$$v^i \equiv \frac{1}{n_{dm}}\int \frac{d^3p}{(2\pi)^3} f_{dm}\frac{p\widehat{p}^i}{E}. \tag{2.28}$$

Referring for the calculation step to the [11], here we define the expand of the *dark matter density* n_{dm} out to include a first-order perturbation:

$$n_{dm} = n^{(0)}_{dm}[1 + \delta(\vec{x}, t)], \tag{2.29}$$

where $n^{(0)}_{dm}$ is the first-order term, with $n^{(0)}_{dm} \propto a^{-3}$, and δ is the *density perturbation* given by $\delta\rho/\rho$.
We can collect zero-order and first-order terms of Boltzmann equation:

$$\frac{\partial n^{(0)}_{dm}}{\partial t} + 3\frac{da/dt}{a} n^{(0)}_{dm} = 0, \tag{2.30}$$

$$\frac{\partial \delta}{\partial t} + \frac{1}{a}\frac{\partial v^i}{\partial x^i} + 3\frac{\partial \Phi}{\partial t} = 0. \tag{2.31}$$

The additional equation is found by extracting the first moment from the Eq.(2.25) with no collision term:

$$\frac{\partial v^j}{\partial t} + \frac{da/dt}{a} v^j + \frac{1}{a}\frac{\partial \Psi}{\partial x^j} = 0. \tag{2.32}$$

The last two equations govern the evolution of the density and velocity of the cold dark matter. In Fourier space the two equations become:

$$\dot{\tilde{\delta}} + ik\tilde{v} + 3\dot{\tilde{\Phi}} = 0, \tag{2.33}$$

$$\dot{\tilde{v}} + \frac{\dot{a}}{a}\tilde{v} + ik\tilde{\Psi} = 0. \tag{2.34}$$

Boltzmann equation for baryonic component.

The Boltzmann equation for the baryonic component includes information on electrons and protons. These are coupled by Coulomb scattering ($e + p \to e + p$), where the scattering rate is much larger than the expansion rate at all epochs of interest. This tight coupling forces the electron and proton overdensities to a common value:

$$\delta_b = \frac{\rho_e - \rho_e^{(0)}}{\rho_e^{(0)}} = \frac{\rho_p - \rho_p^{(0)}}{\rho_p^{(0)}}, \tag{2.35}$$

where δ_b indicates the density perturbation in the baryonic component.
We can write the Boltzmann equation for the electron and proton:

$$\frac{df_e(\vec{x}, \vec{q}, t)}{dt} = \langle c_{ep} \rangle_{QQ'q'} + \langle c_{e\gamma} \rangle_{pp'q'} \tag{2.36a}$$

$$\frac{df_p(\vec{x}, \vec{Q}, t)}{dt} = \langle c_{ep} \rangle_{qq'Q'} \tag{2.36b}$$

where we have indicated the initial and final electron momenta by q and q', of the proton by Q and Q' and for the photon with p and p'. The $\langle c_{xx} \rangle$ indicates the collision term of Compton scattering and the brackets stands for the integration on the indicated momenta.
We multiply both sides of Eq.(2.36aa) by the phase space volume $d^3q/2\pi^3$ and integrate (the cross-section of scattering between protons and photons is very small compared with the cross-section for Compton scattering and it is therefore negligible). The left-hand side then becomes identical to the left-hand side we derived for the cold dark matter, so we can immediately write the Boltzmann equation:

$$\frac{\partial n_e}{\partial t} + \frac{1}{a}\frac{\partial (n_e v_b^i)}{\partial x^i} + 3\left[\frac{da/dt}{a} + \frac{\partial \Phi}{\partial t}\right] n_e = \langle c_{ep} \rangle_{QQ'qq'} + \langle c_{e\gamma} \rangle_{pp'q'q}, \tag{2.37}$$

with v_b velocities of the two species ($v_e = v_p = v_b$). Both terms on the right vanish: the integration measure in the first term on the right is completely symmetric under the interchange of $Q \sim Q'$ and $q \sim q'$ while the term $\langle c_{ep} \rangle$ is antisymmetric under this interchange. The examined process conserves the number of electrons so $dn/dt = 0$.
In Fourier space , the Eq.(2.37) becomes:

$$\dot{\tilde{\delta}}_b + ik\tilde{v}_b + 3\dot{\tilde{\Phi}} = 0 \tag{2.38}$$

The second equation for baryons is obtained by taking the first moments of both Eqs.(2.36a) and adding them together. We did something similar for the dark matter; there we first multiplied by $\vec{p}/E$ and then integrated over all momenta. Since the proton mass is so much larger than the electron mass, the sum of the two left-hand sides will be dominated by protons. So:

$$m_p \frac{\partial (n_b v_b^j)}{\partial t} + 4\frac{da/dt}{a} m_p n_b v_b^j + \frac{m_p n_b}{a}\frac{\partial \Psi}{\partial x^i} = \langle c_{ep}(q^j + Q^j) \rangle_{QQ'q'q} + \langle c_{e\gamma} q^j \rangle_{pp'q'q}. \tag{2.39}$$

Using the conservation of momentum, the integral of $c_{ep}(\vec{q} + \vec{Q})$ over all momenta vanishes. Furthermore, from conservation of total momentum, $\langle c_{e\gamma}\vec{q} \rangle_{pp'q'q} =$

$-\langle c_{e\gamma}(\vec{p})\rangle_{pp'q'q}$. By Eq.(2.20) we define the first-order momentum in perturbation theory Θ_1 and we can write, switching to conformal time and in Fourier space, the previous equation as:

$$\dot{\tilde{v}}_b + \frac{\dot{a}}{a}\tilde{v}_b + ik\tilde{\Psi} = \dot{\tau}\frac{4\rho_\gamma}{3\rho_b}\left[3i\tilde{\Theta}_1 + \tilde{v}_b\right]. \tag{2.40}$$

It quite generally governs the evolution of the baryon velocity.

2.1.2 Perturbed Einstein equations.

With the above consideration, we now have all the equations that determine the evolution of the different components of the universe as functions of the scalar perturbation Φ and Ψ. Now we see how these functions evolve using Einstein's equations, for a complete analysis we refer to [11] (here we limit the analysis briefly reporting the conceptual development and results).
The Eq.(1.16) contains 10 distinct relationships. To determine Φ and Ψ is sufficient to solve only two of these, chosen from the simplest to solve. The first is the one that involves the term $\mu\nu = 00$ of Eq.(1.16), the second involves the spatial part of G_{ij} multiplied by a projection operator allowing the extraction of only the tensor component with zero trace. Evaluating the left-hand side of the Einstein equation (Eq.(1.16)) requires three pre-steps: compute the Christoffel symbols for the perturbed metric of Eq.(2.2), from these form the Ricci tensor $R_{\mu\nu}$[12] and finally contract the Ricci tensor to form the Ricci scalar $R \equiv g^{\mu\nu}R_{\mu\nu}$.
We then consider the first-order part (δR) got through the multiplication of terms and keeping only those first-order in Φ and Ψ. This give:

$$\delta R = -12\Psi\left(H^2 + \frac{d^2a/dt^2}{a}\right) + \frac{2k^2}{a^2}\Psi + 6\Phi_{,00} - 6H(\Psi_{,0} - 4\Phi_{,0}) + 4\frac{k^2\Phi}{a^2}. \tag{2.41}$$

So now we can compute the first-order part of the time-time component and of the spatial part component of the Einstein tensor:

$$\begin{aligned} \delta G^0_0 =& -6H\Phi_{,0} + 6\Psi H^2 - 2\frac{k^2\Phi}{a^2}, \\ G^i_j =& A\delta_{ij} + \frac{k_ik_j(\Psi+\Phi)}{a^2}. \end{aligned} \tag{2.42}$$

To complete our derivation of the first evolution equation for Φ and Ψ, therefore, we need to compute the first-order part of the energy-momentum tensor T^0_0, that corresponds to the sum of the energy density of the components.

$$T^0_0(\vec{x},t) = -\sum_{all\ species\ i} g_i\frac{d^3p}{(2\pi)^3}E_i(p)f_i(\vec{p},\vec{x},t). \tag{2.43}$$

To get the first-order part of the energy-momentum tensor, we must naturally consider the first-order part of the distribution function we defined in the previous section for photons, neutrinos, dark matter and baryons. We find:

[12] Being $R_{\mu\nu} = \Gamma^\alpha_{\mu\nu,\alpha} - \Gamma^\alpha_{\mu\alpha,\nu} + \Gamma^\alpha_{\beta\alpha}\Gamma^\beta_{\mu\nu} - \Gamma^\alpha_{\beta\nu}\Gamma^\beta_{\mu\alpha}$.

- for the photon: $T_0^0 = -\rho_\gamma[1 + 4\Theta_0]$
- for the neutrino: $T_0^0 = -\rho_\nu[1 + 4N_0]$
- for the baryons and dark matter: $T_0^0 = -\rho_i[1 + \delta_i]$

The factor 4 for photon is easily explained: the perturbation variable Θ is the fractional temperature change, while the energy momentum tensor is interested in the perturbed energy density, $\delta\rho$. We should have expected that since $\rho \propto T^4$, $\delta\rho/\rho = 4\delta T/T$.
In principle, we should also include a term for the perturbation to the dark energy. In practice, though, most models of the dark energy predict that it should be smooth and it should be important only very recently and we can neglect the dark energy as a source of perturbations to the metric.
The *perturbed Einstein equations* are (in Fourier space with the convention to omit the tilde):

$$\begin{aligned} k^2\Phi + 3\frac{\dot{a}}{a}\left(\dot{\Phi} - \Psi\frac{\dot{a}}{a}\right) &= 4\pi G a^2[\rho_{dm}\delta_{dm} + \rho_b\delta_b + 4\rho_\gamma\Theta_0 + 4\rho_\nu N_0], \\ k^2(\Psi + \Phi) &= -32\pi G a^2[\rho_\gamma\Theta_2 + \rho_\nu N_2]. \end{aligned} \tag{2.44}$$

In practice, the photons quadrupole contributes little to this sum, because it is very small during the time when it has appreciable energy density. Only the collisionless neutrino has an appreciable quadrupole moment early on when radiation dominates the universe.
The Einstein-Boltzmann equations thus found can be used to describe the behaviour of the cosmological fluid in the linear regime, and to calculate the cosmological observable.

2.1.3 The Einstein-Boltzmann equations at early times.

In the previous sections we have defined the system of differential equations governing the perturbations of the distribution of the different components of the universe. We can now study the initial conditions of the perturbations of matter and radiation as functions of the metric perturbations. We will determine how at primeval times all variables depend on the potential Φ (we remember that Ψ is related to the perturbation to the time-time component g_{00} of the metric and Φ is related to the perturbation of the spatial part g_{ij}).
First, we introduce the two types of initial perturbations mode [30]. The *adiabatic mode* is defined as a perturbation affecting all the cosmological species such that the relative ratios in the number densities remain unperturbed, i.e., such that $\delta(n_X/n_Y) = 0$. It is associated with a *curvature perturbation*, via Einstein's equations, since there is a global perturbation of the matter content (this is why the adiabatic perturbation is also called curvature perturbation). In terms of the energy density contrasts, defined by:

$$\delta_X \equiv \frac{\delta\rho_X}{\rho_X}, \tag{2.45}$$

the adiabatic perturbation is characterized by the relations:

$$\frac{1}{4}\delta_\gamma = \frac{1}{4}\delta_\nu = \frac{1}{3}\delta_b = \frac{1}{3}\delta_{dm}, \tag{2.46}$$

where each coefficient depending on the equation of state of the particular species. Since there are several cosmological species, it is also possible to perturb the matter components without perturbing the geometry. This corresponds to *isocurvature perturbations*, characterized by variations in the particle number ratios but with vanishing curvature perturbation. The variation in the relative particle number densities between two species can be quantified by the so-called entropy perturbation:

$$S_{X,Y} \equiv \frac{\delta n_X}{n_X} - \frac{\delta n_Y}{n_Y}. \tag{2.47}$$

When the equation of state for a given species is such that $\omega \equiv p/\rho =$Const, then one can re-express the entropy perturbation in terms of the density contrast, in the form:

$$S_{X,Y} \equiv \frac{\delta_X}{1+\omega_X} - \frac{\delta_Y}{1+\omega_Y}. \tag{2.48}$$

It is convenient to choose a species of reference, for instance the photons, and to define the *entropy perturbations* of the other species relative to it:

$$S_b \equiv \delta_b - \tfrac{3}{4}\delta_\gamma, \tag{2.49a}$$
$$S_{dm} \equiv \delta_{dm} - \tfrac{3}{4}\delta_\gamma, \tag{2.49b}$$
$$S_\nu \equiv \tfrac{3}{4}\delta_\nu - \tfrac{3}{4}\delta_\gamma, \tag{2.49c}$$

thus define respectively the baryon isocurvature mode, the dark matter isocurvature mode, and the neutrino isocurvature mode. In terms of the entropy perturbations, the adiabatic mode is obviously characterized by $S_b = S_{dm} = S_\nu = 0$.
In summary, we can decompose a general perturbation, described by four density contrasts, into one adiabatic mode and three isocurvature modes. Indeed, the problem is slightly more complicated because the evolution of cosmological perturbations is governed by second order differential equations and a perturbed (perfect) fluid is described locally by its density contrast and by its velocity field. The primordial perturbations are constrained by the requirement that the perturbations do not diverge when going backwards in time deep in the radiation era. With this prescription, there remains one arbitrary relative velocity between the species, which gives an additional mode, usually named the *neutrino isocurvature velocity perturbation.*

During the early times, the universe was still in the radiation-dominated era. In this context, most perturbations had dimension much larger than the Hubble causal horizon. It is hence possible to consider the fact that at this epoch, for most of the perturbations, $k\eta \ll 1$. This inequality allows many simplifications. First, in the Boltzmann equation for photons, $\dot{\Theta} \sim \Theta/\eta$ and $ik\mu\Theta \sim k\Theta$. Then, the terms multiplied by k can be neglected. Moreover, as photons that arrive at point x have only had the time to travel for very short distances, they will all have the same temperature. Hence multipoles with temperatures of orders greater than zero, as for instance the dipole Θ_1, can be neglected. So from the Boltzmann equation,

we obtain the evolution of the temperatures perturbations for the components of universe:

$$\begin{aligned} \dot{\Theta}_0 + \dot{\Phi} &= 0 \\ \dot{N}_0 + \dot{\Phi} &= 0 \\ \dot{\delta}_{dm} &= -3\dot{\Phi} \\ \dot{\delta}_b &= -3\dot{\Phi}. \end{aligned} \tag{2.50}$$

The Einstein equations at early times, ignoring the matter terms that are negligible at early times since radiation dominates, is:

$$3\frac{\dot{a}}{a}\left(\dot{\Phi} - \frac{\dot{a}}{a}\Psi\right) = 16\pi G a^2(\rho_\nu N_0 + \rho_\gamma \Theta_0). \tag{2.51}$$

Since radiation dominates, $a \propto \eta$, so $\dot{a}/a \equiv 1/\eta$. Defining $f_\nu \equiv \frac{\rho_\nu}{\rho_\nu + \rho_\gamma}$ as the ratio of neutrino energy density to the total radiation density, we rewrite the previous formula:

$$\dot{\Phi}\eta - \Psi = 2(f_\nu N_0 + [1 - f_\nu]\Theta_0). \tag{2.52}$$

Differentiating both right- and left-hand sides and using Eq.(2.50) we have:

$$\ddot{\Phi}\eta + \dot{\Phi} - \dot{\Psi} = -2\dot{\Phi}. \tag{2.53}$$

Moreover, as the multipole moments of higher order are negligible, from Eq.(2.44) we obtain $\ddot{\Phi}\eta + 4\dot{\Phi} = 0$. Its solution, substituting in Eq.(2.52) give the relation between the gravitational potential and the neutrino and photon perturbations:

$$\Phi = 2(f_\nu N_0 + [1 - f_\nu]\Theta_0). \tag{2.54}$$

We know from observations that perturbations are mainly adiabatic, i.e. there was no difference between the perturbations of neutrinos and photons. Accordingly, we get $\Theta_0 = N_0$, where both quantities are consequently constant. We finally get the relationship that relates the primeval space-time perturbations to the monopole deviation of the temperature photons:

$$\Phi(k, \eta_i) = 2\Theta_0(k, \eta_i). \tag{2.55}$$

For what concerns matter density, substituting the first of Eq(2.50) in the third of the same set, we have $\delta_{dm} = 3\Theta + const$. The primordial perturbations are so divided into those for which the *const* is zero (adiabatic perturbations) and those for which the *const* is nonzero (isocurvature perturbations). Similar arguments are also made for the baryons.
For the most part, velocities and dipole moments are negligibly small in the very early universe. However, we will encounter situations where we need to know the initial conditions for these as well. We assume the initial conditions [11]:

$$\Theta_1 = N_1 = \frac{iv_b}{3} = \frac{iv}{3} = -\frac{k\Phi}{6aH}. \tag{2.56}$$

2.2 The angular power spectrum.

In order to describe the fluctuations in temperature we can write the temperature field in the following way:

$$T(\vec{x},\eta,\hat{p}) = T(\eta)[1+\Theta(\vec{x},\hat{p},\eta)]. \tag{2.57}$$

The temperature field is defined in any point of space and time, however, it can be observed only in our position defined by $\vec{x}_0$ and at our time given by η_0. The changes in temperature on the sky are identified in terms of the angles θ and ϕ. The perturbation Θ can been written in terms of spherical harmonics:

$$\Theta(\vec{x},\hat{p},\eta) = \sum_{\ell=1}^{\infty}\sum_{m=-1}^{\ell} a_{\ell m}(\vec{x},\eta)Y_{\ell m}(\hat{p}), \tag{2.58}$$

where the indices ℓ and m are the *conjugate variables* of the real unit vector $\hat{p}$. The expansion given by Eq.(2.58) can be thought as a generalization of Fourier transform, where now the complete set of functions in which one expands are given by the *spherical harmonics* $Y_{\ell m}(\hat{p})$. All the information relating to the field of temperature must be contained in the *amplitude coefficient* $a_{\ell m}$.
From Eq.(2.58) it can been derived an expression for the coefficients of the expansion:

$$a_{\ell m}(\vec{x},\eta) = \int \frac{d^3k}{(2\pi)^3} e^{i\vec{k}\vec{x}} \int d\Omega Y^*_{\ell m}(\hat{p})\Theta(\vec{k},\hat{p},\eta), \tag{2.59}$$

where $\Theta(\vec{k})$ is the transformed variable by Fourier transform of $\Theta(\vec{x})$. It is not possible to give an exact theoretical prediction for each $a_{\ell m}$. However, inflation predicts (as we will see later) that these variables must be Gaussian distributed with zero mean $\langle a_{\ell m}\rangle = 0$ and non zero variance C_ℓ, given by:

$$\langle a_{\ell m} a^*_{\ell' m'}\rangle = \delta_{\ell\ell'}\delta_{mm'}C_\ell, \tag{2.60}$$

where the average is taken over different realizations. Clearly it is impossible to measure the value of the anisotropies in several realizations since we have only one universe that we can actually measure. Thanks to the *ergodic theorem* we can however assume that an average on just a portion of the universe will be sufficient to get a good estimate of the variance C_ℓ. However this introduce a fundamental limitation on the measurement of the C_ℓ that will start to be significant only at very large angular scales. Since the C_ℓ are distributed as a chi-square distribution with $2\ell+1$ degrees of freedom, this uncertainty, called *cosmic variance* is given by:

$$\frac{\Delta C_\ell}{C_\ell} = \sqrt{\frac{2}{2\ell+1}}. \tag{2.61}$$

In order to compare data with theory we therefore need to connect the variance C_ℓ with the perturbation variables Θ_ℓ. This can be found by using $\langle\Theta(\vec{k},\hat{p})\Theta^*(\vec{k'},\hat{p'})\rangle$.

The power spectrum in temperature is:

$$C_\ell = \frac{2}{\pi}\int_0^\infty dk k^2 P(k)\left|\frac{\Theta_\ell(k)}{\delta(k)}\right|^2, \tag{2.62}$$

where $P(k)$ is the *power spectrum of primordial fluctuations*, which is usually taken to be a power law $P(k) \propto k^{n-1}$.
In a flat universe the relationship between angular scale and the wavelength λ of a fixed mode is given by the $\theta \sim \lambda/D$, where D identifies the distance from the *last scattering surface* (LSS). This relation changes if the universe is not flat, for example in an open universe the geodesics are such that a particular angular scale correspond to much larger physical scales on the LSS.

2.3 Anisotropies.

Cosmological information of fundamental importance come from the temperature anisotropies of the CMB, they correspond to density fluctuations present at the decoupling epoch. There are several physical processes that have a direct effects on the temperature distribution of the CMB and the common approach is to order them chronologically, starting from those more distant in time. Physical processes around the redshift of last scattering ($z \sim 1100$) produce the *primary anisotropies*, while instead processes between then and the present time produce *secondary anisotropies* which somewhat alter the former.

As the photons decouples from the baryons around redshift $z \sim 10^3$, they carry three different imprints of the region of the last diffusion, corresponding to the gravitational potential, the peculiar radial velocity v_r and to the density fluctuation. Indeed we remember what has already been said:

- The photons diffused from a potential well ($\Psi < 0$) will suffer of a gravitational redshift as they will come out.
- The photons diffused from matter whose peculiar velocity is in the opposite direction respect to the observer $v_r > 0$ will undergo a Doppler redshift and those with $v_r < 0$ a blueshift.
- The photons emerging from, say, an over-dense region ($\delta > 0$) will have a larger temperature, simply because the over-dense regions are hotter, and under-dense regions are colder.

These three effects can be summarized in the following equation:

$$\frac{\Delta T}{T}(\hat{r}) = \Psi(r) - r \cdot v(r) + \frac{1}{3}\delta(r) \tag{2.63}$$

where the length of the vector r is the comoving distance to the LSS and the fields Ψ, v and δ are to be calculated at the time of the recombination at $z \sim 10^3$. In Fig.(2.1) we can see the CMB angular power spectrum and intuitively explain its characteristics in the following way. Adiabatic initial conditions produce a coincidence of the positions of over-densities and potential wells, and so the third term is partially erased with the first one. It follows that, for large scale fluctuations, $\delta \sim -2\Psi$ and so the two terms are combined in $\Psi/3$: this is the so-called *Sachs-Wolfe effect*. It is responsible of the flat left part of the plot, where the pre-factor $\ell(\ell+1)$ is customarily used: in a cosmological model with a primordial power spectrum with $n_s = 1$, the Sachs-Wolfe contribution is proportional to $1/\ell(\ell+1)$ and it is

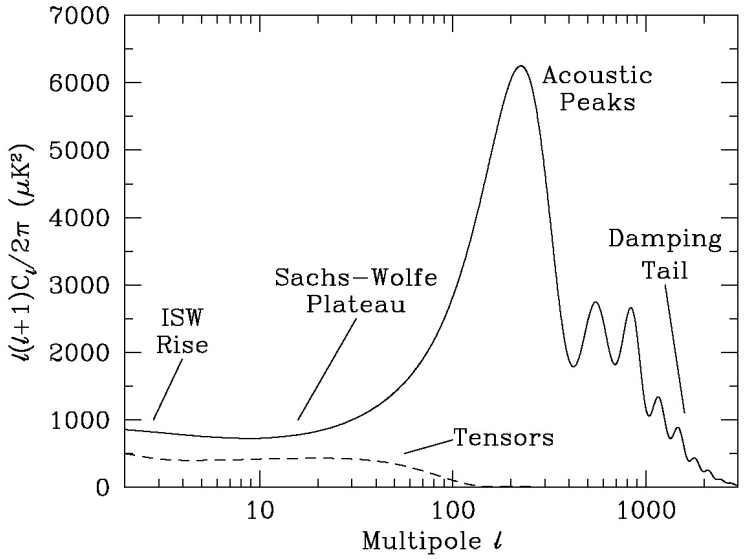

Figure 2.1. CMB power spectrum for a CDM model.

dominant at large scales. On smaller scales, instead, the fluctuations in Ψ, v and δ have time to oscillate acoustically before the recombination and this will produce the *Acoustic peaks* on the right of the same figure. As the LSS is not infinitesimal, the CMB temperature that is measured in a given direction in the sky will be the weighted average of all photons incoming from both the nearest and the farthest part of the LSS. This effect cancel out the fluctuation of scales smaller than the one corresponding to the thickness of the LSS, that is $\ell \sim 10^3$. There exist also secondary and tertiary perturbations referring to processes that the photons undergo in their way from the LSS to us, and we will discuss these effects briefly.

2.3.1 Large-scale.

If we limit to very large angular scales, the anisotropies that we see today are mainly originated by two mechanisms: intrinsic fluctuations of the temperature field at the time of recombination, given by Θ_0, and fluctuations in the gravitational potential, given by the Newtonian potential Ψ. Since we are considering the perturbation in the linear regime, the total anisotropy is just given by the sum of this two terms: $(\Theta_0 + \Psi)$. The Ψ term is introduced because photons must travel outside of the potential in which are trapped at the time of recombination; when photons emerge from the potential well they lose energy.

Let us now study these large scale anisotropies in detail. For modes outside the horizon we have $k\eta \ll 1$, the terms proportional to k in the evolution equations for the baryon component Eq.(2.38), for the matter component Eq.(2.33), and in the perturbed Einstein equation Eq.(2.44) can be eliminated. Neglecting the higher multipoles, the evolution equations are reduced to:

$$3\frac{\dot{a}}{a}\left(\dot{\Phi} + \frac{\dot{a}}{a}\Phi\right) = 4\pi G a^2[\rho_{dm}\delta + 4\rho_\gamma\Theta_0]. \tag{2.64}$$

The solution for the perturbations in radiation at large scales, assuming that recom-

bination takes place long after the era of equality between radiation and matter, takes the form:

$$(\Theta_0 + \Psi)(k, \eta_*) = \frac{1}{3}\Psi(k, \eta_*), \tag{2.65}$$

with η_* evaluated at the time of recombination.
The observed anisotropies expressed in terms of fluctuations of dark matter density are:

$$(\Theta_0 + \Psi)(k, \eta_*) = -\frac{1}{6}\delta(\eta_*). \tag{2.66}$$

The Fourier transform of Eq.(2.66) shows that the anisotropy of a region with high density will be negative. For large scales at the time of recombination, over-dense regions contain more hot photons compared to less dense regions, so $\Theta_0 > 0$ and $\Psi < 0$. However, in order to reach the observer, photons must escape from the potential wells, losing energy. The loss of energy compensates the fact that photons were hotter than the average: $\Theta_0+\Psi$ is a negative quantity when $\Psi < 0$. The blueshift or redshift associated with emerging photons from the potential wells determines the so called *Sachs-Wolfe effect*. In conclusion, the hotter points observed today in the sky really identify regions with lower density at the time of recombination. The large-scale modes evolve very slowly, this is because perturbations with wavelength greater than the horizon are not in causal contact, so the modes called *super-horizon* exhibit a small evolution.

2.3.2 Small-scale, primary anisotropies.

Gravitational potential

Let us now assume that after equality era most of the matter component is in the form of cold dark matter (i.e. we neglect for the moment baryons or hot dark matter). It is possible to infer the evolution of photons and baryons from the potential Ψ. The evolution of the perturbations in cold dark matter density can be derived from a single second order differential equation:

$$\ddot{\delta} + 2\frac{\dot{a}}{a}\dot{\delta} - 4\pi G\bar{\rho}\delta = 0 \tag{2.67}$$

where $\bar{\rho}$ is the total mean energy density. In an era dominated by radiation the last term of Eq.(2.67) is negligible, in this case we have two linearly independent solutions $\delta = cost$ and $\delta \sim \ln t$, i.e. perturbations in the cold dark matter density do not vary too significantly when the universe is radiation dominated. However, in a universe dominated by matter there are two solutions $\delta \propto t^{2/3}$ and $\delta \propto t^{-1}$. Since we assumed a primordial homogeneous universe, we need to consider only the growing solution. It is interesting to note that if we put this solution in the Poisson equation for the Newtonian potential we find in Fourier space $\nabla^2\Psi = 4\pi G\bar{\rho}\delta a^2$. During the matter regime $\delta \sim a$ and $\delta \sim a^{-3}$ and therefore Ψ is independent of time [31].

The acoustic oscillations

Before recombination the photons have to be strongly coupled with the electrons and protons, consequently the mean free time between a photon and the subsequent

collision is small compared to other important timescales. In this approximation, frequent scattering isotropizes the photon distribution, that is characterized by the temperature distribution. Furthermore, the photon and baryon densities are coupled adiabatically: $n_\gamma \propto n_B \propto T^3$. The behavior of the photon-baryon fluid is therefore characterized by a single variable, it is convenient to take as our variable the fractional temperature fluctuation, which is simply one third of the baryon density fluctuation:

$$\Theta(x,t) \equiv \frac{\Delta T}{T}(x,t) = \frac{1}{3}\delta(x,t). \tag{2.68}$$

With these approximations, the dynamics of the photon-baryon fluid is described by the single equation:

$$\frac{d}{d\eta}\left[(1+R)\dot{\Theta}\right] + \frac{k^2}{3}\Theta, \tag{2.69}$$

where $R \equiv 3\rho_B/4\rho_\gamma$ is essentially the baryon-to-photon energy ratio.
Let us now assume that R and Ψ are independent of time. Then the gravitation is the leading term and we can simplifies the Eq.(2.69) [31] as:

$$(1+R)\ddot{\Theta} + \frac{k^2}{3}\Theta = -\frac{k^2}{3}(1+R)\Psi. \tag{2.70}$$

This is the equation for a simple harmonic oscillator, with solution:

$$\Theta(\eta) = -(1+R)\Psi + K1\cos(kc_s\eta) + K2\sin(kc_s\eta). \tag{2.71}$$

Here $K1$ and $K2$ are constants to be fixed by the initial conditions and $c_s = (3(1+R))^{-1/2}$ is the *sound speed*. In this approximation, then, each Fourier mode represents an acoustic plane wave propagating at speed c_s.
There is a simple physical picture underlying this result. The baryon-photon fluid wants to fall into the potential wells, but it is supported by radiation pressure. The balance between pressure and gravity sets up acoustic oscillations. The three terms in Eq.(2.70) come from the inertia of the fluid, the radiation pressure, and the gravitational field.
In many theories, the initial perturbation is adiabatic, meaning that the matter and radiation fluctuations are the same at any particular point. With these initial conditions, $\dot{\Theta} = 0$ at very early times and $\Theta(0) = -2\Psi/3$, so the previous equation becomes:

$$\Theta(\eta) = -\Psi + \frac{1}{3}\Psi\cos(kc_s\eta), \tag{2.72}$$

where we make the important assumption $R = 0$.
Focusing our attention on a single Fourier mode, let us determine what kind of anisotropy we would expect to see on the sky. Ignoring the Doppler term for the moment, we note by Eq.(2.72) that the two terms Ψ and Θ give a pure cosine oscillation, so $\Delta T/T$ is large when $kc_s\eta$ is an integer multiple of π. Therefore, if the initial conditions have a smooth power spectrum, $\Delta T/T$ will have a harmonic series of peaks in k-space, leading to a harmonic series in the angular power spectrum of anisotropy on the sky. This is the origin of the acoustic peaks in Fig.(2.1), caused by modes that have reached maxima of compression and rarefaction at the time of last scattering. The *first peak* is caused by modes that have had time to oscillate

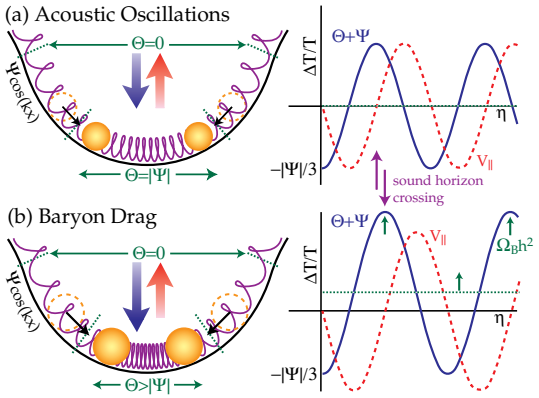

Figure 2.2. In the graphic is shown a simple mechanical model for a single mode of acoustic oscillation of the photon-baryon fluid. In the figure the springs represent the restoring force of the photon pressure and the balls represent the effective mass of the system. The upper panel shows the case in which the baryonic component is negligible, while, the bottom panel includes the effect of baryons in the photo-baryonic fluid. The plots on the right shown that baryons oscillations proceed more slowly and also reduce the Doppler contribution to $\Delta T/T$ relative to the intrinsic and Sachs-Wolfe contributions. Credit: W. Hu *et.al* [32].

through exactly one half of a period before last scattering; the modes that cause the *second peak* have oscillated through a full period, and so on.
The physical scale of the first peak is therefore $\lambda \sim k^{-1} = c_s\eta/\pi \sim 30$Mpc. The distance to the LSS is ~ 6000Mpc, so the angular scale of the first peak is $\lambda/D \sim 0.25°$.
With simple algebra we can derive the Doppler contribution (for a complete discussion we refer to [31]):

$$\left[\frac{\Delta T}{T}\right]_{Doppler} = \frac{i}{3}\Psi \sin(kc_s\eta). \tag{2.73}$$

This has the same amplitude as the $(\Theta + \Psi)$ contribution, but is 90^o out of phase in both time (it goes like a sine instead of a cosine) and space (it has an extra factor of i). The total $\Delta T/T$ is then the quadrature sum of Eq.(2.72) and Eq.(2.74):

$$\left(\frac{\Delta T}{T}\right)^2 \propto \sin^2(kc_s\eta) + \cos^2(kc_s\eta) = 1. \tag{2.74}$$

Let us remove that assumption $R = 0$, but keep the approximation that R is time-independent. The adiabatic solution to Eq.(2.69) is now

$$\Theta(\eta) = \frac{1}{3}(1 + 3R)\Psi \cos(kc_s\eta) - (1 + R)\Psi \tag{2.75}$$

By allowing R to be nonzero:

- the amplitude of the cosine oscillations is increased by a factor $(1 + 3R)$.

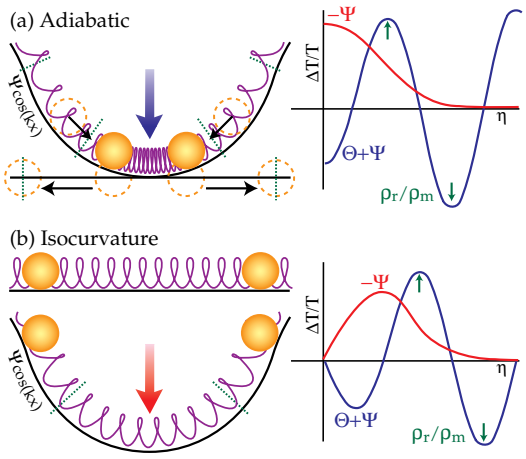

Figure 2.3. In the graphic one can see the different types of trends for the acoustic oscillations, the case of adiabatic initial conditions opposed to a model that provides the initial conditions for isocurvature. In the adiabatic case the potential is not crucial, since causes an increase in amplitude of the oscillations, while in the case of isocurvature is observed that $\Psi + \Theta_0$ is zero at the beginning and the oscillations are driven by the growth of Ψ.

- there is now an offset in the combined Sachs-Wolfe and adiabatic contributions to $\Delta T/T$: in the limit $R \to 0$, we found that $\Theta + \Psi$ oscillated symmetrically around zero, now it oscillates around $-R\Psi$
- reduces the amplitude of the Doppler contribution to the anisotropy, relative to the Sachs-Wolfe contribution. Since the cosine oscillations are now larger in amplitude than the sine oscillations, we do indeed expect to see a series of peaks at $kc_s\eta = m\pi$.

The essential reason of these effect is that baryons contribute to the effective mass of the photon-baryon fluid, but not to the pressure: the first term of Eq.(2.75) representing the effective mass and depends on R, but the second term representing pressure support, does not. The effect of the baryons, therefore, is to slow down the oscillations, and also to make the fluid fall deeper into the potential wells. This explains all three of the key effects we have just mentioned: the increased oscillation amplitude, the offset in the center of the oscillations, and the reduction in importance of the velocity term relative to the other terms. These effects are represented pictorially in Fig.(2.2).

The only condition left to be relaxed is the fact that Eq.(2.69) is constant with time. If the driving term varies significantly with time on a time scale comparable to the period of the oscillations, resonant driving can occur. Ψ is constant during matter domination, but it decays during the radiation epoch. For modes that enter the horizon before matter domination, Ψ decays while that mode is undergoing its oscillations. The decay in Ψ therefore boosts the amplitude of those short-wavelength modes. The modes that receive the largest boost are those that entered the horizon before matter-radiation equality.

If we consider isocurvature models, the effect of the driving term becomes even more evident. In isocurvature models, the total density perturbation vanishes at early times:

$$\delta\rho_{total} = \delta\rho_B + \delta\rho_\gamma + \delta\rho_{CDM} + ... = 0. \tag{2.76}$$

In contrast to the adiabatic case, these isocurvature oscillations are proportional to $\sin kc_s\eta$ rather than $\cos kc_s\eta$. The peaks in an isocurvature spectrum are therefore different in phase from adiabatic peaks. The peak locations in the CMB anisotropy spectrum can distinguish quite robustly between adiabatic and isocurvature models. Fig.(2.3) illustrates the origin of the peaks in isocurvature models.

Diffusion damping

The discussion just completed is valid before recombination, when we can consider the baryon-photon plasma as a single fluid. The decline of the power spectrum on the right of Fig.(2.1) is due to the fact that the recombination is not instantaneous and so there is the fail of the tight coupling approximation, especially around the the last scattering time. Moreover, the LSS is really a shell of some thickness. Oscillations on scales smaller than this thickness do not show up as observable anisotropies on the sky. This diffusion process is known as *Silk damping effect*, and it happens for the greater part around the last scattering epoch because that is the time in which the free mean path becomes large. We have to consider that when we measure the temperature in one direction in the sky, we are actually averaging photons that undergo the last scattering both near the front end and in the background of the LSS. This projection effect erases the fluctuations over scales smaller than the thickness of the LSS.

In conclusion to this argument we would like to point out the dependences of the details of the power spectrum on the variation of some important cosmological parameters.

- Ω_{tot}: lowering the value of the total density has the main effect of shifting the spectrum to the right, towards higher multipoles, mainly due to curvature effect. If $\Omega_{tot} \neq 1$ (models with spatial curvature) the position of the acoustic peaks shifts due to the geodesic deviation. Moreover, the Integrated Sachs Wolfe (ISW) effect raises the power at large scale (see next section). Fig.(2.4) panel (a).

- Λ: the raising of the cosmological constant, keeping the space flat, raises the low multipoles because it increases the distance to the LSS (and again the ISW effect raises the power at large scales). Fig.(2.4) panel (b).

- Ω_b: raising the baryonic fraction makes the peaks higher. Moreover, this enhances the compression peaks in a much higher extent with respect to the rarefaction peaks. Fig.(2.4) panel (c).

- h: lowering h, the epoch of the matter-radiation equivalence is delayed because it reduces the matter density (at a fixed Ω_{tot}); this produces an enhancement of the peaks because of the decaying potential due to the radiation pressure inside the horizon during the radiation domination. Moreover, changing the rate of expansion makes the peaks slightly shift. Fig.(2.4) panel (d).

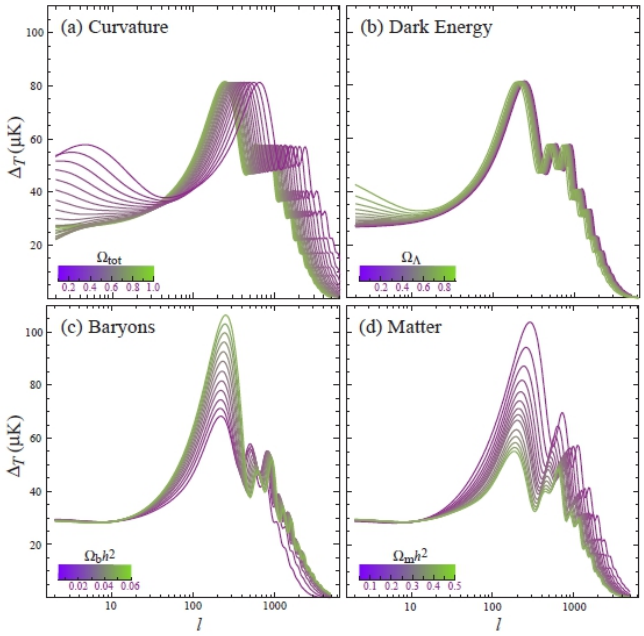

Figure 2.4. Sensitivity of the acoustic temperature spectrum to four fundamental cosmological parameters (a) the curvature as quantified by Ω_{tot} ; (b) the dark energy as quantified by the cosmological constant Ω_Λ; (c) the physical baryon density $\Omega_b h^2$; (d) the physical matter density $\Omega_m h^2$; all varied around a fiducial model of $\Omega_{tot} = 1$, $\Omega_\Lambda = 0.65$, $\Omega_b h^2 = 0.02$, $\Omega_m h^2 = 0.147$, $n = 1$. Credit: Hu and Dodelson 2001 [33].

- n_s: by enhancing the tilt of the primordial power spectrum we are increasing the slope of the angular power spectrum C_ℓ.

2.3.3 Small-scale, secondary anisotropies.

If the intergalactic medium reionize at sufficiently high redshifts, then a fraction of photons will interact again after the last scattering. The main result is that the primary anisotropies are erased, and new fluctuations can be generated from the new LSS. However, this latter surface is extremely thick (because the baryon-photon coupling is weak), so that the nature of the new anisotropies is quite different from the primary anisotropies. Moreover if the intergalactic medium reionized at sufficiently early redshift, then some fraction of the photons will interact again after the time of last scattering.
The causes of the secondary anisotropies are mainly due to gravity, and the dominant effect is the Integrated Sachs-Wolfe effect.

Integrated Sachs-Wolfe effect
The fluctuations in the curvature of space-time yield to two types of anisotropies in the power spectrum of the CMB. The ordinary Sachs-Wolfe effect is simply a gravitational redshift due to the difference between points of emission and reception of photons, while, if the gravitational potential is also time dependent, one has the

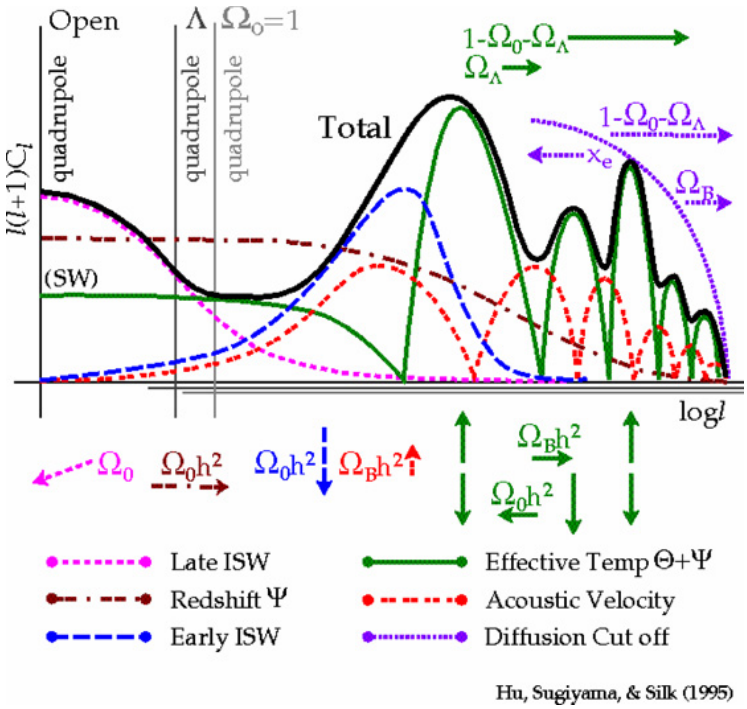

Figure 2.5. Contributions to the CMB temperature power spectrum. Credit: Hu *et al.* [32].

integrated Sachs-Wolfe effect.
If the potential does not change over time, a photon falling and then escaping from a potential well, does not undergo to substantial changes in the energy [31]. In the case in which there is a well with a potential decreasing in time, the photon at the time of escaping will gain energy respect to the time of falling into the well. The magnitude of the Integrated Sachs-Wolfe (ISW) effect is given by the integral along the line of sight between the photon and the observer:

$$\left(\frac{\Delta T}{T}\right) = \int (\dot{\Psi}(\vec{x},\eta) - \dot{\Phi}(\vec{x},\eta))d\eta \tag{2.77}$$

By looking at the previous equation, we understand that the gravitational potential is time-independent only if certain conditions are satisfied: in particular, the universe must be dominated by matter ($\rho_m \gg \rho_r$), the curvature of space-time must be negligible, and, the first term of the perturbation must be appropriate ($\delta \ll 1$).
In most models the equality between matter and radiation occurs close to the epoch of last scattering, in this case the universe is not fully matter dominated at recombination and the gravitational potential has a small time dependence given by the residual amount of radiation. The decay of the gravitational potential around the last scattering gives the early ISW effect. The modes k^{-1} comparable with the time scale in which the potential decays are the most affected. Since the time scale in which the potential decays is of order of the horizon at last scattering, the early ISW effect appears at larger scales $\ell \sim 200$.
The largest scales are affected by late ISW effect, that occurs when the universe start to be dominated by a cosmological constant at redshifts $z \sim 0.3$. Again, the

affected modes are those which have a wavelength the order of size of the horizon at the time of the decay of the potential, i.e. $\ell < 20$.

Gravitational lensing
The weak gravitational lensing is due to the distribution of matter clusters at large scale. The detection comes from the cumulative effect of the structures along the line of sight. The result of the weak gravitational lensing is that our image of the LSS is slightly distorted, as if we were looking at it through an irregular refracting medium. The total detection is predicted to be coherent on scales of $\sim 1^o$, and preserves the luminosity simply by remapping the points in accordance with a detected field. For the anisotropies in temperature, the remapping involves a flattening of the acoustic peaks, the result is a change of 1/10 in the power spectrum C_ℓ^T around $\ell \sim 2000$. A key feature of lensing is to introduce non-Gaussian effects in the spectrum of the CMB.

Reionization
Once structure formation had proceeded to produce the first sources of ionizing radiation, neutral hydrogen and helium began to reionize. The resulting free electron density could then re-scatter CMB photons, and this affected the observed CMB in several ways. The only significant effect for the temperature anisotropies in linear theory is a uniform screening by $e^{-\tau}$, where τ is the *optical depth* through reionization, on scales $\ell < 10$. Anisotropies on such scales are generated from perturbations that are sub-Hubble at the time of reionization. For these modes, the radiation is already significantly anisotropic at reionization since the perturbations vary significantly over the scattering electron's own LSS. The net effect of in-scattering from different lines of sight thus averages to zero, leaving a suppression by $3^{-\tau}$ due to scattering out of the line of sight. In the power spectrum, this becomes $e^{-2\tau}$. However,Fourier modes that are still super-Hubble at reionization produce negligible anisotropy by the time of reionization since the perturbations over the electron own LSS are almost uniform. Scattering isotropic radiation has no effect, and so reionization does not alter the temperature anisotropies from recombination for $\ell < 10$. Scattering around reionization also generates new large-angle polarization and also, at second order, small-scale temperature anisotropies. From what we have said the determination of the amplitude and shape on the primordial power spectrum from temperature data alone rather degenerate with τ

2.4 Polarization.

The main advantage of CMB versus more local probes of large-scale structure is that the fluctuations were created at an epoch when the universe was still in a linear regime. While this fact has long been emphasized for temperature anisotropies, the same holds also for polarization in CMB and as such it offers the same advantages as the temperature anisotropies in the determination of cosmological parameters. The main limitation of polarization is that it is predicted to be small: theoretical calculations show that CMB will be polarized at 5-10% level on small angular scales and much less than that on large angular scales. Anyhow, CMB missions have sufficient sensitivity that even such low signals are measurable and allow us to

exploit the wealth of information present in the polarization.

In general, the polarization is created via Thomson scattering between photons and electrons. The electric field of the incident photon causes the electron to oscillate in the direction of the photon's field. The electron radiates according to the dipole emission formula. Dipole radiation emits preferentially perpendicular to the direction of oscillation, so the light we observe will be polarized. If the radiation that hits the electron is isotropic there will be no net polarization after the scattering, because of the symmetry of the problem. Dipole distribution also does not generate polarization.

Linear polarization is usually decomposed into an electric (E) and magnetic (B) type and they transform, respectively, as a scalar and pseudoscalar. With polarization there are three additional power spectra that can be measured: E and B autocorrelation plus E and T cross-correlation, while all other correlations (TB and EB) vanish for symmetry reasons. This is important because it adds important additional information on the physics of the universe.

The CMB radiation field is characterized by a 2×2 intensity tensor I_{ij} and it is a function of direction on the sky $\vec{n}$ and two directions perpendicular to $\vec{n}$ that are used to define its components ($\hat{e}_1$,$\hat{e}_2$). The Stokes parameters Q and U are defined as $Q = (I_{11} - I_{22})/4$ and $U = I_{12}/2$, and the temperature anisotropy is given by $T = (I_{11} + I_{22})/4$ (the factor of 4 relates fluctuations in the intensity to those in the temperature). In principle there is a fourth Stokes parameter V that describes circular polarization. It can be ignored since it cannot be generated through Thomson scattering.

The Stokes parameters are not invariant under rotations in the plane perpendicular to $\vec{n}$. For this reason it is more convenient to work with scalar and pseudoscalar polarization fields $E(\vec{n})$ and $B(\vec{n})$, which are invariant under rotations. In the small scale we can parametrize the direction in the sky with two-dimensional angle θ, so we have in terms of the Stokes parameters

$$\begin{aligned} E(\ell) &= \int d^2\theta [Q(\theta)\cos(2\phi_\ell) + U(\theta)\sin(2\phi_\ell)] e^{-i\ell\cdot\theta}, \\ B(\ell) &= \int d^2\theta [U(\theta)\cos(2\phi_\ell) - Q(\theta)\sin(2\phi_\ell)] e^{-i\ell\cdot\theta}, \end{aligned} \tag{2.78}$$

with $E(\ell)$ and $B(\ell)$ the components of the two scalar fields.
To obtain them in real space we can perform the transform:

$$\begin{aligned} E(\theta) &= (2\pi)^{-2} \int d^2\ell e^{i\ell\theta} E(\ell), \\ B(\theta) &= (2\pi)^{-2} \int d^2\ell e^{i\ell\theta} B(\ell). \end{aligned} \tag{2.79}$$

These two quantities describe completely the polarization field. By construction, $E(\theta)$ and $B(\theta)$ are rotationally invariant and the variable B is a pseudoscalar.
In the small scales limit, we can test the structure of polarization without measuring the whole sky (as long as the measured field is contiguous) and without worrying about mode coupling because of incomplete sky coverage. E type polarization is the only pattern that is produced by density perturbations and radial polarization pattern is found around the cold spots of E.
To obtain B type polarization we can rotate all polarization "vectors" by 45°. Hot

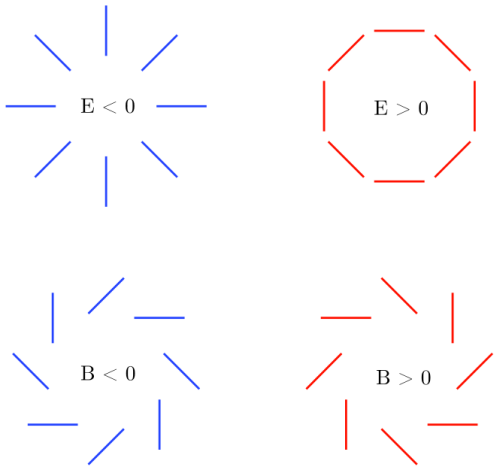

Figure 2.6. Polarization fields examples: E-modes have tangential or radial alignments (top two configurations), while B-modes are aligned at 45 degrees (bottom configurations). Matter and energy density perturbations in the early universe give rise to only E mode in the polarization of the CMB. Gravity waves in the early universe due to inflation produce both E and B modes. Credit: Krauss *et al.* [35].

and cold spots of the B field correspond to places where the polarization vectors circulate in opposite directions. From Fig.(2.6) we can see that such polarization pattern is not invariant under reflections (parity transformation).
Scalar perturbations cannot induce B polarization. A detailed explanation of the reason why can be found in Ref.[34]. In a few words, it depends on the fact that polarization is invariant under the reflection across the axis determined by the $\hat{k}$ (direction of Fourier mode) and $\vec{n}$ (line of sight), because polarization amplitude only depends on the angle between $\hat{k}$ and $\vec{n}$. Therefore any integration around this circle will produce only E and not B. For tensor perturbations this argument no longer applies because here the amplitude of perturbation depends also on the orientation of the stretching of space.

Note that polarization cannot be generated after recombination because the universe becomes transparent for the photons. Therefore, polarization is only generated by quadrupole moment prior to last scattering. The production of polarization takes place almost before the era of decoupling: at that time photons and electrons are strongly coupled, which gives rise to a very small quadrupole term. It is expected that the polarization should not become predominant compared to the temperature anisotropy. A certain amount of polarization is also produced, at the large scales, after the Universe gets reionized at $z \sim 10$.

Chapter 3

Inflation Model

In the previous chapter we derived the general relativistic equations that govern the small fluctuations and we explained the physics of the CMB. However, until now we have not considered the origin of the primordial fluctuations that underlie the observations.

In this chapter, we show how the presence of small quantum fluctuations during a phase of accelerated expansion in the very early universe provides an elegant mechanism to dynamically explain the seeds of all structure in the universe. We analyse then the inflationary paradigm, that provides the initial conditions to solve the equations governing the evolution of perturbations and is the currently-favoured candidate for the origin of structure in the universe, such as galaxies, galaxy clusters and CMB anisotropies. We begin with a quick review of the big-bang model problems which led to the introduction of inflation, like the flatness and homogeneity of our universe. The inflationary theory, indeed, explains why distant, apparently causally disconnected regions of the universe display the same temperature or similar structures and why the curvature of the universe appears to be at or very close to one. We describe the modelling of the inflationary epoch using scalar fields, and discuss the observational predictions and the generation of primordial density fluctuations. Finally, we will see the current observational situation and its tests of the inflationary predictions. Of course, the primary source of information is the analysis of CMB and the large scale distribution of galaxies in the sky, from which we can infer the spectrum of primordial perturbations set during inflation, and thus probe the underlying physics of that age.
We mainly refer in this chapter to the extensive work [36, 37, 38, 39, 40, 41].

3.1 The standard model problems and the inflationary solutions.

The basic picture of big-bang cosmology is a hot and uniform early universe, expanding and cooling at late times. It is very successful and has (so far) passed a battery of increasingly precise tests, explaining the observed primordial abundances of elements, the observed redshifts of distant galaxies, and the presence of the CMB. However, on closer inspection there remain key conceptual puzzles. In particular, how did the

universe get so big, so flat, and so uniform? These observed characteristics of the universe are poorly explained by the standard big-bang scenario, whereas it all make sense if we add, to the standard picture, the inflationary paradigm.

Flatness problem.

From the first Friedmann equation (Eq.(1.25)) we have the definition of Ω_{tot} and we see how from its value depends the universe evolution.
A priori, the general relativity allows any value for Ω_{tot} and the observations show that in the present universe is very close to unity. Moreover, in standard big-bang cosmology, $\Omega_{tot} = 1$ is an unstable solution: any slight difference from unity in the early universe will rapidly grow, e.g. if were 0.9 at one second after the big-bang, it would be only 10^{-14} today; if were 1.1 at one second, then it would grow so rapidly that the universe would have re-collapsed just 45 seconds later. To explain the geometric flatness of space today therefore requires an extreme fine-tuning in the big-bang cosmology without inflation.

Horizon problem.

Observations of the CMB imply the existence of temperature correlations across distances on the sky that corresponded to super-horizon scales at the time when the CMB radiation was released. In fact, regions that in the standard big-bang theory would be causally connected on the LSS correspond to only an angular separation of order 1^o on the sky. This implies that the largest observed scales today were outside the each other horizon at early times. Quantitatively, according to the standard big-bang theory, the CMB at the LSS should have consisted of about 10^4 causally disconnected regions. However, the CMB has nearly the same temperature in all directions on the sky as we can see in the CMB map in Fig.(3.1) where the relative variations from the mean, which presently is still 2.7 K, are only of the order of 5×10^{-5} K. The temperature variations corresponding to the local directions are presented through different colors (the “red" directions are hotter, the “blue" directions cooler than the average). Yet there was no way to establish thermal equilibrium if these points were never in causal contact before last-scattering.
Quantitatively, according to the standard big-bang theory, the CMB at the LSS should have consisted of about 10^4 causally disconnected regions.

Magnetic-monopole problem.

Modern particle theories predict a variety of unwanted cosmological relics, which would violate observations. These include *magnetic monopoles*, domain walls, supersymmetric particles such as the *gravitino* and “moduli" fields associated with superstrings. Typically, the problem is that these are expected to be created very early in the universe history, during the radiation era. But because they are diluted by the expansion more slowly than radiation (eg. as a^{-3} instead of a^{-4}) it is very easy for them to become the dominant component in the universe, in contradiction to observations. One has to dispose of them without harming the conventional matter in the universe.

The inflationary solution.

The inflation scenario was proposed first by Guth in 1981 [43] though some of the key ideas were developed earlier and independently by Starobinsky [44] and others. It attempts to solve these problems by positing a phase in the very early universe, when the dominant form of stress-energy is a component with negative pressure that produces accelerated expansion for a fraction of a second. During inflation, the rate of expansion was accelerating and a small homogeneous patch not bigger than 10^{-26}m (orders of magnitudes smaller than an atomic nucleus) grew within about 10^{-34} seconds to macroscopic size of order one meter. Eventually, the acceleration stopped and the expansion slowed down to the more moderate rate that has characterized our universe ever since. The one meter patch grew to become the observable universe.

Let us assume that the inflation stress-energy component has constant energy density ρ_ϕ. Ignoring matter and radiation but including ρ_ϕ, the Friedmann equation (Eq.(1.22)) is:

$$H^2 = \left(\frac{\dot{a}}{a}\right)^2 = \frac{8\pi G}{3c^2}\rho_\phi - \frac{kc^2}{a^2}. \tag{3.1}$$

In contrast to the matter- or radiation-dominated case, the gravitational term grows relative to the curvature term. Thus, it is driven towards one instead of away from one. Once the curvature term is negligible, the solution to the Friedmann equation is exponential expansion:

$$a = a_0 e^{t/t_H}, \tag{3.2}$$

where the scale factor can grow by an enormous factor in a moderate number of *Hubble times* t_H:

$$t_H = H^{-1} = \left(\frac{8\pi G\rho_\phi}{3c^2}\right)^{-1/2}. \tag{3.3}$$

In similar way, we can write the equation for the acceleration:

$$\frac{\ddot{a}}{a} = -(1+3\omega)\left(\frac{4\pi G}{3}\rho_\phi\right). \tag{3.4}$$

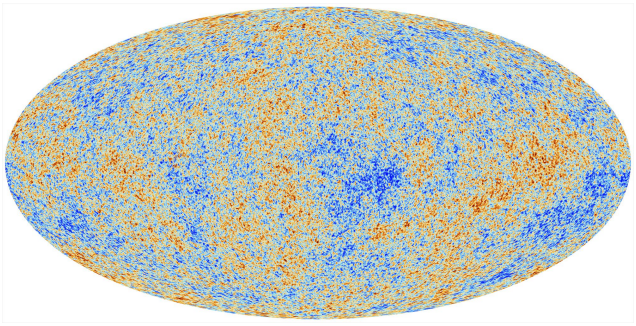

Figure 3.1. Temperature fluctuations in the CMB as seen by ESA's Planck satellite, the most precise image so far of the CMB. Although the temperature of the CMB is almost completely uniform at 2.7 K, there are very tiny anisotropies on the order of 10^{-5} K. Credit: Planck Collaboration [42].

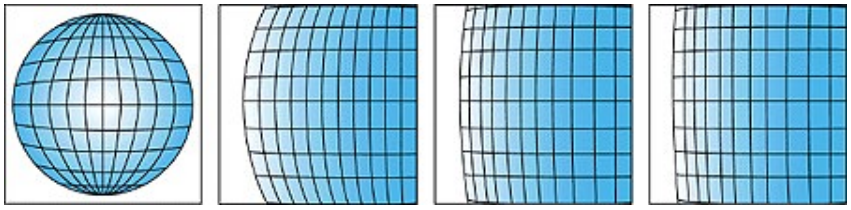

Figure 3.2. Flatness problem: as the sphere becomes larger, its surface becomes flatter and flatter. Similarly the inflation of space causes it to become geometrically flat, and general relativity implies that the mass density of a flat universe must equal the critical value. Credit: A. Guth.

We see immediately that the condition for acceleration $\ddot{a} > 0$ is ensured if the equation of state is characterized by negative pressure, $1 + 3\omega < 0$.

To understand how long the inflationary period should be, we note that in inflationary epoch the size of a causal region was about

$$d_H(t_i) \sim H^{-1} \sim m_{Pl}/T_i^2 \sim 10^{-11}\text{GeV}^{-1},$$

with $m_{Pl} = 10^{19}\text{GeV}/c^2$ the Planck mass and the Newtons constant G written in terms of the Planck mass, so that $G = m_{Pl}^{-2}$ in units where $c = \hbar = 1$. We assume the teperature $T_i \sim 10^{15}$ GeV (the temperature when a grand unification symmetry might break). In order for inflation to solve the horizon problem, this causal region must be blown up to at least the size of the observable universe today,

$$d_H(t_0) \sim H_0^{-1} \sim 10^{41}\text{GeV}^{-1}.$$

So that the scale factor must increase by about

$$\frac{\delta a}{a} \sim \left(\frac{a(t_i)}{a(t_0)}\right)\frac{d_H(t_0)}{d_H(t_i)} \sim \left(\frac{T_0}{T_i}\right)\frac{d_H(t_0)}{d_H(t_i)} \sim 10^{24},$$

or somewhere around a factor of e^{55}, or e-foldings number $N \sim 55$. Assuming from here $N = 60$, the expansion happens in a time of $\sim 60\ H^{-1} \sim 10^{-34}$ seconds, if inflation occurs at T_i.

We will now demonstrate how this brief period of accelerated expansion solves the problems of the standard big-bang cosmology.

- **Resolution of the flatness problem.** If the scale factor grew by at least a factor of e^{60} during inflation, then we see from the Eq.(1.22) that the universe is very flat at the end of inflation, since the curvature term drops while the gravitational term remains constant. Therefore, Ω_{tot} is driven so close to unity that we will still observe it near unity today (even though $\Omega_{tot} = 1$ is unstable). In Fig.(3.2) we see how the expanding sphere illustrates the solution to the flatness problem in inflationary cosmology.

- **Resolution of the horizon problem.** For any FLRW space with constant equation of state, there is a conserved quantity given by:

$$\left(\frac{d}{d_H}\right)^2 |\Omega - 1| = const. \tag{3.5}$$

Using Eq.(3.4), we see that comoving scales grow in size more quickly than the horizon,

$$\frac{d|\Omega - 1|}{d\log a}\frac{d}{d_H} > 0. \tag{3.6}$$

This is a very remarkable behavior. It means that two points that are initially in causal contact ($d < d_H$) will expand so rapidly that they will eventually be causally disconnected: during inflation the universe expands exponentially and physical wavelengths grow faster than the horizon. Fluctuations are hence stretched outside of the horizon during inflation and re-enter the horizon in the late universe. Scales that are outside of the horizon at CMB decoupling were in fact inside the horizon before inflation. The region of space corresponding to the observable universe therefore was in thermal equilibrium before inflation and the uniformity of the CMB is given a causal explanation, as shown in Fig.(3.3). Putting in numbers shows that $N > 60$ e-folds of inflation are required to achieve this, and a brief period of acceleration therefore results in the ability to correlate space over apparently impossible distances.
In effect, inflation answers the horizon paradox by saying that we calculated the particle horizon incorrectly, assuming that the expansion of the universe was always decelerating. The last scales to leave the event horizon during the inflationary epoch are the first ones to reenter the particle horizon during the subsequent radiation/matter dominated era.

- **Resolution of the magnetic-monopole problem.** The rapid expansion of the inflationary stage rapidly dilutes the unwanted relic particles, because the energy density during inflation falls off more slowly (as a^{-2} or slower) than the relic particle density. Very quickly their density becomes negligible. This resolution can only work if, after inflation, the energy density of the universe can be turned into conventional matter without recreating the unwanted relics. This can be achieved by ensuring that during the conversion, known as *reheating*, the temperature never gets hot enough again to allow their thermal recreation. Then reheating can generate solely the things which we want. Such successful reheating allows us to get back into the hot big-bang universe, recovering all its later successes such as nucleosynthesis and the microwave background.

An enormous amount of entropy is created during the reheating epoch, explaining the large entropy within the curvature radius: the energy conservation implies that the enormous energy in ρ_ϕ must be converted into radiation. While we have considered $\rho_\phi = const$, and thus $p_\phi = -\rho_\phi$ and exponential expansion, solving the horizon and flatness problems in this way requires only that the expansion be accelerating (growing faster than $a \propto t$). The acceleration by the Friedmann equation is $\ddot{a} \propto (\rho + 3p)$, so accelerated expansion only requires $\omega \equiv p_\phi/\rho_\phi < 1/3$.

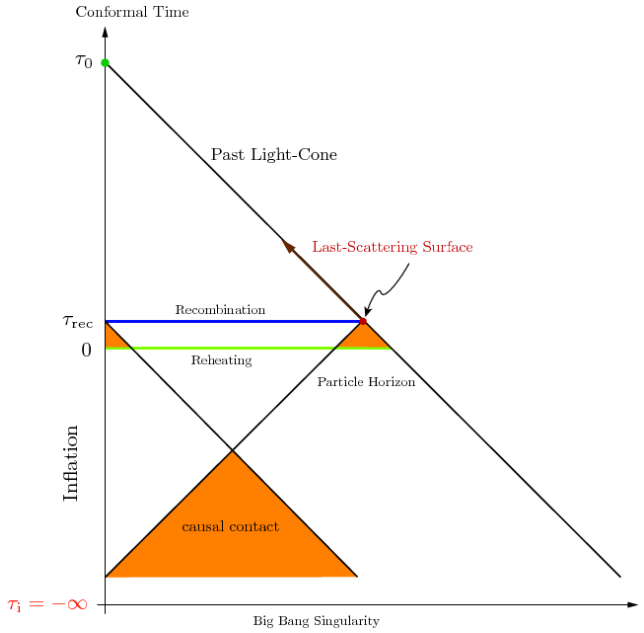

Figure 3.3. Conformal diagram of inflationary cosmology. Inflation extends conformal time to negative values. The end of inflation creates an "apparent" big-bang at $\tau = 0$. There is, however, no singularity at $\tau = 0$ and the light cones intersect at an earlier time if inflation lasts for at least 60 e-folds. Credit: D. Baumann [36]

For $1 < w < 1/3$, ρ_ϕ falls with time but slower than a^2, so the gravitational term still grows relative to the curvature term. Of course, the weaker the acceleration, the longer inflation must last to solve the horizon and flatness problems.

3.2 Physics of Inflation.

Inflation is a very unfamiliar physical phenomenon: within a fraction a second the universe grew exponential at an accelerating rate. In Einstein gravity this requires a negative pressure source or a nearly constant energy density. In this section we describe the physical conditions under which this can arise.

3.2.1 Slow roll inflation.

We have already seen that a cosmological constant due to nonzero vacuum energy results in accelerating cosmological expansion. While this is a good candidate for explaining the observations of Type Ia supernovae, it does not work for explaining inflation at early times for the simple reason that any period of accelerated expansion in the very early universe must end. Therefore the vacuum energy driving inflation must be dynamic. To implement a time-dependent cosmological constant, we require a field with the same quantum numbers as vacuum, i.e. a scalar. We will consider a scalar field minimally coupled to gravity, with potential $V(\phi)$ and Lagrangian

$$\mathcal{L}_\phi = \frac{1}{2} g^{\mu\nu} \partial_\mu \phi \partial_\nu \phi - V(\phi). \tag{3.7}$$

The equation of motion for a homogeneous mode of the field $\phi(t,x)$ called *inflaton* is

$$\ddot{\phi} + 3H\dot{\phi} + \frac{dV}{d\phi} = 0. \tag{3.8}$$

This is the familiar equation for a free scalar field with an extra term, $3H\dot{\phi}$, that comes from the use of the FRW metric in the Lagrangian. This is of interest because the zero mode of the field forms a perfect fluid, with energy density and pressure:

$$\rho_\phi = \tfrac{1}{2}\dot{\phi}^2 + V(\phi)$$
$$p_\phi = \tfrac{1}{2}\dot{\phi}^2 - V(\phi)$$

Note in particular that in the limit $\dot{\phi} \to 0$ we recover a cosmological constant, $p = -\rho$, as long as the potential $V(\phi)$ is nonzero. The Friedmann equations are:

$$H^2 = \frac{8\pi}{3m_{Pl}^2}\left[\frac{1}{2}\dot{\phi}^2 + V(\phi)\right] \tag{3.9}$$

$$\left(\frac{\ddot{a}}{a}\right) = \frac{8\pi}{3m_{Pl}^2}\left[V(\phi) - \dot{\phi}^2\right] \tag{3.10}$$

and in the $\dot{\phi} \to 0$ limit, we have:

$$H^2 = \frac{8\pi}{3m_{Pl}^2}V(\phi) = const \tag{3.11}$$

so that the universe expands exponentially, $a(t) \propto e^{Ht}$.
This can be generalized to a time-dependent field and a quasi-exponential expansion in a straightforward way. If we have a slowly varying field $(1/2)\dot{\phi}^2 \ll V(\phi)$, we can write the equation of motion of the field as

$$3H\dot{\phi} + V'(\phi) \sim 0 \tag{3.12}$$

and the Friedmann equation as

$$H^2(t) \sim \frac{8\pi}{3m_{Pl}^2}V(\phi(t)) \tag{3.13}$$

so that the scale factor evolves as $a(t) \propto \exp\int H(t')dt' \equiv e^{-N(t)}$, with N e-folds number (that is large in the past and decreases as we go forward in time and as the scale factor a increases).
This is known as the *slow roll* approximation, and corresponds physically to the field evolution being dominated by the "friction" term $3H\dot{\phi}$ in the equation of motion. This will be the case if the potential is sufficiently flat, $V'(\phi) \ll V(\phi)$. It is possible to write the equation of state of the field in the slow roll approximation as

$$p = \left[\frac{2}{3}\epsilon(\phi) - 1\right]\rho. \tag{3.14}$$

The ϵ parameter

$$\epsilon \equiv \frac{m_{Pl}^2}{4\pi}\left[\frac{H'(\phi)}{H(\phi)}\right]^2 \sim \frac{m_{Pl}^2}{16\pi}\left[\frac{V'(\phi)}{V(\phi)}\right]^2, \tag{3.15}$$

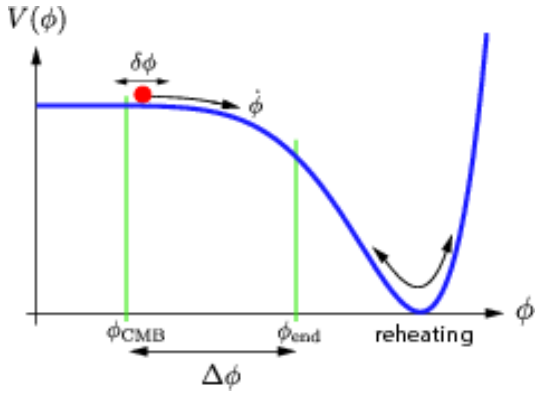

Figure 3.4. Example of an inflaton potential. Acceleration occurs when the potential energy of the field dominates over its kinetic energy. Inflation ends at ϕ_{end} when the kinetic energy has grown to become comparable to the potential energy. CMB fluctuations are created by quantum fluctuations $\delta\phi$ about 60 e-folds before the end of inflation. At reheating, the energy density of the in inflaton is converted into radiation. Credit: Baumann [36]

and the η parameter

$$\eta \equiv \frac{m_{Pl}^2}{4\pi}\left[\frac{H''(\phi)}{H(\phi)}\right] \sim \frac{m_{Pl}^2}{8\pi}\left[\frac{V''(\phi)}{V(\phi)} - \frac{1}{2}\left(\frac{V'(\phi)}{V(\phi)}\right)\right] \tag{3.16}$$

are referred to as *slow roll parameters*, and the slow roll approximation is valid as long as both are small ($\epsilon \ll 1, |\eta| \ll 1$).
This parameterization is convenient because the condition for accelerating expansion $\ddot{a} > 0$ is $\epsilon < 1$:

$$\frac{\ddot{a}}{a} = H^2(1-\epsilon), \tag{3.17}$$

and the parameter ϵ is related to the evolution of the Hubble parameter by

$$\epsilon = -\frac{d\ln H}{d\ln a} = \frac{1}{H}\frac{dH}{dN}. \tag{3.18}$$

In the same way we can write number of e-folds as a function $N(\phi)$ of the field as:

$$N \equiv \ln\frac{a(t_{end})}{a(t_{init})} = -\int H dt = -\int \frac{H}{\dot{\phi}} d\phi = \frac{2\sqrt{\pi}}{m_{Pl}}\int \frac{d\phi}{\sqrt{\eta}} \sim \frac{8\pi}{m_{Pl}^2}\int_{\phi_{end}}^{\phi} \frac{V(\phi)}{V'(\phi)} d\phi. \tag{3.19}$$

Notice that between two scalar field values it can be calculated without needing to solve the equations of motion, and also that it is unchanged if one multiplies $V(\phi)$ by a constant. As seen, the minimum amount of inflation required to solve the various cosmological problems is about 60 e-foldings, but inflation is typically so rapid that most inflation models give much more.

Looking at Fig.(3.4), we can intuitively understand the behavior of the field ϕ. At early times, the energy density of the universe is dominated by the field, that slowly evolves on a nearly constant potential. The universe is exponentially driven toward flatness and homogeneity and inflation ends as the potential becomes more steep and the field begins to oscillate about its vacuum state at the minimum of the potential.

In order to have a transition to a radiation-dominated universe, the energy in the inflaton field must decay into standard model particles. The process is generically called *reheating* and it is model-dependent, but it typically happens very rapidly. The field ϕ need not be a fundamental field like a Higgs boson (although it could in fact be fundamental). The simple single-field described here is an effective representation of a large variety of underlying fundamental theories. All of the physics important to inflation is contained in the shape of the potential $V(\phi)$. The details of the underlying theory are important for understanding the epoch of reheating, because the reheating process depends crucially on the specific couplings of the inflaton to the other degrees of freedom in the theory.
As we know that the universe has to be radiation dominated and in equilibrium by the time of primordial nucleosynthesis, at temperatures of order MeV, a typical assumption is that the reheat temperature is something between 1 TeV and 10^{16} GeV, which translates into a range for $N_{min} \sim [46, 60]$.

3.3 Inhomogeneities.

Inflation models not only explain the large-scale homogeneity of the universe, but also provide a mechanism for explaining the observed level of inhomogeneity as well. During inflation, quantum fluctuations on small scales are quickly red-shifted to scales much larger than the horizon size, where they are “frozen" as perturbations in the background metric. The metric perturbations created during inflation are of two types: scalar, or curvature perturbations,which couple to the stress-energy of matter in the universe and form the seeds for structure formation, and tensor, or gravitational wave perturbations, which do not couple to matter. Both scalar and tensor perturbations contribute to CMB anisotropy. Scalar fluctuations can also be interpreted as fluctuations in the density of the matter in the universe. Scalar fluctuations can be quantitatively characterized by the *comoving curvature perturbation* $\mathcal{R} = H\frac{\delta\phi}{\dot{\phi}}$ and the two-point correlations $\mathcal{P}_\mathcal{R}$. As long as the equation of state ϵ is slowly varying, the power spectrum of curvature perturbation can be shown to be:

$$\mathcal{P}_\mathcal{R}^{1/2}(k) = \left(\frac{H^2}{2\pi\dot{\phi}}\right)_{k=aH} = \left[\frac{H}{m_{Pl}}\frac{1}{\sqrt{\pi\epsilon}}\right]_{k=aH}. \tag{3.20}$$

The fluctuation power spectrum is in general a function of wavenumber k, and is evaluated when a given mode crosses outside the horizon during inflation, $k = aH$. Outside the horizon, modes do not evolve, so the amplitude of the mode when it crosses back inside the horizon during a later radiation- or matter-dominated epoch is just its value when it left the horizon during inflation. Instead of specifying the fluctuation amplitude directly as a function of k, it is convenient to specify it as a function of the number of e-folds N before the end of inflation at which a mode crossed outside the horizon. The *spectral index* n_s for $\mathcal{P}_\mathcal{R}$ is defined by:

$$n_s - 1 \equiv \frac{d\ln\mathcal{P}_\mathcal{R}}{d\ln k}, \tag{3.21}$$

so that a scale-invariant spectrum, in which modes have constant amplitude at horizon crossing, is characterized by $n_s = 1$.

The *power spectrum of tensor fluctuation* modes $\mathcal{T}$ and the corresponding tensor spectral index is given by:

$$P_{\mathcal{T}}^{1/2}(k_N) = \left[\frac{4H}{m_{Pl}\sqrt{\pi}}\right]_N, \tag{3.22a}$$

$$n_{\mathcal{T}} \equiv \frac{d\ln P_{\mathcal{T}}}{d\ln k}. \tag{3.22b}$$

The *ratio of tensor-to-scalar* modes, frequently expressed as a quantity r, is then

$$r = \frac{P_{\mathcal{T}}}{\mathcal{P}_{\mathcal{R}}} = 16\epsilon, \tag{3.23}$$

so that tensor modes are negligible for $\epsilon \ll 1$.
In the limit of slow roll, the spectral indices n_s and $n_{\mathcal{T}}$ vary slowly or not at all with scale. We can write the spectral indices to lowest order in terms of the slow roll parameters ϵ and η as:

$$n_s \sim 1 - 4\epsilon + 2\eta, \tag{3.24a}$$

$$n_{\mathcal{T}} \sim -2\epsilon = -\frac{r}{8}. \tag{3.24b}$$

The second equation is known as the *consistency relation* for inflation.
Deviations from a simple power-law spectrum of perturbations are higher order in the slow-roll parameters, and thus serve as a test of the consistency of the slow-roll approximation. Scale dependence in the observables corresponds to scale dependence in the associated slow-roll parameter, and can be quantified in terms of the infinite hierarchy of inflationary flow equations [45],

$$\begin{aligned}
\frac{d\epsilon}{dN} &= 2\epsilon\left(\eta - \epsilon\right), \\
\frac{d\eta}{dN} &= \xi - \epsilon\eta, \\
&\vdots \\
\frac{d^\ell\lambda}{dN} &= \left[(\ell-1)\eta - \ell\epsilon\right]{}^\ell\lambda + {}^{(\ell+1)}\lambda.
\end{aligned} \tag{3.25}$$

The higher-order flow parameters are defined by

$$\begin{aligned}
\epsilon &\equiv 2m_{Pl}^2\left(\frac{H'(\phi)}{H(\phi)}\right)^2, \\
\eta &\equiv 2m_{Pl}^2\frac{H''(\phi)}{H(\phi)}, \\
\xi &\equiv 4m_{Pl}^4\frac{H'(\phi)H'''(\phi)}{H^2(\phi)}, \\
&\vdots \\
{}^\ell\lambda &\equiv \left(2m_{Pl}^2\right)^\ell\frac{H'(\phi)^{(\ell-1)}}{H(\phi)^\ell}\frac{d^{(\ell+1)}H(\phi)}{d\phi^{(\ell+1)}},
\end{aligned} \tag{3.26}$$

where the prime denotes derivatives with respect to scalar field ϕ.
A given inflation model can therefore be described to lowest order in slow roll by

three independent parameters: $\mathcal{P}_\mathcal{R}$, $P_\mathcal{T}$ and n_s. If we wish to include higher-order effects, we have a fourth parameter describing the *running of the scalar spectral index* $dn_s/d\ln k$. The scale-dependence of the spectral index can be found by relating the wavenumber k to the number of e-folds N,

$$\frac{dn}{d\ln k} \equiv n_{\rm run} = -\frac{1}{1-\epsilon}\frac{d}{dN}(2\eta - 4\epsilon) = 10\epsilon\eta - 8\epsilon^2 + ... \tag{3.27}$$

Since the running depends on higher-order flow parameters than the spectral index itself, it is an independent parameter, even in slow-roll inflation models. In typical single-field inflation models, the running of the spectral index is negligible, so a detection of scale dependence in the spectral index would rule out a large class of viable single-field inflation models, and would therefore be a powerful probe of inflationary physics.

Calculating the CMB fluctuations from a particular inflationary model reduces to the following basic steps:

- from the potential, calculate ϵ and η;
- from ϵ, calculate N as a function of the field ϕ;
- invert $N(\phi)$ to find ϕ_N (where ϕ_N is the value of the inflaton field when there are e-foldings until the end of inflation);
- calculate $\mathcal{P}_\mathcal{R}$, n_s, and $P_\mathcal{T}$ as functions of ϕ, and evaluate them at $\phi = \phi_N$.

3.4 Old Inflation and New Inflation.

In Guth's original inflation scenario [43] , the inflaton field ϕ sits at a local minimum and is trapped in a false vacuum state. The vacuum state of a field or particle is the lowest energy state available to the system. The concept of false vacuum comes from examination of Fig.(3.5). If ϕ is placed in the potential well on the left, the lowest energy available is that of the true vacuum. The only way ϕ can get out of this local minimum is by quantum tunneling, after some characteristic time. As tunneling takes place the universe inflates. Inflation halts when ϕ reaches the true vacuum and bubbles of the true vacuum coalesce releasing the latent heat that was stored in the field. Tunneling that leads to bubble nucleation is a first order phase transition. This is very similar to processes that take place in the study of condensed matter physics, fluid dynamics, and ferromagnetism. The bubbles experience a state of negative pressure. Once created, they continue to expand at an exponential rate. Each expanding bubble corresponds to an expanding domain. However, when one carefully investigates this situation, one finds that the bubbles can collide as they reach the true vacuum. Furthermore, the size of these bubbles expands at too great of a rate and the corresponding universe is left void of structure. One finds that too much inflation occurs and the visible universe is left empty.
Guth and others further tried to remedy these problems by fine-tuning the bubble formation. The problem with this is twofold. One, cosmologists and particle theorists do not like fine-tuning. The idea is to form a model that gives our universe as a

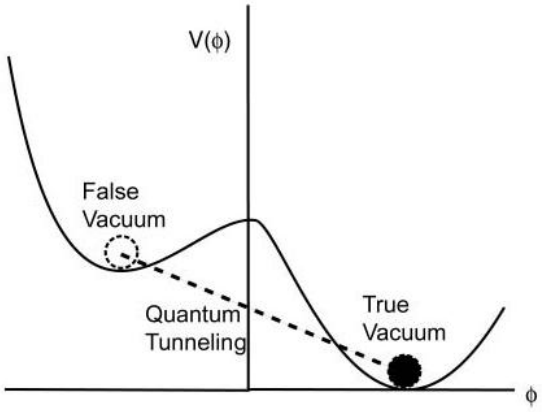

Figure 3.5. Toy Model For Original Inflaton. In this model of inflation the inflaton finds itself trapped in a false minimum. It is freed from this minimum when tunneling is allowed to occur resulting in a first order phase transition in the early universe.

usual result that follows from natural consequences. By natural one means that the scales of the model are related to the fundamental constants of nature; e.g., quantum gravity should occur at the Planck scale, since this scale is the only one natural in units (c, $\hbar$, G). Secondly, if the model is fine-tuned to agree with the observations of the anisotropies in the cosmic background, the bubbles would collide far too often. This results in the appearance of topological defects, like the monopoles. However, this was the whole reason inflation was invoked in the first place.

In 1982, a solution to the problem was proposed by Linde [46] and independently by Steinhardt and Albrecht [47]. This New Inflation model assumes the inflaton field evolves very slowly from its initial state, while undergoing a phase transition of second order. Fig.(3.6, panel a) illustrates this by again considering the evolution of ϕ. If ϕ 'rolls' down the potential at a slow rate, one obtains the amount of inflation needed to solve the initial value problems. After the universe cools to a critical temperature, T_c, ϕ can proceed to its 'true' vacuum state energy. The transition of the potential is a second order phase transition, so this model does not require tunneling. This type of transition is similar to the transitions that occur in ferromagnetic systems.

The majority of current models rely on another concept coined by Linde as *chaotic inflation*. This model differs from old and new inflation in that no phase transitions occur. In this scenario the inflaton is displaced from its true vacuum state by some arbitrary mechanism, perhaps quantum or thermal fluctuations. Given this initial state, the inflaton slowly rolls down the potential returning to the true vacuum (see Fig.(3.6, panel b)). This model has the advantage that no fine-tuning of critical temperature is required. This model presents a scenario, which can be fulfilled by a number of different models. After the displacement of the inflaton, the universe undergoes inflation as the inflaton rolls back down the potential. Once the inflaton returns to its vacuum (true) state, the universe is reheated by the inflaton coupling

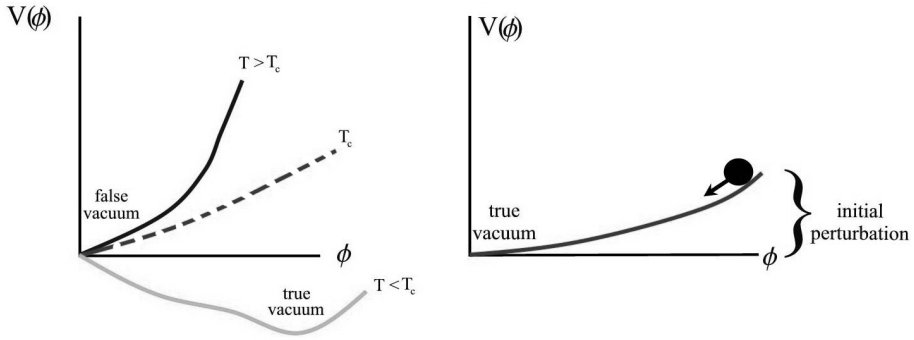

Figure 3.6. Left panel: Toy Model For New Inflation - When the temperature of the universe decreases to the critical temperature T_c, the scalar field potential experiences a second order phase transition. This makes the 'true' vacuum state available to ϕ.
Right panel: Toy Model For Chaotic Inflation - The inflaton finds itself displaced from the true vacuum and proceeds to 'roll' back. Inflation takes place while the inflaton is displaced.

to other matter fields. After reheating, the evolution of the universe proceeds in agreement with the standard big-bang model.
Although the inflaton could in principle be displaced by a very large amount, we must deal with the last moments of the evolution. This is when the perturbations in the scalar field are created that eventually lead to large-scale structure and anisotropies in the cosmic background. As long as the inflaton is displaced by a minimal amount (minimal to be defined in a moment) the initial value problem will be solved. When considering quantum fluctuations resulting in the displacement of ϕ, minimal displacement is easily achieved.

3.5 Single field models.

The standard scenario is associated to one-single field models of inflation, and the observed density perturbations are due to fluctuations of the inflaton field itself. When inflation ends, the inflaton oscillates about the minimum of its potential and decays, thereby reheating the universe. The initial inflaton fluctuations are adiabatic on large scales and are transferred to the radiation fluid during reheating. In such a standard scenario the inflaton decay rate has no spatial fluctuations.
Even restricting ourselves to a simple single-field inflation scenario, the number of models available to choose from is large. It is convenient to define a general classification scheme, or zoology for models of inflation. We divide models into three general types: *large-field*, *small-field*, and *hybrid*, with a fourth classification, *linear* models, serving as a boundary between large- and small-field. In Fig.(3.7) we show the $r - n_s$ plane divided into these regions. A generic single-field potential can be characterized by two independent mass scales: a height Λ^4, corresponding to the vacuum energy density during inflation, and a width μ, corresponding to the change in the field value $\Delta\phi$ during inflation:

$$V(\phi) = \Lambda^4 f\left(\frac{\phi}{\mu}\right) \tag{3.28}$$

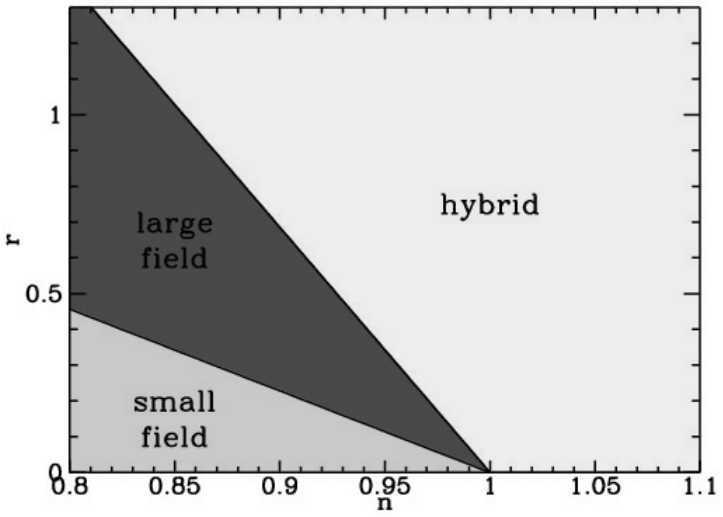

Figure 3.7. Regions in the $r - n_s$ plane corresponding to large field, small field, and hybrid models. Credit: S. Dodelson [48]

Different models have different forms for the function f. The height Λ is fixed by normalization, so the only free parameter is the width μ.
With the normalization fixed, the relevant parameter space for distinguishing between inflation models to lowest order in slow roll is then the $r - n_s$ plane (To next order in slow-roll parameters, one must use the running of n_s Eq.(3.27)). Different classes of models are distinguished by the value of the second derivative of the potential, or, equivalently, by the relationship between the values of the slow-roll parameters ϵ and η.

Large field inflation. $-\epsilon < \eta \leq \epsilon$

Large-field models are characterized by so-called chaotic initial conditions, in which the inflaton field is displaced far from its minimum, typically to values $\phi \sim m_{Pl}$, and rolls toward a minimum at the origin. Such models are characterized by $V''(\phi) > 0$ and $-\epsilon < \eta \leq \epsilon$.
The generic large-field potentials we consider are *polynomial potentials* $V(\phi) = \Lambda^4(\phi/\mu)^p$, and *exponential potentials*, $V(\phi) = \Lambda^4 \exp(\phi/\mu)$.

For the case of an exponential potential, $V(\phi) \propto \exp(\phi/\mu)$, the tensor/scalar ratio r is simply related to the spectral index as:

$$r = 8(1 - n_s), \tag{3.29}$$

and the slow roll parameters are constant (there is no dependence upon N).

For inflation with a polynomial potential, $V(\phi) \propto \phi^p$ in Fig.(3.8), we have:

$$n_s - 1 = -\frac{2+p}{2N}, \tag{3.30a}$$

$$r = \frac{8p}{2N} = 8\left(\frac{p}{p+2}\right)(1 - n_s), \tag{3.30b}$$

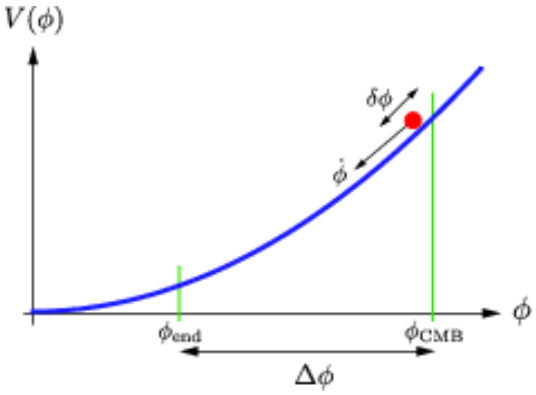

Figure 3.8. Large-field inflation. The inflationary dynamics is driven by a single monomial term in the potential, $V(\phi) \propto \phi^p$. In these models the inflaton field evolves over a super-Planckian range during inflation, $\Delta\phi > M_{Pl}$, and a large amplitude of gravitational waves is produced by quantum mechanical fluctuations. Credit: Baumann [36]

so that tensor modes are large for significantly tilted spectra.
By shifting the number of e-foldings by ΔN one therefore expects

$$\frac{\Delta(n_s - 1)}{n_s - 1} = \frac{\Delta r}{r} = -\frac{\Delta N}{N}. \tag{3.31}$$

From these relations we deduce that sizeable correlated theoretical errors should be expected for those large-field models characterized by large deviations from a flat spectrum and by large values of the tensor-to-scalar amplitude ratio. Furthermore these errors increase with the potential of the polynomial p. Of course, these statements are based on relations valid only at first order in the slow roll parameters. This means that for very large values of $(n_s - 1)$ and r higher order corrections become relevant and may significantly alter the simple relations of Eq.(3.31).
Vice versa, we can note that no intrinsic errors of the observables n_s and r are expected in exponential potential case.

One of the most elegant inflationary models is *natural inflation* where the potential takes the following form, see Fig.(3.9):

$$V(\phi) = V_0 \left[\cos\left(\frac{\phi}{f}\right) + 1\right]. \tag{3.32}$$

This potential often arises if the inflaton field is taken to be an axion. Depending on the parameter f the model can be of the small-field or large-field type. However, it is particularly attractive to consider natural inflation for large-field variations, $2\pi f > m_{Pl}$, since for axions a shift symmetry can be employed to protect the potential from correction terms even over large field ranges.

Small field inflation. $\eta < -\epsilon$

Small-field models are of the form that would be expected as a result of spontaneous symmetry breaking, with a field initially near the origin and rolling toward a

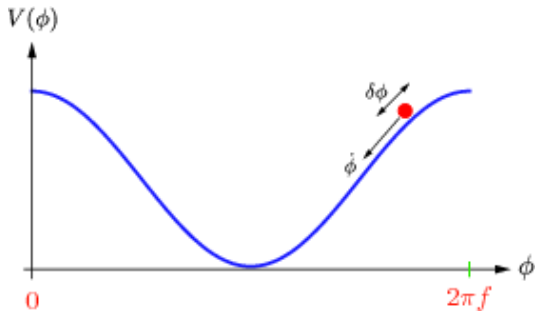

Figure 3.9. Natural Inflation. If the periodicity $2\pi f$ is super-Planckian the model can naturally support a large gravitational wave amplitude. Credit: Baumann [36]

minimum at $\phi \neq 0$. In this case, inflation occurs when the field is small relative to its expectation value.
Small-field models are characterized by $V''(\phi) < 0$ and $\eta < -\epsilon$. Typically ϵ (and hence the tensor amplitude) is close to zero in small-field models. The generic small-field potentials we consider are of the form $V(\phi) = \Lambda^4[1 - (\phi/\mu)^p]$, which can be viewed as a lowest-order Taylor expansion of an arbitrary potential about the origin. The cases $p = 2$ and $p > 2$ have very different behavior:

$$p = 2, n_s - 1 \sim -(1/2\pi)(m_{Pl}/\mu)^2, \tag{3.33a}$$

$$p > 2, n_s \sim 1 - \frac{2}{N}\left(\frac{p-1}{p-2}\right). \tag{3.33b}$$

In the first case there is no dependence upon the number of e-foldings. On the other hand

$$r = 8(1-n)\exp[-1 - N(1-n_s)] \longrightarrow \frac{\Delta r}{r} = (n_s - 1)\Delta N. \tag{3.34}$$

In the second case the scalar spectral index is independent of m_{Pl}/μ. Assuming $\mu < m_{Pl}$ results in an upper bound on r of

$$r < 8\frac{p}{N(p-2)}\left(\frac{8\pi}{Np(p-2)}\right)^{p/(p-2)}. \tag{3.35}$$

The corresponding theoretical errors read

$$\frac{\Delta(n_s - 1)}{(n_s - 1)} = -\frac{\Delta N}{N}\frac{\Delta r}{r} \sim (n_s - 1)\Delta N \sim -\frac{2(p-1)}{p-2}.\frac{\Delta N}{N} \tag{3.36}$$

Due to the tiny predicted values of r, for small field models one expects generically tiny errors in the tensor-to-scalar amplitude ratio, but sizeable errors in the spectral index.

Hybrid inflation. $0 < \epsilon < \eta$

Hybrid models are characterized by a field evolving toward a minimum of the potential with a nonzero vacuum energy. These generally involve more than one scalar field, but can be treated during the inflationary epoch as single-field inflation, with ϕ small and $V''(\phi) > 0$. The end of inflation arises as a result of instability in

a second field. Hybrid inflation is the only class of models which predicts a blue spectrum, $n > 1$.
We consider generic potentials for hybrid inflation of the form $V(\phi) = \Lambda^4[1+(\phi/\mu)^p]$. The field value at the end of inflation is determined by some other physics, so there is a second free parameter characterizing the models. Because of this extra freedom, hybrid models fill a broad region in the $r - n$ plane.
For $(\phi_N/\mu) \gg 1$ one recovers the same results of the large-field models.
On the contrary, when $(\phi_N/\mu) \ll 1$, the dynamics are analogous to small-field models, except that the field is evolving toward, rather than away from, a dynamical fixed point.
This distinction is important because near the fixed point the parameters r and n become independent of the number of e-folds N, and the corresponding theoretical uncertainties due to the uncertainty in N vanish. However, there is an additional degree of freedom not present in other models due to the presence of the additional parameter (the second field). Therefore the theoretical uncertainties in the predictions of a generic hybrid inflation model are decoupled from the physics of reheating. The distinguishing observational feature of many hybrid models is $\eta > 0$ and a blue scalar spectral index, $n_s > 1$. Notice that at first order in the slow roll parameters, there is no overlap in the $r - n_s$ plane between hybrid inflation and other models. However, as we will explicitly show, this feature is lost going beyond first order: by changing N models can flow from the hybrid regions to other model regions; this feature is generic, models can flow from one region to another. Therefore it is important to distinguish between models labeled hybrid in the sense of evolution toward a late-time asymptote and the region labeled hybrid in the zoo plot. The lowest-order correspondence does not always survive to higher order in slow roll.

Linear inflation. $\epsilon = -\eta$

Linear models, $V(\phi) \propto \phi$, live on the boundary between large-field and small-field models, with $V''(\phi) = 0$ and $\eta = -\epsilon$. The spectral index and tensor/scalar ratio are related as:

$$r = \frac{8}{3}(1 - n_s). \tag{3.37}$$

For linear models, Eq.(3.31) applies.

3.6 Multiple fields models.

In this section we get out of the classical treatment of inflation with single field models, speaking briefly of multiple fields models. The presence of more fields during inflation can lead to quite different inflationary dynamics, that might appear unnatural in a single field model, and to spectra of primordial perturbations that would be impossible in single field models.
The presence of multiple light fields leads to the generation of non-adiabatic field perturbations during inflation. This can alter the evolution of the overall curvature perturbation, for instance leading to detectable non-Gaussianity, and may leave residual isocurvature fluctuations in the primordial density perturbation on large scales after inflation, which can be correlated with the curvature perturbation. Such

alternative models are interesting not only as theoretical possibilities, but because they could be distinguished by observations [49].
As we say in section 3.2, the time-evolution of a single, spatially homogeneous scalar field is governed by the Klein-Gordon equation (Eq.(3.8)), while the Friedmann equations for the dynamics of the cosmology is reported in Eq.(3.9). The set of equations of the multiple scalar fields, instead, obey the Klein-Gordon equation:

$$\ddot{\varphi}_I + 3H\dot{\varphi}_I = -\frac{\partial}{\partial\varphi_I}\left(\sum_J U_J\right), \tag{3.38}$$

where one must allow for the possibility that the potential energy is given by a sum over many terms

$$V = \sum_J U_J. \tag{3.39}$$

The wider range of interaction potentials possible in multiple field models leads to possibilities such as *hybrid inflation*.
Another more subtle change enters through the Friedmann constraint:

$$3H^2 = 8\pi G\left(V + \sum_I \frac{1}{2}\dot{\varphi}_I^2\right). \tag{3.40}$$

We note that even in the absence of explicit interactions in the scalar field Lagrangian, the fields will still be coupled gravitationally. The Hubble expansion rate is due to the sum over all fields and this can alter the field dynamics even if the potential for each individual field is left unchanged. The additional Hubble damping present due to multiple fields can be used to drive slow-roll inflation in *assisted inflation models* where the individual potentials would be too steep to drive inflation on their own.
Even though the background dynamics can be reduced to an equivalent single field with a specified potential, there is an important qualitative difference between the inflationary dynamics in multiple field inflation with respect to the single field case. The Hubble damping during inflation drives a single scalar field to a unique attractor solution during slow-roll inflation where the Hubble rate, field time-derivative and all local variables are a function of the local field value: $H(\phi)$, $\dot{\phi}(\phi)$, etc. This means that the evolution rapidly becomes independent of the initial conditions.
In multiple field models we may have a family of trajectories in phase space where, for example, the Hubble rate at a particular value of φ_1 is also dependent upon the value of φ_2. In this case the inflationary dynamics, and hence observational predictions, may be dependent upon the trajectory in phase space and thus the initial field values. It is this that allows non-adiabatic perturbations to survive on super-Hubble scales in multiple field inflation. It is important to distinguish between models, such as most hybrid models, with multiple fields but only one light direction in field space with small effective mass $\partial^2 V/\partial\varphi^2 \ll H^2$ during inflation, and models with many light fields, such as assisted inflation models. Only models with multiple light fields can have multiple slow-roll trajectories.

A topical example of multiple field inflation is Nflation [50]. This model is based on the very large number of fields with a potential energy near the minimum of the

effective potential

$$V = \frac{1}{2}\sum_I m_I^2 \varphi_I^2. \tag{3.41}$$

With a single scalar field the quadratic potential yields the familiar *chaotic inflation model* with a massive field $V = m^2\phi^2/2$. But to obtain inflation with a single massive field the initial value of the scalar field must be several times the Planck mass and there is a worry that we have no control over corrections to the potential at super-Planckian values in the effective field theory. But with many scalar fields the collective dynamics can yield inflation even for sub-Planckian values if there are a sufficiently large number of fields. For random initial conditions, $-m_{Pl} < \varphi_I(0) < m_{Pl}$, the total number of e-folds is given by $n_f/12$, where n_f is the total number of fields. Thus we require $n_f > 600$ for sufficient inflation if none of the fields is allowed to exceed the Planck scale.
As remarked earlier, in the presence of more than one light field, the trajectory in field space at late times, and hence the observable predictions, may be dependent upon the initial conditions for the different fields. Instead, we have evidence that the predicted spectral index, $n_{\rm R}$, is independent of the precise initial conditions for a sufficiently large number of fields [51]. Indeed inflation with an arbitrary number of massive fields always yields a robust prediction for the tensor-to-scalar ratio r in terms of the number of e-foldings, N, from the end of inflation $r = 8/N$, completely independently of the initial conditions. Thus Nflation seems to be an example of a multiple field model of inflation which makes observable predictions which need not depend upon the specific trajectory in field space. In the limit where the masses become degenerate, $m_I^2 \to m$, the Nflation dynamics becomes particularly simple. The fields evolve radially towards the origin and the potential Eq.(3.41) reduces to that for a single field $V \to \frac{1}{2}m^2\sigma^2$ where σ is the inflaton field. Thus in this limit Nflation reproduces the single field prediction for the tensor-scalar ratio $r = 0.16$ and the spectral index $n_R = 0.96$. However the presence of n_f light fields during Nflation also leads to $n_f - 1$ isocurvature modes during inflation and these have an exactly scale-invariant spectrum (up to first order in the slow-roll parameters) in the limit of degenerate masses. For a thorough discussion on the multiple fields models, we refer to [49].

3.7 Evidence for Inflation.

Looking at the CMB, we discuss now the non-trivial qualitative features of the observations that inflation explains naturally.
Inflation produces a nearly scale-invariant spectrum of perturbations,

$$\langle \mathcal{R}_k \mathcal{R}_{k'} \rangle = (2\pi)^3 \delta(k + k')\mathcal{P}_{\mathcal{R}}(k) \tag{3.42}$$

The truly striking aspect of perturbations generated during inflation is that all Fourier modes have the same phase.
Consider a Fourier mode with physical wavelength λ. While the mode is inside the horizon during inflation it oscillates with a frequency given by $k = 2\pi/\lambda$. However, before inflation ends, the mode exits the horizon, i.e. its physical wavelength gets stretched to a length greater than the instantaneous Hubble radius, $\lambda > H^{-1}$. After

that its amplitude remains constant. Only at a much later time, when the mode re-enters the horizon, causal physics can affect it and lead to a time-evolution. Since the fluctuation amplitude was constant outside the horizon, $\mathcal{R}$ is very small at horizon re-entry. In general, each Fourier mode could be a linear combination of a sine and a cosine mode. However, the special feature of inflation is that excites only the cosine mode (defining horizon re-entry as $t = 0$). Once inside the horizon the curvature perturbation $\mathcal{R}$ sources density fluctuations δ which evolve under the influence of gravity and pressure

$$\ddot{\delta} - c_s^2 \bigtriangledown^2 \delta = F_g |\mathcal{R}| \tag{3.43}$$

where c_s is the sound speed and F_g is the gravitational source term. This leads to oscillations in the density field. In the plasma of the early universe, fluctuations in the matter density were strongly coupled to fluctuations in the radiation. The CMB fluctuations therefore provide a direct snapshot of the conditions of the underlying density field at the time of recombination. Imagining that recombination happens instantaneously, that is not a terrible approximation, fluctuations with different wavelengths would be captured at different phases in their oscillations. Modes of a certain wavelength would be captured at maximum or minimum amplitude, while others would be captured at zero amplitude. If all Fourier modes of a given wavelength had the same phases they would interfere coherently and the spectrum of all Fourier would produce a series of peaks and troughs in the CMB power spectrum as seen on the LSS. However, in order for the theory of initial fluctuations to explain this it needs to involve a mechanism that produces coherent initial phases for all Fourier modes. Inflation does precisely that. Because fluctuations freeze when the exit the horizon the phases for Fourier modes were set well before the modes of interest entered the horizon. When we admire the peak structure of the CMB power spectrum we are really admiring the ability of the primordial mechanism for generating fluctuations to coordinate the phases of all Fourier modes. Without this coherence, the CMB power spectrum would simply be white noise with no peaks and troughs.

When we consider CMB polarization, we see that the cross-correlation between CMB temperature fluctuations and the E-mode polarization has a negative peak around $100 < \ell < 200$, as shown in Fig.(3.10) and Fig.(3.11). This anti-correlation signal is also the result of phase coherence, but now the scales involved were not within the horizon at recombination. Hence, there is no causal mechanism (after $\tau = 0$) that could have produced this signal. One is almost forced to consider something like inflation with its shrinking comoving horizon leading to horizon exit and re-entry.
At recombination, the phase difference between the monopole (sourcing T) and the dipole (sourcing E) of the density field, causes the product of the two to be negative for $100 < \ell < 200$ and positive on smaller scales until $\ell \sim 400$. And this is what we can see in Fig.(3.10) and Fig.(3.11) where we observe the WMAP and Planck results. We have clear evidence that the monopole and the dipole were out of phase with each other at recombination. This evidence is exciting for the small scale modes ($\ell > 200$).
Just as the acoustic peaks bear testimony to coherent phases, the cross-correlation of polarization and temperatures speaks to the coherence of the dipole as well. The

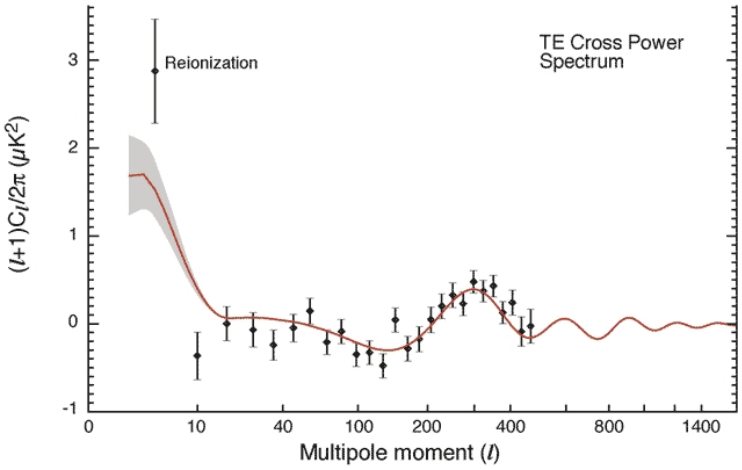

Figure 3.10. Power spectrum of the cross-correlation between temperature and E-mode polarization anisotropies for the WMAP experiment data. The anti-correlation for $\ell = 50 - 200$ (corresponding to angular separations $5^o > \theta > 1^o$) is a distinctive signature of adiabatic fluctuations on superhorizon scales at the epoch of decoupling, confirming a fundamental prediction of the inflationary paradigm. Credit: WMAP [52].

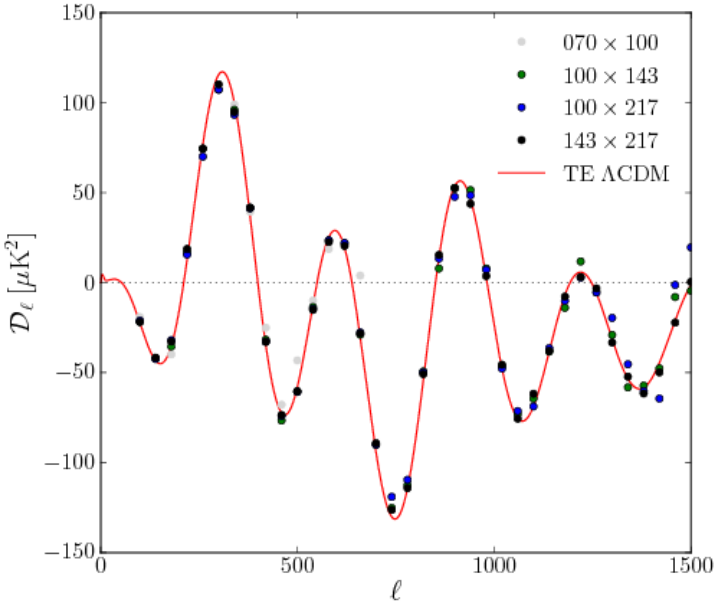

Figure 3.11. Power spectrum of the cross-correlation between temperature and E-mode polarization anisotropies for the Planck experiment data, together with the polarization spectra predicted from the six-parameter ΛCDM model, fit only to the Planck temperature data. In the y-axis $\mathcal{D}_\ell = \ell(\ell+1)\mathcal{C}_\ell/2\pi$. Credit: Planck Collaboration [53].

evidence from the larger scale modes ($\ell < 200$) is a great confirmation. For, these modes were not within the horizon at recombination. So the only way they could have their phases aligned is if some primordial mechanism did the job, when they were in causal contact.

High precision measurements of the B-mode polarization will probe the gravitational radiation produced by inflation, and they will also show whether the energy scale of inflation predicted by the simplest models ($10^{15} - 10^{16}$ GeV) is correct.
We wait for these data by the Planck experiment, although it is unclear if the signal will be visible, or if contamination from foreground sources will interfere with these measurements. Other forthcoming measurements, such as those of 21 centimeter radiation (radiation emitted and absorbed from neutral hydrogen before the first stars turned on), may measure the power spectrum with even greater resolution than the CMB and galaxy surveys, although it is not known if these measurements will be possible or if interference with radio sources on earth and in the galaxy will be too large.

3.8 Testing slow-roll models.

The simplest versions of inflation predict that the scalar perturbations are nearly scale-invariant, Gaussian and adiabatic. In this section we give the latest quantitative constraints on these fundamental predictions of the theory.

Quasi scale-invariants.

Generically, the power spectrum will not be scale independent, with a scale dependence induced by the variation of, e.g., the potential energy and the Hubble parameter as the inflaton field rolls down the potential. The deviation from scale-invariance provides the first test of the detailed time-dependence of the inflationary expansion. In fact, as we have seen, inflation predicts this percent level deviation from scale-invariance: for inflation to end, the Hubble parameter H has to change in time. This time-dependence changes the conditions at the time when each fluctuation mode exits the horizon and therefore gets translated into a scale-dependence of the fluctuations.
In the slow roll regime, however, the scale dependence is rather weak and $\mathcal{P}_{\mathcal{R}}(k)$ can be reasonably well approximated by a power law:

$$\Delta_s^2(k) \equiv \frac{k^3}{2\pi^2}\mathcal{P}_{\mathcal{R}}(k) = A_s(k_\star)\left(\frac{k}{k_\star}\right)^{n_s-1} \tag{3.44}$$

with n_s given by Eq.(3.24a) and the normalization A_s:

$$A_s \sim \frac{1}{24\pi^2}\frac{V}{\epsilon}\bigg|_{k_\star=aH}. \tag{3.45}$$

Measurements of n_s are degenerate with the tensor-to-scalar ratio r so constraints on n_s are often shown as confidence contours in the $n_s - r$ plane. The Planck collaboration's values are reported in the top of Fig.(3.12), while the figure shows

Model	Parameter	*Planck*+WP	*Planck*+WP+lensing	*Planck* + WP+high-ℓ	*Planck*+WP+BAO
ΛCDM + tensor	n_s	0.9624 ± 0.0075	0.9653 ± 0.0069	0.9600 ± 0.0071	0.9643 + 0.0059
	$r_{0.002}$	< 0.12	< 0.13	< 0.11	< 0.12
	$-2\Delta \ln \mathcal{L}_{\max}$	0	0	0	-0.31

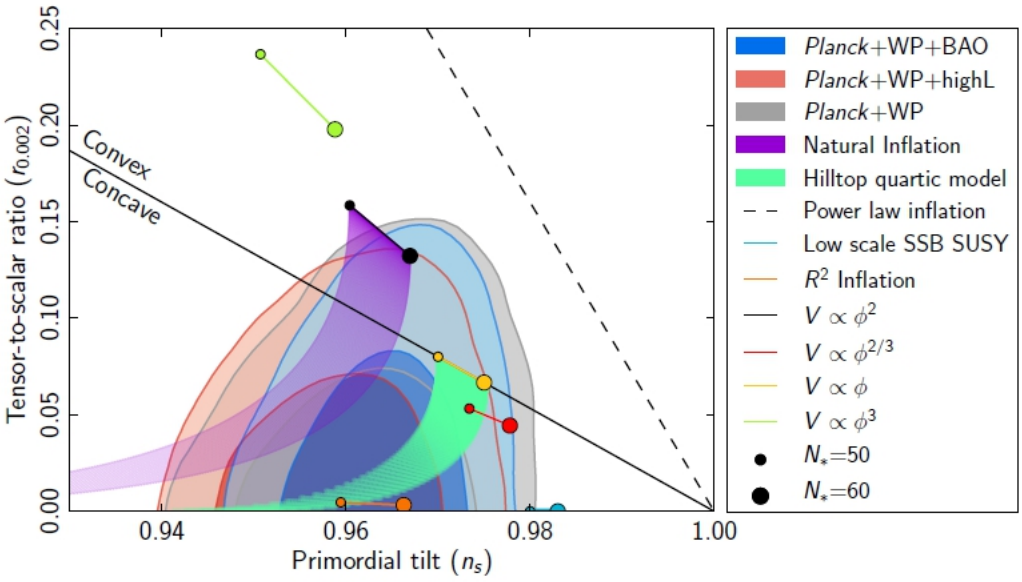

Figure 3.12. Marginalized joint 68% and 95% CL regions for n_s and r using $k_\star = 0.002$ from Planck experiment in combination with other data sets compared to the theoretical predictions of selected inflationary models. Credit: Planck Collaboration [54].

the Planck constraints in the $n_s - r$ plane and indicates the predictions of a number of representative inflationary potentials for a review of particle physics models of inflation [54]. Planck data favour models with a concave potential and most of the joint 95% allowed region lies below the convex potential limit, and concave models with a red tilt in the range $[0.945 - 0.98]$ are allowed by Planck at 95% CL. Models with an exponential potential, a monomial potential with a power larger than two, or hybrid models driven by a quadratic term are disfavored at more than 95% confidence. The quadratic large field model, in the past often cited as the simplest inflationary model, is now at the edge of the 95% CL contours allowed by the data.

Gaussianity.

Inflation predicts that the primordial perturbations will be distributed according to Gaussian statistics, while the non-Gaussianity is suppressed in slow-roll inflation. However, detection of even moderate non-Gaussianity is considerably more difficult. If the perturbations are Gaussian, the two-point correlation function completely describes the perturbations. This is not the case for non-Gaussian fluctuations: higher-order correlations contain additional information and it is a measure of self-interactions of the inflaton field. However, higher-order correlations require more statistics and are therefore more difficult to measure, especially at large angular scales where cosmic variance errors are significant. For the non-Gaussianity, the fluctuations have a non-zero bispectrum $\mathcal{B}_{\mathcal{R}}(k_1; k_2; k_3)$ (corresponding to three-point correlations in real space). In the case of the standard single-field models of inflation in order to characterize the primordial non-Gaussianity we can expand $\mathcal{R}$ in Fourier space as:

$$\mathcal{R}(k) = \mathcal{R}^{(1)}(k) + \frac{1}{(2\pi)^3} \int d^3k_1 d^3k_2 \delta^{(3)}(k_1 + k_2 - k) \times f_{NL}^{\mathcal{R}}(k_1, k_2) \mathcal{R}^{(1)}(k_1) \mathcal{R}^{(1)}(k_2), \tag{3.46}$$

where we have introduced a momentum-dependent non-linearity parameter $f_{NL}(k1, k2)$, that is the non-Gaussianity generated during inflation:

$$f_{NL}^{\mathcal{R}}(k_1, k_2) = \frac{1}{2}(\eta - 3\epsilon) + \mathcal{I}(k_1, k_2) \tag{3.47}$$

where $\mathcal{I}(k1, k2)$ is first order in the slow-roll parameters. Thus the level of non-Gaussianity generated during inflation is typically $f_{NL} \sim 10^{-1} - 10^{-2}$ [55]. Notice that an f_{NL} value of order 100 corresponds to a 0.1% correction to $\mathcal{R}^{(1)}(k) \sim 10^{-5}$. For slow-roll dynamics to occur, the inflaton has to be very weakly self-interacting (the potential is very flat) and the non-Gaussianity is necessarily small. The latest constraint on f_{NL} from Planck experiment [56] is consistent with zero. This result is compatible with zero spatial curvature and a small value of f_{NL}, as predicted in the simplest slow-roll inflationary models.

Adiabaticity.

In single-field inflation, the fluctuations of the inflaton field on large scales (where spatial gradients can be neglected) can be identified with a local shift backwards

or forwards along the trajectory of the homogeneous background field. These shifts along the inflaton trajectory affect the total density in different parts of the universe after inflation, but cannot give rise to variations in the relative density between different components. Hence, single-field inflation produces purely adiabatic primordial density perturbations characterized by an overall curvature perturbations, $\mathcal{R}$. This means that all perturbations of the cosmological fluid (photons, neutrinos, baryons and cold dark matter (CDM) particles) are originated from the same $\mathcal{R}$ and satisfy the adiabaticity property, $\delta(n_m/n_r) = 0$, or

$$\frac{\delta\rho_m}{\rho_m} = \frac{3}{4}\frac{\delta\rho_r}{\rho_r} \tag{3.48}$$

where the index m collectively stands for non-relativistic species (baryons or CDM) and r for relativistic species (photons or neutrinos).
If isocurvature modes are present, the most plausible mechanism for exciting them involves inflation with a multicomponent inflaton field. To have an observable effect at the large scales probed by the CMB, isocurvature modes require long-range correlations. Inflation with a multi-component inflaton provides a well motivated scenario for establishing such correlations. In models of inflation with light (compared to the Hubble expansion rate) transverse directions, the scalar field along these transverse directions becomes disordered in a way described by an approximately scale-invariant spectrum. If the inflaton has M light components, there are $(M-1)$ potential isocurvature modes during inflation. Whether or not the fluctuations along these transverse directions are subsequently transformed into the late-time isocurvature modes depends on the details of what happens after inflation.
The latest data shows no violation of the condition Eq.(3.48). The oscillatory pattern in the Planck temperature spectrum is compatible with purely adiabatic perturbations, and therefore constrains any isocurvature contribution to be small. However, multi-field inflationary scenarios can produce the mixture of curvature and isocurvature fluctuations to provide a good fit to the Planck data. We wait for the Planck high frequency polarization likelihood to make a better analysis and to be able to say something more.

Chapter 4

Constraints on inflationary and neutrino parameters from CMB observation

In the previous chapter we have introduced the theory of cosmological inflation as an initial condition to explain the evolution of the primordial perturbations in the standard model context. We have seen the formulation of the theory, its parameters and its predictions.

Now we will see how the current observational data constrain the cosmological parameters and the difficulty of relating the theory to the observations. Starting from a simple reference scale-invariant model, we complicate the set of parameters considering both inflationary parameters, such as the spectral index and its running, and parameters related to neutrino physics, as the sum of the neutrino masses m_ν and the effective number of relativistic degree of freedom N_{eff} [57]. Both extended models are extremely interesting and are well constrained by observations of the CMB. The high precision measurements of CMB anisotropies made by Planck satellite have provided, indeed, not only a wonderful confirmation of the standard model of cosmological structure formation but also relevant information on key parameters in particle physics. The first release of Planck [58] presented a bound on the total neutrino mass (combining CMB data with BAO data) of $\sum m_\nu < 0.23$ eV, while constrain N_{eff} at 3.3 ± 0.27. The results for N_{eff} are in excellent agreement with big bang nucleosynthesis and the standard value of $N_{eff} = 3.046$, due to non instantaneous decoupling corrections. The bound on neutrino mass is much better than the current laboratory experimental upper limit inferred from a combination of beta-decay experiments and neutrino oscillation data [59].

In inflationary context, this is particularly interesting because a change in neutrino physics can have important implications for interpretation of inflationary parameters from CMB anisotropies [60, 61, 62]. For example, varying N_{eff} can have an impact on determination of n_s and its running, since it changes both the position of the CMB peaks in the angular spectrum and the structure of the "damping tail" at very large multipoles [63]. In general, a higher N_{eff} can put higher values of

n_s in better agreement with the data, *i*.e., there is a positive correlation between the two parameters. Masses for neutrinos also have important implications for interpretation of inflationary parameters from CMB anisotropies. Massive neutrinos damp the dark-matter fluctuations on scales below the horizon when they become non-relativistic [64]. Neutrinos with masses $m_\nu < 0.3$ eV are relativistic at recombination and affect the CMB anisotropy mainly through gravitational lensing, while neutrinos with larger masses slightly increase the CMB small-scale anisotropy by damping the gravitational potential at recombination. The final result is a small anti-correlation with n_s, *i*.e., larger neutrino masses shift the constraints on n_s to smaller values.

In this chapter we so investigate whether there are indications for new physics using both a power spectrum with the addition of parameters motivated by inflationary cosmology and a nonstandard effective neutrino number and/or nonzero neutrino mass. Moreover, we will use the models analysed in order to explain the method of the inflationary potential reconstruction. We therefore realize as the cosmological model studied constrain the shape of the primordial potential.

4.1 Data sets.

Let us start with a brief introduction of the the selection of cosmological data used. We note that the results we refer have been derived prior to Planck 2013 data release, and use the most recent data available at the time.

First, the Wilkinson Microwave Anisotropy Probe (WMAP) experiment data, that we consider in our analysis as the base CMB data set, to be integrated with other data as indicated. WMAP is a NASA mission (launched in 2001) that mapped the pattern of tiny fluctuations in the CMB radiation and produced the first fine-resolution (0.2 degree) full-sky map of the microwave sky. In 2012 were released the nine-year WMAP data and related images [52], covering the range of multipoles of $2 < \ell < 1200$.

Another data set is from the Atacama Cosmology Telescope (ACT) experiment, that is one of the highest permanent, ground-based telescopes in the world. Build in 2007, in 2010 it released results, measuring the statistical properties of the temperature of the CMB down to arcminute scales [65][66].

We also considered the South Pole Telescope (SPT) experiment, that is a 10 meter diameter telescope located at the Amundsen-Scott South Pole Station. It saw first light on 2007, and with the SPTpol camera on 2012 it has measured the B-mode component due to lensing of the polarized CMB [67][68].

The ACT and SPT experiments allow to extend the dynamic range of CMB observations to larger multipoles with respect to WMAP, thus measuring the damping tail of the CMB angular power spectrum. While SPT probes the small scales in the range of multipoles $650 < \ell < 3000$, the ACT telescope spans a range of multipoles that goes up to $\ell = 10000$, although the signal at $\ell > 3000$ is dominated by the power coming from extragalactic point sources. For this reason, for ACT we only consider the less contaminated 148 GHz spectrum up to $\ell_{max} = 3300$ to perform cosmological parameters extraction. We also consider the measurements of Hubble Space Telescope

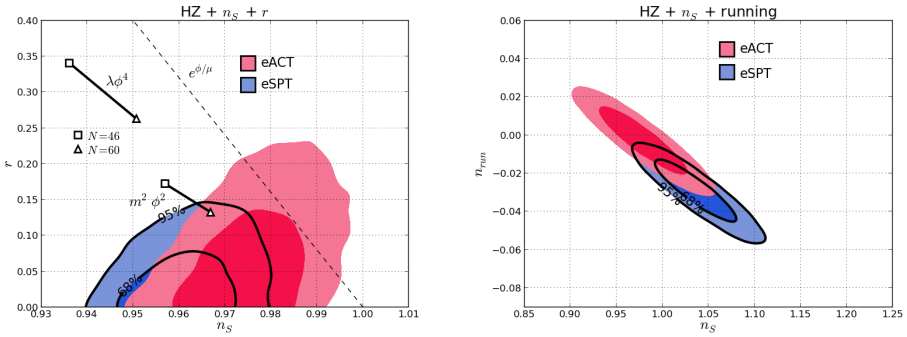

Figure 4.1. Two-dimensional probability in the n_s vs. r plane for the HZ $+n_s + r$ model in the left panel, and the HZ $+n_s + n_{\rm run}$ model in the right panel. Credit: Benetti [57].

[69] using Gaussian prior on the Hubble constant $H_0 = 73.8 \pm 2.4\,{\rm km\,s^{-1}\,Mpc^{-1}}$, and include information from measurements of baryonic acoustic oscillations (BAO) from galaxy surveys [70] [71] [72].

In what follows we will consider two combinations of data sets. We refer to an analysis using the WMAP+ ACT + HST + BAO data sets as the "extended ACT" (eACT) data set and to an analysis with the WMAP+ SPT + HST + BAO data sets as the "extended SPT" (eSPT) data set. Because of the tension between the data shown in Ref. [73], we do not use the combination of ACT + SPT. We will also see that these tensions are evident in our analysis.

4.2 Constraints on inflationary perturbations.

We choose as reference the Harrison-Zel'dovich (HZ) model, which has spectral index $n_s = 1$ and, therefore, a scale-invariant spectrum. We start considering a model in which we only vary the five cosmological parameters: the physical baryon Ω_b, the cold dark matter densities Ω_c, the ratio between the sound horizon and the angular diameter distance at decoupling θ, the optical depth to reionization τ, and the amplitude of the primordial power spectrum A_s. The other parameters are initially fixed as $n_s = 1$, $r = 0$, $n_{\rm run} = 0$, $m_\nu = 0$, $N_{eff} = 3.046$. Then, we will leave these free to vary in different combinations with the cosmological parameters. We therefore constructed, starting from the model HZ, four extended models and constrained them with the two chosen sets of data (eSPT and eACT). The results of our analysis is reported in Tab.(4.1).

For convenience, we report in the Appendix A the explanation of the statistical analysis and the definition of concepts such as posterior, likelihood, best fit, χ^2 and mock analysis. For the comparison, we use the minimum χ^2 values estimated by computing the likelihood ratio between models. As a rule of thumb, given two models $\mathcal{M}_1$ and $\mathcal{M}_2$, where the latter reduces to the former for a particular choice of parameter values (in which case the two models are said to be "nested"), we say that the data show preference for $\mathcal{M}_2$ over $\mathcal{M}_1$ when the absolute value of $\Delta\chi^2 \equiv \chi^2_{\rm min}(\mathcal{M}_2) - \chi^2_{\rm min}(\mathcal{M}_1)$ is larger than the number of additional parameters in the extended model. A more accurate assessment of the relative probability of the

Table 4.1. Augmenting the minimal Harrison-Zel'dovich cosmological model through inflationary parameters. Listed are posterior means for the cosmological parameters from the indicated data sets (errors refer to 68% confidence intervals, unless otherwise stated).

Data	Parameter	Reference Model	Inflation-Motivated Extensions			
		HZ	HZ $+n_s$	HZ $+n_s + r$	HZ $+n_s + n_{\rm run}$	HZ $+n_s + r + n_{\rm run}$
eSPT	$100\,\Omega_b h^2$	2.331 ± 0.025	2.225 ± 0.032	2.228 ± 0.032	2.236 ± 0.031	2.272 ± 0.036
	$\Omega_c h^2$	0.1148 ± 0.0017	0.1167 ± 0.0018	0.1166 ± 0.0018	0.1180 ± 0.0019	0.1178 ± 0.0018
	$100\,\theta$	1.0430 ± 0.0009	1.0419 ± 0.0009	1.0419 ± 0.0010	1.0422 ± 0.0009	1.0424 ± 0.0009
	$\log[10^{10} A_S]$	3.12 ± 0.03	3.21 ± 0.03	3.20 ± 0.03	3.14 ± 0.04	3.04 ± 0.07
	τ	0.096 ± 0.013	0.078 ± 0.012	0.077 ± 0.012	0.090 ± 0.014	0.095 ± 0.015
	n_s	$\equiv 1$	0.959 ± 0.008	0.962 ± 0.008	1.037 ± 0.029	1.107 ± 0.045
	r	$\equiv 0$	$\equiv 0$	< 0.12 [d]	$\equiv 0$	0.28 ± 0.16
	$n_{\rm run}$	$\equiv 0$	$\equiv 0$	$\equiv 0$	-0.029 ± 0.011	-0.051 ± 0.015
	H_0 [a]	71.33 ± 0.65	69.33 ± 0.74	69.42 ± 0.76	69.08 ± 0.76	69.51 ± 0.78
	$-2\log\mathcal{L}$ [b]	7653.4	7624.7	7625.6	7616.8	7615.9
	$\Delta\chi^2$ [c]	$\equiv 0$	-28.7	-27.8	-36.6	-37.5
eACT	$100\,\Omega_b h^2$	2.356 ± 0.027	2.282 ± 0.035	2.290 ± 0.037	2.283 ± 0.035	2.302 ± 0.038
	$\Omega_c h^2$	0.1163 ± 0.0021	0.1165 ± 0.0021	0.1162 ± 0.0021	0.1166 ± 0.0021	0.1167 ± 0.0022
	$100\,\theta$	1.0416 ± 0.0016	1.0399 ± 0.0018	1.0399 ± 0.0017	1.0400 ± 0.0017	1.0403 ± 0.0018
	$\log[10^{10} A_S]$	3.14 ± 0.03	3.19 ± 0.03	3.18 ± 0.03	3.19 ± 0.04	3.13 ± 0.05
	τ	0.102 ± 0.014	0.090 ± 0.014	0.089 ± 0.013	0.092 ± 0.015	0.094 ± 0.015
	n_s	$\equiv 1$	0.971 ± 0.009	0.976 ± 0.009	0.978 ± 0.031	1.016 ± 0.042
	r	$\equiv 0$	$\equiv 0$	< 0.18 [d]	$\equiv 0$	< 0.34 [d]
	$n_{\rm run}$	$\equiv 0$	$\equiv 0$	$\equiv 0$	-0.003 ± 0.011	-0.014 ± 0.014
	H_0 [a]	70.50 ± 0.71	69.24 ± 0.83	69.43 ± 0.83	69.24 ± 0.81	69.47 ± 0.83
	$-2\log\mathcal{L}$ [b]	7617.9	7608.2	7608.4	7608.3	7608.7
	$\Delta\chi^2$ [c]	$\equiv 0$	-9.7	-9.5	-9.6	-9.2

[a] km s^{-1} Mpc^{-1}

[b] When comparing to the χ^2 values reported e.g. in the WMAP9-year paper [74], it should be taken into account that we use a pixel based likelihood at low-ℓs instead than the Gibbs-based likelihood.

[c] $\Delta\chi^2 \equiv (-2\log\mathcal{L}) - (-2\log\mathcal{L}_{HZ})$

[d] 95% c.l.

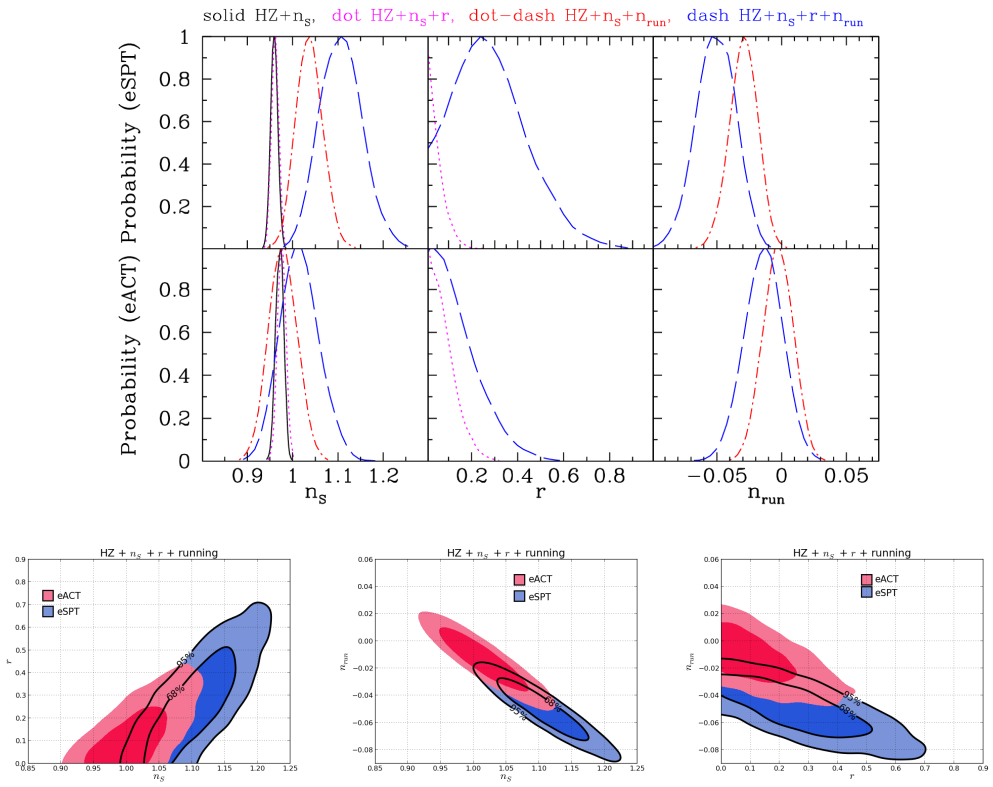

Figure 4.2. One- and two-dimensional posterior probabilities for n_s, r, and n_{run}. Upper panel: One-dimensional parameter posteriors for the models considered in the text, using the eSPT (top row) and eACT (bottom row) datasest. Lower panel: Two-dimensional posteriors for the HZ+n_s+r+running case. Dark- and light-shaded regions correspond to 68 and 95% credible intervals, respectively. Credit: Benetti [57].

two models would require the calculation of the Bayesian evidence; see e.g. Refs. [75] and [76] for an application to inflationary models.
As we can see from the table, both for the eACT and eSPT data sets, models with $n_s \neq 1$ are highly favored over the HZ reference model. For the eSPT data set, allowing one additional parameter, n_s, to vary results in change in χ^2 of

$$\Delta\chi^2 \equiv (-2\log\mathcal{L}) - (-2\log\mathcal{L}_{HZ}) = -28.7. \tag{4.1}$$

For the eACT data set, allowing one additional parameter, n_s, to vary results in

$$\Delta\chi^2 \equiv (-2\log\mathcal{L}) - (-2\log\mathcal{L}_{HZ}) = -9.7. \tag{4.2}$$

If we allow other parameters describing the perturbation spectra to vary, such as $n_{\rm run}$ and r, there are different indications from the different data sets.
Let us first consider the eSPT data set. The natural parameter space for constraining simple slow-roll inflation models is to include the tensor/scalar ratio r in addition to spectral tilt n_s. Two-dimensional contours for n_s vs. r are shown in Fig.(4.1), along with the predictions of three simple slow-roll models. This extended model results

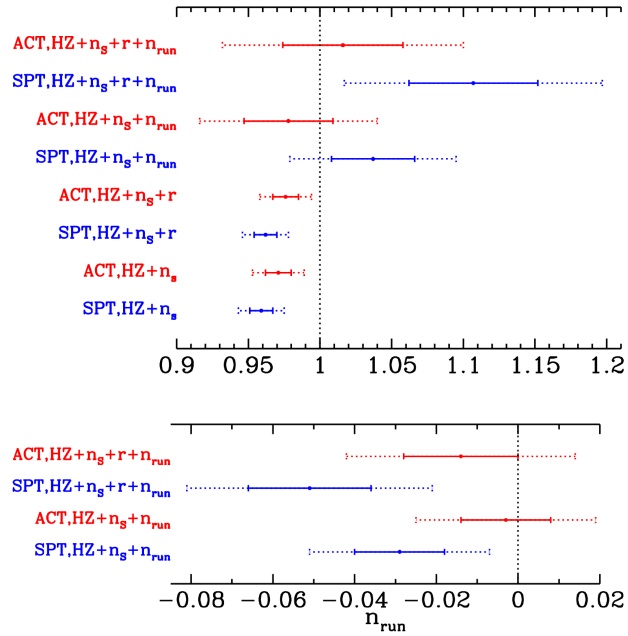

Figure 4.3. Comparing the constraints on n_s (top panel) and $n_{\rm run}$ (bottom panel) for different model/data sets combinations. The solid and dashed bars denote 1- and 2-σ constraints, respectively [57].

in a very marginal decrease in χ^2 of -0.9 compared to a model just allowing n_s to vary. Hence, the data do not seem to call for the additional variable r. However, the situation is quite different if we allow a running of the scalar spectral index, $n_{\rm run} \neq 0$, either keeping $r = 0$ or allowing r to vary.
Adding one additional parameter, $n_{\rm run}$, results in $\Delta\chi^2 = -36.6$ compared to the reference HZ model, which corresponds to a change in χ^2 of -7.9 compared to the HZ $+n_s$ model. If we allow both r and $n_{\rm run}$ to vary (in addition to allowing n_s to vary) there is a gain of $\Delta\chi^2 = -37.5$ compared to the reference HZ model, or a change in χ^2 of -8.8 compared to the HZ $+n_s$ model.

Our conclusion is that the eSPT data strongly prefers a running of the scalar spectral index. The one-dimensional probability distributions for n_s, r and $n_{\rm run}$ with the eSPT data set are shown in Fig.(4.2) in the upper panel. Two-dimensional contours of r vs. n_s, $n_{\rm run}$ vs. n_s and $n_{\rm run}$ vs. r are also shown in Fig.(4.2), lower panel.

The eACT data set also prefers a scalar spectral index different from unity. Recall that adding one additional parameter n_s results in a decrease in χ^2 compared to the reference HZ model of $\Delta\chi^2 = -9.7$. If we then allow one additional parameter, either r or $n_{\rm run}$, there is only a very marginal change in χ^2 beyond the HZ + n_s model. Even allowing both additional parameters $n_{\rm run}$ and r again results in a very marginal decrease in χ^2 at the expense of two additional parameters. The one-dimensional probability distributions for n_s, r and $n_{\rm run}$ with the eACT data set are also shown in Fig.(4.2), and the two-dimensional contours of r vs. n_s, $n_{\rm run}$ vs.

n_s and $n_{\rm run}$ vs. r are also shown in Fig.(4.2).

We summarize our findings with respect to n_s and $n_{\rm run}$ in Fig.(4.3), where we compare the constraints on these parameters for the different model/data set combinations considered here. It is clear from this figure that the tension between the two data sets increases when the model complexity is also increased. Moreover, we also notice that the results of parameter estimation from eACT are more stable, with respect to eSPT, to the increase of the complexity of the model.

Our conclusion is that the eSPT and eACT datasets are not consistent, as long as inflation-motivated extensions to the minimal model are concerned.
While both call for a scalar spectral index different than unity, the eSPT dataset seems to be better described by a more complicated perturbation spectrum than just a scalar spectrum of constant spectral index. On the other hand, the eACT dataset seems to be well described by a constant scalar spectral index (slightly less than unity), and does not seem to require additional complexity.

The extended-ACT data set is perfectly consistent with negligible running of the spectral index, as predicted by simple slow-roll inflation models. The eACT data are consistent at the 95% confidence level with simple chaotic inflation $V(\phi) = m^2\phi^2$, and with power-law inflation, $V(\phi) \propto \exp(\phi/\mu)$, as well as "small-field" models predicting negligible tensors and $n_s < 1$.

The extended-SPT data set, instead, prefers a non-power-law scalar spectral index with a very large variation with scale of the spectral index. The eSPT data, however, are inconsistent with a purely power-law power spectrum, favoring negative running of the spectral index $n_{run} = -0.029 \pm 0.011$ in the case with a prior of $r = 0$, and $n_{run} = -0.051 \pm 0.015$ in the case where $r \neq 0$ is allowed. While the eSPT data are not in disagreement with the most general possible single-field inflation models, they are in significant conflict with slow-roll models predicting $n_{run} \ll n_s$ (the eACT data are consistent with such models).

For the eACT dataset, just adding a tilt to the scalar spectrum seems to be all that is demanded of the data. This would tell us something about inflation, but there are a large number of inflation models that can give a slightly red spectrum.

For the eSPT dataset however, the data seems to demand more than simply a tilt to the scalar spectrum. A much improved fit can be obtained by allowing the possibility of a large running of the scalar spectrum. The running could be so large as to have a large impact in inflation model building and call in doubt the simple slow-roll approximation.

Alternatively, to a non-power-law scalar spectral index with a very large variation of the spectral index, one might invoke models where the flattening of the inflaton potential is obtained through the inclusion of large quantum corrections in the mass parameter which result in large variation of the spectral index with the scale. Or another class of models which allow for a large negative running are models in which inflation occurs near an inflection point of the potential, where the third derivative V''' of the potential is substantial, and the higher-order slow roll parameter ξ is comparable to the lower-order parameters ϵ and η. Inflection point inflation models have

been argued, *e.g.* in Ref. [77], to be characteristic of inflation on the string landscape.

In conclusion, it is very important to assess the data set to use, since the analysis results may depend a lot (as seen) from the chosen data. We note indeed that considering the ACT and SPT data separately results in qualitatively different conclusions about extensions to a standard scale-invariant Λ+Cold Dark Matter concordance cosmology, a the tension from ACT and SPT is not evident when considering combined constraints from ACT and SPT.

4.3 Extensions of the neutrino sector.

In what follows we examine the possibility of new neutrino physics as an alternative to extending the complexity of primordial perturbations.

One direction for new neutrino physics is a change in the effective number of relativistic degrees of freedom, N_{eff}, that defines the physical energy density in relativistic particles $\rho_{\rm rad}$, defined by

$$\rho_{\rm rad} = \left[1 + \frac{7}{8}\left(\frac{4}{11}\right)^{4/3} N_{\rm eff}\right]\rho_\gamma \ , \tag{4.3}$$

where ρ_γ is the energy density of the CMB photons and N_{eff} is the effective number of light neutrino species. In the standard scenario, assuming three active massless neutrino species with standard electroweak interactions and the present CMB temperature of $T_\gamma = 2.726$ K [78], the expected value is $N_{eff} = 3.046$. This is slightly larger than 3 because of non-instantaneous neutrino decoupling [79]. As mentioned previously, any new species that is relativistic around recombination will contribute to N_{eff}, whether it is a neutrino species or not. The exact contribution of a new relativistic species will depend on the number of spin degrees of freedom, whether the new species is a boson or fermion, and the temperature of decoupling of the new species. We also consider the possibility of a mass for one or more of the three known active neutrino species. The present contribution to the overall energy density is given by

$$\Omega_\nu h^2 = \Sigma \frac{m_i}{92.5 \text{ eV}}, \tag{4.4}$$

where m_i are the masses of the three neutrino mass eigenstates.

The constraints from the eSPT and eACT data set are in Tab.(4.2). We see that allowing N_{eff} improves the fits of both eSPT and eACT by about as much as allowing the spectral index to vary from unity. However, allowing the neutrino mass to vary, we again obtain different indications from the two data sets. For the SPT data set, adding a neutrino mass improves the χ^2 by -8.1 if N_{eff} is kept fixed and by -8.8 if it is allowed to vary. For the ACT data set, on the contrary, the goodness of fit improves only marginally (at the price of one additional parameter) by allowing a non-zero neutrino mass, independently of whether N_{eff} is fixed or not.
In Fig.(4.4) we compare the constraints on N_{eff} and $\sum m_\nu$ for the different model/data set combinations considered. Again we see the same trend observed in the case of the spectrum parameters, namely that the values estimated from the two data sets

Table 4.2. Augmenting the minimal Harrison-Zel'dovich cosmological model through new neutrino physics. Listed are posterior means for the cosmological parameters from the indicated data sets (errors refer to 68% credible intervals, unless otherwise stated).

Data	Parameter	Reference Model	Neutrino-Motivated Extensions		
		HZ	HZ $+N_{eff}$	HZ $+m_\nu$	HZ $+N_{eff}+m_\nu$
eSPT	$100\,\Omega_b h^2$	2.331 ± 0.025	2.311 ± 0.024	2.330 ± 0.024	2.332 ± 0.037
	$\Omega_c h^2$	0.1148 ± 0.0017	0.1394 ± 0.0057	0.1100 ± 0.0023	0.1315 ± 0.0057
	$100\,\theta$	1.0430 ± 0.0009	1.0404 ± 0.0010	1.0434 ± 0.0009	1.0412 ± 0.0011
	$\log[10^{10} A_S]$	3.12 ± 0.03	3.15 ± 0.03	3.12 ± 0.03	3.14 ± 0.03
	τ	0.096 ± 0.013	0.085 ± 0.012	0.103 ± 0.014	0.095 ± 0.014
	N_{eff}	$\equiv 3.046$	4.26 ± 0.26	$\equiv 3.046$	4.45 ± 0.32
	$\sum m_\nu$ [a]	$\equiv 0$	$\equiv 0$	0.39 ± 0.14	0.96 ± 0.53
	H_0 [b]	71.33 ± 0.65	75.5 ± 1.1	69.82 ± 0.76	74.0 ± 1.2
	$-2\log\mathcal{L}$ [c]	7653.4	7625.9	7645.3	7617.1
	$\Delta\chi^2$ [d]	$\equiv 0$	-27.5	-8.1	-36.3
eACT	$100\,\Omega_b h^2$	2.356 ± 0.027	2.332 ± 0.029	2.358 ± 0.029	2.337 ± 0.029
	$\Omega_c h^2$	0.1163 ± 0.0021	0.1318 ± 0.0057	0.1156 ± 0.0021	0.1296 ± 0.0057
	$100\,\theta$	1.0416 ± 0.0016	1.0382 ± 0.0020	1.0421 ± 0.0016	1.0387 ± 0.0020
	$\log[10^{10} A_S]$	3.14 ± 0.03	3.16 ± 0.03	3.13 ± 0.03	3.15 ± 0.03
	τ	0.102 ± 0.014	0.097 ± 0.014	0.105 ± 0.015	0.099 ± 0.014
	N_{eff}	$\equiv 3.046$	3.88 ± 0.28	$\equiv 3.046$	3.80 ± 0.28
	$\sum m_\nu$ [a]	$\equiv 0$	$\equiv 0$	0.24 ± 0.15	< 0.46 [e]
	H_0 [b]	70.50 ± 0.71	73.2 ± 1.1	69.82 ± 0.79	72.4 ± 1.2
	$-2\log\mathcal{L}$ [c]	7617.9	7609.7	7616.7	7609.2
	$\Delta\chi^2$ [d]	$\equiv 0$	-8.2	-1.2	-8.7

[a] eV

[b] km s^{-1} Mpc^{-1}

[c] When comparing to the χ^2 values reported e.g. in the WMAP9-year paper [74], it should be taken into account that we use a pixel based likelihood at low-ℓ instead than the gibbs-based likelihood.

[d] $\Delta\chi^2 \equiv (-2\log\mathcal{L}) - (-2\log\mathcal{L}_{HZ})$

[e] 95% c.l.

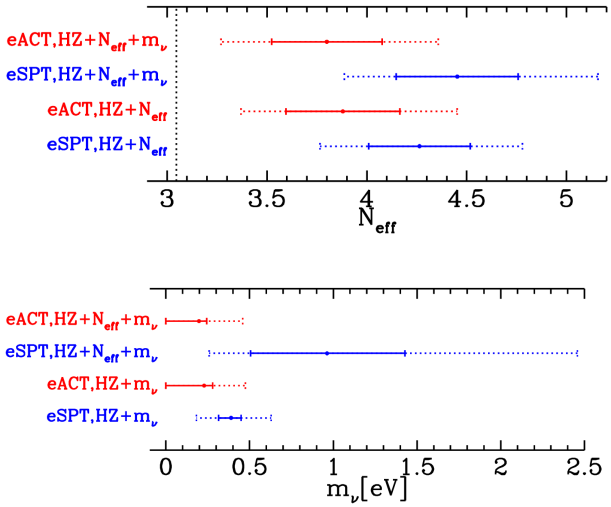

Figure 4.4. Comparing the constraints on N_{eff} (top panel) and $\sum m_\nu$ (bottom panel) for different model/data sets combinations. The solid and dashed bars denote 1- and 2-σ constraints, respectively [57].

tend to diverge as new parameters are added, and that the values estimated from eACT are more stable than those estimated from eSPT when the complexity of the model is increased.

In Fig.(4.5), we report the one- and two-dimensional posterior probabilities and we can see that the eACT data are consistent at 95% with zero neutrino mass, with $\sum m_\nu = 0.24 \pm 0.15$ eV (with $N_{eff} \equiv 3.04$), and $\sum m_\nu < 0.46$ eV (with $N_{eff} \neq 3.04$). Instead, the eSPT data favor nonzero neutrino mass, with $\sum m_\nu = 0.39 \pm 0.14$ eV (with $N_{eff} \equiv 3.04$), and $\sum m_\nu = 0.96 \pm 0.53$ eV (with $N_{eff} \neq 3.04$).

We can conclude that, as in previous scenario of HZ + inflation, the HZ + neutrinos models considering the ACT and SPT data separately results in qualitatively different conclusions about extensions to a standard scale-invariant Λ+Cold Dark Matter concordance cosmology, a tension which is not evident when considering combined constraints from ACT and SPT.

4.4 Monte Carlo Reconstruction of the inflationary potential.

We now show the impact of the different extended models of previous sections on the reconstruction of the inflaton potentials shape by means of a technique known as *Monte Carlo reconstruction* of the inflationary potentials. It is a stochastic method for inverting observational constraints to obtain an ensemble of inflationary potentials compatible with observations. The method basically relies on solving the inflationary flow Eqs.(3.25) for randomly chosen initial values of the inflationary parameters, and is described in Refs. [45, 80, 81], to which we refer the reader for further details. Here we choose to use the parameter $\sigma = 2\eta - 4\epsilon$ in place of η with the advantage that to first order in slow roll, $\sigma = n_s - 1$. So, we recall the main

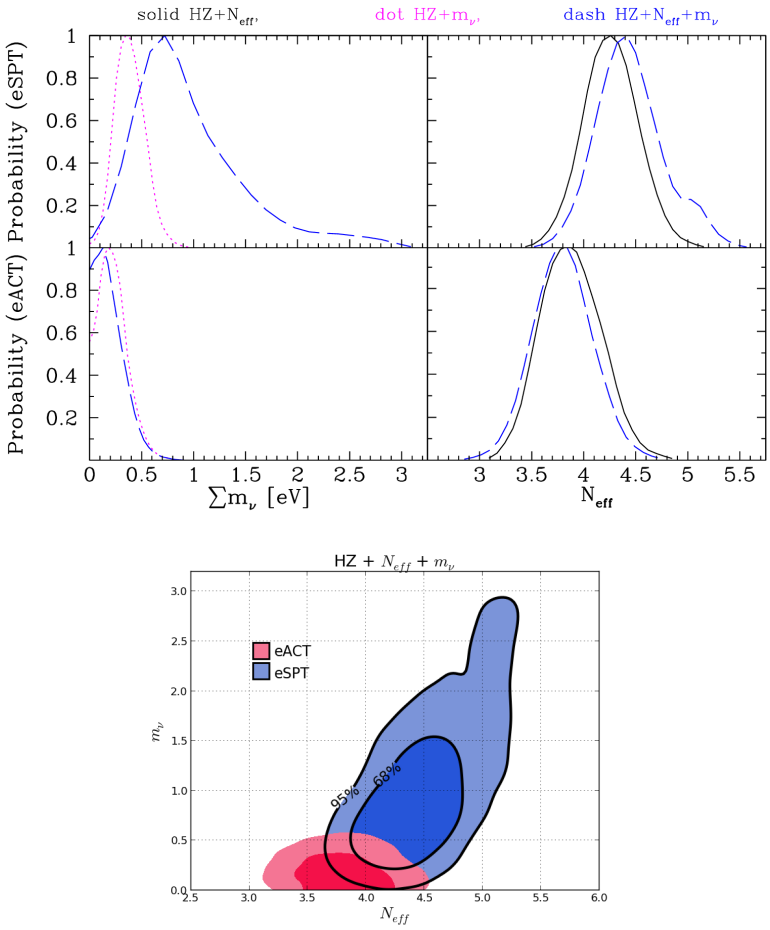

Figure 4.5. One- and two-dimensional posterior probabilities for the eACT and eSPT data for the parameters N_{eff} and $\sum m_\nu$ [57].

steps of the analysis:

1. Choose random initial values for the inflationary parameters in the following ranges:

$$\begin{aligned} N &= [40,\, 70] \\ \epsilon &= [0,\, 0.8] \\ \sigma &= [-0.5,\, 0.5] \\ \xi &= [-0.05,\, 0.05] \\ {}^{3}\lambda &= [-0.005,\, 0.005] \\ &\vdots \\ {}^{6}\lambda &= 0. \end{aligned}$$

   truncated at $M = 6$.

2. Evolve forward in time until either (a) inflation ends ($\epsilon > 1$), or (b) the evolution reaches a late-time fixed point ($\epsilon = {}^{\ell}\lambda = 0$, $\sigma = \text{const}$).

3. In case (a), evolve N e-folds backwards in time from the end of inflation and calculate the observables $n_s - 1$, r, and the running n_{run} at that time; in case (b), calculate the observables at the time the evolution reaches the fixed point.

4. Repeat the above procedure N_{MC} times.

5. Choose a window of acceptable values for the observables $n_s - 1$, r, and the running n_{run}, and then extract from the N_{MC} models those that satisfy the observational constraints.

6. Reconstruct the potential for these models from Eq.(3.13).

We have performed this procedure with $N_{MC} = 5 \times 10^5$. We consider four sets of observational constraints, namely those for the ΛCDM+r+$n_{\rm run}$ and for the ΛCDM+r+n_{run}+ν models, obtained for the eACT and eSPT data sets. In Fig.(4.6), we show a scatter plot of the (n, n_{run}) values corresponding to our ensemble of reconstructed potentials, coloured according to the value of r, together with boxes (ellipses) showing the relevant observational constraints. It is already clear from this plot that, for the case of the ΛCDM+r+n_{run}, it is very difficult to find values of the inflationary parameters satisfying the constraints coming from the eSPT data set. Models with negative running either have a red spectrum and large tensor-to scalar-ratio, or a blue spectrum and a small tensor-to-scalar ratio, while the eSPT data prefer a scalar blue spectrum with negative running and a large value of r. Indeed, out of 500,000 models, we could find only one potential satisfying these constraints at the 1σ level (16 at 2σ).

In Fig.(4.7), we show samples of the reconstructed potentials for the four model-data set combinations under consideration. We indicate the constraints on the inflationary parameters at 68% c.l with the black thick line and 95% c.l. with the blue thin line. We show 50 potentials in each case, with the exception of the ΛCDM+r+n_{run} model with the eSPT data set, for which we have only found 16

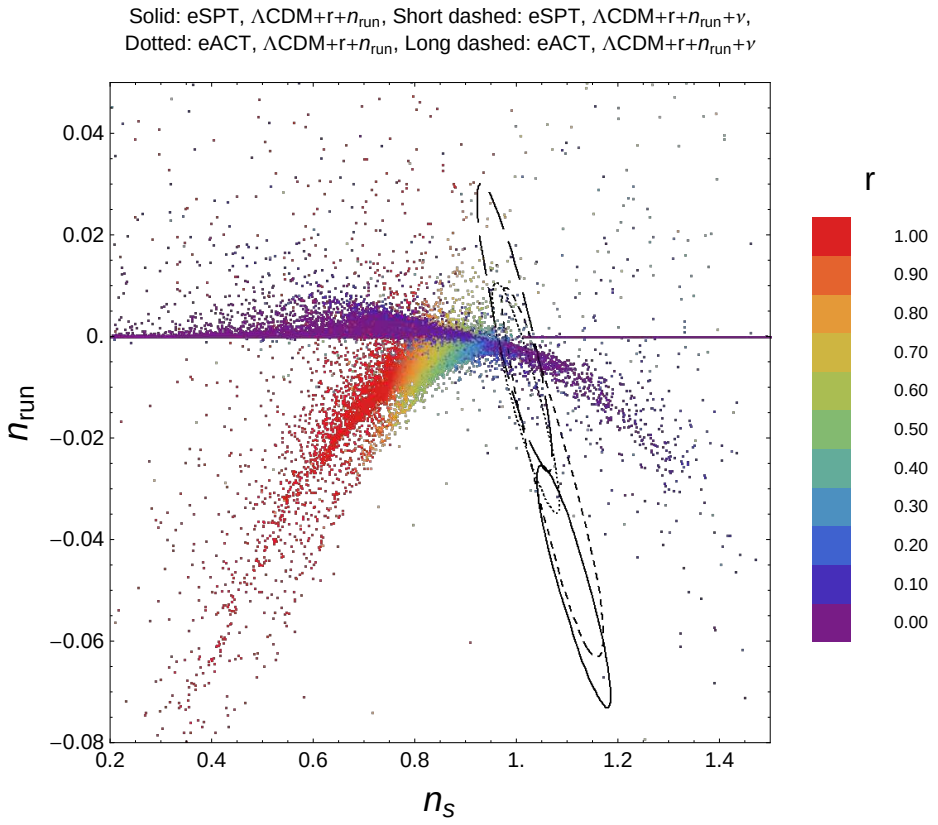

Figure 4.6. Models generated by the Monte Carlo plotted in the (n_s, n_{run}) plane. The points are colored according the value of the tensor-to-scalar ratio of the corresponding model, going from blue $(r = 0)$ to red $(r = 1)$. The boxes show the experimental 1σ constraints corresponding to the four cases described in the text and stated above the graph.

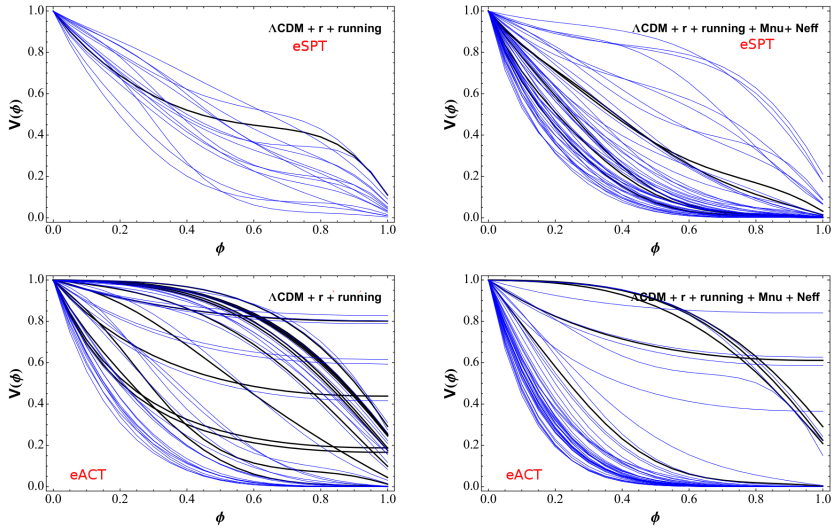

Figure 4.7. Reconstructed potentials satisfying the 68% (black thick) and 95% (blue thin) c.l. constraints on the inflationary parameters. The potential and field values have been renormalized so that $0 \leq V(\phi) \leq 1$ and $0 \leq \phi \leq 1$. We use the eSPT and eACT data set.

acceptable potentials. The main difference between the two data sets is the fact that the very flat potentials typical of the models where the inflationary flow reaches a late time attractor are allowed by the eACT data set but excluded by the eSPT data set. The reason is that the late-time attractor of the "fixed point" models is $\epsilon = 0$ (so that the corresponding potentials end up being very flat), ${}^{\ell}\lambda = 0$ and $\sigma = \text{const}$. This implies, using Eq.(3.27), that in general these models predict $n_{run} \simeq 0$.

Chapter 5

Constraints on interrupted slow roll

In chapter 3 and 4 we have introduced the inflationary cosmology and discussed the observational predictions. In this chapter, we conclude the work of this thesis, going beyond the slow-roll assumptions and looking at models with interrupted slow-roll. In particular, we choose to analyse models with step-like features in the inflationary potential and their signatures on the current observable data.
The idea of introducing features in the inflationary potential has a long history [82]. They came into vogue as a possible explanation for the apparent low multipole glitches at $20 < \ell < 40$ in the angular spectrum of CMB radiation. The common characteristics of models with features are the breaking of the scale-invariance of the power-spectrum and an enhancement of higher-order correlators. The traditional road followed to deal with models with step features is to specify a form for the inflaton potential $V(\phi)$ and then study the background evolution of the field, derive expressions for the modified slow-roll parameters and finally study their effects on the behavior of the correlation functions of curvature perturbations.

So, we begin to generalize the method to spectra corresponding to a whole class of step inflation models with arbitrary (slow-roll) background inflaton potentials. This allows us to derive constraints on parameters characterizing the feature in a more model independent way. Then, we study the observable spectra and the constraints on this kind of models by CMB and matter power spectrum data sets.

5.1 Formalism.

In more general classes of inflationary models, slow roll may be violated for a brief instant [82]. In single-field inflation models, such an effect can be modelled by introducing a feature such as a kink, bump or step [83] to the inflaton potential. A step, in particular, can be regarded as an effective field theory description of a phase transition in more realistic multi-field models [84], which may arise naturally in, e.g., supergravity- [85] or M-theory-inspired inflation models [86]. This interruption of slow-roll will leave possibly detectable traces in the primordial power spectrum. Specifically, wavelengths crossing the horizon during this fast-roll phase will be

affected , leading to a deviation from the usual power-law behaviour at these scales. Such non-standard power spectra have been brought forward to explain the peculiar glitches in the temperature anisotropies as well as the observed low power at the largest scales.

Now, we briefly introduce the exact formalism of calculating the power spectrum from a given inflaton potential and compare it with the slow-roll approximation. In the following, we will set $c = \hbar = 8\pi G = 1$ and use the variable $u = a\delta\phi$, that we can write in terms of the curvature perturbation $\mathcal{R}$:

$$u \equiv -z\mathcal{R} \tag{5.1}$$

where $z \equiv a\dot{\phi}/H$. The Fourier components of u obey to the equation

$$u_k'' + \left(k^2 - \frac{z''}{z}\right) u_k = 0, \tag{5.2}$$

with a prime denoting a derivative with respect to conformal time τ.
In order to find a solution to Eq.(5.2), one needs to know the behaviour of the term z''/z:

$$\frac{z''}{z} = 2a^2H^2\left[1 + \epsilon - \frac{3}{2}\eta + \epsilon^2 - 2\eta\epsilon + \frac{1}{2}\eta^2 + \frac{1}{2}\xi^2\right]. \tag{5.3}$$

Note that these expressions are exact: they do not assume the slow roll parameters to be small. The z''/z evolution is determined by the dynamics of the Hubble parameter and the unperturbed inflaton field, governed by Friedmann equation (Eq.(3.9)) and the Klein-Gordon equation for ϕ (Eq.(3.8)). In terms of N, we can write the system of equations:

$$\begin{aligned} H' &= -\frac{1}{2}H\phi'^2, \\ \phi'' &+ \left(\frac{H'}{H} + 3\right)\phi' + \frac{1}{H^2}\frac{dV}{d\phi} = 0, \\ uk'' &+ \left(\frac{H'}{H} + 1\right)uk' + \left[\frac{k^2}{e^{2(N-N_0)}H^2}\left(2 - 4\frac{H'}{H}\frac{\phi''}{\phi'}\right.\right. \\ &\left.\left. - 2\left(\frac{H'}{H}\right)^2 - 5\frac{H'}{H} - \frac{1}{H^2}\frac{d^2V}{d\phi^2}\right)\right]uk = 0. \end{aligned} \tag{5.4}$$

with N_0 determining the normalization of the scale factor and with a prime denoting the derivative respect to N. This coupled system of differential equations can easily be solved numerically, once a suitable set of initial conditions has been chosen.

Supposing that at a time N_{sr} the system has reached the inflationary attractor solution $\ddot{\phi} \ll 3H\dot{\phi}$, and is rolling slowly, $\dot{\phi}^2 \ll V(\phi)$, the initial condition for ϕ and H will be given by:

$$\begin{aligned} \phi(N_{sr}) &= \phi_{sr}, \\ \phi_{,N}(N_{sr}) &= -\frac{1}{V(\phi_{sr})}\frac{dV}{d\phi}\Big|_{\phi_{sr}}, \\ H(\phi_{sr}) &= \sqrt{\frac{V(\phi_{sr})}{3}}. \end{aligned} \tag{5.5}$$

The initial conditions for u_k can be obtained by requiring the late time solution of Eq.(5.2). The form of the solution depends on the relative sizes of k^2 and z''/z.

In the slow-roll limit $k^2 \gg z''/z$, where $\epsilon,|\eta|,|\xi^2| \ll 1$, with wavelengths much smaller than the horizon, the solution is given by

$$u_k \to \frac{1}{\sqrt{2k}} e^{-ik\tau}, \tag{5.6}$$

where the normalization is determined by the quantum origin of the perturbations [87]. Fixing the irrelevant phase, we obtain the initial conditions for a mode k

$$\begin{aligned} u_k(\tau_0) &= \frac{1}{\sqrt{2k}}, \\ u_k(\tau_0) &= -i\sqrt{\frac{k}{2}}, \end{aligned} \tag{5.7}$$

In the limit $k^2 \ll z''/z$ we have a growing mode solution $u_k \propto z$, which means that the curvature perturbation, $|\mathcal{R}| = |u_k/z|$, remains constant on superhorizon scales, i.e. the perturbations "freeze in".
We can conclude that for a perturbation with $k^2 \sim z''/z$ the spectrum will have its final shape imprinted on horizon exit. It is not until much later, when the modes reenter the horizon during radiation or matter domination, that they will exhibit dynamical behaviour again.

We can also define the primordial power spectrum of curvature perturbations $\mathcal{P}_\mathcal{R}(k)$ via the two-point correlation function of Eq.(3.42). Assuming gaussianity and adiabaticity, this quantity contains all the necessary information for a complete statistical description of the fluctuations. It is related to u_k and z via:

$$\mathcal{P}_\mathcal{R}(k) = \frac{k^3}{2\pi^2} \left|\frac{u_k}{z}\right|^2. \tag{5.8}$$

Tensors perturbations are given by:

$$P_g(k) = \frac{k^3}{2\pi^2} \left|\frac{v_k}{a}\right|^2. \tag{5.9}$$

and the mode equation:

$$v_k'' + \left(k^2 - \frac{a''}{a}\right) v_k = 0. \tag{5.10}$$

This equation is very similar to the scalar one. This similarity can be readily seen if we express the "mass term" a''/a in terms of the slow roll parameters:

$$\begin{aligned} \frac{a''}{a} =& 2a^2H^2\left[1 - \frac{1}{2}\epsilon_H\right] \\ \sim& 2aH^2\left[1 - \frac{1}{2}\epsilon + \frac{2}{3}\epsilon^2 - \frac{1}{3}\epsilon\eta\right], \end{aligned} \tag{5.11}$$

Similarity to the Eq.(3.44), tensor perturbations will also freeze in at horizon exit. In the slow roll case their spectrum is approximately

$$P_g(k) \sim A_{\mathcal{T}}(k_\star) \left(\frac{k}{k_\star}\right)^{n_{\mathcal{T}}} \tag{5.12}$$

with the tensor spectral index $n_{\mathcal{T}} \sim -2\epsilon$ and the normalisation $A_{\mathcal{T}}$:

$$A_{\mathcal{T}} \sim \frac{2}{3\pi^2} V\Big|_{k_\star = aH}. \tag{5.13}$$

5.2 Numerical solution.

Normally, the perturbation spectra of inflationary models driven by a continuously evolving, minimally coupled scalar field can be calculated using the slow roll approximation. However, when the potential has a sharp feature, its derivatives with respect to ϕ and the time derivatives of the field need not be small. Consequently, we evolve the full mode equation numerically, without any approximations other than those already implicit in the use of perturbation theory. In Eq.(5.2), the mode function is expressed in terms of conformal time. The intrinsic time-scale of the dynamics is not constant in conformal time, so we shift the independent variable to $\alpha = \log a$, facilitating the numerical integration. With this replacement, the system of equations we are to solve, with a prime denoting a derivative with respect to α, is:

$$\begin{aligned}
H' =& -4\pi G H \phi'^2, \\
\phi'' &+ \left(\frac{H'}{H} + 3\right)\phi' + \frac{1}{H^2}\frac{dV}{d\phi} = 0, \\
u'' &+ \left(\frac{H'}{H} + 1\right)u' + \\
&\left[\frac{k^2}{e^{2\alpha}H^2}\left(2 - 4\frac{H'}{H}\frac{\phi''}{\phi'} - 2\left(\frac{H'}{H}\right)^2 - 5\frac{H'}{H} - \frac{1}{H^2}\frac{d^2V}{d\phi^2}\right)\right] = 0.
\end{aligned}$$

To compute the spectrum, we repeat the integration for many values of k. In general, u has two distinct solutions since it is a second order linear differential equation, and we must choose the combination which guarantees that the mode equation has the limiting form, Eq.(5.6). We impose the initial conditions when the mode is far inside the horizon assuming that the conformal time τ is zero, which amounts to an irrelevant choice of phase. Consequently,

$$\begin{aligned}
u|_{\tau=0} &= \frac{1}{\sqrt{2k}}, \\
\left.\frac{du}{d\alpha}\right|_{\tau=0} &= -i\sqrt{\frac{k}{2}}\frac{1}{e^{\alpha}H}\Bigg|_{\tau} = 0
\end{aligned} \tag{5.14}$$

Rather than work with complex co-efficents in the numerical code, we define two orthogonal solutions, u_k^1 and u_k^2, such that

$$\begin{aligned} u_k^1\Big|_{\tau=0} &= 1, \\ \frac{du_k^1}{d\alpha}\Big|_{\tau=0} &= 0, \\ u_k^2\Big|_{\tau=0} &= 0, \\ \frac{du_k^2}{d\alpha}\Big|_{\tau=0} &= 1. \end{aligned} \tag{5.15}$$

At any subsequent time u_k is thus

$$u_k = \frac{1}{\sqrt{2k}} u_k^1 - i\sqrt{\frac{k}{2}}\frac{1}{e^{\alpha H}}\Big|_{\tau=0} u_k^2. \tag{5.16}$$

We start the evolution by evolving the two background equations until any initial transient solution has died away but the mode is still well inside the horizon. We then identify the two orthogonal solutions that contribute to u_k and extract the coefficients in Eq.(5.16). This ensures that an initial transient contribution to the background dynamics cannot contaminate the initial values of u and u_α. Finally, to compute the spectrum, we need the asymptotic value of $|u/z|$, and we find this by continuing the integration until the mode is far outside the horizon and this value is effectively constant. The numerical integrations are carried out using the Bulirsch-Stoer algorithm [88], and we check our calculations by ensuring that the results are independent of the distance inside the horizon where we apply the normalization, and the distance beyond the horizon where we evaluate the asymptotic value of $|u/z|$.

5.3 Inflationary potential with step.

The validity of the power-law parameterization of the primordial spectra rests on the assumptions that the slow-roll parameters are small and change slowly with time. Let us relax the latter and allow ϵ and η to change significantly on a timescale $\Delta N \sim 1$. This has the consequence that we can also allow ϵ and/or η to become of order unity momentarily, provided that at a later time, the system returns to the slow roll regime. We also assume here that the system starts in a state where the slow roll conditions are fulfilled, in order to give it enough time to reach the inflationary attractor solution. This effect can be modelled by adding a local feature, such as a step or a bump, to an otherwise flat inflaton potential

The inflationary models with a scale dependent spectrum are often somewhat contrived. However, arguing that using a feature in the inflaton potential to generate a complicated spectrum requires fine tuning assumes that the potential has just one feature, but is otherwise smooth. Adding a large number of features to the potential makes it far more likely that a randomly chosen piece of the perturbation spectrum will exhibit considerable scale dependence. In particular, Adams *et al.* [85] showed

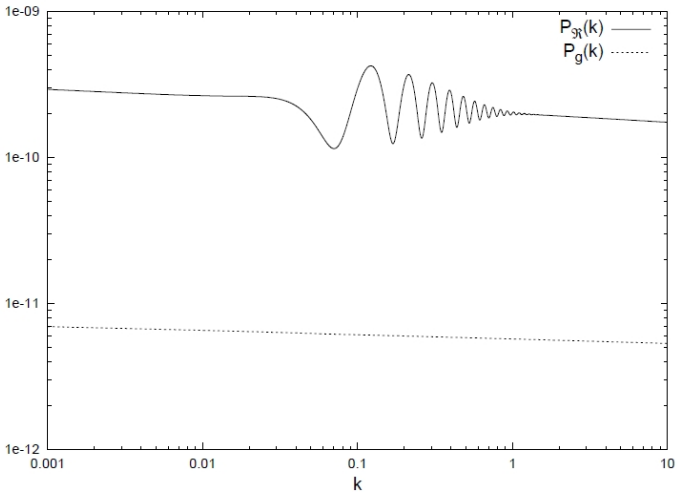

Figure 5.1. The scalar and tensor power spectrum for $c = 0.002$ and $d = 0.01$. The z''/z term for these parameters is shown in Fig.(5.2). Credit: Adams [83]

that a class of models derived from supergravity theories naturally gives rise to inflaton potentials having a large number of sudden steps. Each step corresponds to a symmetry breaking phase transition in a field coupled to the inflaton, since the mass changes suddenly when each transition occurs. In the scenario studied by Adams *et al.*, a spectral feature is expected every $10 - 15$ e-folds, so if this model had driven inflation it is likely that one of these features would be visible in the spectrum extracted from observations of large scale (LS) structure and the CMB.

Motivated by the existence of models which naturally and generically lead to scale dependent spectra, we examine the consequences of introducing a step in the inflaton potential. We focus on spectral features which may be observable in the LS structure or CMB anisotropy, and therefore had their origin around 50 e-folds before the end of inflation.
For physically realistic models, inflation is not interrupted but the effect on the density perturbations is still significant. If inflation is actually interrupted the effect on the perturbation spectrum is severe enough to rule out models where this happens during the interval of inflation corresponding to observable scales.

We can write the potential for the inflaton field in the form:

$$V(\phi) = V_0(\phi)\left[1 + c\tanh\left(\frac{\phi - \phi_{step}}{d}\right)\right], \tag{5.17}$$

This potential describes standard $V_0(\phi) = \frac{1}{2}m^2\phi^2$ chaotic inflation with a step centered around $\phi = \phi_{step}$. The height of the step is determined by c, its gradient by d. We do not want inflation to be interrupted by the step, so we stipulate $|c| \ll 1$ to ensure that the potential energy will always dominate over the kinetic one. We shall work in reduced Planck units, so that all dimensional quantities like m, ϕ_{step} and d should be multiplied by the *reduced Planck mass* $M_p = 2.435 \times 10^{18}$ GeV in order

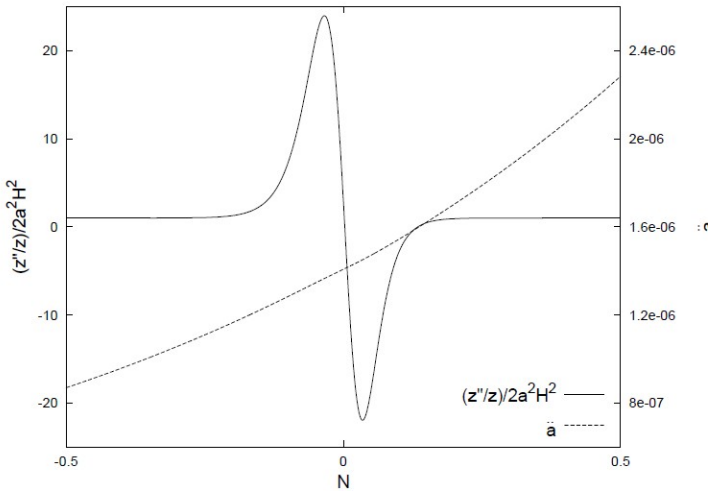

Figure 5.2. Evolution of z''/z and $\ddot{a}$ for $c = 0.02$ and $d = 0.01$ with the number of e-folds of inflation $N = 0$ at the step in the potential. Credit: Adams [83]

to get their values in physical units. In Fig.(5.1) is showed the power spectrum for the potential of Eq.(5.17) with $c = 0.002$, or a 0.4% change in the amplitude of the potential.

As pointed out above, the eventual spectrum crucially depends on the dynamics of z''/z. We can understand the numerical results noting that the energy conservation requires that the change in the inflaton kinetic energy term cannot exceed the change in the potential energy so, if we are originally well inside the vacuum-dominated regime, a small change in the amplitude of the inflaton potential cannot suspend inflation. The evolution of $\ddot{a}$ in Fig.(5.2) clearly shows that the expansion is always accelerating. However the z''/z term of Eq.(5.3), also shown in Fig.(5.2), determines the growth of the scalar perturbations and is very different from $2a^2H^2$. Generically, we find that $(z''/z)2a^2H^2$ has a maximum before the inflaton field reaches ϕ_{step}, a minimum shortly afterwards and it will return to the asymptotic slow roll value. So, it first grows in magnitude as the inflaton field accelerates and then drops to a large negative amplitude as the field slows. However, the tensor power spectrum is unaffected since $\ddot{a}/a$ remains constant throughout the step.

To understand the scalar power spectrum we begin by considering the evolution of a particular scalar mode. The evolution is governed by the competition between the k^2 and z''/z terms. A step in the potential of the magnitude we are interested in only has a lasting effect on k modes within the horizon, and not on modes which are already well outside the horizon. That is the lowest wavenumber affected is approximately given by $k_{low} \sim aH|_{step}$. Moreover, from the form of the $k^2 - z''/z$ term in the mode equation, we can see that the range of k affected by the step will scale roughly with the square root of the maximum value of z''/z in the region of the step.

In Fig.(5.3, right panel) we show the evolution of u_k^1, u_k^2 and u_k for an intermediate

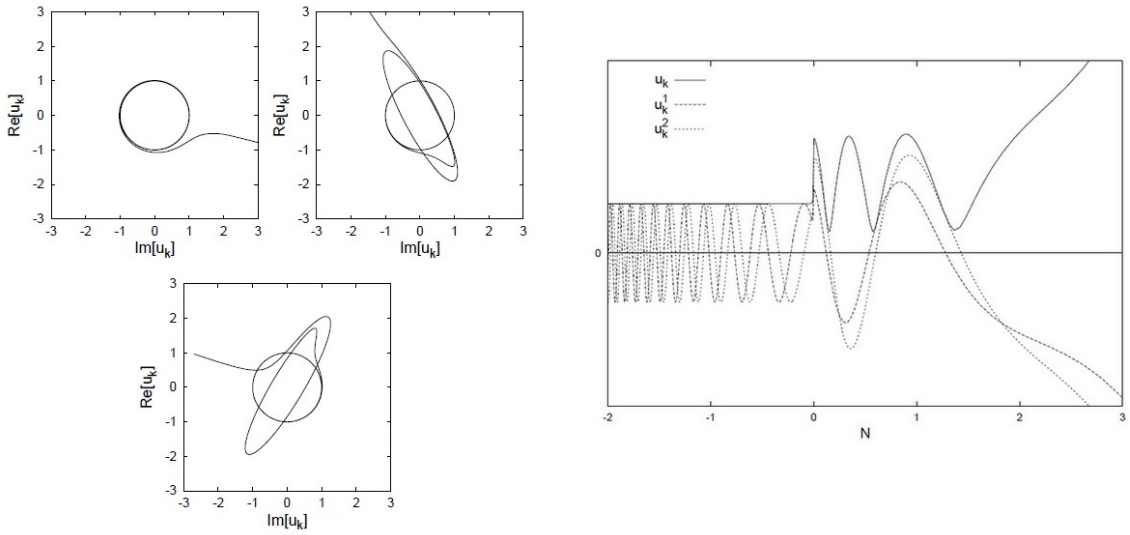

Figure 5.3. Left Panel: These figures show the evolution of u_k in the complex plane, where u_k has been normalised to one in the oscillating limit. The choice of initial conditions (Eq.(5.14)) ensures that the motion will be initially circular. The top left plot shows a mode that is not affected by the feature, so that the circular oscillation goes straight into a growing motion. In the other two plots the circle gets deformed by an intermittent phase of growth triggered by the peak of z''/z , to be followed by another phase of elliptic oscillations (caused by the dip of z''/z) until finally the modes leave the horizon and start growing. Whether a mode is suppressed or enhanced by this mechanism depends on the phase of the oscillation when the growth sets in. Growth along the semi-major axis will lead to an enhancement (top right), whereas growth along the semi-minor axis entails a suppression (bottom) with respect to the modes of the corresponding featureless model. Credit: Hamann [89].
Right panel: Evolution of the independent modes u_k^1 and u_k^2 (with initial conditions for u_k^1 and u_k^2 given in Eq.(5.15)) and the linear combination of their amplitude, Eq.(5.16) for $k = 0.3$. Credit: Adams [83].

wavenumber in the range of k affected. The rise in z''/z introduces a brief interlude of growing mode behavior into the oscillatory regime. The subsequent interval where z''/z is negative causes the amplitude of u_k to briefly resume its oscillatory behavior. It is obvious that modes with $k^2 \gg \text{Max}|z''/z|$, i.e., modes that are well within the horizon at the time of the step, will not be affected at all and u_k will remain in the oscillatory regime. For $k^2 \leq \text{Max}|z''/z|$, the maximum in z''/z will result in a boost of exponential growth for u_k, reverting to oscillations when z''/z goes negative and eventually return to the growing solution. We depict the motion of u_k in the complex plane in Fig.(5.3, left panel). When an oscillatory phase is preceded by a growing phase, the initial circle will be distorted to an ellipse. As the growth sets in again, the mode will be suppressed or enhanced, depending on the phase of the oscillation, which itself is k-dependent. In the spectrum, this can be observed as oscillations. This mechanism will be most effective for modes that are just leaving the horizon, for modes with $k^2 \ll \text{Max}|z''/z|$ the phase difference will be the wavelengths affected by the feature are those that are about to leave the horizon as the inflaton field reaches the centre of the step. In particular, also the frequency of the oscillations of the spectrum is proportional to this scale.

Finally, when the inflaton field resumes slow rolling, the oscillations leave the horizon with altered phase and increased amplitude. Both of the two initially independent solutions are affected similarly, as they now have the same phase, and the amplitude of their linear combination oscillates. In other words, the presence of the step introduces a boundary condition which selects a solution with an oscillating envelope in contrast to the unconstrained plane wave solution with constant envelope seen at small k.
As in the case of a featureless inflaton potential u_k obtains a growing mode solution once it is outside the horizon. However the asymptotic limit reached by the curvature perturbation $|\mathcal{R}_k|$ depends on the oscillation phase of the mode at horizon exit, so that $|\mathcal{R}_k|$ oscillates, with maxima corresponding to the modes which exit at an extremum. Setting the position of the step so that the scale where the oscillations begin, k_{low} (it is probed by observations of the galaxy correlation function and the anisotropy in the CMB), the proper time interval between the step and when the mode with wavenumber k exits is approximately $\Delta\tau \sim 1/aH|_{step} - 1/aH|_{exit} = 1/k_{low} - 1/k$ and in this time the amplitude of the mode will have undergone $1/\pi(k/k_{low} - 1)$ oscillations. Thus the period of the variation in $|\mathcal{R}_k|$ is approximately πk_{low}. For higher wave-numbers the effect of the z''/z term is smaller, the amplitude of their oscillation is not increased and the two modes are not set exactly in phase with each other. However their phases are still altered so that the linear combination u_k oscillates, but with a diminished amplitude compared to the lower k modes. The magnitude of z''/z depends on both the parameters c and d in the potential, and in a well motivated model these will be determined by from particle physics. Alternatively, given accurate observations of the CMB and LS structure, it may be possible to put cosmological constraints on the values of these parameters, and in the next section we examine the observable consequences of a scale dependent primordial spectrum.

What remains is to identify the horizon size at the step with a physical scale

today. This connection can be made if one knows the total number of e-foldings $N_\star$ of inflation that took place after a known physical scale $k_\star$ left the horizon. Technically, we evolve the background Eqs.(5.4) until the end of inflation N_{end}, (defined by $\ddot{a}(N_{end}) = 0$). The scale $k_\star$ can then be determined in units of $aH|_{\phi=\phi_{step}}$ via

$$k_\star \longleftrightarrow \frac{a(N_{end} - N_\star)H(N_{end} - N_\star)}{aH|_{\phi=\phi_{step}}}. \tag{5.18}$$

As long as the spectrum of the $c = 0$ background model is only mildly scale dependent, there will be a strong degeneracy between $N_\star$ and ϕ_{step}: shifting the feature in the potential will have the same effect as shifting the scale of k. In the following we will therefore not treat $N_\star$ as a free parameter, but set $N_\star = 50$ for $k_\star = 0.05\,h\mathrm{Mpc}^{-1}$. If we want the feature to affect scales that are within reach of current observations, this will require ϕ_{step} to lie in the interval $14 < \phi_{step} < 15$.

5.4 Observable spectra.

In this section, we briefly show the effect of the step-like features model on the CMB temperature power spectrum and on the galaxy matter power spectrum. We will show some simulations, simple but meaningful, using different step parameters values. We start by showing the shape of inflationary potential (Eq.(5.17)) varying the step parameters, and the respective primordial power spectrum.

5.4.1 Inflationary potential and primordial power spectrum.

The spectrum of primordial perturbations resulting from the potential in Eq.(5.17) can be calculated as outlined in the previous section, and is found to be essentially a power-law with superimposed oscillations. The oscillations are localized only in a limited range of wavenumbers (centered on a value that depends on ϕ_{step}) so that asymptotically the spectrum recovers the familiar k^{n_s-1} form typical of slow-roll inflationary models.
In particular, for a chaotic potential, the underlying power law has a spectral index $n_s \simeq 0.96$. In Fig.(5.4) we show the shape of potential of Eq.(5.17) for $m = 7.5\times10^{-6}$ and different credible values of the step parameters, compared to a smooth $m^2\phi^2/2$ potential ($c = 0$), while in Fig.(5.5) we show the correspondents primordial power spectrum from Eq.(5.8).

We note that the results obtained in the case of a specific potential will be, by definition, model-dependent. As argued in Ref. [89], we can see this considering a more general potential

$$V(\phi) = V_0 + f(\phi)S(\phi - \phi_{step}) \tag{5.19}$$

As we have seen above, the derivatives of the potential are crucial to determining the spectrum. Near the step, the derivatives of V will have a contribution from the derivatives of S. If the step is sharp enough, the nth derivative of V will be dominated by the nth derivative of S, since the other terms are suppressed with factors of the order of the slow roll parameters of the background model. Hence, the dynamics of z''/z near the step hardly depends on the background, but is determined

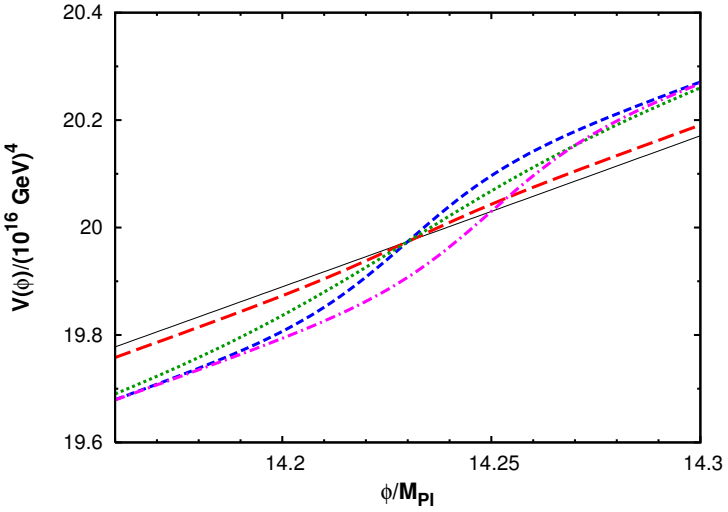

Figure 5.4. Inflationary potential in Eq.(5.17) for $m = 7.5 \times 10^{-6}$. The solid thin black line corresponds to a smooth ($c = 0$) chaotic potential $m^2\phi^2/2$. The long-dashed red curve has $\phi_{step} = 14.23$, $c = 0.001$ and $d = 0.025$ and roughly corresponds to the spectrum giving the best fit to the WMAP7 data. The other curves correspond to $\phi_{step} = 14.23$, $c = 0.005$, $d = 0.025$ (blue short-dashed), $\phi_{step} = 14.23$, $c = 0.005$, $d = 0.05$ (green dotted) and $\phi_{step} = 14.25$, $c = 0.005$, $d = 0.025$ (magenta dot-dashed). As expected, the start point of the oscillation depends on the value of ϕ_{step} [90].

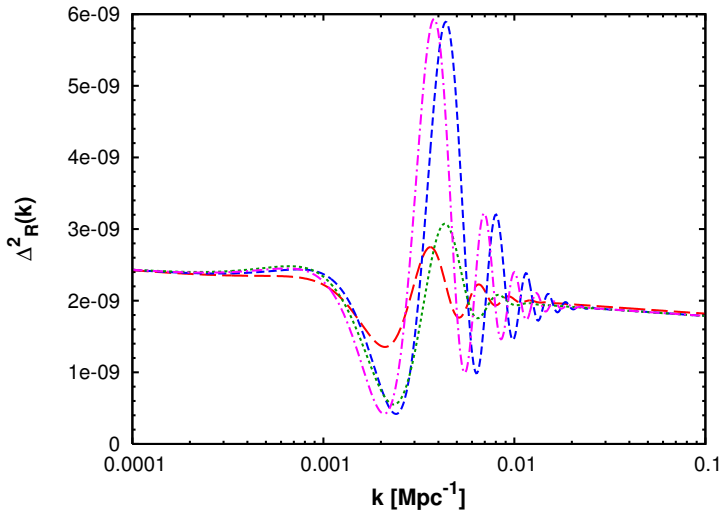

Figure 5.5. Primordial power spectrum for an inflationary potential of the form Eq.(5.17). The values of the step parameters are the same as in Fig.(5.4), namely: $\phi_{step} = 14.23$, $c = 0.001$, $d = 0.025$ (red long-dashed), $\phi_{step} = 14.23$, $c = 0.005$, $d = 0.025$ (blue short-dashed), $\phi_{step} = 14.23$, $c = 0.005$, $d = 0.05$ (green dotted) and $\phi_{step} = 14.25$, $c = 0.005$, $d = 0.025$ (magenta dot-dashed) [90].

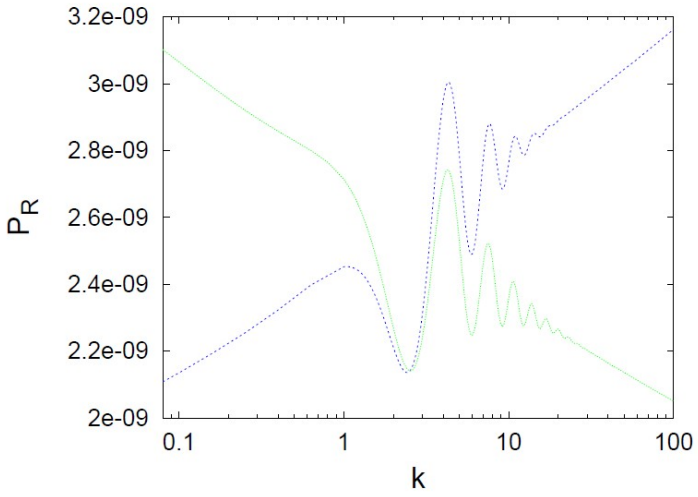

Figure 5.6. Primordial power spectra of a hybrid inflation type step model 5.20 (dashed blue line), and of potential 5.21 (dotted green line). The hybrid inflation background model has $n_s > 1$, suppressing large scale fluctuations, while the $\lambda\phi^4$ model has $n_s < 1$ with more power on large scales. Credit: Hamann [89].

by the form of S. On the other hand, any S that gives a z''/z which roughly shows a behaviour like the one depicted in Fig.(5.2), will lead to a burst of oscillations in the power spectrum. The similarities between spectra of different background models are illustrated in Fig.(5.6), where we plot the spectra of a hybrid inflation type potential

$$V(\phi) = V_0(\phi) + \frac{1}{2}m^2\phi^2\left[1 + c\tanh\left(\frac{\phi - \phi_{step}}{d}\right)\right], \tag{5.20}$$

and another monomial potential

$$V(\phi) = \lambda\phi^4\left[1 + c\arctan\left(\frac{\phi - \phi_{step}}{d}\right)\right], \tag{5.21}$$

with a different form of the step function. Note that despite the difference in background models and step functions, the maxima and minima of the oscillations occur at the same wavelengths. The issue of model dependence can be alleviated in a phenomenological way by restoring the spectral index as a free parameter, i.e., by defining the "generalized" spectrum $\mathcal{P}_{\mathcal{R}}^{\rm gen}$ as

$$\mathcal{P}_{\mathcal{R}}^{\rm gen}(k) = \mathcal{P}_{\mathcal{R}}^{\rm ch}(k) \times \left(\frac{k}{k_0}\right)^{n_s - 0.96}, \tag{5.22}$$

where $\mathcal{P}_{\mathcal{R}}^{\rm ch}(k)$ is the spectrum induced by the chaotic potential of Eq.(5.17). Since the latter has a overall tilt of 0.96, n_s will describe the overall tilt of the generalized spectrum.

5.4.2 Anisotropy and matter power spectra.

Let us now see how the primordial potential Eq.(5.17) produces oscillation on the temperature and matter power spectra. In these simulations we assume a flat geometry, three families of massless neutrinos and the cosmological parameters values fixed to: $\Omega_b h^2 = 0.02258$, $\Omega_c h^2 = 0.1109$, $\tau = 0.088$, $h = 0.71$, $n_s = 0.96$, $n_{run} = 0$. In Fig.(5.7) we show the simulation for the angular anisotropy power spectrum. The potential with step-like features produces intriguing oscillations, and we note that vary the ϕ_{step} value correspond to vary the position of the oscillations in the spectrum, while the variation of c and d values determine the oscillation amplitude (with greater dependence on c value). This dependence is also observed in the spectra of angular temperature-polarization cross-correlation, which is shown in Fig.(5.8).

Of particular interest may be the analysis of the matter power spectrum, which adds important information about LS structure to the CMB analysis. We can construct it by the linear spectrum of matter fluctuations and the linear matter transfer function $T(k)$, appropriate to the (dark) matter content, which tracks the scale-dependent rate of growth of linear perturbations. The spectrum of mass fluctuations after matter domination (per unit logarithmic interval of wavenumber k) is [85]:

$$P_\delta \equiv \mathcal{P}_\mathcal{R} T^2(k) \left(\frac{k}{aH_0}\right)^{3+n}. \tag{5.23}$$

In Fig.(5.9) we show the simulation for the matter power spectrum. In this case, the dependence on the ϕ_{step} parameter of the starting point of the oscillation is clear. The aim of these simulations is only the understanding of the step parameters effect, in Fig.(5.10) we show similar analysis made by Adams *et. al.* using the potential in Eq.(5.17).

5.5 Approximate solution.

We have seen in section 5.2 how to evaluate the density perturbation spectrum by numerical integration of the set of differential equations. As an alternative way, we can employ an approximate form of the power spectrum, reproducing the features caused by a steplike inflaton potential. For the derivation of approximate solutions to the evolution of the inflaton on an inflationary potential that undergoes a sharp downward step, we refer to the works [91, 92]. So, we use the analytical parametrization for the scalar primordial power spectrum given by:

$$P_\mathcal{R}(k) = \exp[\ln P_0(k) + \frac{A_f}{3} D\left(\frac{k\eta_f}{x_d}\right) W'(k\eta_f)], \tag{5.24a}$$

$$D(y) = \frac{y}{\sinh y} \tag{5.24b}$$

$$W'(x) = (-3 + \frac{9}{x^2})\cos 2x + (15 - \frac{9}{x^2})\frac{\sin 2x}{2x}, \tag{5.24c}$$

where $P_0(k) = A_s(\frac{k}{k_\star})^{n_s - 1}$ is the smooth spectrum with the standard power law form, A_f is the kinetic energy perturbation of the step, η_f is the step crossing time

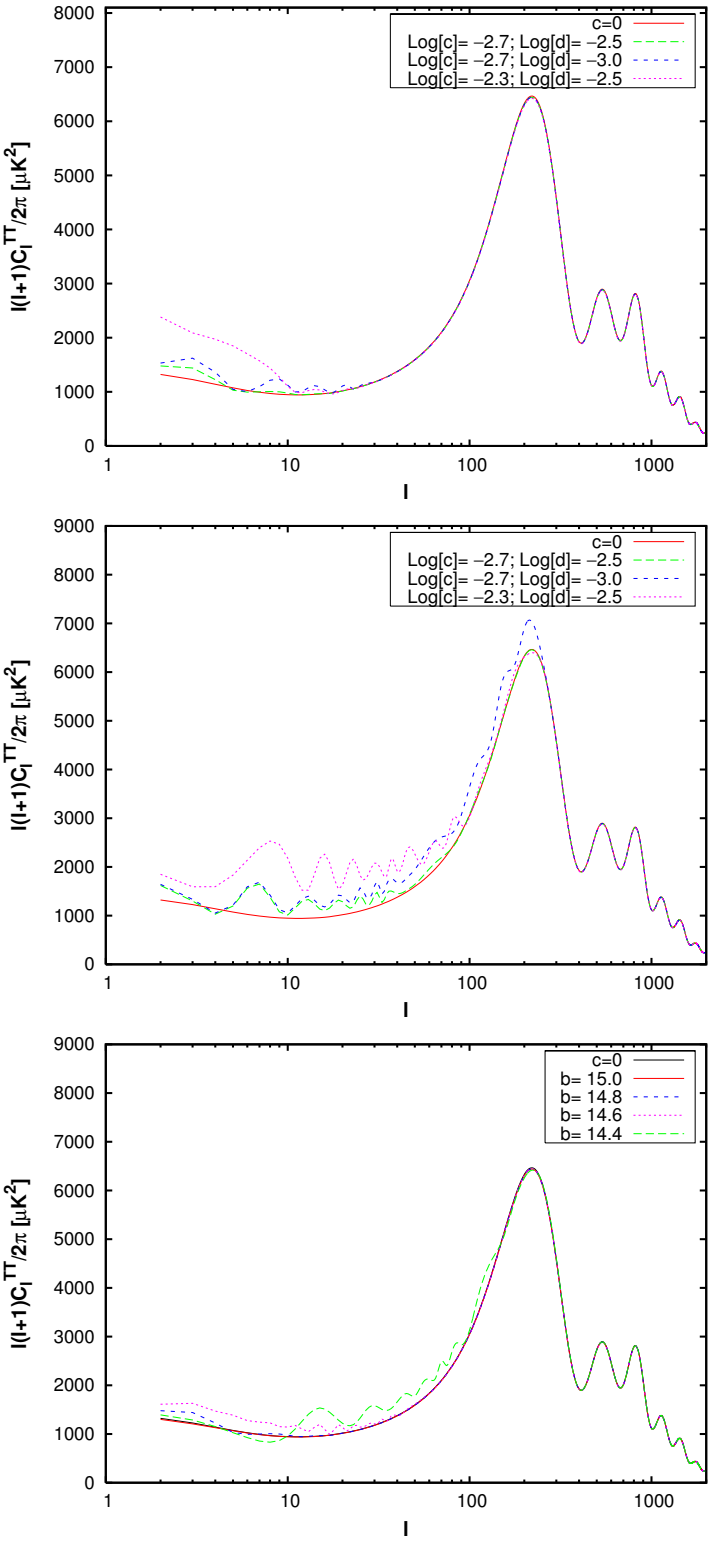

Figure 5.7. Effect of inflationary potential with step on the CMB anisotropy power spectrum. In the upper and middle plot we vary the values of $\log c$ and $\log d$, while ϕ_{step} is set at 14.8 (in top plot) and 14.5 (in middle plot). In the bottom plot we fix the values of $\log c = -2.7$ and $\log d = -2.5$, and vary the value of ϕ_{step}, denoted by " b ".

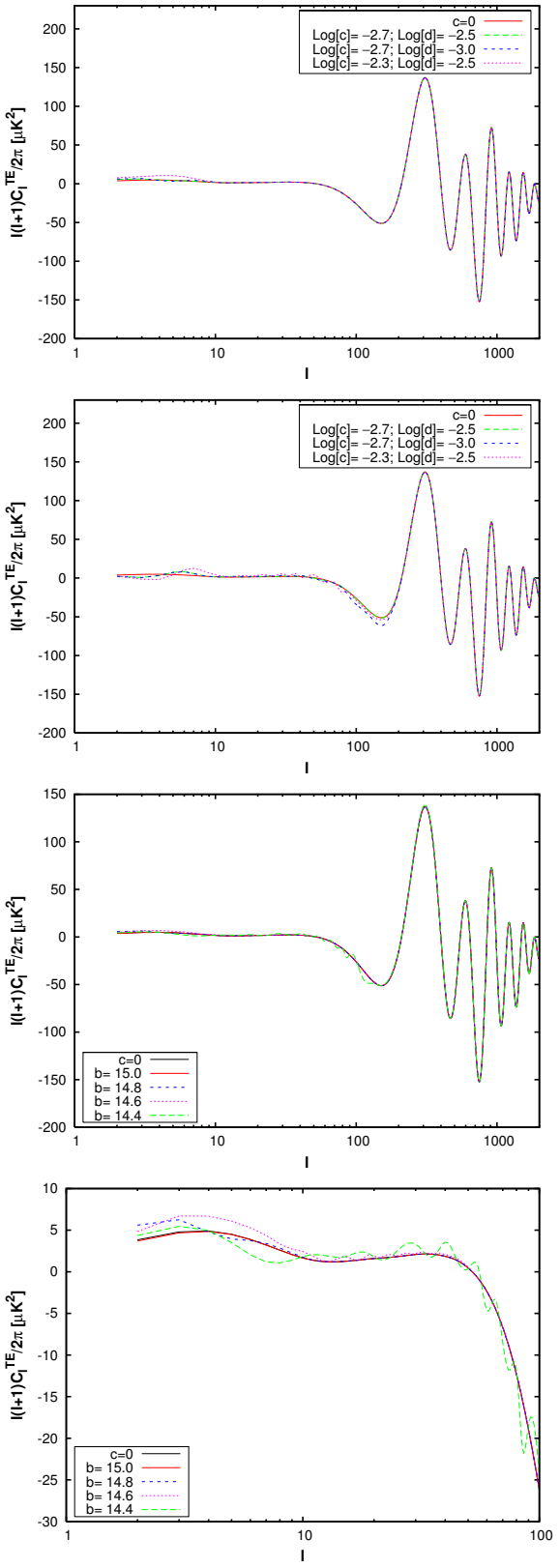

Figure 5.8. Effect of inflationary potential with step on the CMB cross-correlation TE power spectrum. In the first and second plot we vary the values of $\log c$ and $\log d$, while ϕ_{step} is set at 14.8 (in first plot) and 14.5 (in second plot). In the third plot we fix the values of $\log c = -2.7$ and $\log d = -2.5$, and vary the value of ϕ_{step}, denoted by " b ". The last plot is a zoom of the third plot in the range $2 < \ell < 100$.

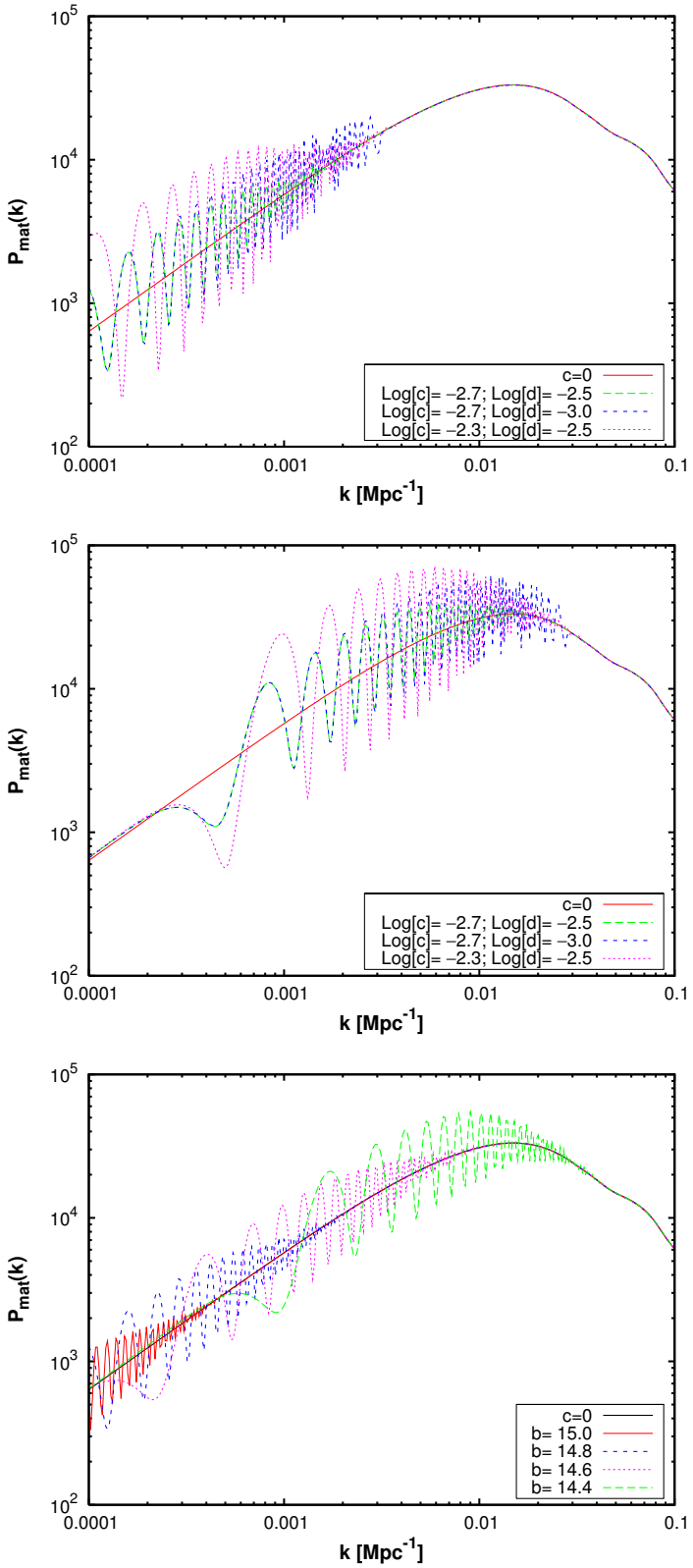

Figure 5.9. Effect of inflationary potential with step on the matter power spectrum. In the upper and middle plot we vary the values of $\log c$ and $\log d$, while ϕ_{step} is set at 14.8 (in top plot) and 14.5 (in middle plot). In the bottom plot we fix the values of $\log c = -2.7$ and $\log d = -2.5$, and vary the value of ϕ_{step}, denoted by " b ". P(k) is in $(h^{-1}\mathrm{Mpc})^3$ unity.

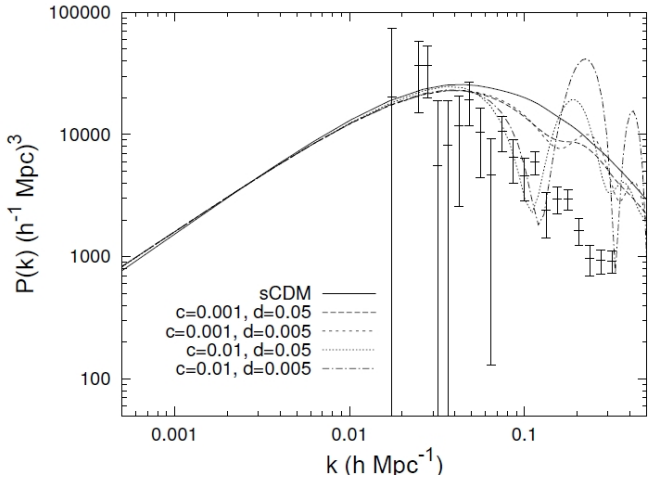

Figure 5.10. Matter power spectrum for the primordial spectra of Eq.(5.17). The data points are from the PSCz catalogue. Credit: Adams [83].

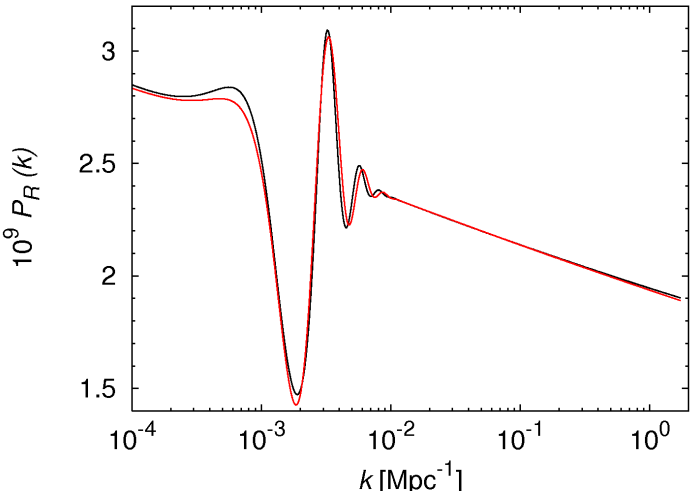

Figure 5.11. Primordial power spectra for inflationary potentials with step. The red line shows the Planck best-fit spectrum in the case of the numerical integration approach with $m = 7.5$ x 10^{-6}, while the black line shows the Planck best-fit spectrum of the respective approximate parametrization analysis.

in units of Mpc and x_d the dimensionless damping scale. This analytic solutions for the power spectrum is valid in the limit that the step is short and sharp.
Briefly, we clarify that these equations were obtained by choosing $F(x) = -\tanh(x)$ and $V_0 = m^2\phi^2/2$ in the generic equation:

$$V(\phi) = V_0(\phi)\left[1 + cF\left(\frac{\phi - \phi_{step}}{d}\right)\right]. \tag{5.25}$$

In Eq.(5.24a), D is the damping envelope for the tanh step profile and we note that different functions F simply change the damping envelope, so also the oscillating windows function W' is modulated by the decaying envelope D.
Using this approach, we have three new step parameter η_f, A_f and x_d, related to the parameters c and d and the slow roll parameter at first order ϵ_0. Indeed, for $c \ll 1$ we have:

$$A_f = \frac{6c}{\epsilon_0 + 3c}, \tag{5.26a}$$

$$x_d = \frac{\sqrt{2\epsilon_0 + 6c}}{\pi d}, \tag{5.26b}$$

while η_f value depends on when the inflaton crosses ϕ_f: $\phi - \phi_f = \sqrt{2\epsilon_0}\ln(\eta/\eta_f)$. Approximately, we can say that for $c = 10^{-5}$, the inflaton crosses ϕ_f at $\eta_f \sim 1455$ Mpc, for $c \sim 10^{-3}$ it correspond to $\eta_f = 1270$ Mpc arriving to $\eta_f = 1456.1$ Mpc for $c = 0$.
Using this method, by placing the features directly on the density power spectrum, we do not integrate the system of differential equations, with a significantly smaller computing time and small deviation from the result of numerical calculation. We can clearly see this in Fig.(5.11), where we plot the primordial power spectra for the best-fit models, using the Planck data, obtained in the case of numerical integration (red line) and for the case of analytical approximation (black line).

5.6 Constraints on inflationary potential with step.

In this section, we compare the proposed model with step-like features in the primordial potential with the data. The work has been carried out over the three years of my Ph.D, the analysis has been implemented step by step with the most recent data, improving the results. The results have been published in several papers in scientific journals with referee (Benetti *et. al.* [90][93][94]), that can be found in the appendix.

In addiction to the WMAP and ACT experiments, introduced in the previous section 4.2, here we consider also the Planck data and matter power spectrum data sets.

Planck is a space observatory operated by the European Space Agency, launched in 2009 and its results are eagerly awaited in recent years. It complements and improves the WMAP results and provides a major source of information relevant to several cosmological and astrophysical issues, such as testing theories of the early universe and the origin of cosmic structure. In 2012 was released the mission's all-sky map of the CMB [53][58], covering the multipoles range $2 < \ell < 2500$.

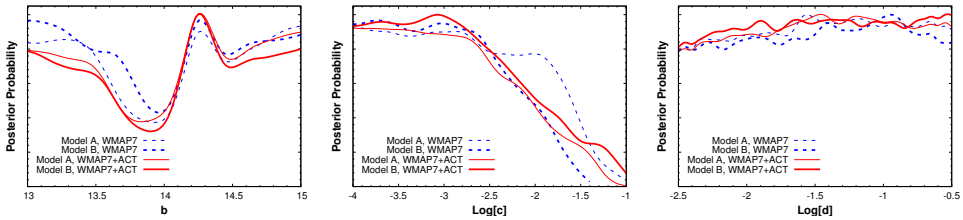

Figure 5.12. One-dimensional posterior probability density for $\phi_{step} = b$ (left panel), $\log c$ (middle panel) and $\log d$ (right panel) for model A (thin curves) and B (thick curves) using WMAP7-year data (dashed curves) and the WMAP7-year+ACT dataset (solid curves).

For the SDSS data sets, we considered data from the Sloan Digital Sky Survey (SDSS), that is a multi-filter imaging and spectroscopic redshift survey using a dedicated 2.5-m wide-angle optical telescope. Data collection began in 2000, now the survey covers more than a quarter of the sky and creates 3-dimensional maps containing more than 930,000 galaxies and more than 120,000 quasars. The last SDSS data released was in 2012, the Data Release 9 (DR9), and includes the first results from the Baryon Oscillation Spectroscopic Survey (BOSS) spectrograph [95]. The SDSS survey for CMB analysis is a extremely interesting independent data set and covers the multipole range $300 < \ell < 9800$. For our analysis we chose to consider data only in the linear scales regime.

In the analysis we choose to work with a ΛCDM model with six cosmological parameters free to vary, to which we add the three parameters of step of inflationary potential. We consider purely adiabatic initial conditions, impose flatness and neglect neutrino masses, and limit our analysis to scalar perturbations.
Before proceeding further, we point out the parameter degeneracies question, stating that the presence of a feature does not bias our estimates for the values and errors of the cosmological parameters. The introduction of the step parameters does not pollute (or has little effect on) the constraints on the cosmological parameters, as we can see later in tables Tab.(5.2) and Tab.(5.3). So, we can say that degeneracies of the oscillation with standard cosmological parameters are virtually non-existent. Moreover, as we have said in the end of section 5.3, we choose to explore the interval $14 < \phi_{step} < 15$. In the case of c and d, since we do not have any *a priori* information on these parameters, not even on their order of magnitude, we find convenient to consider a logarithmic prior on both of them. It can be seen, however, that the probability density becomes half of its asymptotic value at $c = 0$ for $c = 10^{-2}$.

5.6.1 Constraints from WMAP7-year and ACT observations.

Our analysis starts using data from the WMAP7-year [96] and ACT [97][98].
We have compared the theoretical predictions of the chaotic inflation model, where the scalar spectral index is being fixed to $n_s = 0.96$ (Model A), and of a more general phenomenological model, where n_s is being treated as a free parameter (Model B), in order to find constraints on the parameter describing the model. We choose to use $k_\star = 0.025$ Mpc^{-1}, as said in section 5.3 it is in a strong degeneracy with the

ϕ_{step} value: the pivot wavenumber changes the relationship between the value of ϕ_{step} and the position of oscillations in $k-$space; this should be taken into account when comparing the results of different studies. In particular, changing k_0 from 0.05 to 0.002 Mpc^{-1} shifts ϕ_{step} by ~ 0.5 towards lower values.
From the analysis we see that for the cosmological parameters the width of the posterior is much smaller than the prior range, so that the latter is not really relevant. For the step parameters, the situation is complicated by the fact that the posterior does not go to zero in certain directions of the subspace. In Fig.(5.12) we show the one-dimensional posterior distributions results for the step parameters $\phi_{step} = b$, $\log c$ and $\log d$. It can be noted that the posterior for ϕ_{step} has a peculiar shape. The posterior does not drop to zero because it still exist a fair amount of parameter space, i.e., models with low c, than can fit the data even with the oscillations placed in the "wrong" place. The posterior going to a constant value at the edges of the prior range is instead related to the oscillations being moved out of the observable scales. The inclusion of the ACT data in addition to WMAP7-year helps in constraining small values of ϕ_{step}, i.e., oscillations at small scales.
The shape of the $\log c$ posterior is typical of a quantity parameterizing the amplitude of a non-standard effect: it is constant for "small" values of the parameter (when the step model becomes indistinguishable from standard ΛCDM), and then rapidly vanishes above a critical value. It can be seen that the probability density becomes half of its asymptotic value at $c = 0$ for $c \geq 10^{-2}$.
Finally, the posterior for $\log d$ clearly shows that this parameter is largely unconstrained by data.

We have also studied the possibility of detecting the oscillations with the upcoming Planck data. In order to do this, we simulate "mock" data corresponding to the step model that yields the best fit to the WMAP7-year and then perform a statistical analysis on these data as if they were real. The forecast method we use is identical to the one presented in [99] and we refer to this paper for further details and references. The synthetic dataset is generated by considering for each C_ℓ a noise spectrum given by:

$$N_\ell = w^{-1} \exp(\ell(\ell+1) 8 \ln 2/\theta_{\mathrm{b}}^2), \tag{5.27}$$

where θ_{b} is the full width at half maximum (FWHM) of the beam assuming a Gaussian profile and where w^{-1} is the experimental power noise related to the detectors sensitivity σ by $w^{-1} = (\theta_{\mathrm{b}}\sigma)^2$. The experimental parameters are reported in Tab.(5.1).
We have assumed as a fiducial model a generalized step model with step parameters corresponding to the Model B best fit to the WMAP7-year data. The one-dimensional posteriors for ϕ_{step}, $\log c$ and $\log d$ are shown in Fig.(5.13) As we can see the prior range dependence goes away with Planck data and we can quote marginalised credible intervals. We also show the two-dimensional posteriors for the step parameters in Fig.(5.14). It was evident that the Planck data would greatly increased the precision to which the step parameters can be measured; in particular, a detection of oscillations.

Experiment	Channel	FWHM	$\Delta T/T$	$\Delta P/T$
Planck	70	14'	4.7	6.7
$f_{\rm sky} = 0.85$	100	10'	2.5	4.0
	143	7.1'	2.2	4.2

Table 5.1. Planck [100] experimental specifications. Channel frequency is given in GHz, FWHM in arcminutes and noise per pixel for the Stokes I (ΔT/T), Q and U parameters (ΔP/T) is in [$10^{\hat{a}\check{L}\check{S}6}\mu$K/K], where T = $T_{\rm CMB}$ = 2.725K. In the analysis, we assume that beam uncertainties and foreground uncertainties are smaller than the statistical errors.

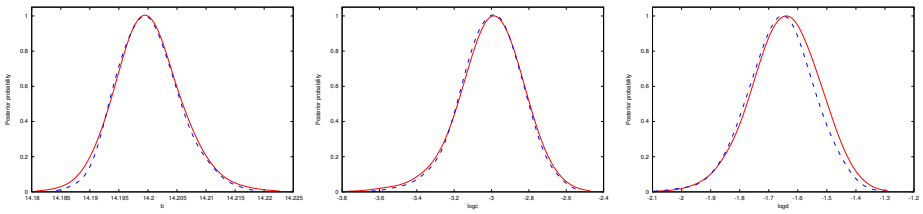

Figure 5.13. One-dimensional posterior probability density for ϕ_{step} named ϕ_{step} (left panel), $\log c$ (middle panel) and $\log d$ (right panel) derived from the mock Planck data, for best-fit models using WMAP data with n_s fixed (dashed curves) and n_s free (solid curves) [90].

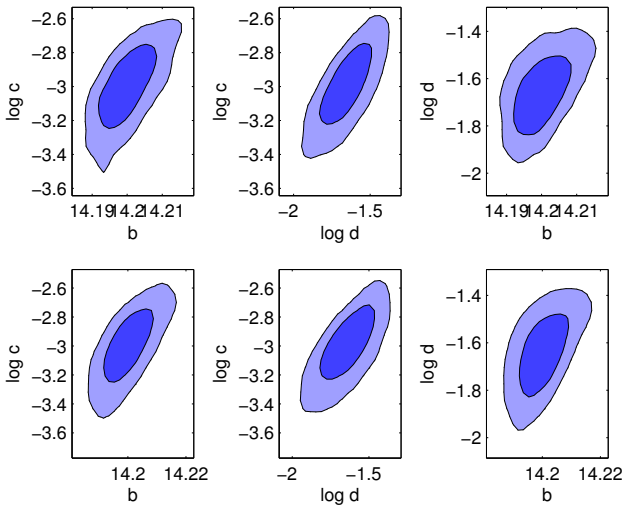

Figure 5.14. Two-dimensional posteriors in the ($\phi_{step} \equiv b - \log c$) (left), ($\log d - \log c$) (middle) and ($\phi_{step} \equiv b - \log d$) (right) planes, for best-fit models using WMAP data with n_s fixed (top) and n_s free (bottom), derived from the mock Planck data. The shaded areas correspond to the 68% (light blue) and 95% (dark blue) confidence regions [90].

5.6.2 Constraints from CMB and LRG observations.

We improve over previous works by using a more complete dataset. For the CMB data, we consider the WMAP7-year temperature and polarization data [96] and the small-scale CMB data from ACT [97][98] and SPT [68], that allow to extend the dynamic range of CMB observations to larger multipoles with the respect of WMAP7-year, thus measuring the damping tail of the CMB angular power spectrum. For the matter power spectrum, we use the Luminous Red Galaxies (LRG) sample of the Sloan Digital Sky Survey (SDSS) 7th data release [101]. The inclusion of different datasets allows us to explore a wider range of scales with respect to previous analyses, going from the Hubble radius down to the smallest linear scales, $k \simeq 0.1$ Mpc^{-1}. In particular, this leads to the clear identification of a "forbidden" range where oscillations are not allowed.
We consider as our basic dataset a combination of three different CMB datasets (WMAP7, ACT and SPT) and we refer to this case simply as "CMB", and then we also consider an enlarged dataset, dubbed "CMB+LRG", where we also add the LRG SDSS catalog, the Supernovae Ia Union Compilation 2 data [102], and impose a prior on the Hubble constant from the Hubble Space Telescope (HST) [103].
In the analysis we choose to work with the pivot wavenumber value $k_\star = 0.05$ Mpc^{-1}.
We initially choose a flat prior for ϕ_{step} in the range $13.5 < \phi_{step} < 15.5$, that conservatively encompasses the whole range probed by the WMAP, ACT, SPT and LRG datasets. We use this prior for the CMB only dataset.
We first focus the best fit parameters, i.e., the parameter values that maximize the likelihood. In the second column of Tab.(5.4) we show the best-fit values, for this dataset, of the primordial spectrum parameters. In the best-fit model, the step in the primordial spectrum is located in $b = 14.66$, consistently with previous studies [104, 90].
We explicitly show the projected likelihood, as well as $\Delta\chi^2 = \chi^2 - \chi^2_{\rm min}$, as a function of ϕ_{step} in the two panels of Fig.(5.15). It is interesting however that a distinct although low peak is present in the likelihood in $\phi_{step} \simeq 14$. We also note that the χ^2 does not become arbitrarily large (i.e., the likelihood does not asymptotically vanish) far from the minimum, but instead tends to a constant value. This is related to the fact that towards the extremes of the ϕ_{step} range the oscillations are moved outside the range of scales probed by the dataset, and thus the model becomes completely equivalent, as long as data fitting is concerned, to ΛCDM. Thus from the plot we can roughly estimate that the best fit at $\phi_{step} = 14.66$ represents a $\Delta\chi^2 \simeq 7$ improvement with respect to the ΛCDM best fit, while for the model with $\phi_{step} = 14$, $\Delta\chi^2 \simeq 3.5$.
The primordial power spectra correspoding to the two minima in the χ^2 are shown in Fig.(5.16). On the other hand, models with $14.1 < \phi_{step} < 14.5$ perform worse with respect to ΛCDM.
For a better understanding, we also show in Fig.(5.17) the comparison between the WMAP7-year best fit, the two models with features corresponding to the two peaks in the likelihood seen in Fig.(5.15), and the data present in the CMB dataset. It is clear from these plots (especially from the plot of residuals shown in the lower panel) that the model with $\phi_{step} = 14.66$ improves over ΛCDM by being able to fit

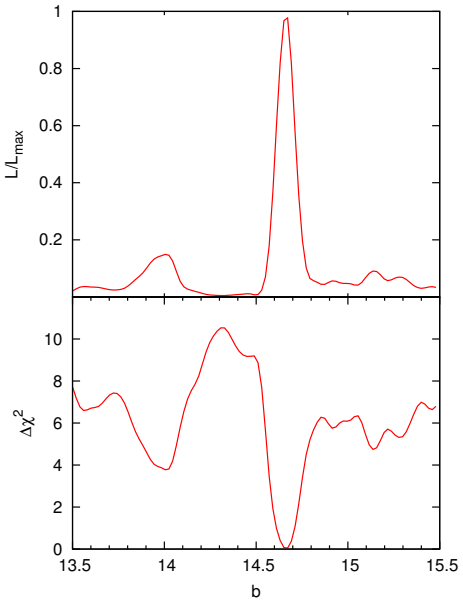

Figure 5.15. Model likelihood (upper panel) and $\Delta\chi^2$ (lower panel) as functions of $\phi_{step} = b$ for the CMB dataset, obtained by maximization.

the two outliers in $\ell = 22$ and $\ell = 40$, thus confirming our previous findings [90]. The interpretation of the peak in $\phi_{step} = 14$ is more puzzling; by looking at the lower panel of Fig.(5.17), however, it can be seen that the CMB spectrum for this model resembles what it would be obtained by adding a negative running $dn_s/d\ln k$ to the scalar spectral index. Thus this result could be reminiscent of the WMAP7-year preference for a negative running, that is indeed even more pronounced when high-ℓ data are added to the analysis [96]: $dn_s/d\ln k = -0.034 \pm 0.026$ (WMAP7 only) and $dn_s/d\ln k = -0.041^{+0.022}_{-0.023}$ (WMAP7+ACBAR+QUaD).

We now turn to the posterior distributions. In Fig.(5.18), we show the one-dimensional posteriors for $\phi_{step} = b$, $\log c$ and $\log d$. The posterior for ϕ_{step} still shows the two peaks in $\phi_{step} \simeq 14.7$ and $\phi_{step} \simeq 14$ that were present in the likelihood. The largest value at the edges of the prior range is due to a volume effect, since the one-dimensional posterior is obtained by marginalization (as opposed to the one-dimensional likelihood that was obtained by maximization). On the other hand, the probability density for $14.1 < \phi_{step} < 14.4$ is practically equal to zero. For what concerns $\log c$, as it could be expected, "large" values are disfavored by the data (as they produce large - in amplitude - oscillations that cannot, on average, be reconciled with observations) while for smaller values the posterior tends to a constant value as the oscillations become so weak as to be practically undetectable for the current experimental precision and thus the value of c becomes unimportant. As already noted, a posterior with this characteristic that extends, in principle, down to $\log c = -\infty$, cannot be properly normalized (since the corresponding probability mass is infinite) and, as a consequence, credible intervals are ill-defined. One could be tempted to impose a lower cut-off but then the credible intervals will end up

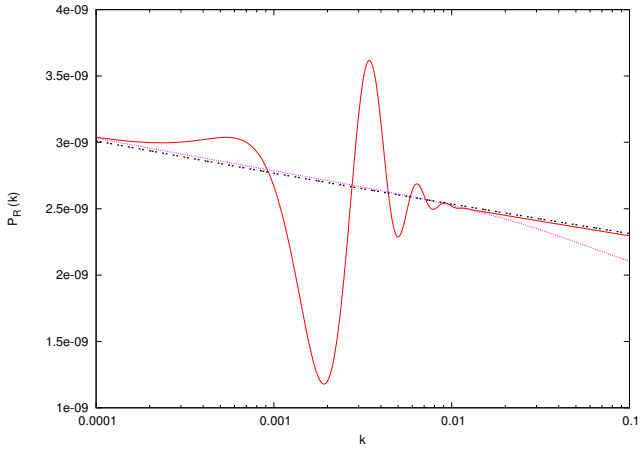

Figure 5.16. Primordial power spectrum for an inflationary potential of the form (5.17) with $m = 7.5 \times 10^{-6}$. The values of the step parameters are : $\phi_{step} = 14.66$, $\log c = -2.75$, $\log d = -1.42$ (red), $\phi_{step} = 14.00$, $\log c = -2.66$, $\log d = -0.54$ (magenta dotted), corresponding to the two peaks in the likelihood. For comparison, we also show the best fit ΛCDM power spectrum (black dot-dashed). We note that the model with $\phi_{step} = 14$ resembles, in the $k-$range considered, a model with a negative running index.

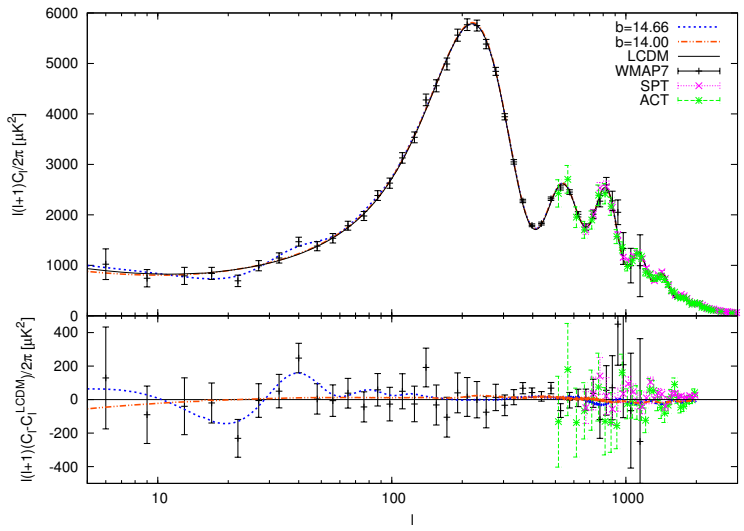

Figure 5.17. Upper panel: Power spectrum of CMB Anisotropies Power Spectrum for the best fit ΛCDM model (black line) and two step models with $\phi_{step} = b = 14$ (red dashed) and $\phi_{step} = b = 14.66$ (blue dot-dashed), corresponding to the two minima in χ^2, compared with WMAP7, ACT and SPT data. Lower panel: The same as above, but plotted in terms of residuals with respect to the ΛCDM best fit.

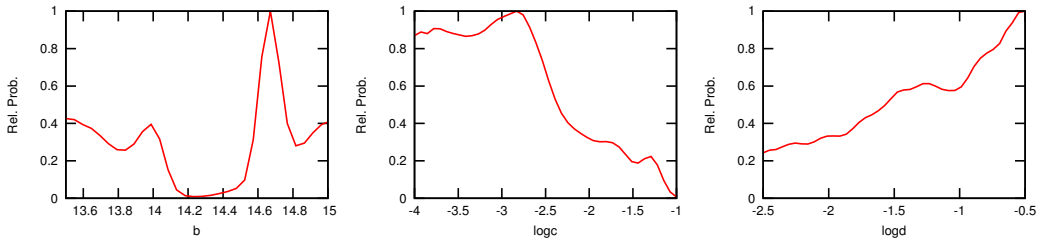

Figure 5.18. One-dimensional posterior probability density for the step parameters from the CMB dataset.

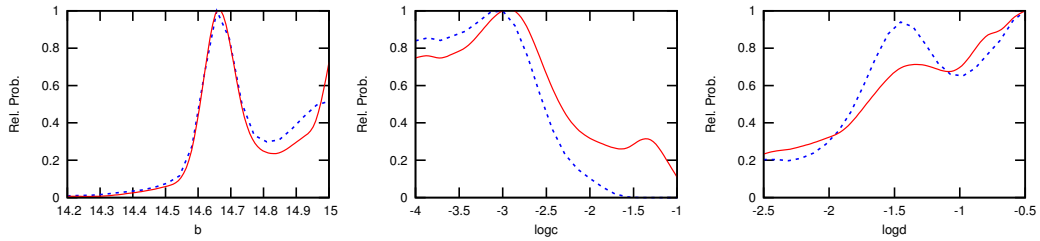

Figure 5.19. Comparison of the one-dimensional posterior probability density for the step parameters from the CMB (red solid line) and CMB+LRG (blue dashed line) datasets.

depending on the choice of the cut-off itself, so this should be avoided, at least in the absence of a clear physical reason for doing so.

We can still, however, compare probability densities, as well as probabilities integrated over finite intervals, since probability ratios do not depend on the overall normalization. We can use, as a benchmark value to compare the constraining power of different datasets, for example, the value of $\log c$ where $P(\log c)$ is half of its asymptotic value for $\log c \to \infty$. This should not be taken as an "upper limit" in the common sense of the word, but as said is a useful tool for comparison. In the case under consideration, we estimate that this happens for $\log c = -2.32$, or $c = 4.8 \times 10^{-3}$.

Finally, we examine the posterior for $\log d$. This is in part similar to the posterior for $\log c$, once one recalls that small values of $\log d$ produce a steep step in the potential and consequently large oscillations, so one should expect the probability to go to zero for small values of $\log d$, as it is. However, in this case, the posterior range is not wide enough to see the asymptotic part, for $\log d \to \infty$ (where ΛCDM should be recovered), of the distribution.

The fact that the posterior is bimodal in ϕ_{step} creates some difficulty for the Monte Carlo, as the chains cannot easily jump from one peak to the other, and thus take a longer time to sample satisfactorily the actual distribution. For this reason, in our second Monte Carlo run, using the CMB+LRG dataset, we have decided to concentrate on the region of the peak at $\phi_{step} = 14.66$ and impose the prior $14.2 \leq \phi_{step} \leq 15$. We find that the best fit for this dataset, shown in the third column of Tab.(5.4) has still $\phi_{step} = 14.66$. In Figs.(5.19) we compare the one-dimensional posteriors for

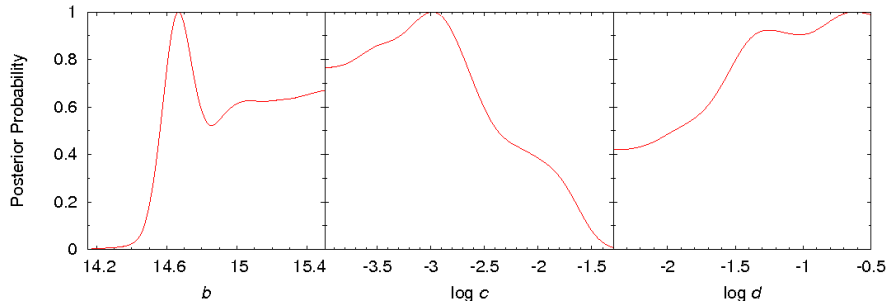

Figure 5.20. One-dimensional posterior probability densities for the step parameters of an inflationary model with steplike features in the potential, obtained by numerical integration of the mode equations using the Planck data [94].

the step parameters in the CMB+LRG dataset with those obtained previously with the CMB dataset. In order to allow for comparison, the distributions for the latter have been obtained by imposing a posteriori the condition $\phi_{step} \geq 14.2$ (which, in practical terms, that we have discarded all samples with $\phi_{step} < 14.2$, and reanalyzed these new chains from scratch). We find that there is practically no difference with respect to the position of the oscillations (which makes sense, since this is driven by the requirement of fitting the outliers in the WMAP7 data at relatively low-ℓ's). The amplitude of the oscillations is slightly more constrained, with the posterior going down at half of its plateau value at $\log c = -2.48$ ($c \simeq 3 \times 10^{-3}$). The posterior for $\log d$ is also slightly different, as it shows a more distinct peak in correspondence of the best-fit value $\log d \simeq -1.5$.

5.6.3 Constraints from Planck observations.

Finally we came to the last analysis, using the recent and highly precise Planck data [53].

We essentially consider three types of analysis with the results reported in Tab.(5.3).

The first analysis assumes a simple ΛCDM model with a featureless spectrum.

For the second analysis we considered the step-like model in the inflationary potential, numerically integrating the relevant equations and assuming the following priors on the corresponding parameters: $14.2 \leq b \leq 15.5$, $-4 \leq \log c \leq -1$, $-2.5 \leq \log d \leq -0.5$.

In the third analysis we used the analytical formula presented in section 5.5 Eq.(5.24a), with the same choice of priors of [54] and given by:

$$0 \leq A_f \leq 0.2, \quad 0 \leq \ln(\eta_f/\mathrm{Mpc}) \leq 12, \quad -1 \leq \ln x_d \leq 5. \tag{5.28}$$

As we can see in Tab.(5.3), introducing oscillations in the primordial spectrum either by numerical integration of the relevant equation or by using the above-mentioned analytical formula, reduces the χ^2 of the best-fit model by $\Delta\chi^2 \sim 9$.

However, the feature parameters are poorly constrained, as also shown in Fig.(5.20) where we report the posterior probabilities for the numerical integrating analysis. We can also note that the posteriors are better defined with respect to those present

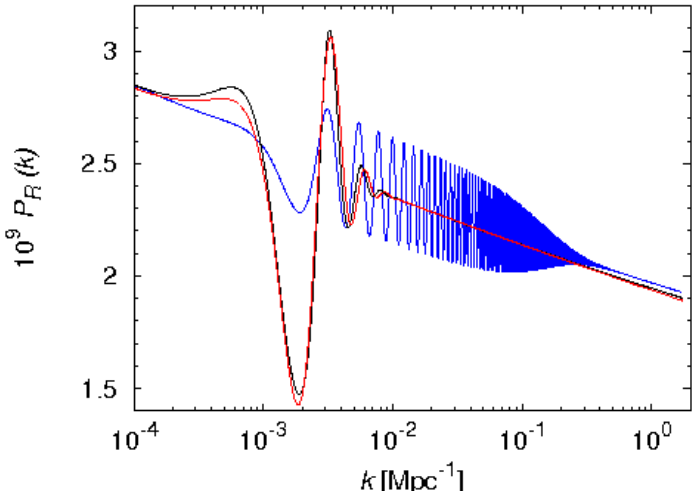

Figure 5.21. Primordial power spectra for inflationary potentials with step. The red line shows the best-fit spectrum in the case of the numerical integration approach exploring low-ℓ region, the black line shows the best-fit spectrum of the approximate parametrization analysis exploring the low-ℓ region, while the blue line plots the best fit of the approximate parametrization analysis exploring the first-peak region [94].

in our previous work of [93] although they are significantly different from a Gaussian distribution. In particular, we see that the use of the Planck data eliminates a bimodal form in the posterior probability for the b parameter, present in the WMAP data.

Both the analytical and the numerical method provide the same reduction in the χ^2 value, but the effects on the CMB angular spectra are drastically different. The best-fit model obtained from a numerical integration provides significantly different oscillations with respect to the best-fit model obtained in the case of the analytical approximation.

We can clearly see this in Fig.(5.16), where we plot the primordial power spectra for the best-fit models obtained in the case of numerical integration (red line) and for the case of analytical approximation (blue line) used in the Planck analysis.

In Fig.(5.22) we compare the best fit CMB angular spectra obtained in the two cases. As we can see, the numerical integration method identifies the oscillations on large angular scales ($10 < \ell < 60$) while the analytical method provides a better fit by producing oscillations around the first Doppler peak.

This difference is essentially due to the different choice of priors on the feature parameters assumed in the two analyses. To check this, we changed the priors for the analysis based on the empirical formula to

$$0.8 \leq A_f \leq 1, \quad 7 \leq \ln(\eta_f/\mathrm{Mpc}) \leq 8, \quad 0 \leq \ln x_d \leq 0.5. \tag{5.29}$$

obtaining the best-fit values reported in Tab.(5.4), last column. As we can see, the best fit has now $A_f \sim 1$, a value that was excluded by the choice of priors used in [54]. The corresponding primordial spectrum is reported in Fig.(5.16) as a black

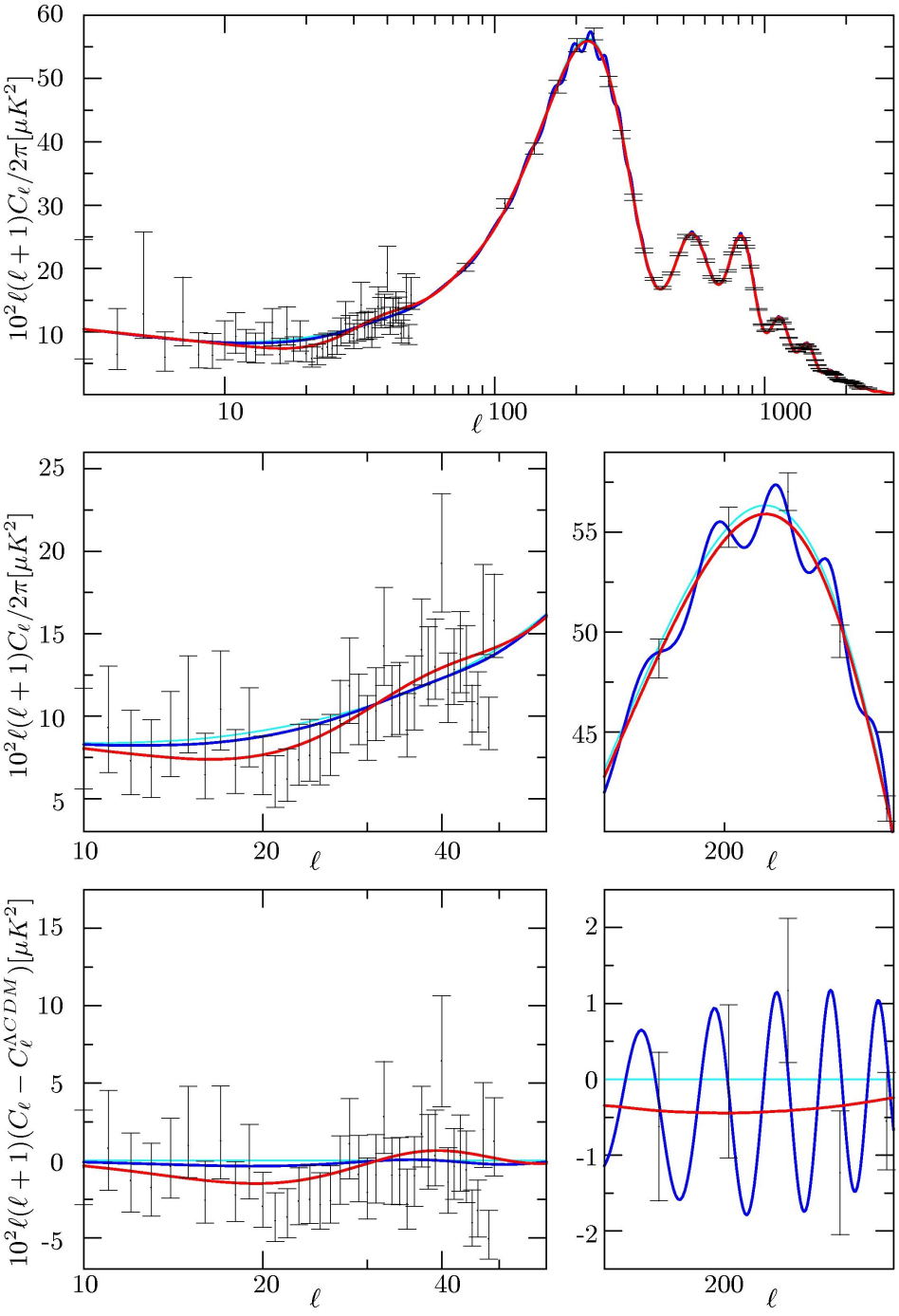

Figure 5.22. Upper panel: Planck temperature power spectrum for the best fit ΛCDM model (light blue line), for best fit of features model using initial potential as Eq.(5.17) with numerical resolution and exploring oscillation in low-ℓ region (red line) and best fit approximate parameterization as Eq.(5.24a) and exploring features in $\ell \sim 200$ (blue line), compared to the Planck temperature data. Middle panel: The same as above, zoomed in the region $10 < \ell < 60$ and $150 < \ell < 300$. Lower panel: The same as above, plotted in terms of residuals with respect to the ΛCDM best fit [94].

Table 5.2. 68% confidence limits for the cosmological parameters using WMAP+ACT+SPT data (column named "Features (CMB)") and WMAP+ACT+SPT+SDSS data (column named "Features (CMB+LRG)"), relate to the ΛCDM model using the WMAP+ACT+SPT data (column named "ΛCDM model").

Parameter	ΛCDM model	Features (CMB)	Features (CMB+LRG)
$100\,\Omega_b h^2$	2.215 ± 0.041	2.204 ± 0.044	2.215 ± 0.037
$\Omega_c h^2$	0.1114 ± 0.0046	0.1125 ± 0.0050	0.1122 ± 0.0029
$100\,\theta$	1.0411 ± 0.0016	1.0409 ± 0.0016	1.0414 ± 0.0015
τ	0.085 ± 0.014	0.086 ± 0.014	0.087 ± 0.015
n_s	0.962 ± 0.011	0.959 ± 0.014	0.959 ± 0.011
$10^9 A_s$ $(k_0 = 0.05\ Mpc^{-1})$	2.17 ± 0.06	2.18 ± 0.08	2.19 ± 0.07
Age [Gyr]	13.78 ± 0.09	13.81 ± 0.09	13.78 ± 0.07
z_{re}	10.4 ± 1.2	10.5 ± 1.2	10.5 ± 1.2
H_0 [km s^{-1} Mpc^{-1}]	70.45 ± 2.1	69.9 ± 2.3	70.3 ± 1.3

line and, as we can see, is in full agreement with the best-fit spectra obtained from the analysis made assuming the numerical integration method.

We can therefore conclude that one needs to be extremely cautious in the choice of priors when looking for features in the CMB spectra since probability distributions for the parameters are highly multi-modal.

From our tests we can observe that the proposed inflationary potential is in good agreement with observed data and that models with a step provide a significantly better fit than standard featureless power-law spectra. We understand also that the data are not yet constraining enough to allow to discriminate between these inflationary models and the standard inflationary scenario.
Furthermore, it is evident that the Planck data greatly increase the precision to which the step parameters can be measured. Future polarization data will further improve the constraints presented here, we therefore await for the next release of the Planck collaboration, in October 2014.

Table 5.3. 68% confidence limits for the cosmological parameters using the Planck data. Second column refer to ΛCDM "vanilla" model; the third column show the constraints on the features model using initial potential as Eq.(5.17) with numerical resolution and exploring oscillation in low-ℓ region; the fourth column refer to analysis using approximate parameterization as Eq.(5.24a) and exploring features in $\ell \sim 200$.

Parameter	ΛCDM model	Features low-ℓ	Features first peak
$100\,\Omega_b h^2$	2.220 ± 0.028	2.220 ± 0.028	2.220 ± 0.029
$\Omega_c h^2$	0.1199 ± 0.0027	0.1203 ± 0.0028	0.1200 ± 0.0026
$100\,\theta$	1.0413 ± 0.0006	1.0413 ± 0.0006	1.0413 ± 0.0006
τ	0.090 ± 0.013	0.091 ± 0.014	0.089 ± 0.010
n_s	0.961 ± 0.007	0.959 ± 0.008	0.960 ± 0.007
$10^9 A_s$ $(k_0 = 0.05\ Mpc^{-1})$	2.20 ± 0.05	2.21 ± 0.06	2.22 ± 0.04
Age [Gyr]	13.82 ± 0.05	13.82 ± 0.05	13.82 ± 0.05
z_{re}	11.1 ± 1.1	11.2 ± 1.2	11.1 ± 0.9
H_0 [km s^{-1} Mpc^{-1}]	67.3 ± 1.2	67.1 ± 1.2	67.3 ± 1.2
$-2\log\mathcal{L}$	9803	9794	9793

Table 5.4. best-fit values for the step parameters using: in second column the WMAP+ACT+SPT data, in third column the WMAP+ACT+SPT+SDSS data, in fourth and fifth columns the Planck data. The name of the columns refer to the analysis reported in the tables 5.2 and 5.3.

	Inflationary potential with step			
Parameter	CMB	CMB+LRG	Planck low-ℓ	Planck first peak
ϕ_{step}	14.66	14.66	14.66	–
$\log c$	−2.69	−2.80	−2.85	–
$\log d$	−1.42	−1.51	−1.44	–
A_f	–	–	–	0.10
$\ln \eta_f/Mpc$	–	–	–	7.25
$\ln x_d$	–	–	–	4.47

Chapter 6

Conclusions

Modern cosmology offers several opportunities for investigating the properties and evolution of our universe. A valuable tool to impose constraints lies in examining the anisotropies of the cosmic microwave background radiation, the first picture available of the history of the universe. Another valuable source of information is the galaxy surveys and the large-scale maps of the universe.
In this thesis we have put new constraints on the inflation theory from the most up-to-date cosmological data. We initially reviewed the standard cosmological model and its theoretical predictions, and discussed the observable effects introduced by the inclusion of the inflationary theory. We proceeded to a comparison with the current state of the observations, in particular with data from the Wilkinson Microwave Anisotropy Probe (WMAP) satellite and others CMB data sets like Atacama Cosmology Telescope (ACT) and South Pole Telescope (SPT) experiment. Also, we considered a particular class of inflationary models, able to produce oscillation at the large scale of the cosmic microwave background anisotropy power spectrum, and compared these models with the data from CMB, in which we consider the first data release of Planck experiment, and Sloan Digital Sky Survey (SDSS) data.
In these conclusions we summarize the main results obtained in the work performed during my Ph.D and presented in this thesis.

In Chapter 4 we analysed the recently released ACT and SPT data in combination with the WMAP9-year data. We tested these data against two cosmological scenarios: (1) a scale-invariant, purely scalar "Harrison-Zel'dovich" (HZ) power spectrum with the addition of parameters motivated by inflationary cosmology, tilt n_s, nonzero tensor/scalar ratio r, and running of the spectral index n_s, and (2) the HZ power spectrum with a nonstandard effective neutrino number N_{eff} and/or neutrino mass m_ν. We find that both the extended ACT data (eACT) and the extended SPT data (eSPT) favor extensions to the simple HZ model to at least 95% confidence.

In the case of the inflation-motivated extensions to HZ, both eACT and eSPT favor a deviation from a scale-invariant power spectrum with "red" tilt, $n_s < 1$, and neither show any evidence for a nonzero tensor/scalar ratio. The eACT data are consistent with negligible running of the spectral index, as predicted by simple slow-roll inflation models. The eACT data are consistent at the 95% confidence level with simple chaotic inflation $V(\phi) = m^2\phi^2$, and with power-law inflation, $V(\phi) \propto \exp(\phi/\mu)$, as well as "small-field" models predicting negligible tensors and

$n_s < 1$.
The eSPT data, however, are inconsistent with a purely power-law power spectrum, favoring negative running of the spectral index $n_{run} = -0.029 \pm 0.011$ in the case with a prior of $r = 0$, and $n_{run} = -0.051 \pm 0.015$ in the case where $r \neq 0$ is allowed. While the eSPT data are not in disagreement with the most general possible single-field inflation models, they are in significant conflict with slow-roll models predicting $n_{run} \ll n_s$. The eACT data are consistent with such models.

In the case of extensions to HZ involving additional light degrees of freedom, eACT and eSPT again produce qualitatively different constraints. Both the eACT and eSPT data favor additional light degrees of freedom, with $N_{eff} = 3.88 \pm 0.28$ for eACT, and $N_{eff} = 4.26 \pm 0.26$ for eSPT (with a prior of $m_\nu = 0$). The eACT and eSPT data differ, however, with respect to nonzero neutrino masses. The eACT data are consistent at 95% with zero neutrino mass, with $\sum m_\nu = 0.24 \pm 0.15$ eV (with a prior of $N_{eff} \equiv 3.04$), and $\sum m_\nu < 0.46$ eV (with $N_{eff} \neq 3.04$). The eSPT data favor nonzero neutrino mass, with $\sum m_\nu = 0.39 \pm 0.14$ eV (with a prior of $N_{eff} \equiv 3.04$), and $\sum m_\nu = 0.96 \pm 0.53$ eV (with $N_{eff} \neq 3.04$).

In either scenario, HZ + inflation or HZ + neutrinos, considering the ACT and SPT data separately results in qualitatively different conclusions about extensions to a standard scale-invariant Λ+Cold Dark Matter concordance cosmology, a tension which is not evident when considering combined constraints from ACT and SPT.

In chapter 5 we have considered inflation models with a small-amplitude step-like feature in the inflaton potential. Features of these kind can be due for example to phase transitions occurring during the slow roll in multi-field inflationary models. In these models the primordial perturbation spectrum has the form of a power-law (as in the standard featureless case) with superimposed oscillations, localized in a finite range of scales that basically depends on the position of the step in the potential and whose presence can be tested through the analysis of CMB and large-scale structures data.

We have compared the theoretical predictions of a specific model, i.e., chaotic inflation, and of a more general phenomenological model [90][93][94]. We use different dataset and step by step we improve the constraints on the inflationary potential parameters. We start using data from the WMAP7-year and ACT, than update the data using the combination WMAP7-year + ACT + SPT data with the LRG-7 sample of the Sloan Digital Sky Survey. Finally, we analyse the model using the Planck data and considering two different methods. The first uses a numerical routine to accurately calculate the primordial density spectrum corresponding to a given inflaton potential. The second employs an approximate form of the power spectrum, reproducing the features caused by a step-like inflaton potential. For the latter analysis, we have also studied the impact of different prior ranges, corresponding to features in the low-ℓ and mid-ℓ ranges.
The analysis done performing the exact integration of the mode equations shows a minimum χ^2 value with $\Delta\chi^2 \simeq 9$ with respect to the featureless ΛCDM model, at the cost of three new parameters. This improvement is due to the presence of oscillations in the multipole range $10 < \ell < 60$.
These results can be matched using instead the analytical approach, choosing to

explore oscillations in the range $150 < \ell < 300$. The improvement in the goodness of fit is still $\Delta\chi^2 \simeq 9$, although it is caused by oscillations in a completely different range of scales.
The possibility of no oscillation at all is still, however, perfectly consistent with the data. In conclusion, although multifield inflationary models can definitely reproduce the two glitches in the large scale temperature spectrum, current data are not yet constraining enough to allow to discriminate between these models and the standard inflationary scenario. Future polarization data, as discussed in [93] will clearly further improve the constraints presented here, possibly confirming the presence of glitches in the region $20 < \ell < 60$.

Appendix A

Statistical Methods in Cosmology

In this appendix we will describe some of the statistical techniques commonly used in cosmology to analyse experimental data, and in particular the general problem of estimating parameters from data (for a complete study we refer to Ref.[105]). Any particular model, from which these parameters are taken, is only able to make statistical predictions about the properties of the universe. Therefore, we need to extract the largest amount of information from the data in order to better characterize the model we are testing.

Most data analysis problems are inverse problems. Typically the problems of interest are divided in three categories: *Hypothesis testing*, *Parameter estimation* and *Model selection*.

Inference is the method by which we translate observations into constraints on our theoretical models. The model is a representation of the physical processes that we believe are relevant in the observables we plan to observe. To be useful, the model must be sufficiently sophisticated to be able to explain the data, and simple enough that we can make predictions for observational data from it.

The goal of parameter estimation is to provide estimates of the parameters and their errors, or ideally the whole probability distribution of the parameters. The data which we obtain by the experiment may be subject only to experimental uncertainties, or they may also have a fundamental statistical uncertainty due to random nature of the underlying physical processes. In cosmology there exist both type of data. For example, the detailed pattern of the CMB is not believed to be predictable even in principle, being only a particular random realization of quantum processes occurring during inflation. Fortunately this type of uncertainty can be modeled and incorporated in addition to measurement one.

Regarding the model selection, several different models might be proposed as an explanations of the observational data. These models would represent alternative physical processes, and as such would correspond to different set of parameters that are to be varied in fitting the data.

A.1 Bayesian inference.

Within cosmology the most commonly used paradigm for statistical analysis is the Bayesian inference. Instead, the traditional practice of particle physicists assumes a *frequentist* approach, although even in this field there is an increasing interest in applying Bayesian methods.
The essence of Bayesian analysis is to assign probabilities to all quantities involved, and to treat them according to a series of rules, among which the Bayes' theorem is the most important. The aim of the procedure is to update our knowledge with new emerging data. An important implication of this way of thinking is that we have to quantify what we thought we knew before collecting the data: this is known as the *prior probability*. All the subsequent steps are algorithmic but the definition of the prior is not, and different researchers may have different views on what is appropriate.
The *posterior probability* is the probability of the parameter of the model to take certain values, after doing the experiment. It can be written as:

$$p(\theta|x), \tag{A.1}$$

where θ is the unknown model parameter and x the observed data. From this, one can calculate the expectation values of the parameters, and their errors.
Often, what may be easily calculable is the opposite, $p(x|\theta)$. For example, consider a model which is a Gaussian with mean μ and variance σ^2. The model has two parameters, $\theta = (\mu, \sigma)$, and the probability of a single variable x given the parameters is

$$p(x|\theta) = \frac{1}{\sqrt{2\pi}\sigma} \exp\left[-\frac{(x-\mu)^2}{2\sigma^2}\right], \tag{A.2}$$

but this is not what we want. However, we can relate this to $p(\theta|x)$ using the *Bayes' Theorem*:

$$p(\theta|x) = \frac{p(\theta, x)}{p(x)} = \frac{p(x|\theta)p(\theta)}{p(x)}, \tag{A.3}$$

where: $p(\theta|x)$ is the posterior probability for the parameters; $p(x|\theta)$ is called the *likelihood* and given its own symbol $\mathcal{L}(x;\theta)$; $p(\theta)$ is called the *prior*, and expresses what we know about the parameters prior to the experiment being done (this may be the result of previous experiments, or theory) and in the absence of any previous information the prior is often assumed to be a constant or "flat prior"; $p(x)$ is the *evidence*. For parameter estimation, the evidence is a normalization of the probabilities,

$$p(x) = \int d\theta p(x|\theta)p(\theta) \tag{A.4}$$

and the relative probabilities of the parameters do not depend on it, so it is often ignored. However, the evidence does play an important role in model selection, when more than one theoretical model is considered, and one wants to discriminate among models, whatever the parameters are.
Actually, all the probabilities above should be conditional probabilities, given any prior information I which we may have. I may be the result of previous experiments, or may be a theoretical prior, in the absence of any data. In such cases, it is common

to adopt the “principle of indifference" and assume that all values of the parameter are equally likely, and take $p(\theta)$ =constant in the range of interest. This is referred to as a flat prior. Thus for flat priors, we have simply

$$p(\theta|x) \propto \mathcal{L}(x;\theta) \tag{A.5}$$

Although we may have the full probability distribution for the parameters, often one simply uses the peak of the distribution as the estimate of the parameters. This is called a *maximum likelihood estimate*. If the priors are not flat, the peak in the posterior $p(\theta|x)$ is not necessarily the maximum likelihood estimate.
For multi-parameter models one is interested to extract from the multivariate posterior distribution the posterior of a subsample of parameters. The posterior probability is mapped onto a lower-dimensional subspace by the process of marginalisation,

$$p(\theta_1) = \int d\theta_2 ....d\theta_N \; p(\theta) \tag{A.6}$$

where $\theta(1)$ represents the parameters in the n-dimensional subspace.
The set of parameters most favored by the data can be figured out finding the set of parameters for which the posterior probability $p(\theta|x)$ has its maximum:

$$\theta_{BF} = |\max{}_\theta \; p(\theta|x)| \, . \tag{A.7}$$

This represents the most probable parameter values given the data and priors, and it is often referred to as the "best fit", although, strictly speaking, the term refers to those values of the parameters that maximize the likelihood and it is equivalent to take θ_{BF} only for uniform priors. On the other hand, one can estimate the best values for the parameters by calculating the posterior mean (also called "marginalized mean").

A.2 Monte Carlo Markov Chains.

If the dimensionality of the parameter space is very large, it becomes rapidly unfeasible to evaluate the likelihood on a grid basis, as the number of grid points grows exponentially with dimension. There are various ways to sample the likelihood surface more efficiently, concentrating the points more densely where the likelihood is high. A widely used solution in cosmology is the Monte Carlo Markov Chain methods.
Monte Carlo methods are algorithms based on random sampling, with the algorithm that is guided by some rules defined to give the desired outcome. An important sub-class of Monte Carlo methods are *Monte Carlo Markov Chain* (MCMC) methods, defined as those in which the next step in the sequence depends only upon the previous one. The sequence of steps is then known as a Markov Chain. Each step correspond to some particular value of the parameters, for which the likelihood is evaluated.
The Markov chain elements are constructed to correspond to random samples from the posterior parameter distribution of the parameters, i.e. each chain element represents the probability that those particular parameter values are the true ones. The simplest algorithm which achieves this is the *Metropolis-Hastings* algorithm. It works as follows:

1. Choose a starting point within the parameter space.

2. Propose a random jump. Any function can be used as the proposed probability distribution for the length and direction of the jump, as long as it satisfies the 'detailed balance' condition for which a jump back to the starting point is as probable as the jump away from it. This is most easily done using a symmetric proposal function, e.g. a multivariate Gaussian about the current point. Evaluate the likelihood at the new point, and hence the posterior by multiplying by the prior at that point.

3. If the probability at the new point is higher, accept the jump. If it is lower, we accept the jump with a probability given by the ratio of the posterior probabilities at the new and at the old point. If the jump is not accepted, stay at the same point, creating a duplicate in the chain.

4. Repeat from Step 2, until the probability distribution is well mapped out. This may be done for instance by comparing several chains run from different starting points, and/or by using convergence statistics among which the *Gelman-Rubin test* [106] is the most commonly used.

The chance of moving to a lower probability point let the algorithm explore accurately the shape of the posterior in the vicinity of the maximum.
The generic behavior of the algorithm is to start in a low likelihood region, and migrate towards the high likelihood regions. The first phase is called “burn in" and has a dependence on the starting point, so it has to be eliminated in the analysis phase of the chain. Once near the top, most possible jumps are in the region of lower probability, and the chain wanders around the maximum mapping its shape. The proposal function should be tuned to the scale of variation of the likelihood near its maximum. The usual choice is of a Gaussian, and its axes should ideally be aligned to the principal directions of the posterior (so as to be able to navigate quickly along parameter degeneracies). Therefore it is a common practice to make a short initial run to roughly map out the posterior distribution which is then used to optimize the proposal function for the actual computation.
It can be demonstrated that the chain should fairly sample the target distribution once it has converged to a stationary distribution.

A widely use tool for Monte Carlo Markov Chain analysis in cosmology is the software CosmoMC [107], that allows to sample several cosmological parameters spaces analysing basically any kind of cosmological data. The calculation of theoretical observables is done through the CAMB (Code for Anisotropies in the Microwave Background) [108] software. The code allows for different sampling algorithms, as the Metropolis-Hastings, and different convergence tests, such as the Gelman-Rubin convergence test.

A.3 Gelman-Rubin convergence.

The classic test of convergence of the chain is the Gelman-Rubin (1992) convergence criterion [106] , calculated by the program *getdist* in the CosmoMC package. This

criterion can be used when a number of chains m are running at the same time. The idea is that the quantities inferred from each chain, such as the sample mean and variance of the simulated draws, should be the same once the chains converged. Thus, Gelman and Rubin suggested to compare these inferences calculated within each chain to the inference made by mixing together the $m \times n$ draws from all the chains, where n is the number of draws in each chain.
After some running time, one can suppose that each of the m chains contains n sampled points in the parameter space. For each parameter θ, with mean value μ and variance equal to σ^2, it is possible to estimate the mean of the variances calculated within each chain j as:

$$W = \frac{1}{m(n-1)} = \sum_{j=1}^{m} \sum_{t=1} n(\theta_{jt} - \bar{\theta}_j)^2, \tag{A.8}$$

where $\bar{\theta}_j$ is the average value of the parameter θ in j-chain. On the other hand, one can also estimate the variance between chains as:

$$\frac{B}{n} = \frac{1}{m-1} \sum_{j=1}^{m} (\bar{\theta}_j - \bar{\theta})^2, \tag{A.9}$$

where $\bar{\theta}$ is the mean of the averages $\bar{\theta}_j$ within each chain. This last quantity is expected to approach zero once the chain reaches the convergence. By using these quantities it is possible to estimate the variance on the parameter θ. This can be found as the weighted mean of the two, and satisfies the following expression:

$$\hat{\sigma}_+^2 = \frac{n-1}{n} W + \frac{B}{n}. \tag{A.10}$$

The estimate variance $\hat{\sigma}_+^2$ is overestimated when the chains have still not reached the convergence. The reason is due to the fact that the chains begin from appropriately dispersed starting points. If they have not all converged to the common favored region of the parameter space, the points of each chain are still around the distant starting points, so the averages $\bar{\theta}_j$ for every chain will be very different from each other. Consequently, this lead to an overestimation of B/n. If the starting points are too close, the variance is underestimated: in this case the convergence diagnostics fails. In order to take into account the sampling variability of the estimator μ, the estimated pooled posterior variance is then equal to:

$$\hat{V} = \hat{\sigma}_+^2 \frac{B}{(mn)}. \tag{A.11}$$

The convergence parameter is defined by using this last expression and by comparing with W, and it takes the following form:

$$R = \frac{\hat{V}}{W} = \frac{n-1}{n} + \frac{\frac{B}{n} + \frac{B}{nm}}{W} \tag{A.12}$$

R is expected to be 1 for a complete convergence of the chains. A run can be considered to have an acceptable level of convergence when the covergence parameter R satisfies this condition $1 - R \ll 0.03$, and this value is what we impose in all our analysis in this thesis.

A.4 Model Selection.

Estimation of cosmological parameters, as described in the previous section, assumes that we have a particular model in mind to explain the data that we assume to be the true one. More commonly, however, there are competing models available to describe the data. Each model corresponds to a different choice of variable parameters, along with a prior distribution for those parameters. An important implication of Bayesian analysis is that there is a clear distinction between a model where a quantity is fixed to a definite value, versus a more general model where that parameter is allowed to vary but happens to take on that special value. Assume we have two competing models by M and M' and furthermore that M' is a simpler model, which has fewer ($n' < n$) parameters in it. Moreover, assume that it is nested in Model M', i.e. the n'parameters of model M' are common to M, which has $p \equiv n - n'$ extra parameters in it. These parameters are fixed to fiducial values in M'.
We denote by x the data vector, and by θ and θ' the parameter vectors (of length n and n'). The posterior probability of each model comes from Bayes' theorem:

$$p(M|x) = \frac{p(x|M)p(M)}{p(x)} \tag{A.13}$$

and similarly for M'. The marginalisation of $p(x|M)$ is the *evidence* and it is:

$$p(M|x) = \int d\theta p(x|\theta M)p(\theta|M) \tag{A.14}$$

which is a multidimensional integration. The ratio of the posterior probabilities of the two models is

$$\frac{p(M'|x)}{p(M|x)} = \frac{p(M')}{p(M)} \frac{\int d\theta' p(x|\theta' M')p(\theta'|M')}{\int d\theta p(x|\theta M)p(\theta|M)} \tag{A.15}$$

If we do not have preferences about any model $p(M') = p(M)$, this ratio simplifies to the ratio of evidences, called the *Bayes Factor*,

$$B = \frac{\int d\theta' p(x|\theta' M')p(\theta'|M')}{\int d\theta p(x|\theta M)p(\theta|M)} \tag{A.16}$$

The complicated model M will (if M' is nested) inevitably lead to a higher likelihood, but the evidence will favor the simpler model if the fit is nearly as good, through the smaller prior volume. We assume uniform (and hence separable) priors in each parameter, we can write $p(\theta|M) = (\Delta\theta_1 \ ... \ \Delta\theta_n)^{-1}$ and

$$B = \frac{\int d\theta' p(x|\theta',\ M')}{\int d\theta p(x|\theta,\ M)} \frac{(\Delta\theta_1 \ ... \ \Delta\theta_n)}{(\Delta\theta'_1 \ ... \ \Delta\theta'_{n'})} \tag{A.17}$$

So from this equation it is clear that to get the evidence we need to integrate the likelihood throughout the parameter space. In principle this is a standard mathematical problem, but it is made difficult because the integrand is likely to be extremely highly peaked and we do not know in advance where is the peak in parameter space. Further, the parameter space is multi-dimensional the individual likelihood evaluations are computationally expensive. Successful Bayesian model

selection algorithms are therefore dependent on efficient algorithms for tackling this type of integral. Model probabilities are meaningful in themselves and do not require further interpretation, but it is useful to have a scale by which to judge differences in evidence. The usual scale employed is the Jeffreys scale [109] which, given a difference $\Delta \ln E$ between the evidences E of two models, reads:

- $\Delta \ln E < 1$ Not worth more than a bare mention.
- $1 < \Delta \ln E < 2.5$ Significant.
- $2.5 < \Delta \ln E < 5$ Strong to very strong.
- $5 < \Delta \ln E$ Decisive.

In practice the divisions at 2.5 (corresponding to posterior odds of about $13 : 1$) and 5 (corresponding to posterior odds of about 150:1) are the most useful.

Appendix B

Refereed Publications

- "Features in the primordial spectrum: new constraints from WMAP7+ACT data and prospects for Planck";
  M. Benetti, M. Lattanzi, E. Calabrese, A. Melchiorri;
  Physical Review D 84, id. 063509 (2011).

- "Featuring the primordial power spectrum: new constraints on interrupted slow-roll from CMB and LRG data";
  M. Benetti, S. Pandolfi, M. Lattanzi, M. Martinelli, A. Melchiorri;
  Physical Review D 87, id. 023519 (2013).

- "Cosmological data and indications for new physics";
  M. Benetti, M. Gerbino, W. H. Kinney, E. W. Kolb, M. Lattanzi, A. Melchiorri, L. Pagano, A. Riotto;
  JCAP *Journal of Cosmology and Astroparticle Physics* 10, 030 (2013).

- "Updating constraints by Planck data on inflationary features model";
  M. Benetti;
  Physical Review D 88, id. 087302 (2013).

Conference proceedings

- "New constraints on features in the primordial spectrum"; **M. Benetti**, as a proceedings for the "3rd Galileo - Xu Guangqi meeting" held in Beijing, China.

- "Features in the primordial spectrum - New constraints"; **M. Benetti**, as a proceedings for the 'New Horizons for Observational Cosmology " held in Varenna, Italy.

PHYSICAL REVIEW D **84,** 063509 (2011)

Features in the primordial spectrum: New constraints from WMAP7 and ACT data and prospects for the Planck mission

Micol Benetti,[1,2] Massimiliano Lattanzi,[1,3] Erminia Calabrese,[2] and Alessandro Melchiorri[2]

[1]*Physics Department and ICRA, Università di Roma "La Sapienza", Ple. Aldo Moro 2, 00185, Rome, Italy*
[2]*Physics Department and INFN, Università di Roma "La Sapienza", Ple. Aldo Moro 2, 00185, Rome, Italy*
[3]*Oxford Astrophysics, Denys Wilkinson Building, Keble Road, OX1 3RH Oxford, United Kingdom*
(Received 28 July 2011; published 6 September 2011)

We update the constraints on possible features in the primordial inflationary density perturbation spectrum by using the latest data from the WMAP7 and ACT (Atacama Cosmology Telescope) cosmic microwave background experiments. The inclusion of new data significantly improves the constraints with respect to older work, especially to smaller angular scales. While we found no clear statistical evidence in the data for extensions to the simplest, featureless, inflationary model, models with a step provide a significantly better fit than standard featureless power-law spectra. We show that the possibility of a step in the inflationary potential like the one preferred by current data will soon be tested by the forthcoming temperature and polarization data from the Planck satellite mission.

DOI: 10.1103/PhysRevD.84.063509 PACS numbers: 98.80.Cq, 98.70.Vc, 98.80.Es

I. INTRODUCTION

Current cosmological observations can be explained in terms of the so-called concordance ΛCDM model in which the primordial fluctuations are created during an early period of inflationary expansion of the Universe. In particular, the spectrum of anisotropies of the cosmic microwave background (CMB) is in excellent agreement with the inflationary prediction of adiabatic primordial perturbations with a nearly scale-invariant power spectrum [1–5]. In its simplest implementation, inflation is driven by the potential energy of a single scalar field, the inflaton, slowly rolling down towards a minimum of its potential; curvature perturbations, that constitute the primordial seeds for structure formation, are originated during the slow roll from quantum fluctuations in the inflaton itself. The scale invariance of the spectrum is directly related to the flatness and smoothness of the inflaton potential that are necessary to ensure that the slow-roll phase lasts long enough to solve the paradoxes of the big bang model.

However, in more general inflationary models, there is the possibility that slow roll is briefly violated. This naturally happens in theories with many interacting scalar fields, as it is the case, for example, in a class of multifield, supergravity-inspired models [6,7], where supersymmetry-breaking phase transitions occur during inflation. These phase transitions correspond to sudden changes in the inflaton effective mass and can be modeled as steps in the inflationary potential. If the transition is very strong, it can stop the inflationary phase as it happens in the usual hybrid inflation scenario; on the contrary, inflation can continue but the inflationary perturbations and thus the shape of the primordial power spectrum are affected. Departures from the standard power-law behavior can also be caused by changes in the initial conditions due to trans-Planckian physics [8–10] or to unusual initial field dynamics [11,12]

A violation of slow roll will possibly lead to detectable effects on the cosmological observables, or at least to the opportunity to constrain these models by the absence of such effects. In particular, steplike features in the primordial power spectrum have been shown [13,14] to lead to characteristic localized oscillations in the power spectrum of the primordial curvature perturbation. Such oscillations have been considered as a possible explanation to the "glitches" observed by the Wilkinson Microwave Anisotropy Probe (WMAP) in the temperature anisotropy spectrum of the CMB, although the WMAP team notes that these could be caused simply by having neglected beam asymmetry, the gravitational lensing of the CMB, non-Gaussianity in the CMB maps and other "small" ($\lesssim 1\%$) contributions to the covariance matrix. In the following we will assume that these features have indeed a cosmological origin as in the class of extended models described above, and we will use CMB data to constrain the phenomenological parameters describing the step in the inflaton potential.

Constraints on oscillation in the primordial perturbation spectrum, as well as best-fit values for the step parameters, have been previously derived in Refs. [15–19]. Here we improve on the previous analyses in several aspects. First, we use more recent CMB data, in particular, the WMAP 7-year and the Atacama Cosmology Telescope (ACT) data. This allows us to derive tighter constraints on the parameters; in particular, we get an upper limit on the step height (related to the amplitude of oscillations) that is independent on the position of the step itself in the prior range considered. We also find a clear correlation between the position and the height of the step. Second, we generate mock data corresponding to the model providing the best fit to the WMAP data, and use these data to assess the ability of the Planck satellite to detect the presence of oscillations in the primordial spectrum.

The paper is organized as follows. In Sec. II we describe the evolution of perturbations in interrupted slow roll and the phenomenological model used to describe a step in the inflationary potential. In Sec. III we discuss the analysis method adopted. In Sec. IV we present the results and in Sec. V we derive our conclusions.

II. INFLATIONARY PERTURBATIONS IN MODELS WITH INTERRUPTED SLOW ROLL

Steps in the potential can naturally appear in ''multiple inflation'' models, where the inflaton field ϕ is gravitationally coupled to a ''flat direction'' field ρ (belonging to the visible sector of the theory), i.e. a direction in field space along which the potential vanishes. The ρ-field can undergo a symmetry-breaking phase transition and acquire a vacuum expectation value $\langle\rho\rangle$. The gravitational coupling between the ρ and the inflaton field will cause the effective mass-squared of the latter to change; for example, in the case in which the coupling between the two fields is described by a term $\lambda\phi^2\rho^2/2$ in the Lagrangian, the inflaton mass-squared after the phase transition will become $m^2_{\rm eff}(\phi) = m_0^2 + \lambda\langle\rho^2\rangle$. It is worth noticing that the presence of flat field directions also opens the possibility to have inflation with a curved trajectory in field space; however, in the following, we will disregard this scenario.

The exact behavior of the inflaton mass will depend on the dynamics of the phase transition; however, this is so fast that the ρ-field reaches the minimum of its potential very rapidly. It is then very reasonable to model the inflaton mass in a phenomenological way as

$$m^2_{\rm eff}(\phi) = m^2\left[1 + c\tanh\left(\frac{\phi - b}{d}\right)\right]. \tag{1}$$

Here, the parameter b is of the order of the critical value of the inflaton field for which the phase transition occurs, c is the height of the step (related to the change in the inflaton mass), and d is its width (related to the duration of the phase transition). In the following we shall work in reduced Planck units ($c = \hbar = 8\pi G = 1$), so that all dimensional quantities like m, b, and d should be multiplied by the reduced Planck mass $M_p = 2.435 \times 10^{18}$ GeV in order to get their values in physical units.

Let us now briefly recall how to compute the spectrum of primordial perturbations, as discussed in detail by Adams *et al.* [13]. For the moment, we do not specify the exact form of the inflaton potential $V(\phi)$; we will return to this in the next section. In the case of scalar perturbations, it is useful to define the gauge-invariant quantity [20] $u \equiv -z\mathcal{R}$, where $z = a\dot{\phi}/H$, a is the scale factor, H is the Hubble parameter, $\mathcal{R}$ is the curvature perturbation, and dots denote derivatives with respect to the cosmological time t. The Fourier components of u evolve according to

$$u_k'' + \left(k^2 - \frac{z''}{z}\right)u_k = 0, \tag{2}$$

where k is the wave number of the mode, and primes denote derivatives with respect to conformal time η. When $k^2 \gg z''/z$, the solution to the above equation tends to the free-field solution $u_k = e^{-ik\eta}/\sqrt{2k}$.

In the slow-roll approximation, $z''/z \simeq 2a^2H^2$. However, in the models considered here this expectation can be grossly violated near the phase transition, and the time evolution of z has to be derived by solving the equations for the inflaton field and for the Hubble parameter:

$$\ddot{\phi} + 3H\dot{\phi} + \frac{dV}{d\phi} = 0, \tag{3}$$

$$3H^2 = \frac{\dot{\phi}^2}{2} + V(\phi). \tag{4}$$

Once the form of the potential is given, these can be integrated to get H and ϕ, and thus z, as a function of time. At this point, it is possible to integrate Eq. (2) to get $u_k(\eta)$ for free-field initial conditions when $k^2 \gg z''/z$. Finally, knowing the solution for the mode k, the power spectrum of the curvature perturbation $P_{\mathcal{R}}$ can be computed by means of

$$P_{\mathcal{R}} = \frac{k^3}{2\pi}\left|\frac{u_k}{z}\right|^2 \tag{5}$$

evaluated when the mode crosses the horizon. The resulting spectrum for models with a step in the potential is essentially a power law with superimposed oscillations; thus, asymptotically, the spectrum will recover the familiar k^{n_s-1} form typical of slow-roll inflationary models.

In practice, however, one has to relate the horizon size at the step with a physical wave number. For a general wave number $k_\star$ one can write $k_\star \equiv a_\star H_\star = a_{\rm end}e^{-N_\star}H_\star$, where $a_\star$ and $H_\star$ are the scale factor and the Hubble parameter at the time the mode crossed the horizon, $a_{\rm end}$ is the scale factor at the end of inflation, and $N_\star$ is the number of e-fold taking place after the mode left the horizon. We choose $N_\star = 50$ for the pivot wave number $k_\star = k_0 = 0.0025$ Mpc^{-1}. A different choice would correspond to a translation in the position of the step in ϕ and would thus be highly degenerate with b. For this reason we do not treat $N_\star$ as a free parameter, consistent with what has been done in previous studies [16,17].

III. ANALYSIS METHOD

We compare the theoretical predictions of a class of inflationary models with a step in the inflaton potential with observational data. We use a modified version of the CAMB code that solves Eqs. (2)–(4) numerically using a Bulirsch-Stoer algorithm in order to compute the initial perturbation spectrum (5) and, from that, the CMB anisotropy spectrum for given values of the relevant parameters describing the model. CAMB is then interfaced with a modified version of the Markov chain Monte Carlo package COSMOMC [21], that we use to find the best-fit value of

the parameters, to reconstruct their posterior probability density function, and to infer constraints on the parameter themselves.

Models. We consider a chaotic inflation potential of the form $V(\phi) = m_{\rm eff}^2(\phi)\phi^2/2$. Using Eq. (1), this corresponds to a potential

$$V(\phi) = \frac{1}{2}m^2\phi^2\left[1 + c\tanh\left(\frac{\phi - b}{d}\right)\right]. \qquad (6)$$

In Fig. 1 we show the shape of this potential for $m = 7.5 \times 10^{-6}$ and different values of the step parameters (close to the best-fit values), compared to a smooth $m^2\phi^2/2$ potential ($c = 0$).

The potential (6) uniquely defines the spectrum of perturbations $\mathcal{P}_\mathcal{R}$. The parameters that define the primordial spectrum and the initial conditions for the evolution of cosmological perturbations are then the inflaton mass m and the step parameters b, c, and d. The inflaton mass sets the overall scale for the potential and consequently for the amplitude of the perturbations; it can then be traded, in the Monte Carlo analysis, for the more familiar parameter A_s, i.e., the amplitude of the primordial spectrum at the pivot wave number $k_0 = 0.0025$ Mpc^{-1}. On the other hand, as already noted above, a step in the potential produces a perturbation spectrum with oscillations superimposed over a smooth power law. In the case of the potential (6), the underlying power law has a fixed spectral index $n_s = 0.96$. In Fig. 2 we show the primordal spectrum for different values of the step parameters.

The results obtained in the case of a specific potential will be, by definition, model-dependent. However, as

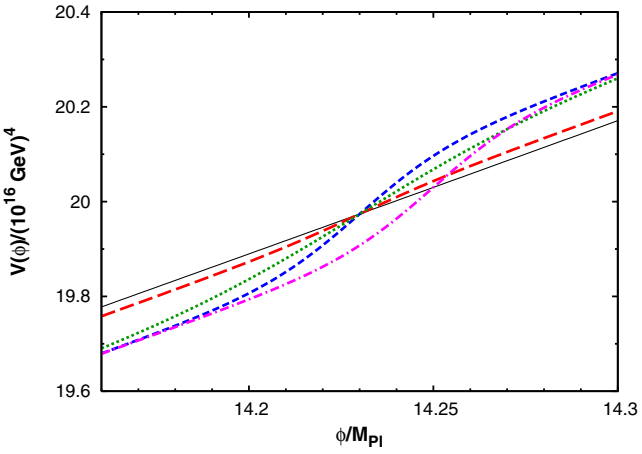

FIG. 1 (color online). Inflationary potential (6) for $m = 7.5 \times 10^{-6}$. The solid thin black line corresponds to a smooth ($c = 0$) chaotic potential $m^2\phi^2/2$. The long dashed red curve has $b = 14.23$, $c = 0.001$, and $d = 0.025$ and roughly corresponds to the spectrum giving the best fit to the WMAP7 data (see Sec. IV below). The other curves correspond to $b = 14.23$, $c = 0.005$, $d = 0.025$ (blue short dashed line), $b = 14.23$, $c = 0.005$, $d = 0.05$ (green dotted line), and $b = 14.25$, $c = 0.005$, $d = 0.025$ (magenta dotted dashed line).

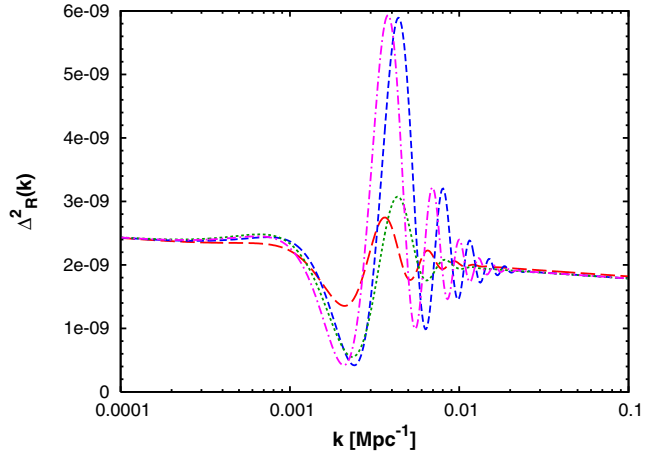

FIG. 2 (color online). Primordial power spectrum for an inflationary potential of the form (6). The values of the step parameters are the same as in Fig. 1, namely, $b = 14.23$, $c = 0.001$, $d = 0.025$ (red long dashed line), $b = 14.23$, $c = 0.005$, $d = 0.025$ (blue short dashed line), $b = 14.23$, $c = 0.005$, $d = 0.05$ (green dotted line), and $b = 14.25$, $c = 0.005$, $d = 0.025$ (magenta dotted-dashed line).

argued in Ref. [17], the issue of model dependence can be alleviated in a phenomenological way by restoring the spectral index as a free parameter, i.e., by defining the "generalized" spectrum $\mathcal{P}_\mathcal{R}^{\rm gen}$ as

$$\mathcal{P}_\mathcal{R}^{\rm gen}(k) = \mathcal{P}_\mathcal{R}^{\rm ch}(k) \times \left(\frac{k}{k_0}\right)^{n_s - 0.96}, \qquad (7)$$

where $\mathcal{P}_\mathcal{R}^{\rm ch}(k)$ is the spectrum induced by the chaotic potential (6). Since the latter has an overall tilt of 0.96, n_s will describe the overall tilt of the generalized spectrum.

Summarizing, we consider two classes of models. Models belonging to the first class (referred to as class A) corresponding to the potential (6), are described by eight parameters: the physical baryon and cold dark matter densities $\omega_b = \Omega_b h^2$ and $\omega_c = \Omega_c h^2$, the ratio θ between the sound horizon and the angular diameter distance at decoupling, the optical depth to reionization τ, the parameters b, c, and d of the step-inflation model, and the overall normalization of the primordial power spectrum $\mathcal{A}_s$ (equivalent to specifying m^2 as discussed above). Models in the second class, referred to as class B, correspond to the generalized step model (7) and are described by the effective tilt n_s in addition to the eight parameters of the first class. In both cases, we consider purely adiabatic initial conditions, impose flatness, and neglect neutrino masses. We limit our analysis to scalar perturbations.

Priors. Apart from the hard-coded priors of COSMOMC on H_0 (40 km s^{-1} Mpc^{-1} $< H_0 <$ 100 km s^{-1} Mpc^{-1}) and the age of the Universe (10 Gyr $< t_0 <$ 20 Gyr), we impose flat priors on ω_b, ω_c, θ, τ and, when considered, n_s and a logarithmic prior on $\mathcal{A}_s$. As we shall see, for these parameters the width of the posterior is much smaller than

the prior range, so that the latter is not really relevant. For the step parameters, the situation is complicated by the fact that the likelihood (and the posterior) does not go to zero in certain directions of the subspace. This happens, in particular, for very small values of c, for which the spectrum becomes indistinguishable from a power law, and for values of b either too large or too small so that the features in the spectrum are moved outside the range of observable scales. Then we choose for b a flat prior $13 \leq b \leq 15$, that roughly encompasses said range. In the case of c and d, since we do not have any *a priori* information on these parameters, not even on their order of magnitude, we find it convenient to consider a logarithmic prior on both of them. Hence, we take (in the following, log$x$ denotes the base 10 logarithm) $-6 \leq \log c \leq -1$ and $-2.5 \leq \log d \leq -0.5$. Additionally, since the combination c/d^2 is better constrained by the data than d alone, we also impose *a priori* $-5 \leq \log(c/d^2) \leq 3$. Finally, we recall that, since the posteriors for b, log$c$, and log$d$ do not necessarily vanish at the edge of the prior range, all integrals of the probability density function depend on the extremes of integration and are thus somewhat ill defined. Care should then be taken when quoting confidence limits in the b, log$c$, and log$d$ subspaces.

Data sets. We perform the statistical analysis for each of the models by comparing the theoretical predictions to two different data sets. The first includes the WMAP 7-year temperature and polarization anisotropy data (WMAP7). The likelihood is computed using the the WMAP likelihood code publicly available at the LAMBDA Web site [22]. We marginalize over the amplitude of the Sunyaev-Zel'dovich signal. The second data set includes the WMAP7 data with the addition of the small-scale CMB temperature anisotropy data from the ACT experiment. For the ACT data set we also consider two extra parameters accounting for the Poisson and clustering point sources foregrounds components. The ACT data set is considered up to $\ell_{\rm max} = 2500$.

Other than deriving the limits on the models from existing data, we also assess the ability of future experiments, in particular, of the Planck satellite, to improve these constraints. In order to do this, we simulate "mock" data corresponding to the step model that yields the best fit to the WMAP 7 and then perform a statistical analysis on these data as if they were real. The forecast method we use is identical to the one presented in [23] and we refer to this paper for further details and references. The synthetic data set is generated by considering for each C_ℓ a noise spectrum given by

$$N_\ell = w^{-1} \exp(\ell(\ell+1) 8 \ln 2/\theta_b^2), \tag{8}$$

where θ_b is the full width at half maximum (FWHM) of the beam assuming a Gaussian profile and where w^{-1} is the experimental power noise related to the detectors sensitivity σ by $w^{-1} = (\theta_b \sigma)^2$. The experimental parameters are reported in Table I.

TABLE I. Planck [24] experimental specifications. Channel frequency is given in GHz, FWHM in arcminutes and noise per pixel for the Stokes I ($\Delta T/T$), Q and U parameters ($\Delta P/T$) is in [10^6 μK/K], where $T = T_{\rm CMB} = 2.725$ K. In the analysis, we assume that beam uncertainties and foreground uncertainties are smaller than the statistical errors.

Experiment	Channel	FWHM	$\Delta T/T$	$\Delta P/T$
Planck	70	$14'$	4.7	6.7
$f_{\rm sky} = 0.85$	100	$10'$	2.5	4.0
	143	$7.1'$	2.2	4.2

Together with the primary anisotropy signal we also take into account information from CMB weak lensing, considering the power spectrum of the deflection field C_ℓ^{dd} and its cross correlation with temperature maps C_ℓ^{Td}.

Analysis. We derive our constraints from parallel chains generated using the Metropolis-Hastings algorithm. We use the Gelman and Rubin R parameter to evaluate the convergence of the chains, demanding that $R - 1 < 0.03$. The one- and two-dimensional posteriors are derived by marginalizing over the other parameters.

IV. RESULTS AND DISCUSSION

We first consider the WMAP7 and WMAP7 + ACT data sets. We find that the ΛCDM fit to both data sets can be improved by the inclusion of a step in the inflationary potential, in both cases when the scalar spectral index is being fixed to $n_s = 0.96$ (model A), and when it is being treated as a free parameter (model B). The best-fit values for the step parameters are reported in Table II. We also show the full likelihood for b in Fig. 3. It can be seen that in all cases the maximum in the likelihood occurs for $b \simeq 14.2$; as we show below, this is due to oscillations placed in correspondence to the WMAP glitches at $\ell \sim 20$ and $\ell \sim 40$ and thus able to improve, for suitable values of the other parameters, the goodness-of-fit with respect to the vanilla ΛCDM model. We found that in the case of the WMAP7 analysis the best-fit vanilla Λ-CDM model is at about $\Delta\chi^2_{\rm eff} \sim 6$ from the global best fit with features.

TABLE II. Best-fit values for the parameters of the primordial spectrum.

Parameter	Model A WMAP7	Model A WMAP7 + ACT	Model B WMAP7	Model B W7 + ACT
b	14.23	14.25	14.24	14.25
log$c$	−3.11	−2.71	−2.97	−2.67
log$d$	−1.58	−1.60	−1.65	−1.45
n_s	−	−	0.953	0.959
$\ln[10^{10}A_s]$	3.08	3.06	3.07	3.08
χ^2	7469.4	7489.6	7467.9	7491.4

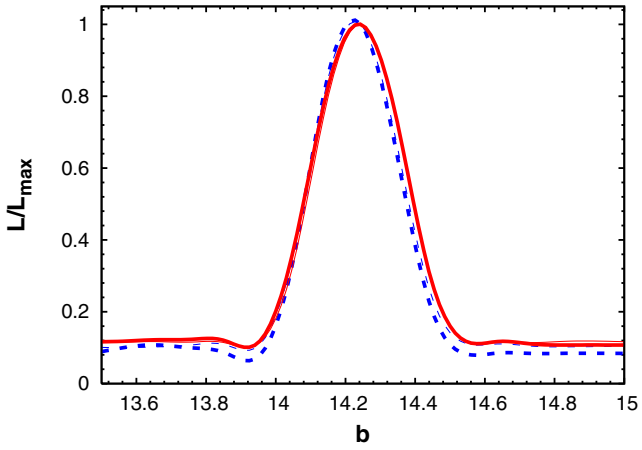

FIG. 3 (color online). Model likelihood as a function of b for model A (thin curves) and B (thick curves) using WMAP7 data (dashed curves) and the WMAP7 + ACT data set (solid curves).

As far as Bayesian statistics is concerned, the actual probability density distribution for a parameter is not given by the likelihood (the probability of the data given the parameters) but instead by the posterior (the probability of the parameters given the data). In Fig. 4 we show the one-dimensional posterior distributions for the step parameters b, log$c$, and log$d$. It can be noted that the posterior for b has a peculiar shape, presenting a peak for $b \simeq 14.2$ and a fairly wide dip for $b \lesssim 14$. The peak traces the peak in the likelihood discussed above. The decrease for $b < 14$ is instead due to the fact that, lowering b, the oscillations are moved to larger multipoles where they tend to spoil the ΛCDM fit unless c is set to a very small value.

This is clearly illustrated in Fig. 5, where we compare the WMAP7 data with three realizations of the CMB spectrum: the ΛCDM best fit to the WMAP data, the generalized step model best fit to the same data (corresponding to the third column of Table II), and a generalized step model with the same parameters as the best fit, with the exception of b that is set to $b = 13.9$. It is clear, especially from the second panel, that for $b = 14.2$ the oscillations improve the fit in the region $20 \lesssim \ell \lesssim 50$. On the other hand, when $b = 13.9$ the height of the first peak is diminished so that the predicted spectrum is completely at variance with the data. The posterior does not drop to zero because a fair amount of parameter space still exists, i.e.,

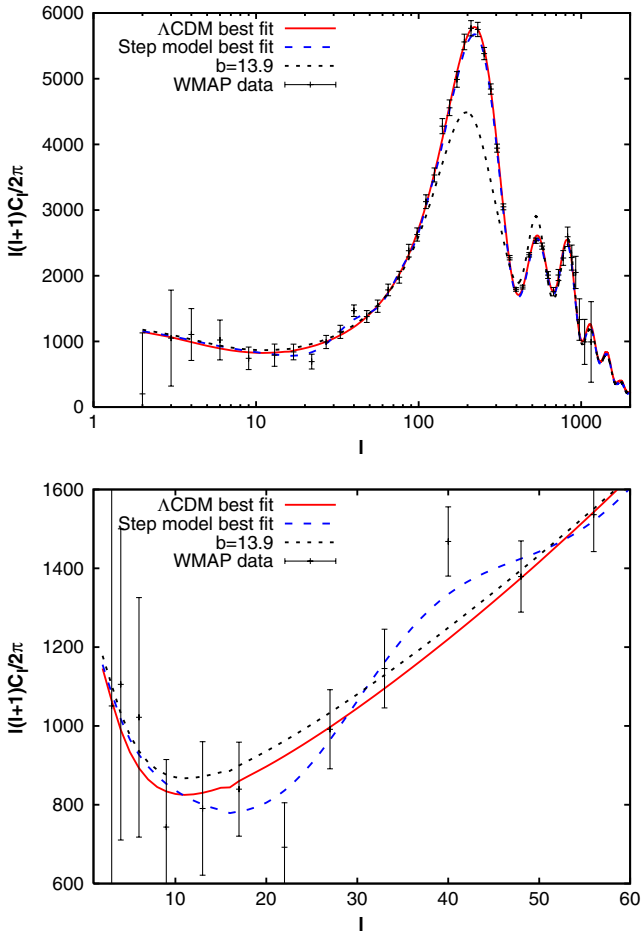

FIG. 5 (color online). (Top) CMB anisotropy spectrum for the ΛCDM (red solid line) and generalized step model (blue long dashed line) best fits, and for a step model with $b = 13.9$ (black short dashed line), compared with the WMAP7 data. (Bottom) Zoom of the region $\ell \leq 60$, showing the improved fit of the step model.

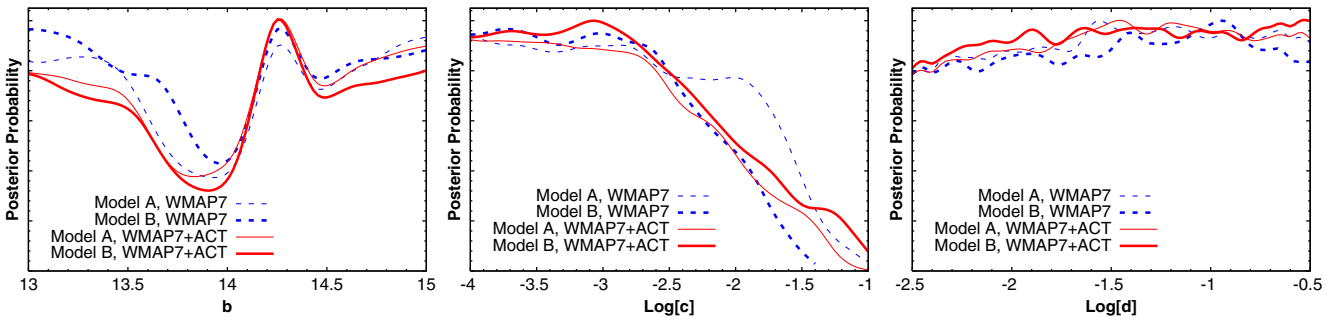

FIG. 4 (color online). One-dimensional posterior probability density for b (left), log$c$ (middle), and log$d$ (right) for model A (thin curves) and B (thick curves) using WMAP7 data (dashed curves) and the WMAP7 + ACT data set (solid curves).

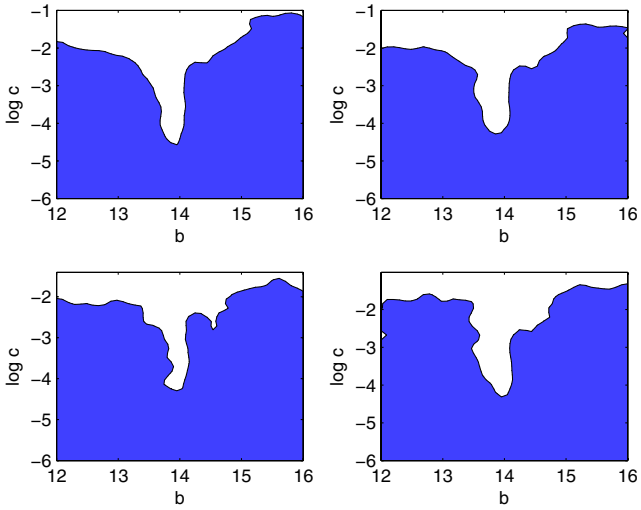

FIG. 6 (color online). 95% two-dimensional confidence region in the (b–log$c$) plane. The four panels correspond to, from left to right and from top to bottom: class A, WMAP7 + ACT; class B, WMAP7 + ACT; class A, WMAP7; class B, WMAP7.

models with low c, than can fit the data even with the oscillations placed in the "wrong" place. The posterior going to a constant value at the edges of the prior range is instead related to the oscillations being moved out of the observable scales. The inclusion of the ACT data in addition to WMAP7 helps in constraining small values of b, i.e., oscillations at small scales (large ℓ's).

The shape of the log$c$ posterior is typical of a quantity parametrizing the amplitude of a nonstandard effect: it is constant for small values of the parameter (when the step model becomes indistinguishable from standard ΛCDM), and then rapidly vanishes above a critical value. It can be seen that the probability density becomes half of its asymptotic value at $c = 0$ for $c \geq 10^{-2}$. Finally, the posterior for log$c$ clearly shows that this parameter is largely unconstrained by data.

We do not quote one-dimensional confidence limits on the parameters because, as noted in Sec. III, the posteriors do not vanish at the edge of the prior range and in this case the confidence limits depend on the integration range chosen. However, for illustrative purposes, in Fig. 6 we show the two-dimensional 95% confidence regions, computed assuming that the posterior vanishes outside the prior range, in the (b–log$c$) plane. It is clear from the plots that there is a region below $b = 14$ where the data are more sensitive to the value of c; this is related as noted above to the oscillations being placed in the region where the data are more accurate and favor a smooth spectrum over one with oscillations.

TABLE III. Parameter constraints from Planck.

Parameter	Model A	Model B
b	14.200 ± 0.010	14.200 ± 0.011
log$c$	-3.00 ± 0.32	-3.00 ± 0.34
log$d$	-1.66 ± 0.22	-1.64 ± 0.23
n_s	0.96 (fixed)	0.957 ± 0.007
$\ln[10^{10} A_s]$	3.073 ± 0.016	3.074 ± 0.016

The results presented here are fully compatible with the analysis made by [25] where the WMAP5 data set was considered. The apparently different value for the best-fit b parameter found in that paper is due to the different choice of the pivot scale ($k_0 = 0.05$ Mpc^{-1} instead of $k_0 = 0.0025$ Mpc^{-1} as assumed in our analysis). We have checked that performing the analysis on the WMAP7 data set with the assumption of $k_0 = 0.05$ Mpc^{-1} results in a best-fit value of $b \sim 14.7$ in agreement with the results of [25].

Finally, we show our results on the sensitivity of Planck to the step parameters. We have assumed as a fiducial model a generalized step model with $b = 14.2$, log$c = -2.97$, log$d = 1.65$, $n_s = 0.953$, $A_s = 2.16 \times 10^{-9}$ (basically corresponding to the model B best fit to the WMAP7 data, i.e., the third column of Table II). The one-dimensional posteriors for b, log$c$, and log$d$ are shown in Fig. 7, while in Table III we report the mean values for the primordial spectrum parameters together with their 2σ error. As we can see, the prior range dependence goes away with Planck data and we can quote marginalized credible intervals. We also show the two-dimensional posteriors for the step parameters in Fig. 8. It is evident that the Planck

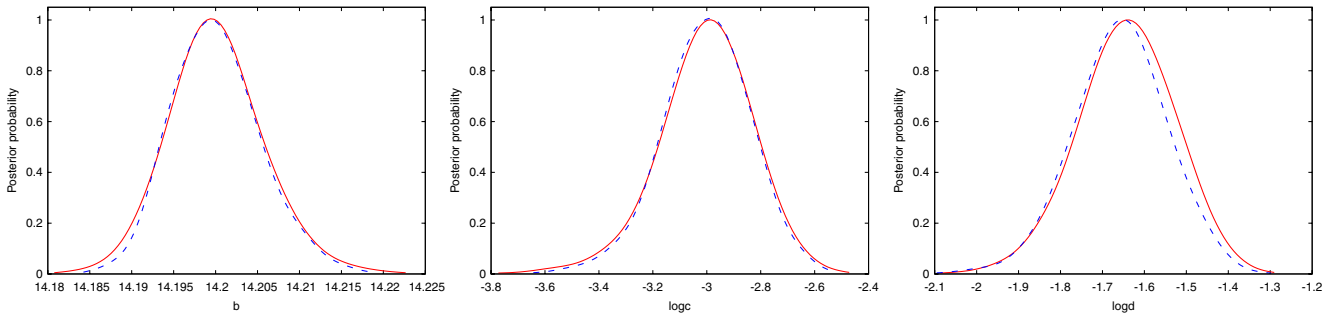

FIG. 7 (color online). One-dimensional posterior probability density for b (left), log$c$ (middle), and log$d$ (right) derived from the mock Planck data, for models of class A (dashed curves) and B (solid curves).

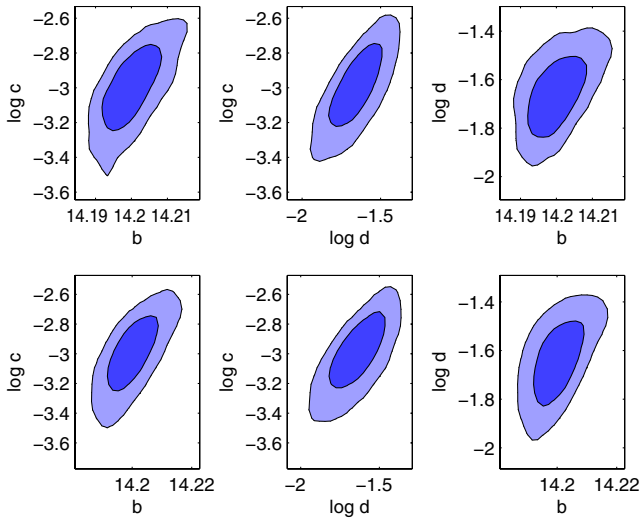

FIG. 8 (color online). Two-dimensional posteriors in the ($b-\log c$) (left), ($\log d-\log c$) (middle), and ($b-\log d$) (right) planes, for models of class A (top) and B (bottom), derived from the mock Planck data. The shaded areas correspond to the 68% (light blue) and 95% (dark blue) confidence regions.

data will greatly increase the precision to which the step parameters can be measured; in particular, a detection of oscillations will be possible.

V. CONCLUDING REMARKS

We have considered inflation models with a small-amplitude steplike feature in the inflaton potential. Features of this kind can be due, for example, to phase transitions occurring during the slow roll in multifield inflationary models. In these models the primordial perturbation spectrum has the form of a power law (as in the standard featureless case) with superimposed oscillations, localized in a finite range of scales that basically depends on the position of the step in the potential. We have compared the theoretical predictions of a specific model, i.e., chaotic inflation, and of a more general phenomenological model to the WMAP7 and ACT data, in order to find constraints on the parameter describing the model. We have also studied the possibility of detecting the oscillations with the upcoming Planck data in the case that they really exist.

We have found that models with features can improve the fit to the WMAP7 data when the step in the potential is placed in such a way as to produce oscillations in the region $20 \lesssim \ell \lesssim 60$, where the WMAP7 data shows some glitches. We found no further evidence for small scales glitches from the recent ACT data, this is fully consistent with the recent analysis of [5]. We have also found that models with too high a step are excluded by the data. Finally, assuming as a fiducial model the generalized step model that provides the best fit to the WMAP7 data, we have found that the Planck data will allow one to measure the parameters of the model with remarkable precision, possibly confirming the presence of glitches in the region $20 \lesssim \ell \lesssim 60$.

ACKNOWLEDGMENTS

It is a pleasure to thank Jan Hamann for providing us the numerical code that computes the primordial inflationary spectra. This work is supported by PRIN-INAF, "Astronomy Probes Fundamental Physics." Support was given by the Italian Space Agency through the ASI contracts Euclid-IC (I/031/10/0). M. L. acknowledges support from Accademia dei Lincei/Royal Society.

[1] E. Komatsu *et al.* (WMAP Collaboration), Astrophys. J. Suppl. Ser. **192**, 18 (2011).
[2] D. Larson *et al.*, Astrophys. J. Suppl. Ser. **192**, 16 (2011).
[3] S. Das *et al.*, Astrophys. J. **729**, 62 (2011).
[4] J. Dunkley *et al.*, arXiv:1009.0866.
[5] R. Hlozek *et al.*, arXiv:1105.4887.
[6] J. A. Adams, G. G. Ross, and S. Sarkar, Phys. Lett. B **391**, 271 (1997).
[7] J. A. Adams, G. G. Ross, and S. Sarkar, Nucl. Phys. **B503**, 405 (1997).
[8] R. H. Brandenberger and J. Martin, Mod. Phys. Lett. A **16**, 999 (2001).
[9] R. Easther, B. R. Greene, W. H. Kinney, and G. Shiu, Phys. Rev. D **66**, 023518 (2002).
[10] J. Martin and R. Brandenberger, Phys. Rev. D **68**, 063513 (2003).
[11] C. P. Burgess, J. M. Cline, F. Lemieux, and R. Holman, J. High Energy Phys. 02 (2003) 048.
[12] C. R. Contaldi, M. Peloso, L. Kofman, and A. D. Linde, J. Cosmol. Astropart. Phys. 07 (2003) 002.
[13] J. A. Adams, B. Cresswell, and R. Easther, Phys. Rev. D **64**, 123514 (2001).
[14] P. Hunt and S. Sarkar, Phys. Rev. D **70**, 103518 (2004).
[15] H. V. Peiris *et al.* (WMAP), Astrophys. J. Suppl. Ser. **148**, 213 (2003).
[16] L. Covi, J. Hamann, A. Melchiorri, A. Slosar, and I. Sorbera, Phys. Rev. D **74**, 083509 (2006).
[17] J. Hamann, L. Covi, A. Melchiorri, and A. Slosar, Phys. Rev. D **76**, 023503 (2007).
[18] M. J. Mortonson, C. Dvorkin, H. V. Peiris, and W. Hu, Phys. Rev. D **79**, 103519 (2009).

[19] D. K. Hazra, M. Aich, R. K. Jain, L. Sriramkumar, and T. Souradeep, J. Cosmol. Astropart. Phys. 10 (2010) 008.
[20] E. D. Stewart and D. H. Lyth, Phys. Lett. B **302**, 171 (1993).
[21] A. Lewis and S. Bridle, Phys. Rev. D **66**, 103511 (2002).
[22] LAMBDA Web site, http://lambda.gsfc.nasa.gov/.
[23] S. Galli *et al.*, Phys. Rev. D **82**, 123504 (2010).
[24] Planck Collaboration, arXiv:astro-ph/0604069.
[25] M. J. Mortonson, C. Dvorkin, H. V. Peiris, and W. Hu, Phys. Rev. D **79**, 103519 (2009).

PHYSICAL REVIEW D **87,** 023519 (2013)

Featuring the primordial power spectrum: New constraints on interrupted slow-roll from CMB and LRG data

Micol Benetti,[1,2,*] Stefania Pandolfi,[3] Massimiliano Lattanzi,[4,5,†] Matteo Martinelli,[6,7] and Alessandro Melchiorri[2]

[1]*Physics Department and ICRA, Università di Roma "La Sapienza", Piazzale Aldo Moro 2, 00185 Rome, Italy*
[2]*Physics Department and INFN, Università di Roma "La Sapienza", Piazzale Aldo Moro 2, 00185 Rome, Italy*
[3]*Dark Cosmology Centre, Niels Bohr Institute, University of Copnehagen, Juliane Maries Vej 30, 2100 Copenhagen, Denmark*
[4]*Dipartimento di Fisica G. Occhialini, Università Milano-Bicocca and INFN, Sezione di Milano-Bicocca, Piazza della Scienza 3, I-20126 Milano, Italy*
[5]*Dipartimento di Fisica, Università di Ferrara and INFN, Sezione di Ferrara, Polo Scientifico e Tecnologico—Edificio C Via Saragat, 1, I-44122 Ferrara, Italy*
[6]*SISSA, Via Bonomea 265, Trieste 34136, Italy*
[7]*INFN, Sezione di Trieste, Via Valerio 2, 34127 Trieste, Italy*

(Received 17 October 2012; published 24 January 2013)

Using the most recent data from the WMAP, ACT and SPT experiments, we update the constraints on models with oscillatory features in the primordial power spectrum of scalar perturbations. This kind of features can appear in models of inflation where slow-roll is interrupted, like multifield models. We also derive constraints for the case in which, in addition to cosmic microwave observations, we also consider the data on the spectrum of luminous red galaxies from the 7th SDSS catalog, and the SNIa Union Compilation 2 data. We have found that: (i) considering a model with features in the primordial power spectrum increases the agreement with data compared to the featureless "vanilla" ΛCDM model by $\Delta\chi^2 = 6.7$, representing an improvement with respect to the expected value $\Delta\chi^2 = 3$ for an equivalent model with three additional parameters; (ii) the uncertainty on the determination of the standard parameters is not degraded when features are included; (iii) the best fit for the features model locates the step in the primordial spectrum at a scale $k \simeq 0.005$ Mpc^{-1}, corresponding to the scale where the outliers in the WMAP7 data at $\ell = 22$ and $\ell = 40$ are located.; (iv) a distinct, albeit less statistically significant peak is present in the likelihood at smaller scales, whose presence might be related to the WMAP7 preference for a negative value of the running of the scalar spectral index parameter; (v) the inclusion of the LRG-7 data does not change significantly the best fit model, but allows to better constrain the amplitude of the oscillations.

DOI: 10.1103/PhysRevD.87.023519 PACS numbers: 98.80.Cq, 98.70.Vc, 98.80.Es

I. INTRODUCTION

The inflationary paradigm is an integral part of the currently accepted concordance cosmological model, explaining the flatness and homogeneity of the observed Universe, as well as providing a mechanism to produce the primordial curvature perturbations that eventually led to the formation of structures. The shape of the power spectrum of primordial perturbations can be constrained, at least at the largest scales, using cosmic microwave background (CMB) data. The 7-year WMAP data are in excellent agreement with the assumption of a nearly scale-invariant power spectrum of scalar perturbations [1,2]. Such a spectrum, described by a simple power law with spectral index n_s very close to (albeit different from) unity, is the one that would be produced in the simplest inflationary scenario, that of a single, minimally coupled scalar field slowly rolling down a smooth potential. The expectation of a power-law spectrum continues to hold up against scrutiny also when tested against observations at scales smaller than those probed by WMAP, like the small-scale CMB measurements of the Atacama Cosmology Telescope (ACT) [3–5] and South Pole Telescope (SPT) [6], and the spectrum of luminous red galaxies [7]. Nevertheless, a scale invariant power spectrum with $n_s = 1$ could be easily put in agreement with data in some nonminimal models, e.g., considering an extended reionization process [8–10], nonstandard processes during recombination like dark matter annihilation [11–14], extra relativistic particles (see e.g., Refs. [15,16]) and so on.

In spite of this, however, models with localized "features" in the primordial power spectrum provide a better fit to the data [17–23] with respect to a smooth power-law spectrum. This is mainly due to the presence, in the WMAP temperature anisotropy spectrum, of two outliers in correspondence of $\ell = 22$ and $\ell = 40$. In particular, these "glitches" are well fitted by a primordial power spectrum featuring oscillations localized in a suitable range of wave numbers. On the other hand, it is worth noticing that the "glitches" could have a more conventional explanation, steaming from some still unknown systematics in the WMAP data.

Features in the primordial power spectrum can be generated following departures from slow roll, that can happen in more general inflationary models. In particular,

*Micol.Benetti@roma1.infn.it
†lattanzi@ferrara.infn.it

in multifield supergravity- or M-theory-inspired models [24,25], a field coupled to the inflaton can undergo a symmetry-breaking phase transition and acquire a vacuum expectation value. Such a phase transition corresponds to a sudden change in the inflaton effective mass and can be modeled as a step in the inflationary potential. The presence of the step produces, in turn, a burst of oscillations in the power spectrum of curvature perturbations [26,27], localized around the scale that is crossing the horizon at the time the phase transition occurred. Departures from the standard power-law behavior can also be present in transplanckian models [28–31], in models with a phase of fast roll [32], or with a sudden change in the speed of sound [33–35]. Similarly, in the so-called Starobinsky model [36], a change in the slope of the potential causes a step in the perturbation spectrum. In addition to their effect on the power spectrum, these nonstandard inflationary scenarios can also be constrained through their predicted bispectrum [35,37,38].

The purpose of the present work is to use current data to update previous constraints that have been put on the presence of such a steplike feature in the inflaton potential. We improve over previous works by using a more complete dataset that includes the WMAP temperature and polarization data, the small-scale CMB data from ACT and SPT, and the matter power spectrum obtained from the Luminous Red Galaxies (LRG) sample of the Sloan Digital Sky Survey (SDSS) 7th data release [39]). The inclusion of different datasets allows us to explore a wider range of scales with respect to previous analyses, going from the Hubble radius down to the smallest linear scales, $k \simeq 0.1\ \mathrm{Mpc}^{-1}$. In particular, this leads to the clear identification of a "forbidden" range where oscillations are not allowed.

The paper is organized as follows: in Sec. II we briefly recall the theory concerning the evolution of inflationary perturbations in interrupted slow roll models; in Sec. III we describe the phenomenological model used to describe a step in the inflationary potential, and the analysis method adopted in the present work; in Sec. IV we present the results of the analysis, and in Sec. V we derive our conclusion.

II. INFLATIONARY PERTURBATIONS IN MODELS WITH INTERRUPTED SLOW ROLL

A. Inflationary perturbations

Let us start by briefly recalling how to compute the spectrum of primordial perturbations for a given inflationary potential $V(\phi)$ [26]. In the following we shall work in reduced Planck units ($c = \hbar = 8\pi G = 1$). The first step is to solve the Friedmann and Klein-Gordon equations (dots denote derivatives with respect to the cosmological time t):

$$3H^2 = \frac{\dot{\phi}^2}{2} + V(\phi), \tag{1}$$

$$\ddot{\phi} + 3H\dot{\phi} + \frac{dV}{d\phi} = 0 \tag{2}$$

to determine the background dynamics of the Hubble parameter H and of the (unperturbed) inflaton field ϕ.

In order to study the evolution of the curvature perturbation $\mathcal{R}$, one introduces the gauge-invariant quantity [40–42] $u \equiv -z\mathcal{R}$, where $z = a\dot{\phi}/H$ and a is the scale factor. The Fourier modes u_k of u evolve according to (primes denote derivatives with respect to conformal time η):

$$u_k'' + \left(k^2 - \frac{z''}{z}\right)u_k = 0. \tag{3}$$

In the limit $k^2 \gg z''/z$, the solution to the above equation should match the free-field solution $u_k = e^{-ik\eta}/\sqrt{2k}$. The evolution of z is determined directly by the solution of Eqs. (1) and (2), although during slow roll one can approximate $z''/z \simeq 2a^2H^2$. At this point, it is possible to integrate Eq. (3) to get $u_k(\eta)$ for free-field initial conditions.

Finally, the power spectrum of the curvature perturbation $P_{\mathcal{R}}$ is related to u and z through

$$P_{\mathcal{R}} = \frac{k^3}{2\pi}\left|\frac{u_k}{z}\right|^2, \tag{4}$$

evaluated when the mode crosses the horizon.

B. Models with interrupted slow roll

In the following we shall consider models where slow roll is briefly violated. Phenomenologically, these can be described by adding a step feature to a $V(\phi) = m^2\phi^2/2$ chaotic potential, i.e., by considering a potential of the form

$$V(\phi) = \frac{1}{2}m^2\phi^2\left[1 + c\tanh\left(\frac{\phi - b}{d}\right)\right], \tag{5}$$

where b is the value of the field where the step is located, c is the height of the step and d its slope. Although the underlying potential is taken to be the one of chaotic inflation, we shall see below that this form can also be used to describe different kinds of potential.

A sharp step in the inflaton potential, like that described by Eq. (5), can appear for example in multifield inflation models, following a symmetry-breaking phase transition undergone by another field coupled to the inflaton. This induces a rapid variation in the inflaton effective mass m_{eff} that is reflected in the potential (indeed, the potential (5) is of the form $V(\phi) = \frac{1}{2}m_{\mathrm{eff}}^2\phi^2$, with a step in m_{eff}). In this regard, one can think of b as being related to the time when the phase transition occurs, c to the change in the inflaton mass, and d to the width of the transition.

The spectrum of primordial perturbations resulting from the potential (5) can be calculated as outlined in the previous section, and is found to be essentially a power-law with superimposed oscillations. The oscillations are

localized only in a limited range of wavenumbers (centered on a value that depends on b) so that asymptotically the spectrum recovers the familiar k^{n_s-1} form typical of slow-roll inflationary models. In particular, for a chaotic potential, the underlying power law has a spectral index $n_s \simeq 0.96$.

One issue that we have left aside so far is how to relate the horizon size at the time the step occurs to a physical scale. This depends on the number $N_\star$ of e-folds taking place between the time a given mode has left the horizon and the end of inflation. We choose $N_\star = 50$ for the pivot wavenumber $k_\star = k_0 = 0.05\ \mathrm{Mpc}^{-1}$. This choice is somewhat arbitrary; however, a different choice would correspond to a translation in the position of the step in ϕ and would thus be highly degenerate with b. For this reason we do not treat $N_\star$ as a free parameter, consistent with what has been done in previous studies [18,19].

III. ANALYSIS METHOD

In order to compare the theoretical predictions for the constraints on the parameters characterizing inflationary models with a step in the inflaton potential with observational data, we performed a Monte Carlo Markov Chain analysis via the publicly available package COSMOMC [43]. We used a modified version of the CAMB ([44]) code in which we numerically solve Eqs. (1)–(3) using a Bulirsch-Stoer algorithm in order to theoretically calculate the initial perturbation spectrum (4), needed to compute the CMB anisotropies spectrum for any given values of the parameters describing this type of inflationary model. Then we compare these theoretical models with two different combination of data sets. We will briefly come back on describing the principal characteristics of each of the dataset considered in this work.

We consider chaotic inflation potentials of the type of Eq. (5). Following the prescription described in Sec. II A, this potential leads to a well-defined primordial perturbation spectrum $\mathcal{P}_\mathcal{R}$. The free parameters in Eq. (5) are then the inflaton mass m and the step parameters b, c and d. In our analysis we map the mass m onto A_s, i.e., the amplitude of the primordial spectrum at the pivot wavenumber $k_0 = 0.05\ \mathrm{Mpc}^{-1}$, as indeed the inflaton mass sets the overall scale for the potential and consequently for the amplitude of the perturbations. We note also that the choice of the pivot wavenumber changes the relationship between the value of b and the position of oscillations in k—space; this should be taken into account when comparing the results of different studies. In particular, changing k_0 from 0.05 to $0.002\ \mathrm{Mpc}^{-1}$ shifts b by ~ 0.5 towards lower values.

As previously noted in Sec. II B, for the chaotic potential of Eq. (5) the smooth power law has a fixed spectral index, that is $n_s \simeq 0.96$. However, as noted in Ref. [19], more general forms of the potential can be phenomenologically taken into account by promoting n_s back to a free parameter and defining a "generalized" primordial spectrum as

$$\mathcal{P}_\mathcal{R}^{\mathrm{gen}}(k) = \mathcal{P}_\mathcal{R}^{\mathrm{ch}}(k) \times \left(\frac{k}{k_0}\right)^{n_s - 0.96}, \tag{6}$$

where $\mathcal{P}_\mathcal{R}^{\mathrm{ch}}(k)$ is the spectrum induced by the chaotic potential (5).

Therefore the theoretical model we are considering is described by the following set of parameters:

$$\{\omega_b, \omega_c, \theta, \tau, b, c, d, \mathcal{A}_s, n_s\}, \tag{7}$$

where $\omega_b = \Omega_b h^2$ and $\omega_c = \Omega_c h^2$ are the physical baryon and cold dark matter densities, θ is the ratio between the sound horizon and the angular diameter distance at decoupling, τ is the optical depth to reionization, b, c and d are the parameters of the step-inflation model, $\mathcal{A}_s$ is the overall normalization of the primordial power spectrum (equivalent to specifying m^2 as discussed above), and n_s is the effective tilt. We consider purely adiabatic initial conditions, impose flatness and neglect neutrino masses, and limit our analysis to scalar perturbations.

We consider as our basic dataset a combination of three different CMB datasets: WMAP7 (both temperature and polarization), ACT and SPT (in what follows we will refer to this case simply as "CMB"), and then we also consider an enlarged dataset, dubbed "CMB + LRG", where we also add the information on the power spectrum of the halo density field as derived from the LRG sample of SDSS catalog [7], the Supernovae Ia Union Compilation 2 data [45], and impose a prior on the Hubble constant from the Hubble Space Telescope [46]. We choose not to use the information associated to the presence of baryon acoustic oscillations (BAO) [47] in the matter power spectrum since the very presence of oscillations induced by features in the inflationary potential would spoil the distinction between the "smooth" part of the spectrum, and the "wiggles" induced by BAO, that is necessary to correctly interpret the observations. In other words, applying the BAO likelihood as described in Ref. [47] without properly accounting for the possible presence of oscillations of primordial origin (as opposed to those induced by BAO) could lead to biased results (see e.g., Ref. [15] for a detailed discussion).

To compute the likelihood of the data we have properly modified the COSMOMC package in order to make use of the routines supplied by the WMAP and ACT teams for their datasets, both publicly available from the LAMBDA website [48], and of the likelihood code provided by the SPT team [6] for the SPT dataset.

The ACT and SPT experiments allow to extend the dynamic range of CMB observations to larger multipoles with the respect of WMAP7, thus measuring the damping tail of the CMB angular power spectrum. While SPT probes the small scales in the range of multipoles $650 < \ell < 3000$, the ACT telescope spans a range of multipoles that goes up to $\ell = 10000$, although the signal at $\ell \gtrsim 3000$ is dominated by the power coming from extragalactic point sources. For this reason, for ACT we only consider the less

contaminated 148 GHz spectrum up to $\ell_{\rm max} = 3300$ to perform cosmological parameters extraction. In order to account for the foreground contributions at $\ell \lesssim 3000$, we add three extra amplitude parameters: the Sunyaev-Zel'dovich (SZ) amplitude $A_{\rm SZ}$, the clustered point sources amplitude A_C and the amplitude of Poisson distributed point sources A_P. We consider for both ACT and SPT experiments a joint amplitude parameter for each component and the templates provided by Ref. [6]. No SZ contribution is considered for WMAP7, as explained in the analysis performed by Ref. [6]. We have however verified that different choices for the foreground templates has negligible effect on the constraints of cosmological parameters and produces minimal effects on foreground parameters.

For what concerns the SDSS LRG7 catalog, we chose to consider data only in the linear scales regime, i.e., up to $k = 0.1\ {\rm h\,Mpc^{-1}}$. Indeed, HALOFIT, the CAMB routine that should correct for nonlinearity effects at the smallest scales, is tested only for a smooth primordial power spectrum and therefore is not appropriate for dealing with power spectra with features, like those considered in the present analysis.

Regarding the prior on the model parameters, we impose flat priors on ω_b, ω_c, θ, τ and n_s and a logarithmic prior on $\mathcal{A}_s$. We check a posteriori that these priors result to be much wider than the corresponding posteriors and thus their upper and lower limits do not affect our final results. The priors on the step parameters need however to be discussed in more detail. The parameter b controls the position of the oscillations in k—space. Larger values of b correspond to ''later'' phase transitions and thus move the oscillations towards larger scales (smaller values of k and ℓ). Viceversa, smaller values of b shift the oscillations in the direction of large wave numbers. As a rule of thumb, we note that the peak in the oscillations is located at $k \simeq 0.015\ {\rm Mpc^{-1}}$ ($\ell \simeq 200$) for $b = 14.5$, and that it is shifted down (up) by roughly a factor 2 in k for each 0.1 increment (decrement) in b. Thus, outside of a given range in b, oscillations are moved to wave numbers that are not probed by observations of the CMB nor of large scale structures. Based on the considerations above, we initially choose a flat prior for b in the range $13.5 \leq b \leq 15.5$, that conservatively encompasses the whole range probed by the WMAP, ACT, SPT and LRG datasets. We use this prior for the CMB only dataset. Then, in view of the results of the first Monte Carlo run, we also consider a restricted prior $14.2 \leq b \leq 15$, that we use for the analysis of the enlarged dataset. We have also explicitly checked that adding, in $b = 13.5$ or $b = 15.5$, a step-like feature with $c = 10^{-2}$ (a value already large enough to produce, on average, oscillations that are at variance with observations [22]) and $d = 3 \times 10^{-2}$ (the median point of our prior) to the WMAP7 best-fit model produces no appreciable effect (at least within CAMB's numerical precision) in the CMB spectrum up to $\ell = 3000$ nor in the matter power spectrum between $k = 0.02$ and $k = 0.1\ {\rm Mpc^{-1}}$. For what concerns c and d, parameterizing the height and width of the step respectively, we choose a logarithmic prior for both of them, i.e., a uniform prior on $\log c$ and $\log d$. The reason for this choice is that we want for these parameters to, potentially, assume values spanning several orders of magnitude with equal *a priori* probability. Indeed this is accomplished using a logarithmic prior that naturally assigns equal probability to each decade. In particular, we take $-4 \leq \log c \leq -1$ and $-2.5 \leq \log d \leq -0.5$.

We derive posterior distributions and parameter constraints from parallel Markov chains generated using the Metropolis-Hastings (MH) algorithm. We use the Gelman and Rubin R parameter to evaluate the convergence of the chains, demanding that $R - 1 < 0.04$. Since as we shall see the resulting posterior distributions are highly non-Gaussian, we have also explicitly checked that sub-sets of the chains yield the same one-dimensional distributions. We note that there are some issues related to the fact that some of the posteriors do not vanish at infinity; we address them in Sec. IV.

In addition to reconstructing the posterior distribution, we also find the best-fit values of the parameters of the models, and assess the improvement in χ^2 of the features model with respect to standard ΛCDM. Since the MH algorithm needs to evaluate the model likelihood at each point traversed by the chains, it gives, as a by-product, the position in parameter space of the best-fit model and the associated χ^2. However, the MH algorithm is designed to draw samples from the posterior distribution, and not to find the best-fit model, so that its assessment of the latter can be grossly wrong. A better approach is to use optimization methods, like for example the conjugate gradient method. This method unfortunately has the disadvantage that it does not work for parameters with priors that cut the posterior where this is not negligible, as it is the case for the features parameters. However, the new version of CosmoMC released in October 2012 implements to this purpose the Bounded Optimization BY Quadratic Approximation (BOBYQA) algorithm developed by Powell [49], that works also in this case. Thus in the following section we quote results for the best-fit values of the parameters, as well as for the value of the χ^2 itself, obtained using Powell's routines as implemented in CosmoMC. We have explicitly checked that our results were unchanged when increasing the accuracy settings of the algorithm.

IV. RESULTS AND DISCUSSION

First of all, we check how the constraints on the six ''vanilla'' parameters are changed when the possibility of having features in the primordial power spectrum is considered. To this purpose, we show in Table I the mean of the posterior distribution, and the corresponding 68% credible

TABLE I. Posterior mean for the vanilla cosmological parameters. The errors refer to 68% credible intervals.

Parameter	ΛCDM (CMB)[a]	Features (CMB)[b]	Features (CMB + LRG)[c]
$100\Omega_b h^2$	2.215 ± 0.041	2.204 ± 0.044	2.215 ± 0.037
$\Omega_c h^2$	0.1114 ± 0.0046	0.1125 ± 0.0050	0.1122 ± 0.0029
100θ	1.0411 ± 0.0016	1.0409 ± 0.0016	1.0414 ± 0.0015
τ	0.085 ± 0.014	0.086 ± 0.014	0.087 ± 0.015
n_s	0.962 ± 0.011	0.959 ± 0.014	0.959 ± 0.011
$10^9 A_s$[d]	2.17 ± 0.06	2.18 ± 0.08	2.19 ± 0.07
Age [Gyr]	13.78 ± 0.09	13.81 ± 0.09	13.78 ± 0.07
z_{re}	10.4 ± 1.2	10.5 ± 1.2	10.5 ± 1.2
H_0 [km s^{-1} Mpc^{-1}]	70.5 ± 2.1	69.9 ± 2.3	70.3 ± 1.3

[a]Posterior mean for the parameters of the ΛCDM model, using the CMB dataset.
[b]Posterior mean for the parameters of the features model, using the CMB dataset.
[c]Posterior mean for the parameters of the features model, using the CMB + LRG dataset.
[d]$k_0 = 0.05$ Mpc^{-1}.

intervals, for each vanilla parameter, as well as for some derived parameters (most notably the reionization redshift z_{re}, the age of the Universe, the Hubble constant H_0), and compare them with the corresponding values found in a test ΛCDM run using the CMB dataset. We note that the uncertainty on the determination of the vanilla parameters is not degraded when features are included (and it is actually better for the CMB + LRG dataset, although this should probably be ascribed to the inclusion of additional data). The mean values found for the features model are all within one sigma of the corresponding ΛCDM values.

Now let us analyze the results on the primordial spectrum parameters from one dataset at a time, starting from the CMB-only dataset. We recall that this analysis assumes the prior $13.5 \leq b \leq 15.5$. We first focus the best-fit parameters, i.e., the parameter values that maximize the likelihood. In the second column of Table II we show the best-fit values, for this dataset, of the primordial spectrum parameters. With the precision settings used, the accuracy in the determination of these values is of 10^{-3} or better. In the best-fit model, the step in the primordial spectrum is located in $b = 14.66$, consistently with previous studies [20,22]. The best-fit model has $\chi^2 = 7528.5$; for comparison, the minimum χ^2 found in our test ΛCDM run was 7535.2. Thus the features model represent an improvement of $\Delta\chi^2 = 6.7$ with respect to standard ΛCDM. This should be compared with the value of $\Delta\chi^2 = 3$ (given the number of additional parameters of the features model) expected if the two models were equivalent.

TABLE II. Bestfit values.

Parameter	CMB	CMB + LRG
b	14.66	14.66
log$c$	−2.69	−2.80
log$d$	−1.42	−1.51
n_s	0.949	0.959
$\ln[10^{10} A_s]$	3.08	3.09
$-2\log(\mathcal{L})$	7528.5	8086.0

For illustrative purposes, we also explicitly show the projected likelihood, as well as $\Delta\chi^2 = \chi^2 - \chi^2_{\rm min}$, as a function of b in the two panels of Fig. 1. We remark that the shape of the likelihood function is obtained through the chains generated using the MH algorithm (see discussion in the previous section). We note that there is a distinct although lower peak in the likelihood in $b \simeq 14$, having $\Delta\chi^2 \simeq 3.5$, as can be inferred from Fig. 1. Nevertheless, we stress that the MH algorithm is not fully efficient, especially in the presence of multimodal likelihood distributions, thus the $\Delta\chi^2$ values that can be inferred from the plot are not completely trustworthy (as opposed to those obtained using Powell's algorithm). In order to operate a

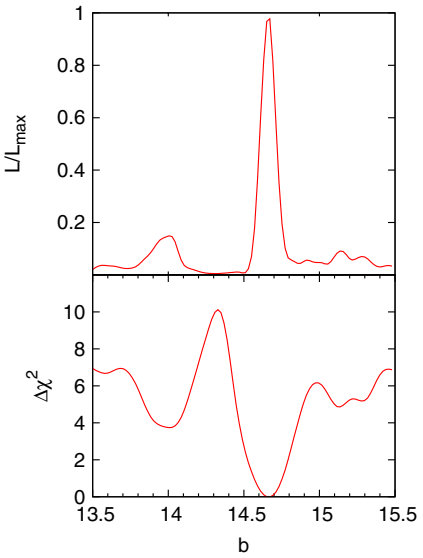

FIG. 1 (color online). Model likelihood (upper panel) and $\Delta\chi^2$ (lower panel) as functions of b for the CMB dataset, obtained by maximization.

more accurate statistical analysis of this secondary peak a different sampling method should be used (like a nested sampling algorithm, see e.g., Ref. [50]), but this type of investigation is beyond the scopes of the present work.

We also note that the χ^2 does not become arbitrarily large (i.e., the likelihood does not asymptotically vanish) far from the minimum, but instead tends to a constant value. This is related to the fact that, as explained to the previous section, towards the extremes of the b range the oscillations are moved outside the range of scales probed by the dataset, and thus the model is expected to tend to ΛCDM, as long as data fitting is concerned.

The primordial power spectra corresponding to the two minima in the χ^2 are shown in Fig. 2. On the other hand, models with $14.1 \lesssim b \lesssim 14.5$ perform worse with respect to ΛCDM.

For a better understanding, we also show in Figs. 3 and 4 the comparison between the WMAP7 best-fit, the two models with features corresponding to the two peaks in the likelihood seen in Fig. 1, and the data present in the CMB dataset. It is clear from these plots (especially from the plot of residuals shown in the lower panel) that the model with $b = 14.66$ improves over ΛCDM by being able to fit the two outliers in $\ell = 22$ and $\ell = 40$, thus confirming our previous findings [22]. The interpretation of the peak in $b = 14$ is more puzzling; by looking at the lower panel of Fig. 3, however, it can be seen that the CMB spectrum for this model resembles what it would be obtained by adding a negative running $dn_s/d\ln k$ to the scalar spectral index. Thus this result could be reminiscent of the WMAP7 preference for a negative running, that is indeed even more pronounced when high-ℓ data are added to the analysis [1]: $dn_s/d\ln k = -0.034 \pm 0.026$ (WMAP7 only) and $dn_s/d\ln k = -0.041^{+0.022}_{-0.023}$ (WMAP7 + ACBAR + QUaD). We however think that a deeper investigation is in order, although it goes beyond the aim of the present paper.

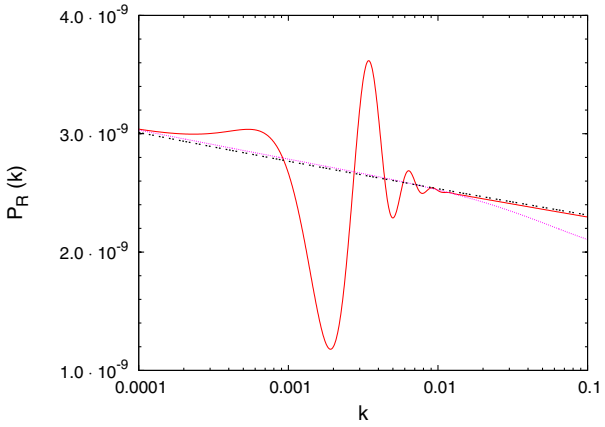

FIG. 2 (color online). Primordial power spectrum for an inflationary potential of the form (5) with $m = 7.5 \times 10^{-6}$. The values of the step parameters are: $b = 14.66$, $\log c = -2.75$, $\log d = -1.42$ (red), $b = 14.00$, $\log c = -2.66$, $\log d = -0.54$ (magenta dotted), corresponding to the two peaks in the likelihood. For comparison, we also show the best-fit ΛCDM power spectrum (black dot-dashed). We note that the model with $b = 14$ resembles, in the k—range considered, a model with a negative running index.

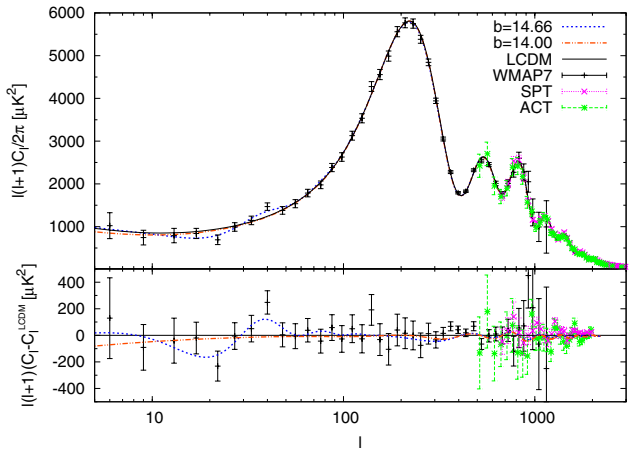

FIG. 3 (color online). Upper panel: Power spectrum of CMB Anisotropies Power Spectrum for the best-fit ΛCDM model (black line) and two step models with $b = 14$ (red dashed) and $b = 14.66$ (blue dot-dashed), corresponding to the two minima in χ^2, compared with WMAP7, ACT and SPT data. Lower panel: The same as above, but plotted in terms of residuals with respect to the ΛCDM best fit.

We now turn to the posterior distributions. In Fig. 5, we show the one-dimensional posteriors for b, $\log c$ and $\log d$. We recall that standard ΛCDM is recovered for $\log c \to -\infty$ or $\log d \to +\infty$, as it is clear from expression (5) for the inflationary potential. The posterior for b still shows the two peaks in $b \simeq 14.7$ and $b \simeq 14$ that were present in the likelihood. The largest value at the edges of the prior range is due to a volume effect, since the one-dimensional posterior is obtained by marginalization

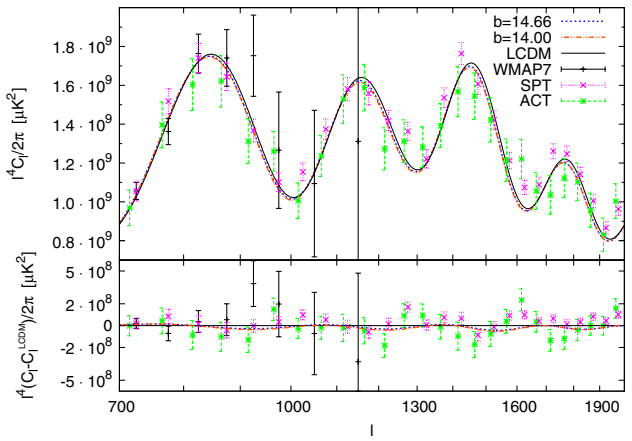

FIG. 4 (color online). The same as Fig. 3, but zoomed in the region $700 \leq \ell \leq 2000$. Note that in order to improve clarity, the vertical axis shows $\ell^4 C_\ell$ instead than $\ell(\ell+1)C_\ell$.

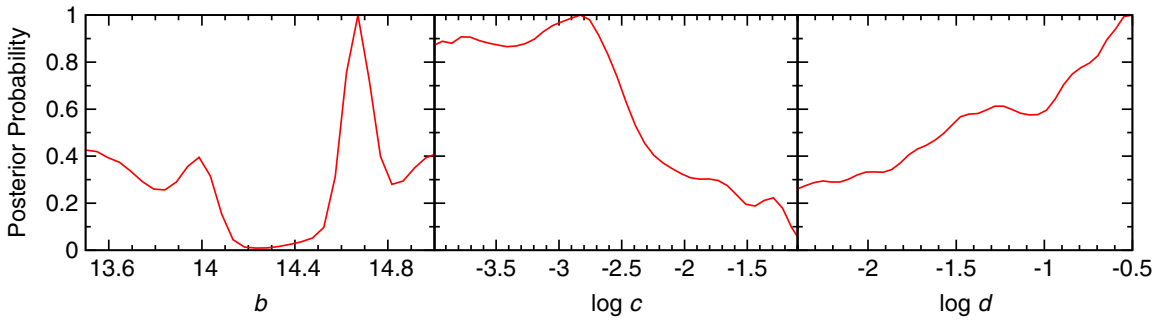

FIG. 5 (color online). One-dimensional posterior probability density for the step parameters from the CMB dataset. Standard ΛCDM is recovered for $\log c \to -\infty$ or $\log d \to +\infty$.

(as opposed to the one-dimensional likelihood that was obtained by maximization). On the other hand, the probability density for $14.1 \lesssim b \lesssim 14.4$ is practically equal to zero. For what concerns $\log c$, as it could be expected, "large" values are disfavored by the data (as they produce large—in amplitude—oscillations that cannot, on average, be reconciled with observations) while for smaller values the posterior tends to a constant value as the oscillations become so weak as to be practically undetectable for the current experimental precision and thus the value of c becomes unimportant. As already noted, a posterior with this characteristic that extends, in principle, down to $\log c = -\infty$, cannot be properly normalized (since the corresponding probability mass is infinite) and, as a consequence, credible intervals are ill-defined. One could be tempted to impose a lower cut-off but then the credible intervals will end up depending on the choice of the cut-off itself, so this should be avoided, at least in the absence of a clear physical reason for doing so.

We can still, however, compare probability densities, as well as probabilities integrated over finite intervals, since probability ratios *do not* depend on the overall normalization. We can use, as a benchmark value to compare the constraining power of different datasets, for example, the value of $\log c$ where $P(\log c)$ is half of its asymptotic value for $\log c \to \infty$. This should not be taken as an "upper limit" in the common sense of the word, but as said is a useful tool for comparison. In the case under consideration, we estimate that this happens for $\log c = -2.32$, or $c = 4.8 \times 10^{-3}$.

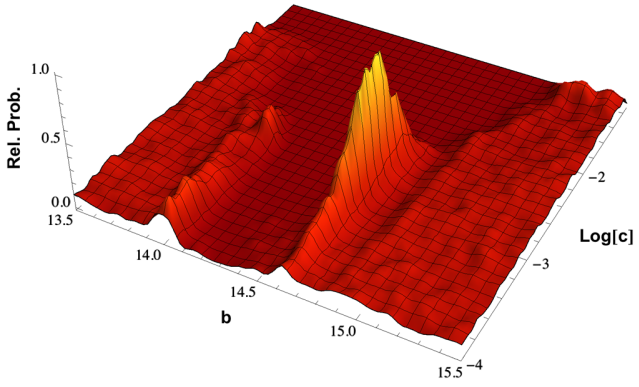

FIG. 6 (color online). Joint two-dimensional posterior for $(b, \log c)$ using the CMB dataset.

For comparison, the corresponding value that we had previously found using WMAP7 and ACT data only was $\log c = -2$ [22]. We also show, in Fig. 6 the two-dimensional posterior $P(b, \log c)$ where it is clear that probability is concentrated in two distinct, disconnected regions. One corresponds to models with $b \simeq 14.7$ and $\log c \simeq -3$, while the other to models with $b \simeq 14$ and $\log c$ located more towards the edge of the prior range, $\log c \lesssim -3.5$. Finally, we examine the posterior for $\log d$. This is in part similar to the posterior for $\log c$, once one recalls that small values of $\log d$ produce a steep step in the potential and consequently large oscillations, so one should expect the probability to go to zero for small values of $\log d$, as it is. However, in this case, the posterior range is not wide enough to see the asymptotic part, for $\log d \to \infty$ (where ΛCDM should be recovered), of the distribution.

The fact that the posterior is bimodal in b creates some difficulty for the Monte Carlo, as the chains cannot easily jump from one peak to the other, and thus take a longer time to sample satisfactorily the actual distribution. For this reason, in our second Monte Carlo run, using the CMB + LRG dataset, we have decided to concentrate on the region of the peak at $b = 14.66$ and impose the prior $14.2 \leq b \leq 15$. We find that the best-fit for this dataset, shown in the third column of Table II has still $b = 14.66$. In Figs. 7 and 8 we compare the one-dimensional likelihoods and posteriors, respectively, for the step parameters in the CMB + LRG dataset with those obtained previously with the CMB dataset. In order to allow for comparison, the distributions for the latter have been obtained by imposing a posteriori the condition $b \geq 14.2$ (which means, in practical terms, that we have discarded all samples with $b < 14.2$, and reanalyzed these new chains from scratch). We find that there is practically no difference with respect to the position of the oscillations (which makes sense, since this is driven by the requirement of fitting the outliers in the WMAP7 data at relatively low ℓ's). The amplitude of the oscillations is slightly more

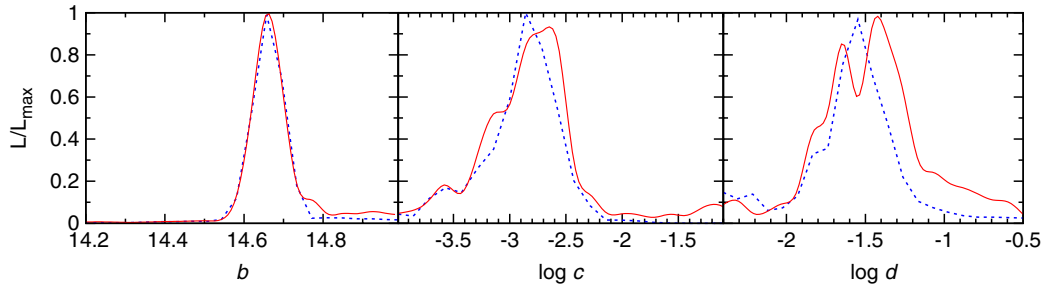

FIG. 7 (color online). Comparison of the model likelihood as a function of the step parameters, obtained from the CMB (red solid line) and CMB + LRG (blue dashed) datasets.

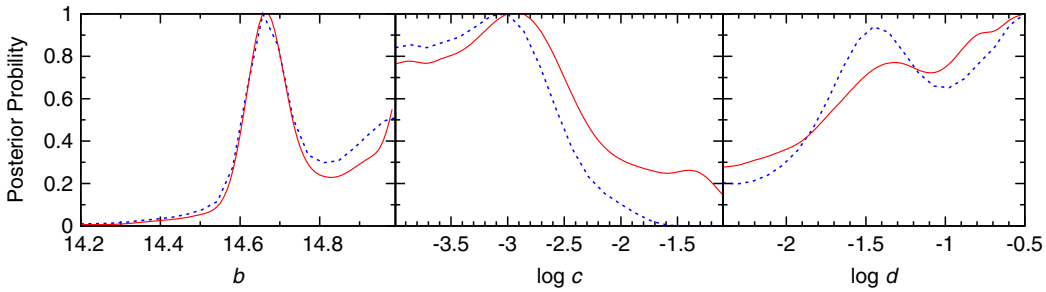

FIG. 8 (color online). Comparison of the one-dimensional posterior probability density for the step parameters from the CMB (red solid line) and CMB + LRG (blue dashed line) datasets.

constrained, with the posterior going down at half of its plateau value at $\log c = -2.48$ ($c \simeq 3 \times 10^{-3}$). The posterior for $\log d$ is also slightly different, as it shows a more distinct peak in correspondence of the best-fit value $\log d \simeq -1.5$.

Tighter constraints on the features model parameters could be placed by future precision polarization data. Indeed, as the authors of Ref. [20] pointed out, the appearing of the features (also) in the polarization power spectrum is important for a cross-check with the temperature power spectrum on the constraints obtained on the features. It is important either for features appearing at $\ell < 30$ (because in the TT spectrum these would be smoothed out by projection effects), or for features appearing at $\ell > 30$ (to verify the possible sources of error in the significant determination of the parameter constraints, such as the inclusion of tensor modes and the relaxation of the instantaneous reionization hypothesis) (for further details we refer the reader to Ref. [20] and references therein).

V. CONCLUDING REMARKS

We have studied cosmological models with a steplike feature in the inflationary potential. Such a feature would produce oscillations in the primordial spectrum of scalar perturbations, whose presence can be tested through the analysis of CMB and large-scale structures data. We have found, consistently with previous studies, that in these models the agreement with the CMB data is improved, with respect to the ΛCDM model, when the oscillations are placed in such a way as to match the two outliers in the WMAP7 spectrum at $\ell = 22$ and $\ell = 40$ (in particular, the χ^2 changes by $\Delta\chi^2 = 6.7$). The posterior probability also has a maximum close to this point, corresponding to $b = 14.66$, while it clearly shows that oscillations in the range $14.1 \leq b \leq 14.5$ are currently forbidden by the data. The possibility of no oscillation at all is still, however, perfectly consistent with the data. In conclusion, although multifield inflationary models can definitely reproduce the two glitches in the WMAP7 temperature spectrum, current data are not yet constraining enough to allow to discriminate between these models and the standard inflationary scenario.

ACKNOWLEDGMENTS

The Dark Cosmology Centre is funded by the Danish National Research Foundation. The work of M. L. has been supported by Ministero dell'Istruzione, dell'Università e della Ricerca (MIUR) through the PRIN grants "Matter-antimatter asymmetry, Dark Matter and Dark Energy in the LHC era" (Contract No. PRIN 2008NR3EBK-005) and "Galactic and extragalactic polarized microwave emission" (Contract No. PRIN 2009XZ54H2-002). We would like to thank Erminia Calabrese and Luca Pagano for useful discussion.

[1] E. Komatsu *et al.* (WMAP Collaboration), Astrophys. J. Suppl. Ser. **192**, 18 (2011).

[2] D. Larson, J. Dunkley, G. Hinshaw, E. Komatsu, M. R. Nolta, C. L. Bennett, B. Gold, and M. Halpern *et al.*, Astrophys. J. Suppl. Ser. **192**, 16 (2011).

[3] S. Das, T. A. Marriage, P. A. R. Ade, P. Aguirre, M. Amir, J. W. Appel, L. F. Barrientos, and E. S. Battistelli *et al.*, Astrophys. J. **729**, 62 (2011).

[4] J. Dunkley, R. Hlozek, J. Sievers, V. Acquaviva, P. A. R. Ade, P. Aguirre, M. Amiri, and J. W. Appel *et al.*, Astrophys. J. **739**, 52 (2011).

[5] R. Hlozek, J. Dunkley, G. Addison, J. W. Appel, J. R. Bond, C. S. Carvalho, S. Das, and M. Devlin *et al.*, Astrophys. J. **749**, 90 (2012).

[6] R. Keisler, C. L. Reichardt, K. A. Aird, B. A. Benson, L. E. Bleem, J. E. Carlstrom, C. L. Chang, and H. M. Cho *et al.*, Astrophys. J. **743**, 28 (2011).

[7] B. A. Reid *et al.*, Mon. Not. R. Astron. Soc. **404**, 60 (2010).

[8] M. J. Mortonson and W. Hu, Astrophys. J. **686**, L53 (2008).

[9] S. Pandolfi, A. Cooray, E. Giusarma, E. W. Kolb, A. Melchiorri, O. Mena, and P. Serra, Phys. Rev. D **81**, 123509 (2010).

[10] S. Pandolfi, E. Giusarma, E. W. Kolb, M. Lattanzi, A. Melchiorri, O. Mena, M. Pena, A. Cooray, and P. Serra, Phys. Rev. D **82**, 123527 (2010).

[11] S. Galli, F. Iocco, G. Bertone, and A. Melchiorri, Phys. Rev. D **80**, 023505 (2009).

[12] S. Galli, F. Iocco, G. Bertone, and A. Melchiorri, Phys. Rev. D **84**, 027302 (2011).

[13] G. Giesen, J. Lesgourgues, B. Audren, and Y. Ali-Haimoud, J. Cosmol. Astropart. Phys. 12 (2012) 008.

[14] C. Evoli, S. Pandolfi, and A. Ferrara, arXiv:1210.6845.

[15] J. Hamann, S. Hannestad, J. Lesgourgues, C. Rampf, and Y. Y. Y. Wong, J. Cosmol. Astropart. Phys. 07 (2010) 022.

[16] M. Archidiacono, E. Calabrese, and A. Melchiorri, Phys. Rev. D **84**, 123008 (2011).

[17] H. V. Peiris *et al.* (WMAP Collaboration), Astrophys. J. Suppl. Ser. **148**, 213 (2003).

[18] L. Covi, J. Hamann, A. Melchiorri, A. Slosar, and I. Sorbera, Phys. Rev. D **74**, 083509 (2006).

[19] J. Hamann, L. Covi, A. Melchiorri, and A. Slosar, Phys. Rev. D **76**, 023503 (2007).

[20] M. J. Mortonson, C. Dvorkin, H. V. Peiris, and W. Hu, Phys. Rev. D **79**, 103519 (2009).

[21] D. K. Hazra, M. Aich, R. K. Jain, L. Sriramkumar, and T. Souradeep, J. Cosmol. Astropart. Phys. 10 (2010) 008.

[22] M. Benetti, M. Lattanzi, E. Calabrese, and A. Melchiorri, Phys. Rev. D **84**, 063509 (2011).

[23] P. D. Meerburg, R. Wijers, and J. P. van der Schaar, arXiv:1109.5264.

[24] J. A. Adams, G. G. Ross, and S. Sarkar, Phys. Lett. B **391**, 271 (1997).

[25] J. A. Adams, G. G. Ross, and S. Sarkar, Nucl. Phys. **B503**, 405 (1997).

[26] J. A. Adams, B. Cresswell, and R. Easther, Phys. Rev. D **64**, 123514 (2001).

[27] P. Hunt and S. Sarkar, Phys. Rev. D **70**, 103518 (2004).

[28] R. H. Brandenberger and J. Martin, Mod. Phys. Lett. A **16**, 999 (2001).

[29] R. Easther, B. R. Greene, W. H. Kinney, and G. Shiu, Phys. Rev. D **66**, 023518 (2002).

[30] J. Martin and R. Brandenberger, Phys. Rev. D **68**, 063513 (2003).

[31] C. P. Burgess, J. M. Cline, F. Lemieux, and R. Holman, J. High Energy Phys. 02 (2003) 048.

[32] C. R. Contaldi, M. Peloso, L. Kofman, and A. D. Linde, J. Cosmol. Astropart. Phys. 07 (2003) 002.

[33] R. Bean, X. Chen, G. Hailu, S.-H. H. Tye, and J. Xu, J. Cosmol. Astropart. Phys. 03 (2008) 026.

[34] M. Nakashima, R. Saito, Y.-i. Takamizu, and J.'i. Yokoyama, Prog. Theor. Phys. **125**, 1035 (2011).

[35] M. Park and L. Sorbo, Phys. Rev. D **85**, 083520 (2012).

[36] A. A. Starobinsky, Pis'ma Zh. Eksp. Teor. Fiz. **55**, 477 (1992) [JETP Lett. **55**, 489 (1992)].

[37] J. Martin and L. Sriramkumar, J. Cosmol. Astropart. Phys. 01 (2012) 008.

[38] P. Adshead, C. Dvorkin, W. Hu, and E. A. Lim, Phys. Rev. D **85**, 023531 (2012).

[39] K. N. Abazajian *et al.* (SDSS Collaboration), Astrophys. J. Suppl. Ser. **182**, 543 (2009).

[40] M. Sasaki, Prog. Theor. Phys. **76**, 1036 (1986).

[41] V. F. Mukhanov, Zh. Eksp. Teor. Fiz. **94**, 1 (1988) [Sov. Phys. JETP **67**, 1297 (1988)].

[42] E. D. Stewart and D. H. Lyth, Phys. Lett. B **302**, 171 (1993).

[43] A. Lewis and S. Bridle, Phys. Rev. D **66**, 103511 (2002).

[44] A. Lewis, A. Challinor, and A. Lasenby, Astrophys. J. **538**, 473 (2000).

[45] R. Amanullah, C. Lidman, D. Rubin, G. Aldering, P. Astier, K. Barbary, M. S. Burns, and A. Conley *et al.*, Astrophys. J. **716**, 712 (2010).

[46] A. G. Riess, L. Macri, S. Casertano, M. Sosey, H. Lampeitl, H. C. Ferguson, A. V. Filippenko, and S. W. Jha *et al.*, Astrophys. J. **699**, 539 (2009).

[47] W. J. Percival *et al.* (SDSS Collaboration), Mon. Not. R. Astron. Soc. **401**, 2148 (2010).

[48] http://lambda.gsfc.nasa.gov/.

[49] M. J. D. Powell, University of Cambridge Report No. DAMTP 2009/NA06, 2009.

[50] F. Feroz and M. P. Hobson, Mon. Not. R. Astron. Soc. **384**, 449 (2008).

Journal of Cosmology and Astroparticle Physics
An IOP and SISSA journal

Cosmological data and indications for new physics

Micol Benetti,[a,b] **Martina Gerbino,**[b] **William H. Kinney,**[c] **Edward W. Kolb,**[d] **Massimiliano Lattanzi,**[e] **Alessandro Melchiorri,**[b] **Luca Pagano**[b] **and Antonio Riotto**[f]

[a]Physics Department and ICRA, Università di Roma "La Sapienza", Ple. Aldo Moro 2, 00185, Rome, Italy
[b]Physics Department and INFN, Università di Roma "La Sapienza", Ple Aldo Moro 2, 00185, Rome, Italy
[c]Department of Physics, University at Buffalo, the State University of New York, Buffalo, NY 14260-1500, U.S.A.
[d]Department of Astronomy and Astrophysics, Enrico Fermi Institute, and Kavli Institute for Cosmological Physics, University of Chicago, Chicago, Illinois 60637-1433, U.S.A.
[e]Dipartimento di Fisica e Science della Terra, Università di Ferrara and INFN, sezione di Ferrara, Polo Scientifico e Tecnologico - Edificio C Via Saragat, 1, I-44122 Ferrara Italy
[f]Department of Theoretical Physics and Center for Astroparticle Physics (CAP) 24 quai E. Ansermet, CH-1211 Geneva 4, Switzerland

E-mail: micol.benetti@roma1.infn.it, martina.gerbino@roma1.infn.it, whkinney@buffalo.edu, Rocky.Kolb@uchicago.edu, lattanzi@fe.infn.it, alessandro.melchiorri@roma1.infn.it, luca.pagano@roma1.infn.it, antonio.riotto@unige.ch

Received March 28, 2013
Accepted September 17, 2013
Published October 16, 2013

Abstract. Data from the Atacama Cosmology Telescope (ACT) and the South Pole Telescope (SPT), combined with the nine-year data release from the WMAP satellite, provide very precise measurements of the cosmic microwave background (CMB) angular anisotropies down to very small angular scales. Augmented with measurements from Baryonic Acoustic Oscillations surveys and determinations of the Hubble constant, we investigate whether there are indications for new physics beyond a Harrison-Zel'dovich model for primordial perturbations and the standard number of relativistic degrees of freedom at primordial recombination. All combinations of datasets point to physics beyond the minimal Harrison-Zel'dovich model in the form of either a scalar spectral index different from unity or additional relativistic degrees of freedom at recombination (e.g., additional light neutrinos). Beyond that, the extended datasets including either ACT or SPT provide very different indications: while

doi:10.1088/1475-7516/2013/10/030

JCAP10(2013)030

the extended-ACT (eACT) dataset is perfectly consistent with the predictions of standard slow-roll inflation, the extended-SPT (eSPT) dataset prefers a non-power-law scalar spectral index with a very large variation with scale of the spectral index. Both eACT and eSPT favor additional light degrees of freedom on top of the Harrison-Zel'dovich model. eACT is consistent with zero neutrino masses, while eSPT favors nonzero neutrino masses at more than 95% confidence.

Keywords: inflation, cosmological neutrinos, cosmological parameters from CMBR

ArXiv ePrint: 1303.4317

JCAP10(2013)030

Contents

1 Introduction

A wide variety of observations of Cosmic Microwave Background (CMB) and Large Scale Structure (LSS) power spectra over the last decade have indicated that cosmic structures originated from seed fluctuations in the very early universe. The leading theory explaining the origin of the cosmological seed perturbations is cosmic inflation [1], a period of accelerated expansion at very early times. During the inflationary stage, microscopic quantum fluctuations were stretched to macroscopic scales to provide both the initial seeds for the primordial density perturbations and tensor (gravitational-wave) fluctuations [2–6]. Despite the simplicity of the inflationary paradigm, the exact mechanism by which cosmological perturbations are generated is not yet established.

In the standard slow-roll inflationary scenario associated with the dynamics of a single scalar field (the inflaton), density perturbations are due to fluctuations of the inflaton itself as it slowly rolls down along its potential. In the simplest case, fluctuations are of the adiabatic type, namely they are sourced by the degree of freedom that is dominating the energy density during inflation (the inflaton). In other mechanisms for the generation of perturbations, e.g., the curvaton mechanism [7], the final adiabatic perturbations are produced from an initial isocurvature mode associated with quantum fluctuations of a light scalar degree of freedom (other than the inflaton), whose energy density is negligible during inflation. The isocurvature perturbations are then transformed into adiabatic perturbations when the extra scalar degree of freedom (the curvaton) decays into radiation after the end of inflation. A precise measurement of the spectral index, n_S, of the scalar perturbations together with a detection of gravity-wave signals in CMB anisotropies through its B-mode polarization will provide a strong hint in favor of single-field models of inflation. Indeed, alternative mechanisms predict an amplitude of gravity waves far too small to be detectable by experiments aimed at observing the B-mode of the CMB polarization.

While inflation is the leading candidate model for the generation of primordial perturbations, in the words of ref. [8]: "Inflation is at the same time a spectacular phenomenological

JCAP10(2013)030

success, and an enduring theoretical challenge." The phenomenological success is that inflation is a simple model for the generation of seed perturbations. The theoretical challenge is to understand how inflation is embedded in a broader theory or model of fundamental physics. Detailed examination of the CMB perturbations are a possible way to discriminate among inflation models [9], perhaps even leading to a reconstruction of the inflaton potential [10] (see also ref. [11] for a recently-developed approach to the issue of how to constrain the inflationary scenario from the new CMB data).

Another application of CMB data is to search for evidence of "new" physics, like additional relativistic degrees of freedom at recombination [12], neutrino masses [13], early dark energy [14], modified gravity [15], or variation of fundamental constants like the fine-structure constant [16] or the gravitational constant [17].

The goal of this paper is to examine whether existing cosmological datasets can provide evidence for the dynamics of the inflaton field during inflation or evidence for new "neutrino" physics. Evidence for the dynamics of the inflaton field during inflation would be a departure from the Harrison-Zel'dovich (HZ) model (a scalar spectral index of unity and no tensor perturbations).[1] The departure from the HZ model could take the form of a scalar spectral index different than unity, a "running" (a scale-dependence) of the scalar spectral index, or evidence for tensor modes.[2]

The type of new "neutrino" physics we model would be a mass for neutrinos or additional relativistic degrees of freedom contributing to the expansion rate around the time of recombination.[3]

Our analysis will include CMB data from the nine-year data release of the Wilkinson Microwave Anisotropy Probe (WMAP9) [23], the South Pole Telescope (SPT) [24], and the Atacama Cosmology Telescope (ACT) [25], including measurements up to a maximum multipole number of $l_{\rm max} \simeq 3000$. We will also include information from measurements of baryonic acoustic oscillations (BAO) from galaxy surveys in the form of three datasets: data release 7 (SDSS-DR7) [26] and data release 9 (SDSS-DR9) [27] from the Sloan Digital Sky Survey, and the WiggleZ project [28]. We will also use data on the Hubble constant [29].

This study has two motivations. On one hand, the Planck collaboration [30] will release soon their first flow of data regarding the CMB anisotropies, and therefore it is timely to have a state-of-the-art pre-Planck assessment of slow-roll inflation. On the other hand, we wish to answer three basic questions:

1. Is the simple Harrison-Zel'dovich model compatible with current cosmological datasets, or is there support for a more complicated perturbation spectrum?

2. Is standard neutrino physics consistent with current cosmological datasets, or is there support for new neutrino physics in the form of a neutrino mass in excess of a few tenths of an electron volt or a change in the effective number of light neutrinos?

[1] We note that a scalar spectral index of unity is possible within slow-roll inflation [18, 19].

[2] Note that the estimated values for these parameters somewhat depend, other than on the data used, also on the assumptions about the underlying cosmological model. For example, the effect of considering more general reionization scenarios on the extraction of inflationary parameters has been investigated in refs. [20–22].

[3] Although we parameterize the additional relativistic degrees of freedom as a contribution to the effective number of light neutrinos, $N_{\rm eff}$, of course the new relativistic species need not be neutrinos.

JCAP10(2013)030

3. In the event that there is support for physics beyond the HZ spectrum and standard neutrinos, can one tell whether the data provides information about the primordial perturbation spectrum or the neutrino sector?

As we will see, all combinations of current datasets point to physics beyond the minimal HZ model with standard neutrino physics. In particular, allowing for either a scalar spectral index different from unity or an additional number of relativistic degrees of freedom, produces a significant increase in the goodness of fit with respect to the minimal HZ model. Information beyond that depends on the dataset used.

For a dataset with ACT (and not SPT), there is no significant increase in the goodness of fit by increasing the complexity of the perturbation spectra by allowing for running of the scalar perturbations and/or a tensor component. Concerning neutrino physics, there is no significant further increase in the goodness of fit by allowing for a nonzero neutrino mass. For the dataset with ACT, we can only say that a model with a scalar spectral index different than unity is a much better fit than the HZ model, and a model with a non-standard number of neutrinos is also a much better fit. In the sections below we will quantify these statements.

The situation is much different if we examine a dataset with SPT (and not ACT).[4] There are a significant increases in goodness of fit allowing either a running of the scalar spectral index (and not much increase in goodness of fit just by allowing a tensor component) on top of the HZ+n_s model, or a nonzero neutrino mass to the HZ model. Again, in the sections below we will quantify these statements.

Therefore, we conclude that a cosmological dataset including SPT suggests either a more complex perturbation spectrum than simply a scalar spectral index different than unity, or some other new physics such as a modification of the number of relativistic degrees of freedom. The data do not prefer one approach over the other.

The papers is organized as follows: in the next section we review the pertinent features of slow-roll inflation. In section 3 we review how neutrinos (or other light species) affect the CMB anisotropies. In section 4 we discuss our data analysis method and the datasets examined. Section 5 presents our results for cosmological parameters and the maximum likelihood for various models. In section 6 we discuss implications for physics beyond the HZ model for neutrino physics and for inflation. Section 7 contains our conclusions.

2 Slow-roll inflation and CMB anisotropies

As mentioned in the introduction, we will work under the hypothesis that the adiabatic perturbations originated within the single-field, slow-roll framework of inflation. It should be kept in mind that if future experiments do not detect isocurvature modes or large non-Gaussianity it will not be possible to distinguish directly the inflaton contribution from the, e.g., curvaton contribution, see ref. [32]. On the other hand, a detection of a significant amount of tensor modes through CMB anisotropies will disfavor curvaton-like models as they tend to generate a negligible tensor contribution.

Within the single-field slow-roll paradigm, many specific models for inflation have been proposed. We limit ourselves here to models with "normal" gravity (i.e., general relativity)

[4] Ref. [31] concluded that datasets including either ACT or SPT give a consistent picture for cosmological parameters, as long as HZ+n_S and HZ+n_s + $N_{\rm eff}$ are concerned. We find however that the answer to the question of whether cosmological data points to physics beyond an HZ +n_S model strongly depends on the choice of whether the dataset includes ACT or SPT.

JCAP10(2013)030

and a single order parameter for the vacuum, described by a canonical scalar field ϕ, the inflaton, with Lagrangian

$$\mathcal{L} = \frac{1}{2} g^{\mu\nu} \partial_\mu \phi \partial_\nu \phi - V(\phi). \tag{2.1}$$

The equations of motion for the spacetime are given by the Friedmann Equations, which for a homogeneous field ϕ are

$$\begin{aligned} H^2 &= \left(\frac{\dot{a}}{a}\right)^2 = \frac{8\pi}{3m_{\rm Pl}^2}\left[\frac{1}{2}\dot{\phi}^2 + V(\phi)\right], \\ \left(\frac{\ddot{a}}{a}\right) &= -\frac{4\pi}{3m_{\rm Pl}^2}\left[\dot{\phi}^2 - V(\phi)\right]. \end{aligned} \tag{2.2}$$

The equation of motion for the field ϕ is

$$\ddot{\phi} + 3H\dot{\phi} + V'(\phi) = 0. \tag{2.3}$$

We have assumed a flat Friedmann-Robertson-Walker metric $g_{\mu\nu} = \mathrm{diag}(1, -a^2, -a^2 - a^2)$, where $a(t)$ is the scale factor of the universe. Inflation is defined to be a period of accelerated expansion, $\ddot{a} > 0$. If the field evolution is monotonic in time, we can write the scale factor $a(\phi)$ and Hubble parameter $H(\phi)$ as functions of the field ϕ rather than time, i.e., we define all of our physical parameters along the trajectory in phase space $\dot{\phi}(\phi)$ corresponding to the classical solution to the equations of motion. Equations (2.2) and (2.3) can then be re-written exactly in the Hamilton-Jacobi form

$$\begin{aligned} \dot{\phi} &= -\frac{m_{\rm Pl}^2}{4\pi} H'(\phi), \\ \left[H'(\phi)\right]^2 - \frac{12\pi}{m_{\rm Pl}^2} H^2(\phi) &= -\frac{32\pi^2}{m_{\rm Pl}^4} V(\phi). \end{aligned} \tag{2.4}$$

These are completely equivalent to the second-order equation of motion. The second of the above equations is referred to as the Hamilton-Jacobi equation, and can be written in the useful form

$$H^2(\phi)\left[1 - \frac{1}{3}\epsilon(\phi)\right] = \left(\frac{8\pi}{3m_{\rm Pl}^2}\right) V(\phi), \tag{2.5}$$

where ϵ is defined to be

$$\epsilon(\phi) \equiv \frac{m_{\rm Pl}^2}{4\pi}\left(\frac{H'(\phi)}{H(\phi)}\right)^2. \tag{2.6}$$

The physical meaning of $\epsilon(\phi)$ can be seen by expressing $\ddot{a}$ in eq. (2.2) as

$$\left(\frac{\ddot{a}}{a}\right) = H^2(\phi)\left[1 - \epsilon(\phi)\right], \tag{2.7}$$

so that the condition for inflation, $(\ddot{a}/a) > 0$, is equivalent to $\epsilon < 1$. The scale factor is given by

$$a \propto e^N = \exp\left[\int_{t_0}^{t} H\, dt\right], \tag{2.8}$$

where the number of e-folds N is

$$N \equiv \int_t^{t_e} H\, dt = \int_\phi^{\phi_e} \frac{H}{\dot{\phi}}\, d\phi = \frac{2\sqrt{\pi}}{m_{\rm Pl}} \int_{\phi_e}^{\phi} \frac{d\phi}{\sqrt{\epsilon(\phi)}}. \tag{2.9}$$

JCAP10(2013)030

Most simple inflation models satisfy the slow-roll approximation, which is the assumption that the evolution of the field is dominated by the drag from the cosmological expansion, so that $\ddot{\phi} \simeq 0$ and $\dot{\phi} \simeq -V'/3H$. The equation of state of the scalar field is dominated by the potential, so that $p \simeq -\rho$, and the expansion rate is approximately $H^2 \simeq 8\pi V(\phi)/3m_{\rm Pl}^2$. The slow roll approximation is consistent if both the slope and curvature of the potential are small, V', $V'' \ll V$ (in units of the Planck mass $m_{\rm Pl}$). In this case the parameter ϵ can be expressed in terms of the potential as

$$\epsilon \equiv \frac{m_{\rm Pl}^2}{4\pi}\left(\frac{H'(\phi)}{H(\phi)}\right)^2 \simeq \frac{m_{\rm Pl}^2}{16\pi}\left(\frac{V'(\phi)}{V(\phi)}\right)^2. \tag{2.10}$$

We will also define a second "slow-roll parameter" η by

$$\begin{aligned}\eta(\phi) &\equiv \frac{m_{\rm Pl}^2}{4\pi}\left(\frac{H''(\phi)}{H(\phi)}\right) \\ &\simeq \frac{m_{\rm Pl}^2}{8\pi}\left[\frac{V''(\phi)}{V(\phi)} - \frac{1}{2}\left(\frac{V'(\phi)}{V(\phi)}\right)^2\right].\end{aligned} \tag{2.11}$$

Slow roll is then a consistent approximation for $\epsilon,\ \eta \ll 1$.

Perturbations created during inflation are of two types: scalar (or curvature) perturbations, which couple to the stress-energy of matter in the universe and form the "seeds" for structure formation, and tensor, or gravitational-wave perturbations, which do not couple to matter. Both scalar and tensor perturbations contribute to CMB anisotropies. Scalar fluctuations can also be interpreted as fluctuations in the density of the matter in the universe. Scalar fluctuations can be quantitatively characterized by the comoving curvature perturbation $P_{\mathcal{R}}$. As long as slow roll is attained, the curvature (scalar) perturbation at horizon crossing can be shown to be [1]

$$P_{\mathcal{R}}^{1/2}(k) = \left(\frac{H^2}{2\pi\dot{\phi}}\right)_{k=aH} = \left[\frac{H}{m_{\rm Pl}}\frac{1}{\sqrt{\pi\epsilon}}\right]_{k=aH}. \tag{2.12}$$

The fluctuation power spectrum is, in general, a function of wavenumber k, and is evaluated when a given mode crosses outside the horizon during inflation, $k = aH$. Outside the horizon, modes do not evolve, so the amplitude of the mode when it crosses back inside the horizon during a later radiation- or matter-dominated epoch is just its value when it left the horizon during inflation. Instead of specifying the fluctuation amplitude directly as a function of k, it is convenient to specify it as a function of the number of e-folds N before the end of inflation at which a mode crossed outside the horizon.

The scalar spectral index n_S for $P_{\mathcal{R}}$ is defined by

$$n_S - 1 \equiv \frac{d\ln P_{\mathcal{R}}}{d\ln k}, \tag{2.13}$$

so that a scale-invariant spectrum, in which modes have constant amplitude at horizon crossing, is characterized by $n_S = 1$.

To lowest order in slow roll, the power spectrum of tensor fluctuation modes and the corresponding tensor spectral index is given by [1]

$$\begin{aligned}P_T^{1/2}(k_N) &= \left[\frac{4H}{m_{\rm Pl}\sqrt{\pi}}\right]_{k=aH}, \\ n_T &\equiv \frac{d\ln P_T}{d\ln k}.\end{aligned} \tag{2.14}$$

The ratio of tensor-to-scalar modes is then $P_T/P_{\mathcal{R}} = 16\epsilon$, so that tensor modes are negligible for $\epsilon \ll 1$. In the limit of slow roll, the spectral indices n_S and n_T vary slowly or not at all with scale. We can write the spectral indices n_S and n_T to lowest order in terms of the slow-roll parameters ϵ and η as

$$\begin{aligned} n_S &\simeq 1 - 4\epsilon + 2\eta, \\ n_T &\simeq -2\epsilon. \end{aligned} \tag{2.15}$$

The tensor/scalar ratio is frequently expressed as a quantity r, which is conventionally normalized as

$$r \equiv 16\epsilon = \frac{P_T}{P_{\mathcal{R}}}. \tag{2.16}$$

The tensor spectral index is not an independent parameter, but is proportional to the tensor/scalar ratio, given to lowest order in slow roll by $n_T \simeq -2\epsilon = -r/8$. A given inflation model can therefore be described to lowest order in slow roll by three independent parameters: $P_{\mathcal{R}}$, P_T, and n_S.

Deviations from a simple power-law spectrum of perturbations are higher order in the slow-roll parameters, and thus serve as a test of the consistency of the slow-roll approximation. Scale dependence in the observables corresponds to scale dependence in the associated slow-roll parameter, and can be quantified in terms of the infinite hierarchy of inflationary flow equations [33],

$$\begin{aligned} \frac{d\epsilon}{dN} &= 2\epsilon\left(\eta - \epsilon\right), \\ \frac{d\eta}{dN} &= {}^2\lambda - \epsilon\eta, \\ &\vdots \\ \frac{d^\ell\lambda}{dN} &= \left[(\ell-1)\eta - \ell\epsilon\right]{}^\ell\lambda + {}^{(\ell+1)}\lambda. \end{aligned} \tag{2.17}$$

The higher-order flow parameters are defined by

$$\begin{aligned} \epsilon &\equiv 2M_P^2\left(\frac{H'(\phi)}{H(\phi)}\right)^2, \\ \eta &\equiv 2M_P^2\frac{H''(\phi)}{H(\phi)}, \\ {}^2\lambda &\equiv 4M_P^4\frac{H'(\phi)H'''(\phi)}{H^2(\phi)}, \\ &\vdots \\ {}^\ell\lambda &\equiv \left(2M_P^2\right)^\ell\frac{H'(\phi)^{(\ell-1)}}{H(\phi)^\ell}\frac{d^{(\ell+1)}H(\phi)}{d\phi^{(\ell+1)}}, \end{aligned} \tag{2.18}$$

where the prime denotes derivatives with respect to scalar field ϕ. It is then straightforward to calculate the scale-dependence of the spectral index by relating the wavenumber k to the number of e-folds N,

$$\begin{aligned} \frac{dn}{d\ln k} \equiv n_{\rm run} &= -\frac{1}{1-\epsilon}\frac{d}{dN}\left(2\eta - 4\epsilon\right) \\ &= 10\epsilon\eta - 8\epsilon^2 - 2\left({}^2\lambda\right) + \mathcal{O}(\epsilon^3) + \cdots. \end{aligned} \tag{2.19}$$

Since the running depends on higher-order flow parameters than the spectral index itself, it is an independent parameter, even in slow-roll inflation models. In typical single-field inflation models, the running of the spectral index is negligible, so a detection of scale dependence in the spectral index would rule out a large class of viable single-field inflation models, and would therefore be a powerful probe of inflationary physics.

3 Neutrinos and CMB anisotropies

In what follows we we examine the possibility of new neutrino physics as an alternative to extending the complexity of primordial perturbations.

One direction for new neutrino physics is a change in the effective number of relativistic degrees of freedom, $N_{\rm eff}$, that defines the physical energy density in relativistic particles $\rho_{\rm rad}$, defined by

$$\rho_{\rm rad} = \left[1 + \frac{7}{8}\left(\frac{4}{11}\right)^{4/3} N_{\rm eff}\right]\rho_\gamma\,, \tag{3.1}$$

where ρ_γ is the energy density of the CMB photons and $N_{\rm eff}$ is the effective number of light neutrino species. In the standard scenario, assuming three active massless neutrino species with standard electroweak interactions and the present CMB temperature of $T_\gamma = 2.726K$ (see, e.g., ref. [34]), the expected value is $N_{\rm eff} = 3.046$. This is slightly larger than 3 because of non-instantaneous neutrino decoupling (see, e.g., ref. [35]). As mentioned previously, any new species that is relativistic around recombination will contribute to $N_{\rm eff}$, whether it is a neutrino species or not. The exact contribution of a new relativistic species will depend on the number of spin degrees of freedom, whether the new species is a boson or fermion, and the temperature of decoupling of the new species.

We also consider the possibility of a mass for one or more of the three known active neutrino species. The present contribution to the overall energy density is given by

$$\Omega_\nu h^2 = \Sigma_{i=1,2,3}\ \ \frac{m_i}{92.5\ {\rm eV}}, \tag{3.2}$$

where m_i are the masses of the three neutrino mass eigenstates.

A change in neutrino physics can have important implications for interpretation of inflationary parameters from CMB anisotropies, see refs. [36–38]. For example, varying $N_{\rm eff}$ can have an impact on determination of n_S and its running, since it changes both the position of the CMB peaks in the angular spectrum and the structure of the "damping tail" at very large multipoles (see ref. [12]). In general, a higher $N_{\rm eff}$ can put higher values of n_S in better agreement with the data, i.e., there is a positive correlation between the two parameters.

Masses for neutrinos also have important implications for interpretation of inflationary parameters from CMB anisotropies. Massive neutrinos damp the dark-matter fluctuations on scales below the horizon when they become nonrelativistic (see e.g., [39]). Neutrinos with masses $m_\nu \lesssim 0.3\,{\rm eV}$ are relativistic at recombination and affect the CMB anisotropy mainly through gravitational lensing, while neutrinos with larger masses slightly increase the CMB small-scale anisotropy by damping the gravitational potential at recombination. The final result is a small anti-correlation with n_S, i.e., larger neutrino masses shift the constraints on n_S to smaller values.

JCAP10(2013)030

4 Data analysis method

The analysis method we adopt is based on the publicly available Monte Carlo Markov Chain (MCMC) package *cosmomc* [40] with a convergence diagnostic done through the Gelman and Rubin statistic.

We sample the following four-dimensional standard set of cosmological parameters, adopting flat priors on them: the baryon and cold dark matter densities Ω_b and Ω_c, the angular size of the sound horizon at decoupling θ, and the optical depth to reionization τ.

As discussed in a separate section, we will also vary the relativistic number of degrees of freedom parameter $N_{\rm eff}$ and the total neutrino mass Σm_ν. The standard three-neutrino framework predicts $N_{\rm eff} = 3.046$, while oscillation neutrino experiments place a lower bound $\Sigma m_\nu > 0.05\,{\rm eV}$ [41].

For the inflationary parameters we consider the scalar spectral index n_S and its running $n_{\rm run}$, the overall normalization of the spectrum A_S at $k = 0.002\ {\rm Mpc}^{-1}$ and the amplitude of the tensor modes relative to the scalar, $r = A_T/A_S$, again at $k = 0.002\ {\rm Mpc}^{-1}$.

We consider purely adiabatic initial conditions and we impose spatial flatness.

We analyze the following set of CMB data: WMAP9 [23], SPT [24], and ACT [25], including measurements up to a maximum multipole number of $l_{\rm max} \simeq 3000$. For all these experiments we make use of the publicly available codes and data. For the ACT experiment we use the "lite" version of the likelihood [42].

We also consider the effect of including additional datasets to the basic datasets just described. Consistently with the measurements of HST [29], we consider a Gaussian prior on the Hubble constant $H_0 = 73.8 \pm 2.4\,{\rm km\,s^{-1}\,Mpc^{-1}}$. We also include information from measurements of baryonic acoustic oscillations (BAO) from galaxy surveys. Here, we follow the approach presented in ref. [23] combining three datasets: SDSS-DR7 [26], SDSS-DR9 [27] and WiggleZ [28].

Since, as we see in the next section, the ACT and the SPT datasets are providing significantly different conclusions on inflationary parameters, we will include them separately. In what follows we will consider two combinations of datasets. We refer to an analysis using the WMAP9 + ACT + HST + BAO datasets as the "extended ACT" (eACT) dataset and to an analysis with the WMAP9 + SPT + HST + BAO datasets as the "extended SPT" (eSPT) dataset.

We use the Markov chains obtained from CosmoMC to reconstruct the posterior distributions of each of the model parameters. In the tables, we present our results in the form of the 68% credible interval for each parameter, i.e., the interval symmetric around the mean containing 68% of the total posterior probability. We make an exception to this rule in those cases where the posterior probability is not vanishingly small at the edge of the prior range; this happens in particular around $r = 0$ and $\sum m_\nu = 0$. In this case we adopt the following rule: if the maximum of the posterior distribution is clearly distinguished from zero, we quote the 68% interval as above; otherwise, we quote a 95% upper limit.

We also use our Markov chains to recover the maximum likelihood (i.e., minimum χ^2) parameter values. We use the minimum χ^2 values estimated from the chains to perform an approximate model comparison by computing the likelihood ratio (actually, equivalently, the difference in χ^2) between models. As a rule of thumb, given two models $\mathcal{M}_1$ and $\mathcal{M}_2$, where the latter reduces to the former for a particular choice of parameter values (in which case the two models are said to be "nested"), we say that the data show preference for $\mathcal{M}_2$ over $\mathcal{M}_1$ when the absolute value of $\Delta\chi^2 \equiv \chi^2_{\rm min}(\mathcal{M}_2) - \chi^2_{\rm min}(\mathcal{M}_1)$ is larger than the number of

JCAP10(2013)030

additional parameters in the extended model. A more accurate assessment of the relative probability of the two models would require the calculation of the Bayesian evidence; see e.g. refs. [43] and [44] for an application to models with extra neutrinos and to inflationary models, respectively.

We note however that MCMC methods are usually optimized to sample the full posterior distribution around the region of maximum probablity, and not to recover the exact value and position of the maximum likelihood. The precision to be associated with our estimate of the minimum χ^2 can be evaluated by computing the probability of finding in the chains a sample having a χ^2 within $\delta(\chi^2)$ from the actual minimum (see e.g. [45]). This probability depends on the dimensionality of the parameter space and on the number of independent samples in the chains. We let our chains run until we can claim a 95% probability of having found the best-fit model with an uncertainty $\delta(\chi^2) \leq 1$.

5 Extensions of the HZ model and eACT and eSPT

As a first step in our analysis we evaluate the compatibility of current cosmological datasets eSPT and eACT with a simple reference model, which we choose to be the Harrison-Zel'dovich (HZ) model with $n_S = 1$, $r = 0$, $n_{\rm run} = 0$, $m_\nu = 0$, and $N_{\rm eff} = 3.046$. We then consider extensions of this model involving more complex perturbation spectra, with various combinations of $n_S \neq 1$, $r > 0$, and $n_{\rm run} \neq 0$. Then we examine extensions of the HZ model with nonstandard neutrino physics with combinations of $m_\nu \neq 0$ and/or $N_{\rm eff} \neq 3.046$.

5.1 Extensions of the perturbation sector

The results of our analysis with regard to perturbation spectra is reported in table 1. As stated in the previous section, we analyze the eACT and eSPT datasets and we consider different cases for primordial perturbations and compare them with the reference HZ model. In all models analyzed in this section we assume massless neutrinos and $N_{\rm eff} = 3.046$.

As we can see from the table, both for the eACT and eSPT datasets, models with $n_S \neq 1$ are highly favored over the HZ reference model.

For the eSPT dataset, allowing one additional parameter, n_S, to vary results in change in χ^2 of $\Delta\chi^2 \equiv (-2\log\mathcal{L}) - (-2\log\mathcal{L}_{HZ}) = -28.7$. The one-dimensional probability distribution for n_S with the eSPT dataset is shown in figure 1. For the eACT dataset, allowing one additional parameter, n_S, to vary results in $\Delta\chi^2 \equiv (-2\log\mathcal{L}) - (-2\log\mathcal{L}_{HZ}) = -9.7$. The one-dimensional probability distribution for n_S with the eACT dataset is also shown in figure 1.

If we allow other parameters describing the perturbation spectra to vary, such as $n_{\rm run}$ and r, there are different indications from the different datasets. Let us first consider the eSPT dataset.

The natural parameter space for constraining simple slow-roll inflation models is to include the tensor/scalar ratio r in addition to spectral tilt n_S. Two-dimensional contours for n_S vs. r are shown in figure 2, along with the predictions of three simple slow-roll models. For the eSPT dataset, allowing r to vary in addition to allowing n_S to vary results in a very marginal decrease in χ^2 of -0.9 compared to a model just allowing n_S to vary. Hence, the data do not seem to call for the additional variable r. However, the situation is quite different if we allow a running of the scalar spectral index, $n_{\rm run} \neq 0$, either keeping $r = 0$ or allowing r to vary. Adding one additional parameter, $n_{\rm run}$, results in $\Delta\chi^2 = -36.6$ compared to the reference HZ model, which corresponds to a change in χ^2 of -7.9 compared to the HZ $+n_S$

JCAP10(2013)030

Dataset	Parameter	Reference Model	Inflation-Motivated Extensions			
		HZ	HZ $+n_S$	HZ $+n_S + r$	HZ $+n_S + n_{\rm run}$	HZ $+n_S + r + n_{\rm run}$
eSPT	$100\,\Omega_b h^2$	2.331 ± 0.025	2.225 ± 0.032	2.228 ± 0.032	2.236 ± 0.031	2.272 ± 0.036
	$\Omega_c h^2$	0.1148 ± 0.0017	0.1167 ± 0.0018	0.1166 ± 0.0018	0.1180 ± 0.0019	0.1178 ± 0.0018
	$100\,\theta$	1.0430 ± 0.0009	1.0419 ± 0.0009	1.0419 ± 0.0010	1.0422 ± 0.0009	1.0424 ± 0.0009
	$\log[10^{10} A_S]$	3.12 ± 0.03	3.21 ± 0.03	3.20 ± 0.03	3.14 ± 0.04	3.04 ± 0.07
	τ	0.096 ± 0.013	0.078 ± 0.012	0.077 ± 0.012	0.090 ± 0.014	0.095 ± 0.015
	n_S	$\equiv 1$	0.959 ± 0.008	0.962 ± 0.008	1.037 ± 0.029	1.107 ± 0.045
	r	$\equiv 0$	$\equiv 0$	< 0.12 [d]	$\equiv 0$	0.28 ± 0.16
	$n_{\rm run}$	$\equiv 0$	$\equiv 0$	$\equiv 0$	-0.029 ± 0.011	-0.051 ± 0.015
	H_0 [a]	71.33 ± 0.65	69.33 ± 0.74	69.42 ± 0.76	69.08 ± 0.76	69.51 ± 0.78
	$-2\log\mathcal{L}$ [b]	7653.4	7624.7	7625.6	7616.8	7615.9
	$\Delta\chi^2$ [c]	$\equiv 0$	-28.7	-27.8	-36.6	-37.5
eACT	$100\,\Omega_b h^2$	2.356 ± 0.027	2.282 ± 0.035	2.290 ± 0.037	2.283 ± 0.035	2.302 ± 0.038
	$\Omega_c h^2$	0.1163 ± 0.0021	0.1165 ± 0.0021	0.1162 ± 0.0021	0.1166 ± 0.0021	0.1167 ± 0.0022
	$100\,\theta$	1.0416 ± 0.0016	1.0399 ± 0.0018	1.0399 ± 0.0017	1.0400 ± 0.0017	1.0403 ± 0.0018
	$\log[10^{10} A_S]$	3.14 ± 0.03	3.19 ± 0.03	3.18 ± 0.03	3.19 ± 0.04	3.13 ± 0.05
	τ	0.102 ± 0.014	0.090 ± 0.014	0.089 ± 0.013	0.092 ± 0.015	0.094 ± 0.015
	n_S	$\equiv 1$	0.971 ± 0.009	0.976 ± 0.009	0.978 ± 0.031	1.016 ± 0.042
	r	$\equiv 0$	$\equiv 0$	< 0.18 [d]	$\equiv 0$	< 0.34 [d]
	$n_{\rm run}$	$\equiv 0$	$\equiv 0$	$\equiv 0$	-0.003 ± 0.011	-0.014 ± 0.014
	H_0 [a]	70.50 ± 0.71	69.24 ± 0.83	69.43 ± 0.83	69.24 ± 0.81	69.47 ± 0.83
	$-2\log\mathcal{L}$ [b]	7617.9	7608.2	7608.4	7608.3	7608.7
	$\Delta\chi^2$ [c]	$\equiv 0$	-9.7	-9.5	-9.6	-9.2

[a] km s^{-1} Mpc^{-1}.

[b] When comparing to the χ^2 values reported e.g. in the WMAP9 paper [23], it should be taken into account that we use a pixel based likelihood at low ls instead than the Gibbs-based likelihood.

[c] $\Delta\chi^2 \equiv (-2\log\mathcal{L}) - (-2\log\mathcal{L}_{HZ})$.

[d] 95% c.l.

Table 1. Augmenting the minimal Harrison-Zel'dovich cosmological model through inflationary parameters. Listed are posterior means for the cosmological parameters from the indicated datasets (errors refer to 68% confidence intervals, unless otherwise stated).

model. If we allow *both* r and $n_{\rm run}$ to vary (in addition to allowing n_S to vary) there is a gain of $\Delta\chi^2 = -37.5$ compared to the reference HZ model, or a change in χ^2 of -8.8 compared to the HZ $+n_S$ model. The eSPT dataset strongly prefers a running of the scalar spectral index. The one-dimensional probability distributions for n_S, r and $n_{\rm run}$ with the eSPT dataset are shown in figure 1. Two-dimensional contours of r vs. n_S, $n_{\rm run}$ vs. n_S and $n_{\rm run}$ vs. r are also shown in figure 1.

The eACT dataset also prefers a scalar spectral index different from unity. Recall that adding one additional parameter n_S results in a decrease in χ^2 compared to the reference HZ model of $\Delta\chi^2 = -9.7$. If we then allow one additional parameter, either r or $n_{\rm run}$, there is only a very marginal change in χ^2 beyond the HZ + n_S model. Even allowing both additional parameters $n_{\rm run}$ and r again results in a very marginal decrease in χ^2 at the expense of two

JCAP10(2013)030

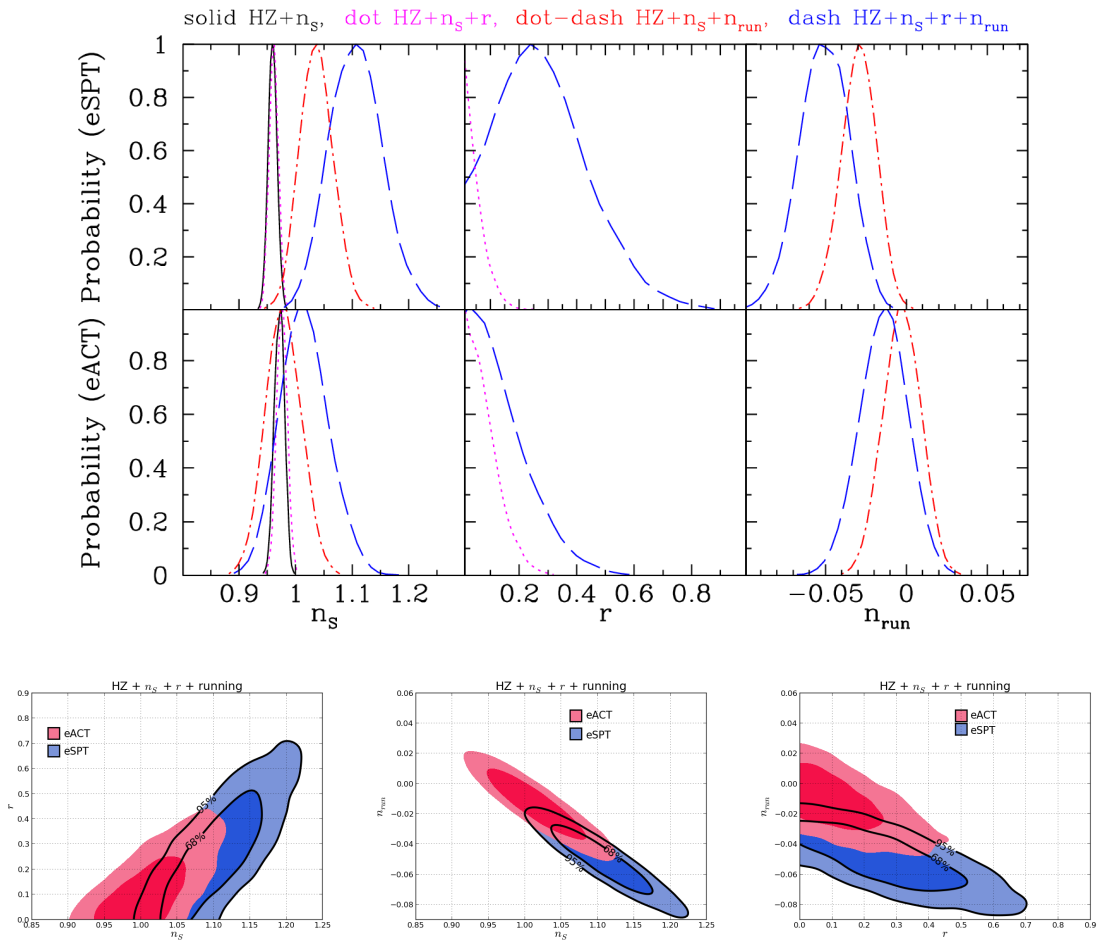

Figure 1. One- and two-dimensional posterior probabilities for n_S, r, and $n_{\rm run}$. Upper panel: one-dimensional parameter posteriors for the models considered in the text, using the eSPT (top row) and eACT (bottom row) datasest. Lower panel: two-dimensional posteriors for the HZ+n_s+r+running case. Dark- and light-shaded regions correspond to 68 and 95% credible intervals, respectively.

additional parameters. The one-dimensional probability distributions for n_S, r and $n_{\rm run}$ with the eACT dataset are also shown in figure 1, and the two-dimensional contours of r vs. n_S, $n_{\rm run}$ vs. n_S and $n_{\rm run}$ vs. r are also shown in figure 1.

We summarize our findings with respect to n_s and $n_{\rm run}$ in figure 3, where we compare the constraints on these parameters for the different model/dataset combinations considered in the paper. It is clear from this figure that the tension between the two datasets increases when the model complexity is also increased. Moreover, as discussed above in the context of the goodness-of-fit of the various models, we also notice that the results of parameter estimation from eACT are more stable, with respect to eSPT, to the increase of the complexity of the model.

Our conclusion is that the eSPT and eACT datasets are not consistent, as long as inflation-motivated extensions to the minimal model are concerned. While both call for a scalar spectral index different than unity, the eSPT dataset seems to be better described by a more complicated perturbation spectrum than just a scalar spectrum of constant spectral

JCAP10(2013)030

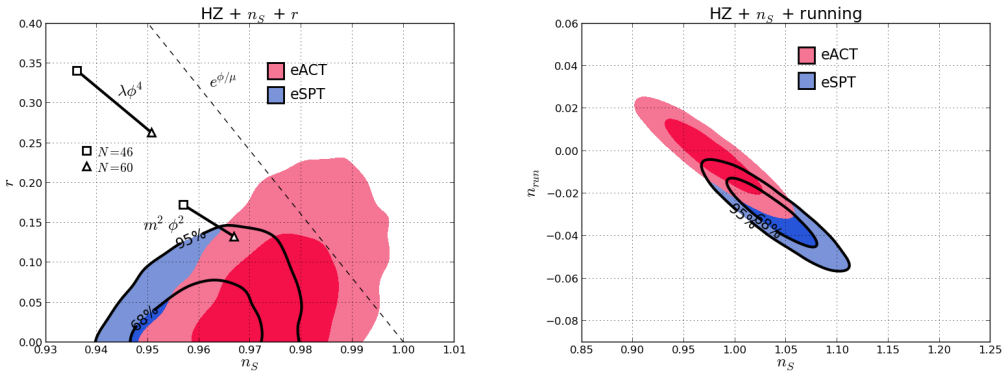

Figure 2. Two-dimensional probability in the n_S vs. r plane for the HZ $+n_S + r$ model in the left panel, and the HZ $+n_S + n_{run}$ model in the right panel.

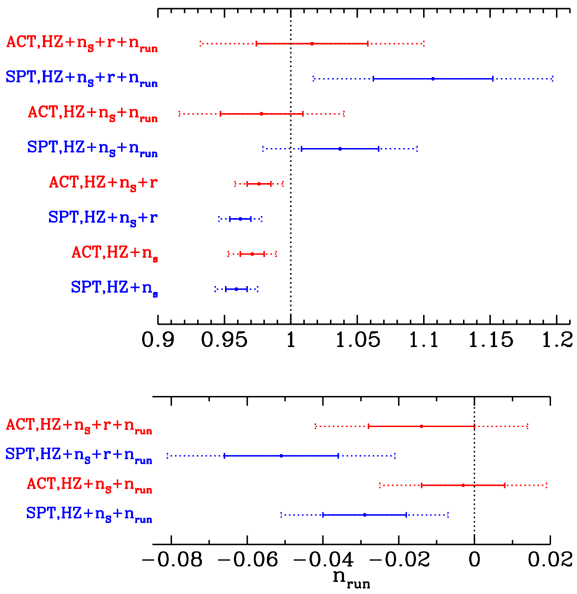

Figure 3. Comparing the constraints on n_s (top panel) and $n_{\rm run}$ (bottom panel) for different model/datasets combinations. The solid and dashed bars denote 1- and 2-σ constraints, respectively.

index. On the other hand, the eACT dataset seems to be well described by a constant scalar spectral index (slightly less than unity), and does not seem to require additional complexity.

5.2 Extensions of the neutrino sector

We now repeat the analysis presented in previous subsection but now considering the possibility of an extra effective neutrino number and including neutrino masses.

The constraints from the eSPT and eACT dataset are in table 2. For both datasets, adding the additional parameter $N_{\rm eff}$ greatly improves the fit. In fact, allowing $N_{\rm eff}$ improves the fits of both eSPT and eACT by about as much as allowing the spectral index to vary from unity.

However, allowing the neutrino mass to vary, we again again obtain different indications from the two datasets. For the SPT dataset, adding a neutrino mass improves the χ^2 by -8.1

JCAP10(2013)030

Dataset	Parameter	Reference Model	Neutrino-Motivated Extensions		
		HZ	HZ $+N_{\rm eff}$	HZ $+m_\nu$	HZ $+N_{\rm eff}+m_\nu$
eSPT	$100\,\Omega_b h^2$	2.331 ± 0.025	2.311 ± 0.024	2.330 ± 0.024	2.332 ± 0.037
	$\Omega_c h^2$	0.1148 ± 0.0017	0.1394 ± 0.0057	0.1100 ± 0.0023	0.1315 ± 0.0057
	$100\,\theta$	1.0430 ± 0.0009	1.0404 ± 0.0010	1.0434 ± 0.0009	1.0412 ± 0.0011
	$\log[10^{10} A_S]$	3.12 ± 0.03	3.15 ± 0.03	3.12 ± 0.03	3.14 ± 0.03
	τ	0.096 ± 0.013	0.085 ± 0.012	0.103 ± 0.014	0.095 ± 0.014
	$N_{\rm eff}$	$\equiv 3.046$	4.26 ± 0.26	$\equiv 3.046$	4.45 ± 0.32
	$\sum m_\nu$ [a]	$\equiv 0$	$\equiv 0$	0.39 ± 0.14	0.96 ± 0.53
	H_0 [b]	71.33 ± 0.65	75.5 ± 1.1	69.82 ± 0.76	74.0 ± 1.2
	$-2\log\mathcal{L}$ [c]	7653.4	7625.9	7645.3	7617.1
	$\Delta\chi^2$ [d]	$\equiv 0$	-27.5	-8.1	-36.3
eACT	$100\,\Omega_b h^2$	2.356 ± 0.027	2.332 ± 0.029	2.358 ± 0.029	2.337 ± 0.029
	$\Omega_c h^2$	0.1163 ± 0.0021	0.1318 ± 0.0057	0.1156 ± 0.0021	0.1296 ± 0.0057
	$100\,\theta$	1.0416 ± 0.0016	1.0382 ± 0.0020	1.0421 ± 0.0016	1.0387 ± 0.0020
	$\log[10^{10} A_S]$	3.14 ± 0.03	3.16 ± 0.03	3.13 ± 0.03	3.15 ± 0.03
	τ	0.102 ± 0.014	0.097 ± 0.014	0.105 ± 0.015	0.099 ± 0.014
	$N_{\rm eff}$	$\equiv 3.046$	3.88 ± 0.28	$\equiv 3.046$	3.80 ± 0.28
	$\sum m_\nu$ [a]	$\equiv 0$	$\equiv 0$	0.24 ± 0.15	< 0.46 [e]
	H_0 [b]	70.50 ± 0.71	73.2 ± 1.1	69.82 ± 0.79	72.4 ± 1.2
	$-2\log\mathcal{L}$ [c]	7617.9	7609.7	7616.7	7609.2
	$\Delta\chi^2$ [d]	$\equiv 0$	-8.2	-1.2	-8.7

[a] eV.
[b] km s^{-1} Mpc^{-1}.
[c] When comparing to the χ^2 values reported e.g. in the WMAP9 paper [23], it should be taken into account that we use a pixel based likelihood at low ls instead than the gibbs-based likelihood.
[d] $\Delta\chi^2 \equiv (-2\log\mathcal{L}) - (-2\log\mathcal{L}_{HZ})$.
[e] 95% c.l.

Table 2. Augmenting the minimal Harrison-Zel'dovich cosmological model through new neutrino physics. Listed are posterior means for the cosmological parameters from the indicated datasets (errors refer to 68% credible intervals, unless otherwise stated).

if $N_{\rm eff}$ is kept fixed and by -8.8 if it is allowed to vary. For the ACT dataset, on the contrary, the goodness of fit improves only marginally (at the price of one additional parameter) by allowing a non-zero neutrino mass, independently of whether $N_{\rm eff}$ is fixed or not.

In figure 5 we compare the constraints on $N_{\rm eff}$ and $\sum m_\nu$ for the different model/dataset combinations considered in the paper. Again we see the same trend observed in the case of the spectrum parameters, namely that the values estimated from the two datasets tend to diverge as new parameters are added, and that the values estimated from eACT are more stable than those estimated from eSPT when the complexity of the model is increased.

JCAP10(2013)030

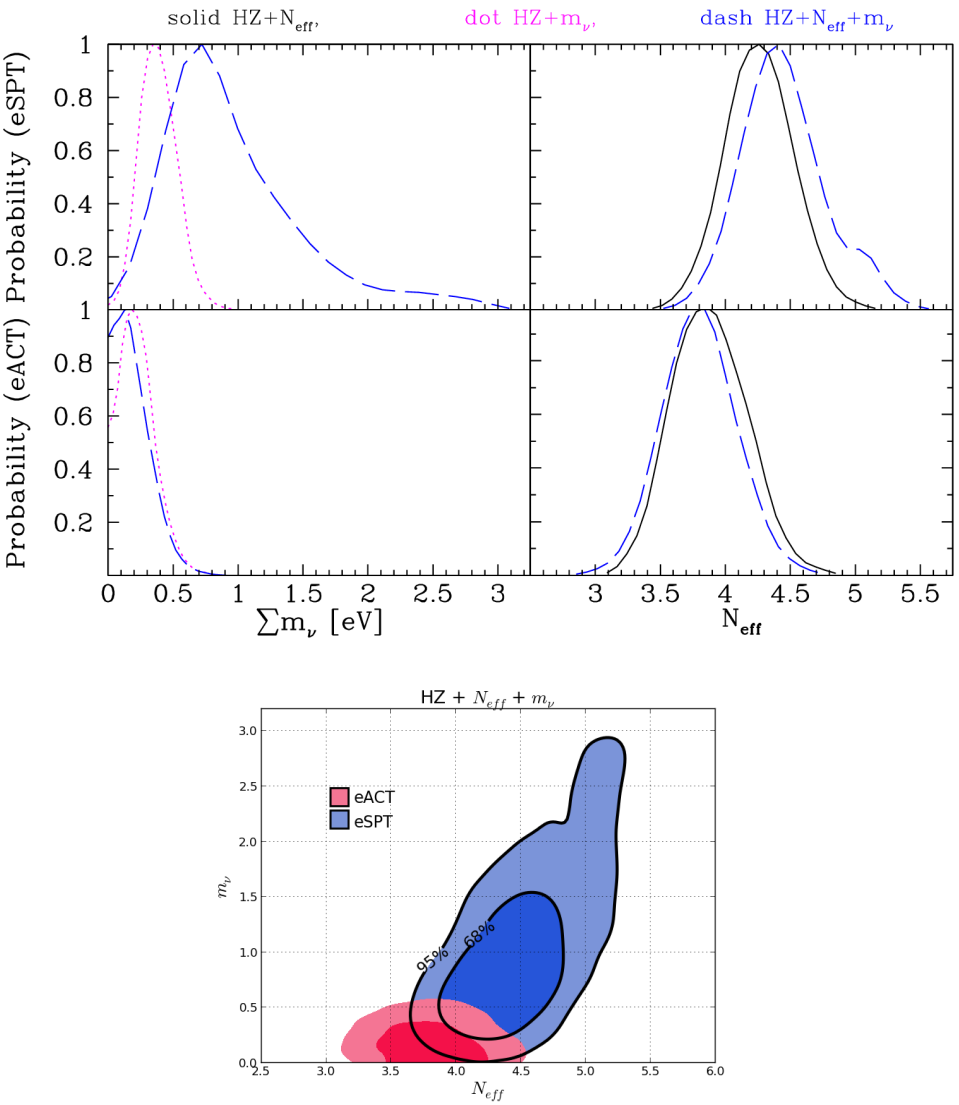

Figure 4. One- and two-dimensional posterior probabilities for the eACT and eSPT data for the parameters $N_{\rm eff}$ and m_ν.

6 Directions for new physics

Using the two data combinations described here, models with either primordial perturbations beyond the HZ model or additional light degrees of freedom provide a much better fit than the HZ model. Thus, cosmological data point to some interesting new physics. Unfortunately, the direction is unclear.

Probably the most dramatic explanation would be additional light degrees of freedom: it would be very surprising if there is a new light species beyond the standard model of particle physics (as we have emphasized, it need not be extra neutrino species, although we parameterize them as such).

For the eACT dataset, just adding a tilt to the scalar spectrum seems to be all that is demanded of the data. This would tell us something about inflation, but there are a large number of inflation models that can give a slightly red spectrum.

JCAP10(2013)030

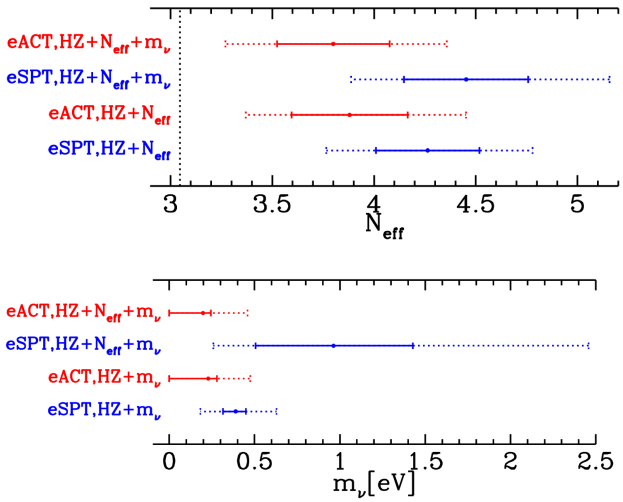

Figure 5. Comparing the constraints on $N_{\rm eff}$ (top panel) and m_ν (bottom panel) for different model/datasets combinations. The solid and dashed bars denote 1- and 2-σ constraints, respectively.

For the eSPT dataset however, the data seems to demand more than simply a tilt to the scalar spectrum. A much improved fit can be obtained by allowing the possibility of a large running of the scalar spectrum. The running could be so large as to have a large impact in inflation model building and call in doubt the simple slow-roll approximation. Alternatively, as data seem to indicate a non-power-law scalar spectral index with a very large variation of the spectral index, one might invoke models where the flattening of the inflaton potential is obtained through the inclusion of large quantum corrections in the mass parameter [46] which result in large variation of the spectral index with the scale. Another class of models which allow for a large negative running are models in which inflation occurs near an inflection point of the potential, where the third derivative V''' of the potential is substantial, and the higher-order slow roll parameter ${}^2\lambda$ is comparable to the lower-order parameters ϵ and η. Inflection point inflation models have been argued, e.g. in ref. [47], to be characteristic of inflation on the string landscape.

7 Conclusions

We analyzed the recently released Atacama Cosmology Telescope (ACT) and South Pole Telescope (SPT) data in combination with the Wilkinson Microwave Anisotropy Probe 9-year data (WMAP9), the Sloan Digital Sky Survey Data Release 9, the WiggleZ large-scale structure data, and the Hubble Space Telescope determination of the Hubble parameter (HST). We tested these data against two cosmological scenarios: (1) a scale-invariant, purely scalar "Harrison-Zel'dovich" (HZ) power spectrum with the addition of parameters motivated by inflationary cosmology, tilt n_S, nonzero tensor/scalar ratio r, and running of the spectral index n_S, and (2) the HZ power spectrum with a nonstandard effective neutrino number $N_{\rm eff}$ and/or neutrino mass m_ν. We find that both the extended ACT data (eACT) and the extended SPT data (eSPT) favor extensions to the simple HZ model to at least 95% confidence.

In the case of the inflation-motivated extensions to HZ, both eACT and eSPT favor a deviation from a scale-invariant power spectrum with "red" tilt, $n_S < 1$, and neither show

JCAP10(2013)030

any evidence for a nonzero tensor/scalar ratio. The eACT data are consistent with negligible running of the spectral index, as predicted by simple slow-roll inflation models. The eACT data are consistent at the 95% confidence level with simple chaotic inflation $V(\phi) = m^2\phi^2$, and with power-law inflation, $V(\phi) \propto \exp(\phi/\mu)$, as well as "small-field" models predicting negligible tensors and $n_S < 1$. The eSPT data, however, are inconsistent with a purely power-law power spectrum, favoring negative running of the spectral index $n_{\rm run} = -0.029 \pm 0.011$ in the case with a prior of $r = 0$, and $n_{\rm run} = -0.051 \pm 0.015$ in the case where $r \neq 0$ is allowed. While the eSPT data are not in disagreement with the most general possible single-field inflation models, they are in significant conflict with slow-roll models predicting $n_{\rm run} \ll n_S$. The eACT data are consistent with such models.

In the case of extensions to HZ involving additional light degrees of freedom, eACT and eSPT again produce qualitatively different constraints. Both the eACT and eSPT data favor additional light degrees of freedom, with $N_{\rm eff} = 3.88 \pm 0.28$ for eACT, and $N_{\rm eff} = 4.26 \pm 0.26$ for eSPT (with a prior of $m_\nu = 0$). The eACT and eSPT data differ, however, with respect to nonzero neutrino masses. The eACT data are consistent at 95% with zero neutrino mass, with $\sum m_\nu = 0.24 \pm 0.15\,{\rm eV}$ (with a prior of $N_{\rm eff} \equiv 3.04$), and $\sum m_\nu < 0.46\,{\rm eV}$ (with $N_{\rm eff} \neq 3.04$). The eSPT data favor nonzero neutrino mass, with $\sum m_\nu = 0.39 \pm 0.14\,{\rm eV}$ (with a prior of $N_{\rm eff} \equiv 3.04$), and $\sum m_\nu = 0.96 \pm 0.53\,{\rm eV}$ (with $N_{\rm eff} \neq 3.04$).

In either scenario, HZ + inflation or HZ + neutrinos, considering the ACT and SPT data separately results in qualitatively different conclusions about extensions to a standard scale-invariant Λ+Cold Dark Matter concordance cosmology, a tension which is not evident when considering combined constraints from ACT and SPT.

Acknowledgments

A.R. is supported by the Swiss National Science Foundation (SNSF), project "The non-Gaussian Universe" (project number: 200021140236). WHK is funded by the U.S. National Science Foundation grant NSF-PHY-1066278. The work of ML has been supported by Ministero dell'Istruzione, dell'Università e della Ricerca (MIUR) through the PRIN grant "Galactic and extragalactic polarized microwave emission" (contract number PRIN 2009XZ54H2-002). We would like to thank Luca Amendola for useful discussion.

References

[1] For reviews, see D.H. Lyth and A. Riotto, *Particle physics models of inflation and the cosmological density perturbation*, *Phys. Rept.* **314** (1999) 1 [hep-ph/9807278] [INSPIRE]; W.H. Kinney, *Cosmology, inflation and the physics of nothing*, astro-ph/0301448 [INSPIRE].

[2] A.A. Starobinsky, *Relict Gravitation Radiation Spectrum and Initial State of the Universe. (In Russian)*, *JETP Lett.* **30** (1979) 682 [Pisma Zh. Eksp. Teor. Fiz. **30** (1979) 719] [INSPIRE].

[3] V.F. Mukhanov and G.V. Chibisov, *Quantum Fluctuation and Nonsingular Universe. (In Russian)*, *JETP Lett.* **33** (1981) 532 [INSPIRE].

[4] A.H. Guth and S. Pi, *Fluctuations in the New Inflationary Universe*, *Phys. Rev. Lett.* **49** (1982) 1110 [INSPIRE].

[5] S. Hawking, *The Development of Irregularities in a Single Bubble Inflationary Universe*, *Phys. Lett.* **B 115** (1982) 295 [INSPIRE].

[6] J.M. Bardeen, P.J. Steinhardt and M.S. Turner, *Spontaneous Creation of Almost Scale - Free Density Perturbations in an Inflationary Universe*, *Phys. Rev.* **D 28** (1983) 679 [INSPIRE].

JCAP10(2013)030

[7] S. Mollerach, *Isocurvature Baryon Perturbations and Inflation*, *Phys. Rev.* **D 42** (1990) 313 [INSPIRE];
K. Enqvist and M.S. Sloth, *Adiabatic CMB perturbations in pre - big bang string cosmology*, *Nucl. Phys.* **B 626** (2002) 395 [hep-ph/0109214] [INSPIRE];
D.H. Lyth and D. Wands, *Generating the curvature perturbation without an inflaton*, *Phys. Lett.* **B 524** (2002) 5 [hep-ph/0110002] [INSPIRE];
T. Moroi and T. Takahashi, *Effects of cosmological moduli fields on cosmic microwave background*, *Phys. Lett.* **B 522** (2001) 215 [*Erratum ibid.* **B 539** (2002) 303] [hep-ph/0110096] [INSPIRE].

[8] E. Martinec, P. Adshead and M. Wyman, *Chern-Simons EM-flation*, *JHEP* **02** (2013) 027 [arXiv:1206.2889] [INSPIRE].

[9] S. Dodelson, W.H. Kinney and E.W. Kolb, *Cosmic microwave background measurements can discriminate among inflation models*, *Phys. Rev.* **D 56** (1997) 3207 [astro-ph/9702166] [INSPIRE].

[10] J.E. Lidsey, A.R. Liddle, E.W. Kolb, E.J. Copeland, T. Barreiro et al., *Reconstructing the inflation potential : An overview*, *Rev. Mod. Phys.* **69** (1997) 373 [astro-ph/9508078] [INSPIRE].

[11] J. Martin, C. Ringeval and V. Vennin, *Encyclopaedia Inflationaris*, arXiv:1303.3787 [INSPIRE].

[12] Z. Hou, R. Keisler, L. Knox, M. Millea and C. Reichardt, *How Massless Neutrinos Affect the Cosmic Microwave Background Damping Tail*, *Phys. Rev.* **D 87** (2013) 083008 [arXiv:1104.2333] [INSPIRE].

[13] J. Lesgourgues and S. Pastor, *Massive neutrinos and cosmology*, *Phys. Rept.* **429** (2006) 307 [astro-ph/0603494] [INSPIRE].

[14] E. Calabrese, D. Huterer, E.V. Linder, A. Melchiorri and L. Pagano, *Limits on Dark Radiation, Early Dark Energy and Relativistic Degrees of Freedom*, *Phys. Rev.* **D 83** (2011) 123504 [arXiv:1103.4132] [INSPIRE].

[15] E. Di Valentino, A. Melchiorri, V. Salvatelli and A. Silvestri, *Parametrised modified gravity and the CMB Bispectrum*, *Phys. Rev.* **D 86** (2012) 063517 [arXiv:1204.5352] [INSPIRE].

[16] E. Menegoni, M. Archidiacono, E. Calabrese, S. Galli, C. Martins et al., *The Fine Structure Constant and the CMB Damping Scale*, *Phys. Rev.* **D 85** (2012) 107301 [arXiv:1202.1476] [INSPIRE].

[17] S. Galli, A. Melchiorri, G.F. Smoot and O. Zahn, *From Cavendish to PLANCK: Constraining Newton's Gravitational Constant with CMB Temperature and Polarization Anisotropy*, *Phys. Rev.* **D 80** (2009) 023508 [arXiv:0905.1808] [INSPIRE].

[18] A. Vallinotto, E.J. Copeland, E.W. Kolb, A.R. Liddle and D.A. Steer, *Inflationary potentials yielding constant scalar perturbation spectral indices*, *Phys. Rev.* **D 69** (2004) 103519 [astro-ph/0311005] [INSPIRE].

[19] A.A. Starobinsky, *Inflaton field potential producing the exactly flat spectrum of adiabatic perturbations*, *JETP Lett.* **82** (2005) 169 [Pisma Zh. Eksp. Teor. Fiz. **82** (2005) 187] [astro-ph/0507193] [INSPIRE].

[20] S. Pandolfi, A. Cooray, E. Giusarma, E.W. Kolb, A. Melchiorri et al., *Harrison-Z'eldovich primordial spectrum is consistent with observations*, *Phys. Rev.* **D 81** (2010) 123509 [arXiv:1003.4763] [INSPIRE].

[21] S. Pandolfi, E. Giusarma, E.W. Kolb, M. Lattanzi, A. Melchiorri et al., *Impact of general reionization scenarios on extraction of inflationary parameters*, *Phys. Rev.* **D 82** (2010) 123527 [arXiv:1009.5433] [INSPIRE].

JCAP10(2013)030

[22] S. Pandolfi, A. Ferrara, T.R. Choudhury, A. Melchiorri and S. Mitra, *Data-constrained reionization and its effects on cosmological parameters*, *Phys. Rev.* **D 84** (2011) 123522 [arXiv:1111.3570] [INSPIRE].

[23] WMAP collaboration, G. Hinshaw et al., *Nine-Year Wilkinson Microwave Anisotropy Probe (WMAP) Observations: Cosmological Parameter Results*, *Astrophys. J. Suppl.* **208** (2013) 19 [arXiv:1212.5226] [INSPIRE].

[24] Z. Hou, C. Reichardt, K. Story, B. Follin, R. Keisler et al., *Constraints on Cosmology from the Cosmic Microwave Background Power Spectrum of the 2500-square degree SPT-SZ Survey*, arXiv:1212.6267 [INSPIRE].

[25] J.L. Sievers, R.A. Hlozek, M.R. Nolta, V. Acquaviva, G.E. Addison et al., *The Atacama Cosmology Telescope: Cosmological parameters from three seasons of data*, arXiv:1301.0824 [INSPIRE].

[26] N. Padmanabhan, X. Xu, D.J. Eisenstein, R. Scalzo, A.J. Cuesta et al., *A 2 per cent distance to z=0.35 by reconstructing baryon acoustic oscillations - I. Methods and application to the Sloan Digital Sky Survey*, *Mon. Not. Roy. Astron. Soc.* **427** (2012) 2132 [arXiv:1202.0090] [INSPIRE].

[27] L. Anderson, E. Aubourg, S. Bailey, D. Bizyaev, M. Blanton et al., *The clustering of galaxies in the SDSS-III Baryon Oscillation Spectroscopic Survey: Baryon Acoustic Oscillations in the Data Release 9 Spectroscopic Galaxy Sample*, *Mon. Not. Roy. Astron. Soc.* **427** (2013) 3435 [arXiv:1203.6594] [INSPIRE].

[28] C. Blake, S. Brough, M. Colless, C. Contreras, W. Couch et al., *The WiggleZ Dark Energy Survey: Joint measurements of the expansion and growth history at $z < 1$*, *Mon. Not. Roy. Astron. Soc.* **425** (2012) 405 [arXiv:1204.3674] [INSPIRE].

[29] A.G. Riess, L. Macri, S. Casertano, H. Lampeitl, H.C. Ferguson et al., *A 3Space Telescope and Wide Field Camera 3*, *Astrophys. J.* **730** (2011) 119 [*Erratum ibid.* **732** (2011) 129] [arXiv:1103.2976] [INSPIRE];
W.L. Freedman, B.F. Madore, V. Scowcroft, C. Burns, A. Monson et al., *Carnegie Hubble Program: A Mid-Infrared Calibration of the Hubble Constant*, *Astrophys. J.* **758** (2012) 24 [arXiv:1208.3281] [INSPIRE].

[30] See http://www.rssd.esa.int/index.php?project=planck.

[31] E. Calabrese, R.A. Hlozek, N. Battaglia, E.S. Battistelli, J.R. Bond et al., *Cosmological Parameters from Pre-Planck CMB Measurements*, arXiv:1302.1841 [INSPIRE].

[32] W.H. Kinney, A.M. Dizgah, B.A. Powell and A. Riotto, *Inflaton or Curvaton? Constraints on Bimodal Primordial Spectra from Mixed Perturbations*, *Phys. Rev.* **D 86** (2012) 023527 [arXiv:1203.0693] [INSPIRE].

[33] W.H. Kinney, *Inflation: Flow, fixed points and observables to arbitrary order in slow roll*, *Phys. Rev.* **D 66** (2002) 083508 [astro-ph/0206032] [INSPIRE].

[34] D. Fixsen, *The Temperature of the Cosmic Microwave Background*, *Astrophys. J.* **707** (2009) 916 [arXiv:0911.1955] [INSPIRE].

[35] G. Mangano, G. Miele, S. Pastor, T. Pinto, O. Pisanti et al., *Relic neutrino decoupling including flavor oscillations*, *Nucl. Phys.* **B 729** (2005) 221 [hep-ph/0506164] [INSPIRE].

[36] M. Archidiacono, E. Calabrese and A. Melchiorri, *The Case for Dark Radiation*, *Phys. Rev.* **D 84** (2011) 123008 [arXiv:1109.2767] [INSPIRE].

[37] J. Hamann, S. Hannestad, J. Lesgourgues, C. Rampf and Y.Y. Wong, *Cosmological parameters from large scale structure - geometric versus shape information*, *JCAP* **07** (2010) 022 [arXiv:1003.3999] [INSPIRE].

JCAP10(2013)030

[38] R. Bowen, S.H. Hansen, A. Melchiorri, J. Silk and R. Trotta, *The Impact of an extra background of relativistic particles on the cosmological parameters derived from microwave background anisotropies*, *Mon. Not. Roy. Astron. Soc.* **334** (2002) 760 [astro-ph/0110636] [INSPIRE].

[39] W. Hu, D.J. Eisenstein and M. Tegmark, *Weighing neutrinos with galaxy surveys*, *Phys. Rev. Lett.* **80** (1998) 5255 [astro-ph/9712057] [INSPIRE].

[40] A. Lewis and S. Bridle, *Cosmological parameters from CMB and other data: A Monte Carlo approach*, *Phys. Rev.* **D 66** (2002) 103511 [astro-ph/0205436] [INSPIRE].

[41] G.L. Fogli, E. Lisi, A. Marrone, A. Melchiorri, A. Palazzo, P. Serra, J. Silk and A. Slosar, *A global analysis of neutrino oscillations*, *Conf. Proc. C* **060726** (2006) 284.

[42] J. Dunkley, E. Calabrese, J. Sievers, G. Addison, N. Battaglia et al., *The Atacama Cosmology Telescope: likelihood for small-scale CMB data*, arXiv:1301.0776 [INSPIRE].

[43] J. Norena, C. Wagner, L. Verde, H.V. Peiris and R. Easther, *Bayesian Analysis of Inflation III: Slow Roll Reconstruction Using Model Selection*, *Phys. Rev.* **D 86** (2012) 023505 [arXiv:1202.0304] [INSPIRE].

[44] S.M. Feeney, H.V. Peiris and L. Verde, *Is there evidence for additional neutrino species from cosmology?*, *JCAP* **04** (2013) 036 [arXiv:1302.0014] [INSPIRE].

[45] J. Hamann, *Evidence for extra radiation? Profile likelihood versus Bayesian posterior*, *JCAP* **03** (2012) 021 [arXiv:1110.4271] [INSPIRE].

[46] E.D. Stewart, *Flattening the inflaton's potential with quantum corrections*, *Phys. Lett.* **B 391** (1997) 34 [hep-ph/9606241] [INSPIRE].

[47] L. McAllister, S. Renaux-Petel and G. Xu, *A Statistical Approach to Multifield Inflation: Many-field Perturbations Beyond Slow Roll*, *JCAP* **10** (2012) 046 [arXiv:1207.0317] [INSPIRE].

JCAP10(2013)030

PHYSICAL REVIEW D **88,** 087302 (2013)

Updating constraints on inflationary features in the primordial power spectrum with the Planck data

Micol Benetti*

Physics Department and ICRA, Università di Roma La Sapienza, Piazzale Aldo Moro 2, 00185 Rome, Italy
Physics Department and INFN, Università di Roma La Sapienza, Piazzale Aldo Moro 2, 00185 Rome, Italy
(Received 12 September 2013; published 21 October 2013)

We present new constraints on possible features in the primordial inflationary density perturbation power spectrum in light of the recent cosmic microwave background anisotropy measurements from the Planck satellite. We found that the Planck data hints for the presence of features in two different ranges of angular scales, corresponding to multipoles $10 < \ell < 60$ and $150 < \ell < 300$, with a decrease in the best-fit χ^2 value with respect to the featureless "vanilla" ΛCDM model of $\Delta\chi^2 \simeq 9$ in both cases.

DOI: 10.1103/PhysRevD.88.087302 PACS numbers: 98.80.Es, 98.80.Jk, 95.30.Sf

I. INTRODUCTION

The recent results from the Planck satellite on the cosmic microwave background (CMB, hereafter) angular power spectrum are in very good agreement with the theoretical expectations of the simplest inflationary model based on a single, minimally coupled, scalar field [1].

However, as already discussed in [2], some interesting hints for deviations from scale invariance are present in the Planck data and are certainly worthwhile of further investigation.

In this brief paper, we present new constraints on an inflationary model with steplike features as proposed by [3,4].

Steplike features in the inflationary potential are expected in theories with multiple interacting scalar fields as supergravity-inspired models, where supersymmetry-breaking phase transitions occur during inflation. At the same time, steplike features are able to produce localized oscillations in the CMB angular power spectra and, in particular, as we have already shown in [5], to provide a better fit with respect to the featureless case using the WMAP data. It is therefore timely to analyze the new Planck data, which covers a larger multipole range respect to WMAP, and to quantify the compatibility of the features with this new data set.

A first analysis has already been provided by the Planck collaboration in [2]. However, as we will discuss in the next section, this analysis assumed an analytical and, therefore, approximate formula for the features and investigated a range of angular scales different from the one analyzed in [5]. In particular, as we will discuss below, the analysis presented in [2] for steplike feature did not cover the range of low multipoles. Moreover, the remaining cosmological parameters were not let to vary freely but fixed at their best-fit values, therefore neglecting possible correlations.

Here, on the contrary, we assume the same parameter range of [5] and we integrate the set of differential equations to accurately compute the oscillations in the CMB angular spectrum, given a steplike feature in the inflationary potential (again, see [5]). Moreover, we let all the parameters to vary freely, taking into account possible correlations between the parameters. For comparison, we also use the analytical model adopted in [2].

The paper is organized as follows: in Sec. II we briefly explain the analysis method adopted; in Sec. III we present the results of our analysis and in Sec. IV we summarize our conclusions.

II. MODEL AND ANALYSIS METHOD

Following the work of Adams *et al.* [6], we consider a model with a steplike feature added to a chaotic potential $V(\phi) = m^2\phi^2/2$, for the inflaton field ϕ, of the form

$$V(\phi) = \frac{1}{2}m^2\phi^2\left[1 + c\tanh\left(\frac{\phi - b}{d}\right)\right], \tag{1}$$

where b is the value of the field where the step is located, c is the height of the step, and d its slope.

In order to evaluate the density perturbation spectrum we numerically evolve the relevant equations that, for brevity, we do not report here and we refer the reader to [5–14].

Moreover, we also adopt an analytical parametrization for the scalar primordial power spectrum given by [15,16]:

$$P_R(k) = \exp\left[\ln P_0(k) + \frac{A_f}{3}\frac{k\eta_f}{\sinh\left(\frac{k\eta_f}{x_d}\right)}W'(k\eta_f)\right], \tag{2a}$$

$$W'(x) = \left(-3 + \frac{9}{x^2}\right)\cos 2x + \left(15 - \frac{9}{x^2}\right)\frac{\sin 2x}{2x}, \tag{2b}$$

where $P_0(k) = A_s\left(\frac{k}{k_*}\right)^{n_s - 1}$ is the smooth spectrum with the standard power law form, A_f is the kinetic energy perturbation of the step, η_f is the step crossing time in units of Mpc and x_d the dimensionless damping scale. Using this method, by placing the features directly on the density power spectrum, we do not integrate the system of differential equations, with a significantly smaller computing time. This is the same approach that has been used in [2].

*Micol.Benetti@Roma1.infn.it

TABLE I. Best-fit values and 68% confidence limits for the cosmological and step parameters. The second and third columns refer to ΛCDM model; the fourth, fifth and sixth column show the constraints on the features model using the same prior ranges of [5] with, respectively, the numerical integration approach and the analytical approximate approach; the last two columns show the constraints obtained using the analytical approach and the parameter range of [2].

	ΛCDM model		Numerical integration[a]		Approximate[b,d]	Approximate parametrization[c,d]	
Parameter	Best-fit[e]	68% limits	Best-fit[e]	68% limits	Best-fit[e]	Best-fit[e]	68% limits
$100\Omega_b h^2$	2.210	2.220 ± 0.028	2.220	2.220 ± 0.028	2.199	2.220	2.220 ± 0.029
$\Omega_c h^2$	0.1203	0.1199 ± 0.0027	0.1212	0.1203 ± 0.0028	0.1212	0.1209	0.1200 ± 0.0026
$100\ \theta$	1.0413	1.0413 ± 0.0006	1.0411	1.0413 ± 0.0006	1.0410	1.0410	1.0413 ± 0.0006
τ	0.090	0.090 ± 0.013	0.089	0.091 ± 0.014	0.092	0.094	0.089 ± 0.010
n_s	0.963	0.961 ± 0.007	0.959	0.959 ± 0.008	0.958	0.960	0.960 ± 0.007
$10^9 A_s$[f]	2.21	2.20 ± 0.05	2.20	2.21 ± 0.06	2.22	2.22	2.22 ± 0.04
b	⋯	⋯	14.66	14.99 ± 0.29	⋯	⋯	⋯
$\log c$	⋯	⋯	−2.85	-2.99 ± 0.61	⋯	⋯	⋯
$\log d$	⋯	⋯	−1.44	-1.32 ± 0.54	⋯	⋯	⋯
A_f	⋯	⋯	⋯	⋯	0.90	0.10	0.10 ± 0.06
$\ln \eta_f/\mathrm{Mpc}$	⋯	⋯	⋯	⋯	7.17	7.25	6.34 ± 3.7
Age [Gyr]	13.82	13.82 ± 0.05	13.83	13.82 ± 0.05	13.83	13.84	13.82 ± 0.05
z_{re}	11.3	11.1 ± 1.1	11.1	11.2 ± 1.2	11.4	11.5	11.1 ± 0.9
H_0 [km s^{-1} Mpc^{-1}]	67.2	67.3 ± 1.2	66.7	67.1 ± 1.2	66.7	66.7	67.3 ± 1.2
$-2 \log \mathcal{L}$		9803		9794	9794	9793	

[a]Uses initial potential as Eq. (1).
[b]Uses low-ℓ priors.
[c]Uses Planck [2] priors.
[d]Uses approximate parametrization as Eq. (2).
[e]Calculated using BOBYQA algorithm.
[f]$k_0 = 0.05$ Mpc^{-1}.

We therefore consider a "vanilla" theoretical model with the addition of features in the primordial spectrum, parametrized in both cases (numerical and analytical) by three parameters. Together with these parameters we vary the usual cosmological parameters as the baryon density, ω_b, the cold dark matter density, ω_c, the ratio between the sound horizon and the angular diameter distance at decoupling, θ, the optical depth, τ, the primordial scalar amplitude, $\mathcal{A}_s$, and, finally the primordial spectral index n_s. We also vary the nuisance foreground parameters [17], we consider purely adiabatic initial conditions, fix the sum of neutrino masses to 0.06 eV, and we limit the analysis to scalar perturbations.

We then perform a Monte Carlo Markov chain analysis via the publicly available package COSMOMC [18]. We use a modified version of the CAMB ([19]) code, needed to compute the CMB anisotropies spectrum for given values of the parameters describing this type of inflationary model. The Gelman and Rubin criteria is used to evaluate the convergence of the chains, demanding that $R - 1 \leq 0.02$. By default COSMOMC uses a simple Metropolis-Hastings algorithm that needs to evaluate the model likelihood at each point traversed by the chains. It is designed to draw samples from the posterior distribution and not to find the best-fit model. Thus, in the analysis we use the bound optimization BY quadratic approximation (BOBYQA) algorithm, developed by Powell [20], that is an optimized method for minimizing functions of more variables and is implemented in COSMOMC. The quoted results in this paper for the best-fit values of the parameters, as well as for the value of the χ^2 itself, are obtained using Powell's routines.

The data set considered in this work, available from the European Space Agency website,[1] are:

(i) high-l Planck temperature ($50 < \ell < 2500$, derived from the CAMSPEC likelihood by combining spectra in the frequency range 100–217 GHz [17]),
(ii) low-ℓ Planck temperature ($2 < \ell < 49$, derived from a component-separation algorithm, Commander, applied to maps in the frequency range 30–353 GHz [21]),
(iii) low-ℓ WMAP 9-year polarization [22].

The likelihood code is provided by the Planck collaboration [17].

The pivot wave number selected is $k_\star = k_0 = 0.05$ Mpc^{-1}, which is the same value chosen by the Planck collaboration for this type of study. This parameter is degenerate with the value of the position of the step in ϕ, e.g. changing k_0 from 0.05 to 0.002 Mpc^{-1} shifts the step value b by ∼0.5 towards lower values (see [5]).

[1]http://www.sciops.esa.int.

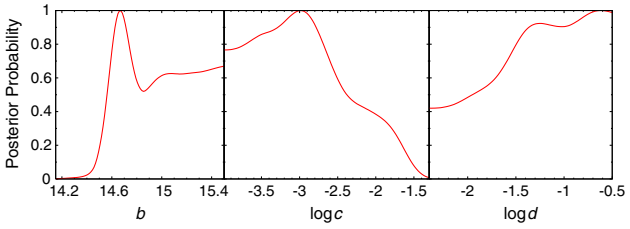

FIG. 1 (color online). One-dimensional posterior probability densities for the step parameters of an inflationary model with steplike features in the potential, obtained by numerical integration of the mode equations.

III. RESULTS AND DISCUSSION

We essentially consider three types of analysis with the results reported in Table I. The first analysis assumes a simple ΛCDM model with a featureless spectrum. For the second analysis we considered the steplike model in the inflationary potential, numerically integrating the relevant equations and assuming the following priors on the corresponding parameters: $14.2 \leq b \leq 15.5$, $-4 \leq \log c \leq -1$, $-2.5 \leq \log d \leq -0.5$. These results are reported in the fourth and fifth columns of Table I. The comparison between the results presented in the two tables is useful in order to identify the impact of primordial features on the constraints on the standard ΛCDM parameters.

In the third analysis we used the analytical formula presented in [2] with the same choice of priors and given by $0 \leq A_f \leq 0.2$, $0 \leq \ln(\eta_f/\mathrm{Mpc}) \leq 12$, $-1 \leq \ln x_d \leq 5$. These values are reported in the last two columns of Table I.

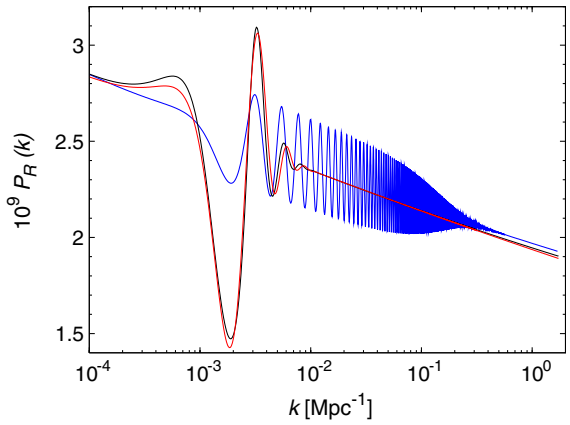

FIG. 2 (color online). Primordial power spectra for inflationary potentials with step. The red line shows the best-fit spectrum in the case of the numerical integration approach with $m = 7.5 \times 10^{-6}$, using the prior ranges of [5], while the black line shows the best-fit spectrum of the respective approximate parametrization analysis. The blue line plots the best-fit approximate scalar power in the range of parameters of [2], which causes features in $150 < \ell < 300$.

As we can see, introducing oscillations in the primordial spectrum either by numerical integration of the relevant equation or by using the above-mentioned analytical formula, reduces the χ^2 of the best-fit model by $\Delta\chi^2 \sim 9$. However, the feature parameters are poorly constrained, as also shown in Fig. 1 where we report the posterior probabilities for the numerical integrating analysis. Moreover, the introduction of features has little effect on the constraints on the remaining, nuisance, cosmological parameters.

In Fig. 1 we can also note that the posteriors are better defined with respect to those present in our previous work of [5] although they are significantly different from a Gaussian distribution. In particular, we see that the use of the Planck data eliminates a bimodal form in the posterior

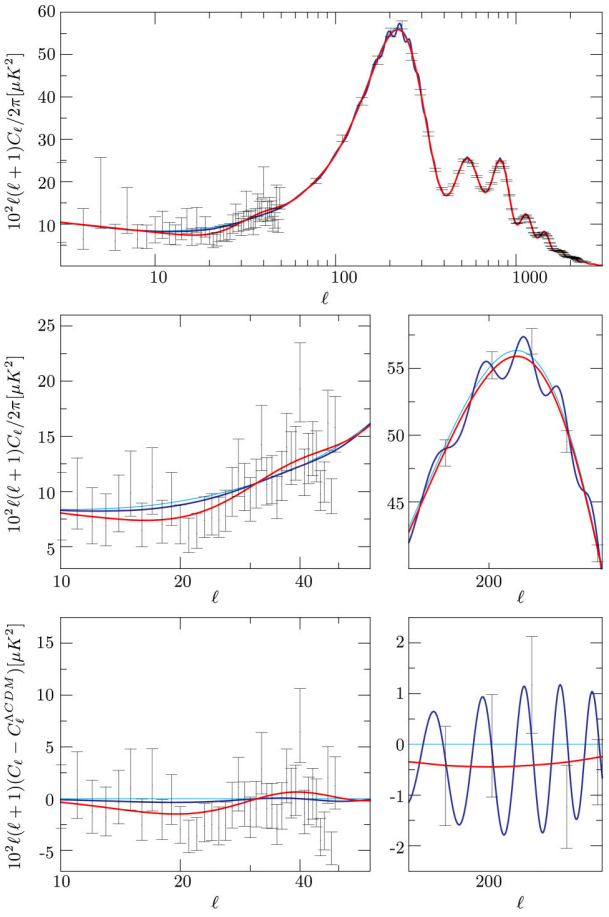

FIG. 3 (color online). Upper panel: Temperature power spectrum for the best-fit ΛCDM model (light blue line) and for two step models with features at low-ℓ (red line) and features at the first peak (blue line), corresponding to the best-fit of the numerical integration (with the same priors as [5]) and analytical approach (with the same priors as [2]), compared to the Planck temperature data. Middle panel: The same as above, zoomed in the region $10 < \ell < 60$ and $150 < \ell < 300$. Lower panel: The same as above, plotted in terms of residuals with respect to the ΛCDM best-fit.

probability for the b parameter, present in the WMAP9 data. As we see in Table I, both the analytical and the numerical method provide the same reduction in the χ^2 value. In particular, the results for the analytical method are fully consistent with those reported in [2].

However, the effects on the CMB angular spectra are drastically different. The best-fit model obtained from a numerical integration provides significantly different oscillations with respect to the best-fit model obtained in the case of the analytical approximation.

We can clearly see this in Fig. 2, where we plot the primordial power spectra for the best-fit models obtained in the case of numerical integration (red line) and for the case of analytical approximation (blue line) used in the Planck analysis.

In Fig. 3 we compare the best-fit CMB angular spectra obtained in the two cases. As we can see, the numerical integration method identifies the oscillations on large angular scales ($10 < \ell < 60$) while the analytical method provides a better fit by producing oscillations around the first Doppler peak.

This difference is essentially due to the different choice of priors on the feature parameters assumed in the two analyses. To check this, we changed the priors for the analysis based on the analytical formula to $0.8 \leq A_f \leq 1$, $7 \leq \ln(\eta_f/\mathrm{Mpc}) \leq 8$, $0 \leq \ln x_d \leq 0.5$, obtaining the best-fit values reported in Table I, sixth column. As we can see, the best-fit has now $A_f \sim 0.9$, a value that was excluded by the choice of priors used in [2]. The corresponding primordial spectrum is reported in Fig. 2 as a black line and, as we can see, is in full agreement with the best-fit spectra obtained from the analysis made assuming the numerical integration method.

We can therefore conclude that one needs to be extremely cautious in the choice of priors when looking for features in the CMB spectra since probability distributions for the parameters are highly multimodal.

IV. CONCLUDING REMARKS

We have presented updated constraints on an inflationary model with a steplike feature in the inflaton potential, using WMAP9 low-ℓ polarization data and the recent temperature data released by the Planck experiment. Such a feature would induce oscillations in the anisotropy power spectrum with magnitude, extent and position depending on three step parameters.

We have considered two different methods. The first uses a numerical routine to accurately calculate the primordial density spectrum corresponding to a given inflaton potential. The second employs an approximate form of the power spectrum, reproducing the features caused by a steplike inflaton potential. For the latter analysis, we have also studied the impact of different prior ranges, corresponding to features in the low-ℓ and mid-ℓ ranges.

The analysis done performing the exact integration of the mode equations shows a minimum χ^2 value with $\Delta\chi^2 \simeq 9$ with respect to the featureless ΛCDM model, at the cost of three new parameters. This improvement is due to the presence of oscillations in the multipole range $10 < \ell < 60$. These results can be matched using instead the analytical approach, by choosing a suitable prior range for the parameters, different from the one used in [2]. On the other hand, the results for the analytical method with the same prior range as [2], corresponding instead to oscillations in the range $150 < \ell < 300$, are fully consistent with those reported there. The improvement in the goodness of fit is still $\Delta\chi^2 \simeq 9$, although it is caused by oscillations in a completely different range of scales.

Finally, the constraints on the step parameters are improved with respect to our previous work [5].

Future polarization data, as discussed in [5] will clearly further improve the constraints presented here.

Our results are in reasonable agreement, given the different method of analysis adopted, also with those recently presented in [23].

ACKNOWLEDGMENTS

It is a pleasure to thank Jan Hamann for providing the numerical code that computes the primordial inflationary spectra. I would like to thank Carlo Luciano Bianco for useful discussion.

[1] P. A. R. Ade *et al.* (Planck Collaboration), arXiv:1303.5076.
[2] P. A. R. Ade *et al.* (Planck Collaboration), arXiv:1303.5082.
[3] J. A. Adams, G. G. Ross, and S. Sarkar, Phys. Lett. B **391**, 271 (1997).
[4] J. A. Adams, G. G. Ross, and S. Sarkar, Nucl. Phys. **B503**, 405 (1997).
[5] M. Benetti, S. Pandolfi, M. Lattanzi, M. Martinelli, and A. Melchiorri, Phys. Rev. D **87**, 023519 (2013).
[6] J. A. Adams, B. Cresswell, and R. Easther, Phys. Rev. D **64**, 123514 (2001).
[7] S. M. Leach and A. R. Liddle, Phys. Rev. D **63**, 043508 (2001).
[8] S. M. Leach, M. Sasaki, D. Wands, and A. R. Liddle, Phys. Rev. D **64**, 023512 (2001).
[9] H. V. Peiris *et al.* (WMAP Collaboration), Astrophys. J. Suppl. Ser. **148**, 213 (2003).

[10] J. Hamann, L. Covi, A. Melchiorri, and A. Slosar, Phys. Rev. D **76**, 023503 (2007).
[11] L. Covi, J. Hamann, A. Melchiorri, A. Slosar, and I. Sorbera, Phys. Rev. D **74**, 083509 (2006).
[12] M. J. Mortonson, C. Dvorkin, H. V. Peiris, and W. Hu, Phys. Rev. D **79**, 103519 (2009).
[13] D. K. Hazra, M. Aich, R. K. Jain, L. Sriramkumar, and T. Souradeep, J. Cosmol. Astropart. Phys. 10 (2010) 008.
[14] A. Ashoorioon and A. Krause, arXiv:hep-th/0607001.
[15] P. Adshead and W. Hu, Phys. Rev. D **85**, 103531 (2012).
[16] P. Adshead, C. Dvorkin, W. Hu, and E. A. Lim, Phys. Rev. D **85**, 023531 (2012).
[17] P. A. R. Ade *et al.* (Planck Collaboration), arXiv:1303.5075.
[18] A. Lewis and S. Bridle, Phys. Rev. D **66**, 103511 (2002).
[19] A. Lewis, A. Challinor, and A. Lasenby, Astrophys. J. **538**, 473 (2000).
[20] M. J. D. Powell, University of Cambridge Report No. DAMTP 2009/NA06.
[21] P. A. R. Ade *et al.* (Planck Collaboration), arXiv:1303.5072.
[22] G. Hinshaw, D. Larson, E. Komatsu, D. N. Spergel, C. L. Bennett, J. Dunkley, M. R. Nolta, M. Halpern *et al.*, arXiv:1212.5226.
[23] P. D. Meerburg and D. N. Spergel, arXiv:1308.3705.

Bibliography

[1] E. W. Kolb, M. S. Turner, “The Early Universe," AddisonWesley Publishing Company (1993)

[2] A. Friedmann, Zeitschrift fur Physik, Vol. 21, Issue 1, p.326-332 (1924)

[3] G. Lemaitre, Annales de la Societe Scientifique de Bruxelles, A47, p. 49-59 (1927)

[4] H. P. Robertson, Astrophys. J. 82: 284-301 (1935)

[5] A. G. Walker, Proceedings of the London Mathematical Society 2 42 (1): 90-127 (1936)

[6] B. Ryden, “Introduction to cosmology,” San Francisco, USA: Addison-Wesley (2003)

[7] V. M. Slipher, Popular Astronomy, Vol. 23, p. 21-24 (1915)

[8] C. Wirtz, Astronomische Nachrichten, Vol. 215; p. 349 (1922)

[9] E. Hubble, Vol. 15, p. 618 (1929)

[10] W. L. Freedman *et al.*, Astrophys. J. **758**, 24 (2012)

[11] S. Dodelson, “Modern Cosmology," Oxford University Press (2008)

[12] M. Trodden and S. M. Carroll, “TASI lectures: Introduction to cosmology,” astro-ph/0401547.

[13] Planck 2013 Results Papers, http://www.sciops.esa.int/

[14] F. Zwicky, Helv. Phys. Acta **6**, 110 (1933)

[15] V. C. Rubin, A. H. Waterman and J. D. P. Kenney, Astron. J. **118**, 236 (1999)

[16] A. Einstein, Science **84**, 506 (1936)

[17] M. F. L’Annunziata “Radioactivity, Introduction and History," ISBN: 978-0-444-52715-8

[18] B. Pontecorvo, Sov. Phys. JETP **26**, 984 (1968) [Zh. Eksp. Teor. Fiz. **53**, 1717 (1967)].

[19] A. Goobar, S. Hannestad, E. Mortsell and H. Tu, JCAP **0606**, 019 (2006)

[20] K. Ichikawa, J. Phys. Conf. Ser. **120**, 022004 (2008)

[21] G. F. Smoot *et al.*, Astrophys. J. **396**, L1 (1992)

[22] A. G. Riess *et al.* [Supernova Search Team Collaboration], Astron. J. **116**, 1009 (1998)

[23] P. J. E. Peebles and B. Ratra, Rev. Mod. Phys. **75**, 559 (2003)

[24] Sean M. Carroll, "The Cosmological Constant", Living Rev. Relativity 4 (2001)

[25] R. Durrer, Phil. Trans. Roy. Soc. Lond. A **369**, 5102 (2011)

[26] S. Chatrchyan *et al.* [CMS Collaboration], Phys. Lett. B **716**, 30 (2012)

[27] A. D. Sakharov, Pisma Zh. Eksp. Teor. Fiz. **5**, 32 (1967)

[28] J. H. Jeans Vol. 199, (1902), p. 1-53, Published by: The Royal Society

[29] C. -P. Ma and E. Bertschinger, Astrophys. J. **455**, 7 (1995)

[30] D. Langlois, C. R. Physique 4 (2003) 953-959.

[31] E. F. Bunn, astro-ph/9607088.

[32] W. Hu, N. Sugiyama and J. Silk, astro-ph/9504057.

[33] W. Hu and S. Dodelson, Ann. Rev. Astron. Astrophys. **40**, 171 (2002)

[34] U. Seljak and M. Zaldarriaga, astro-ph/9805010.

[35] L. Krauss, S. Dodelson and S. Meyer, Science **328**, 989 (2010)

[36] D. Baumann, astro-ph/0907.5424

[37] W. H. Kinney, astro-ph/0902.1529

[38] W. H. Kinney, astro-ph/0301448.

[39] D. Baumann and H. V. Peiris, Adv. Sci. Lett. **2**, 105 (2009)

[40] A. R. Liddle, astro-ph/9901124.

[41] A. R. Liddle and D. H. Lyth, "Cosmological inflation and large scale structure," Cambridge, UK: Univ. Pr. (2000) 400 p

[42] P. A. R. Ade *et al.* [Planck Collaboration], astro-ph/1303.5062 .

[43] A. H. Guth, Phys. Rev. D **23**, 347 (1981)

[44] A. A. Starobinsky, Phys. Lett. B **91**, 99 (1980)

[45] W. H. Kinney, Phys. Rev. D **66**, 083508 (2002)

[46] A. D. Linde, JETP Lett. **38**, 176 (1983) [Pisma Zh. Eksp. Teor. Fiz. **38**, 149 (1983)]

[47] A. Albrecht and P. J. Steinhardt, Phys. Rev. Lett. **48**, 1220 (1982)

[48] S. Dodelson, W. H. Kinney and E. W. Kolb, Phys. Rev. D **56**, 3207 (1997)

[49] D. Wands, Lect. Notes Phys. **738**, 275 (2008)

[50] S. Dimopoulos, S. Kachru, J. McGreevy and J. G. Wacker, JCAP **0808**, 003 (2008)

[51] S. AKim and A. RLiddle, Phys. Rev. D **74**, 023513 (2006)

[52] C. L. Bennett *et al.* [WMAP Collaboration], Astrophys. J. Suppl. **208**, 20 (2013)

[53] P. A. R. Ade *et al.* [Planck Collaboration], astro-ph/1303.5075.

[54] P. A. R. Ade *et al.* [Planck Collaboration], astro-ph/1303.5082.

[55] N. Bartolo, E. Komatsu, S. Matarrese and A. Riotto, Phys. Rept. **402**, 103 (2004)

[56] P. A. R. Ade *et al.* [Planck Collaboration], astro-ph/1303.5084.

[57] M. Benetti, M. Gerbino, W. H. Kinney, E. W. Kolb, M. Lattanzi, A. Melchiorri, L. Pagano and A. Riotto, JCAP, Issue 10, article id. 030, pp. (2013)

[58] P. A. R. Ade *et al.* [Planck Collaboration], astro-ph/1303.5076.

[59] G. L. Fogli, E. Lisi, A. Marrone, A. Melchiorri, A. Palazzo, A. M. Rotunno, P. Serra and J. Silk *et al.*, Phys. Rev. D **78**, 033010 (2008)

[60] M. Archidiacono, E. Calabrese and A. Melchiorri, Phys. Rev. D **84**, 123008 (2011)

[61] J. Hamann, S. Hannestad, J. Lesgourgues, C. Rampf and Y. Y. Y. Wong, JCAP **1007** (2010) 022

[62] R. Bowen, S. H. Hansen, A. Melchiorri, J. Silk and R. Trotta, Mon. Not. Roy. Astron. Soc. **334** (2002) 760

[63] Z. Hou, R. Keisler, L. Knox, M. Millea and C. Reichardt, astro-ph/1104.2333 .

[64] W. Hu, D. J. Eisenstein and M. Tegmark, Phys. Rev. Lett. **80** (1998) 5255

[65] J. L. Sievers *et al.* [Atacama Cosmology Telescope Collaboration], JCAP **1310**, 060 (2013)

[66] S. Das *et al.*, astro-ph/1301.1037

[67] D. Hanson *et al.* [SPTpol Collaboration], Phys. Rev. Lett. **111**, 141301 (2013)

[68] K. T. Story, C. L. Reichardt, Z. Hou, R. Keisler, K. A. Aird, B. A. Benson, L. E. Bleem and J. E. Carlstrom *et al.*, Astrophys. J. **779**, 86 (2013)

[69] A. G. Riess *et al.*, Astrophys. J. **730**, 119 (2011) W. L. Freedman *et al.*, Astrophys. J. **758**, 24 (2012)

[70] Padmanabhan*et al.*, (2012) astro-ph/1202.0090.

[71] L. Anderson*et al.*, (2012) astro-ph/1203.6594.

[72] C. Blake *et al.*, Montly Notices of the Royal Astronomical Society, 425, 405 (2012).

[73] E. Di Valentino, S. Galli, M. Lattanzi, A. Melchiorri, P. Natoli, L. Pagano and N. Said, Phys. Rev. D **88**, no. 2, 023501 (2013)

[74] G. Hinshaw *et al.* [WMAP Collaboration], Astrophys. J. Suppl. **208**, 19 (2013)

[75] J. Norena, C. Wagner, L. Verde, H. V. Peiris, R. Easther and , Phys. Rev. D **86**, 023505 (2012)

[76] S. M. Feeney, H. V. Peiris, L. Verde and , astro-ph/1302.0014.

[77] L. McAllister, S. Renaux-Petel and G. Xu, JCAP **1210**, 046 (2012)

[78] D. J. Fixsen, Astrophys. J. **707**, 916 (2009)

[79] G. Mangano, G. Miele, S. Pastor, T. Pinto, O. Pisanti and P. D. Serpico, Nucl. Phys. B **729** 221 (2005)

[80] R. Easther and W. H. Kinney, Phys. Rev. D **67**, 043511 (2003)

[81] W. H. Kinney, E. W. Kolb, A. Melchiorri and A. Riotto, Phys. Rev. D **69**, 103516 (2004)

[82] A. A. Starobinsky, JETP Lett. **55**, 489 (1992) [Pisma Zh. Eksp. Teor. Fiz. **55**, 477 (1992)].

[83] J. A. Adams, B. Cresswell and R. Easther, Phys. Rev. D **64**, 123514 (2001)

[84] J. Lesgourgues, Nucl. Phys. B **582**, 593 (2000)

[85] J. A. Adams, G. G. Ross and S. Sarkar, Nucl. Phys. B **503**, 405 (1997)

[86] A. Ashoorioon and A. Krause, hep-th/0607001.

[87] J. E. Lidsey, A. R. Liddle, E. W. Kolb, E. J. Copeland, T. Barreiro and M. Abney, Rev. Mod. Phys. **69**, 373 (1997)

[88] W. H. Press, S. A. Teukolsky, W .T. Vetterling, B. P. Flannery, Numerical Recipes in Fortran 90: The Art of Parallel Scientific Computing, Volume 2 of Fortran Numerical Recipes, Second Edition (New York: Cambridge University Press, 1996).

[89] J. Hamann, L. Covi, A. Melchiorri and A. Slosar, Phys. Rev. D **76**, 023503 (2007)

[90] M. Benetti, M. Lattanzi, E. Calabrese and A. Melchiorri, Phys. Rev. D **84**, 063509 (2011)

[91] P. Adshead and W. Hu, Phys. Rev. D **85** 10353 (2012)

[92] P. Adshead, C. Dvorkin, W. Hu, and E. A. Lim, Phys. Rev. D **85** 023531 (2012)

[93] M. Benetti, S. Pandolfi, M. Lattanzi, M. Martinelli and A. Melchiorri, Phys. Rev. D **87**, 023519 (2013)

[94] M. Benetti, Phys. Rev. D **88**, Issue 8, id. 087302

[95] C. P. Ahn *et al.* [SDSS Collaboration], Astrophys. J. Suppl. **203**, 21 (2012)

[96] E. Komatsu *et al.* [WMAP Collaboration], Astrophys. J. Suppl. **192**, 18 (2011)

[97] S. Das *et al.*, Astrophys. J. **729**, 62 (2011)

[98] J. Dunkleyl *et al.*, Astrophys. J. **739**, 52 (2011)

[99] S. Galli, M. Martinelli, A. Melchiorri, L. Pagano, B. D. Sherwin and D. N. Spergel, Phys. Rev. D **82**, 123504 (2010)

[100] J. Tauber *et al.* [Planck Collaboration], astro-ph/0604069.

[101] K. N. Abazajian *et al.* [SDSS Collaboration], Astrophys. J. Suppl. **182**, 543 (2009)

[102] R. Amanullah, C. Lidman, D. Rubin, G. Aldering, P. Astier, K. Barbary, M. S. Burns and A. Conley *et al.*, Astrophys. J. **716**, 712 (2010)

[103] A. G. Riess, L. Macri, S. Casertano, M. Sosey, H. Lampeitl, H. C. Ferguson, A. V. Filippenko and S. W. Jha *et al.*, Astrophys. J. **699**, 539 (2009)

[104] M. J. Mortonson, C. Dvorkin, H. V. Peiris and W. Hu, Phys. Rev. D **79**, 103519 (2009)

[105] R. Trotta, Contemp. Phys. **49**, 71 (2008)

[106] A. Gelman and D. B. Rubin, Statist. Sci. **7**, 457 (1992)

[107] A. Lewis and S. Bridle, Phys. Rev. D **66**, 103511 (2002)

[108] A. Lewis, A. Challinor and A. Lasenby, Astrophys. J. **538**, 473 (2000)

[109] H. Jeffreys , “Theory of Probability", Oxford University Press (Oxford, UK), 1961.